Nanoscale properties of self-assembled and laterally nanostructured surface systems

Marcos Paradinas Aranjuelo

Supervisor: Prof. Carmen Ocal García

Tutor: Prof. Jordi Pascual Gainza

Programa de Doctorat en Ciència de Materials
Departamento de Física
Universitat Autònoma de Barcelona
Institut de Ciència de Materials de Barcelona
Consejo Superior de Investigaciones Científicas
Bellaterra, September 2014

Carmen Ocal García, investigadora del CSIC a l'Institut de Ciència de Materials de Barcelona, i **Jordi Pascual Gainza,** investigador i professor a la Universitat Autònoma de Barcelona

CERTIFIQUEN

Que **Marcos Paradinas Aranjuelo**, llicenciat en Ciències Físiques, ha dut a terme sota la seva direcció i tutoria el treball que porta per títol *" Nanoscale properties of self-assembled and laterally nanostructured surface systems"* i queda recollit en aquesta memòria per optar al grau de Doctor en Ciència de Materials.

I per a que així consti, signen el present certificat.

Directora	Tutor
Prof. Carmen Ocal García	Prof. Jordi Pascual Gainza

Marcos Paradinas Aranjuelo

Bellaterra, Setembre 2014

That we find a crystal or a poppy beautiful means that we are less alone, that we are more deeply inserted into existence than the course of a single life would lead us to believe.

John Berger, The White Bird

Abstract

The present work lies within the scope of the morphological, mechanical, electrostatic and conductive characterization of self-assembled and nanostructured systems, including organic thin films and inorganic surfaces. Scanning probe microscopy (SPM) techniques, in general, and scanning force microscopy (SFM), in particular has become one of the most powerful tools in nanotechnology because they offer the combined capability of surface properties characterization and manipulation of material surfaces in the nanoscale. In this work we make use of SPM, both SFM and scanning tunneling microscopy (STM), techniques under controlled ambient conditions for the characterization and manipulation of different self-assembled and nanostructured systems. We mainly focus on the use of SFM in contact, dynamic, friction force microscopy (FFM), conductive scanning force microscopy (CSFM) and Kelvin probe force microcopy (KPFM) operating modes for such a purpose.

The thesis is organized in the following way: the motivations for this work are presented in chapter 1, and a short introduction to the self-assembled concept and nanostructured systems in organic thin films and inorganic surfaces is done in chapter 2.

Chapter 3 introduces the fundamental description of the experimental techniques and procedures used. The main experimental characterization SPM techniques are introduced and a particular attention is devoted to explain the different SFM techniques used. In the same chapter, the growth techniques of organic thin film are explained, including, the solution based methods, the soft lithography µ-contact printing (μCP) and the organic molecular beam deposition (OMBD).

In chapter 4 we investigate the influence of the supramolecular structure of self-assembled monolayers (SAMs) into the morphological, mechanical, electrostatic and conductive properties of a functionalized surface. For this purpose we study the $CH_3(C_6H_4)_2(CH_2)_4SH)$ (BP4) molecule SAM on the $Au(111)$ surface presenting two different coexisting supramolecular arrangements.

We show how the supramolecular order of the SAM is a decisive factor influencing the nanoscale properties of the surface and also demonstrate how FFM can be employed to differentiate SAM domains with different orientation. In addition, based on electron current measurements, the combined use of STM and CSFM allows us interpreting the differences in apparent height as measured by one or the other technique in non-homogeneous organic layers.

In chapter 5 we study the properties of the nanopatterned $SrTiO_3$ (001) surface and explore its use as template for the selective adsorption of SAMs. We find that stearic acid molecules (containing a $COOH$ headgroup) selectively chemisorb on the TiO_2 surface. This fact allows us to investigate SAMs adsorption influence on the mechanical and electrostatic properties of this oxide surface. We address the main characteristics of the nanopatterned $SrTiO_3$ (001) surface and we describe the selective adsorption of SAMs on the TiO_2 surface, discussing how this influences the local mechanical and electrostatic properties of the surface.

Finally, in chapter 6 we present two different tip-induced effects which can be use to manipulate organic thin film materials. We address the mechanical induced growth of pentacene molecular layers, a phenomena that can be used as a local nanolithography approach for nanostructuration. And we also provide a way for peeling a layered organic molecular material when a voltage is applied between the conducting system and the conducting probe of the SFM, which is important to take into account for the design of organic electronic devices.

Resumen

Las microscopías de campo cercano en general (SPM) y la microscopia de fuerzas (SFM) en particular, se han convertido en una poderosa herramienta en nanotecnología, ya que permiten tanto caracterizar como manipular las superficies de los materiales en la nanoescala. En el presente trabajo de investigación se han estudiado las propiedades morfológicas, mecánicas, electrostáticas y de conducción de sistemas autoensamblados y nanoestructurados que incluyen películas delgadas orgánicas y superficies inorgánicas mediante estas técnicas de SPM, SFM y microscopía de efecto túnel (STM), en condiciones de ambiente controlado. Nos centramos principalmente en el uso de técnicas de SFM en modos de operación de contacto, dinámico, microscopía de fuerzas de fricción (FFM), conductividad con SFM (CSFM) y microscopía de sonda Kelvin (KPFM).

El manuscrito de la tesis está organizado del siguiente modo: en el capítulo 1 se exponen las motivaciones del trabajo y en el capítulo 2 se hace una pequeña introducción al concepto de autoensamblado y a los sistemas nanoestructurados en los sistemas bajo estudio, películas delgadas orgánicas y superficies inorgánicas.

En el capítulo 3 se introducen las distintas técnicas y procedimientos experimentales. Se explican las características generales del SPM, haciendo particular hincapié en los modos de operación de SFM empleados. En el mismo capítulo se explican los procedimientos empleados para el crecimiento de películas delgadas orgánicas, incluyendo los métodos químicos de solución molecular, la litografía “microcontact printing” (μCP) y la deposición de moléculas orgánicas por haces moleculares (OMBD).

En el capítulo 4 investigamos el impacto de la estructura supramolecular de las capas orgánicas autoensambladas (SAMs) en las propiedades morfológicas, electrostáticas y de conducción de superficies funcionalizadas. Con este propósito y para poder realizar un análisis comparativo basado en el uso de referencias in-situ, estudiamos la SAM formada por dos fases supramoleculares de la

misma molécula $CH_3(C_6H_4)_2(CH_2)_4SH$) (BP4) coexistiendo en la superficie $Au(111)$. Mostramos como la organización supramolecular (estructura interna de la película orgánica) es un factor decisivo que determina las propiedades de la superficie y demostramos como la técnica FFM puede emplearse, por ejemplo, para diferenciar dominios moleculares de distinta orientación cristalina. Además, gracias al uso combinado del STM y CSFM en medidas de transporte electrónico, interpretamos la diferencia en la altura aparente medida por una u otra técnica en películas orgánicas inhomogéneas.

En el capítulo 5 estudiamos las propiedades de la superficie $SrTiO_3(001)$ nanoestructurada. La nanoestructuración en este caso viene dada por la coexistencia de las dos posibles terminaciones, TiO_2 y SrO, lateralmente diferenciadas, que empleamos como plantilla para la adsorción selectiva de SAMs. Demostramos que la molécula de ácido esteárico (con funcionalidad $COOH$) se adsorbe selectivamente en la superficie TiO_2 y estudiamos el impacto de su adsorción sobre las propiedades mecánicas y electrostáticas de la superficie. Así, describimos las principales características de la superficie $SrTiO_3$ (001) nanoestructurada, la adsorción de la SAM en la superficie TiO_2 y discutimos el impacto de esta adsorción en las propiedades de la superficie.

Finalmente, en el capítulo 6 presentamos dos efectos inducidos por la punta del SFM susceptibles de usarse para la manipulación local y controlada de películas orgánicas. Mostramos el crecimiento de multicapas de pentaceno inducido mecánicamente y un efecto de pelado de capas moleculares al aplicar voltajes entre una punta conductora y materiales moleculares conductores, un efecto a tener en cuenta en el diseño de futuros dispositivos en electrónica molecular.

Contents

Chapter 1

Motivation

In the last decades nanoscience and nanotechnology, understood as the investigation and design of materials at the atomic and molecular level, have emerged as a field of science and applications in which both research and technology develop together (in the length scale of approximately $1 - 100\,nm$) to provide a fundamental understanding of phenomena in materials that have novel properties and functionalities because their small size Schaefer [1]. Far from being a dream, manipulating matter at the atomic level is already possible and, therefore, this discipline starts playing an important role for the next future applications. In this context, designing nanostructured surfaces with specific physical and/or chemical properties is of enormous importance from an applied point of view. In addition, the structuration of materials on the atomic or molecular scale is also important from a fundamental point of view, since they constitute model systems for studying different fundamental questions and new phenomena. Many different aspects and characteristics of nanostructured surfaces still remain unraveled and in consequence deserve further specific and directed studies.

The different approaches employed in nanotechnology for nanostructuring materials synthesizing are classified in two categories, the so called top-down and bottom-up methodologies. Top-bottom techniques are based in carving nanomaterials out of bulk materials. Methodologies in this category are referred to as different forms of lithography and include writing and replicating. Writing involves designing a pattern on a negative (usually a mask), and replication involves transferring the pattern on the negative to a functional material. Nanostructures writing can be also performed by locally manipulating atoms or molecules using a nanometric size probe. On the other hand, the most common bottom up strategies are based on fabricating nanomaterials out of independent individual building blocks. In particular, the chemical self-assembly or spontaneous organization of atoms and/or molecules to form ordered arrangements and well defined structures. That is, thanks to the interatomic or intermolecular forces, the spontaneous formation of complex architectures and/or nanostructures can be obtained. In general this is a simple and low cost process which can cover from the nano to the micrometer scale, making the idea attractive from a technological point of view. This is basically the main reason why, during the last two decades, much effort has been done in structuring matter by bottom-up self-assembling processes, one of the most promising fields of research in nanoscience and material science. In the present work we make use of methods that are categorized within both, bottom-up and top-down techniques to obtain nano and micro structured surface systems.

Among the wide variety of functional materials, organic materials are attracting increasing interest because their importance in the development of diverse emerging areas in nanoscience and technology. Those materials are important for a large number of applications including devices for molecular electronics, energy conversion, etc... Besides, due to the synthetic capabilities of organic chemistry there is nearly no limitation on the creation of new functional materials. In addition, organic molecular materials present the ability to self-assembly and form well ordered thin films on a wide variety of inorganic surfaces that make them appealing for device fabrication. Moreover, gaining insight into the characteristics of those hybrid organic-inorganic systems and interfaces, such as metal or oxide supported organic films, is the first step in the pursuit of molecular-scale devices. Besides constituting excellent candidates to solve practical issues in nanotechnology, organic thin films are intrinsically interesting from the point of view of basic science, since they are systems for studying different fundamental process occurring at surfaces and interfaces.

Much of the progress in nanotechnology and material science stems from the emergence of scanning probe microscopy techniques (SPM). Nowadays, SPM techniques are the most versatile tools in nanotechnology because they enable both, the study of local surface properties and the manipulation of matter at the molecular and atomic scale. The scanning tunneling microscopy (STM) usually offers better spatial resolution than scanning probe microscopy (SFM), however, SFM offers the main advantage to image surfaces independently of their conductive properties, and in addition, it presents the capability of simultaneously measuring morphology and other surface properties such as mechanical, conductive, electrostatic, magnetic, etc.... For these reasons, in this work we have used high-resolution SPM techniques in general and scanning force microscopy (SFM) in particular following different strategies to unravel those properties for nanostructured systems, including organic thin films and inorganic surfaces.

Chapter 2

Self-assembling and nanostructuration

2.1 Self-assembly concept

The term self-assembly is nowadays extensively used, which occasionally causes confusion. In a general sense, it can be defined as the spontaneous process in which a disordered system of pre-existing components forms an organized structure as a consequence of specific local interactions among the components themselves without guidance from an outside source. However, in each scientific discipline the concept of self-assembly is understood on its own particular way and the term is sometimes used interchangeably with the term self-organization, that sometimes causes confusion [1–4]. For a critical review of the concepts of self-assembly and self-ordering in different disciplines we refer to [4].

More specifically related to the main topic of this work, molecular self-assembly is the phenomenon in which a number of independent organic molecules in a very diluted solution come together to form an ordered aggregate without guidance from an outside source. The molecular self-assembly is driven through noncovalent interactions such as, van der Waals forces, hydrogen bonds, $\pi - \pi$ interactions, etc... [2, 5]. In the context of the present work, the self-assembled organic films are formed when molecules organize themselves in a given arrangement on the surface of a substrate. In the following section 2.2 a brief introduction to the self-assembled organic films is done.

In this work we also make use of the term self-assembly in the context of self-ordering of inorganic material (in chapter 5). In this context, the self-assembling words indicate that no direct control on the atomic level is applied, the system evolves by atomic diffusion being influenced only by macroscopic parameters (e.g. temperature, atmosphere, etc...).

2.2 Organic thin films

Soft and molecular materials comprised of low molecular weight organic molecules are attracting increasing interest because their importance in the development of a number of emerging areas in nanoscience and technology. Those materials are important for a wide variety of applications including molecular electronics, nanosystems for energy conversion, devices etc. Besides, due to the synthetic capabilities of organic chemistry there is nearly no limitation on the creation of new functional materials and devices [5, 6]. Although the organic thin films are not a discovery of the past 20th century, over the last decades they are attracting considerable attention because they face the relevant issue in nanoscience of dimensionality reduction [5]. Furthermore, the ability of organic molecular materials to self-assembly and form well ordered thin films on a wide variety of surfaces make them appealing for device fabrication by the so-called bottom-up strategies.

In the context of the present work, we make a distinction between the molecular thin films formed by chemisorption or physisorption of the molecules on surfaces. We use the term self-assembled monolayers (SAM) for the ordered molecular assemblies formed spontaneously by their chemisorption and arrangement on a solid surface, whereas we use the term small organic molecule layers for those cases where molecules physisorb and self-assemble on the surface. In the following sections 2.2.1 and 2.2.2 we make a brief introduction to these organic molecular layers.

2.2.1 Self-assembled monolayers

Self-assembled monolayers (SAMs) are ordered molecular assemblies that are formed spontaneously by the adsorption of molecules with a specific affinity of their headgroup to a substrate [5]. The main reason that has made this systems so interesting is that these SAMs are easy to generate and form densely packed and precisely oriented films, with determined thickness and surface properties. SAMs can be grown either by immersion in molecular solution or under vacuum conditions by molecular deposition from the gas phase, however due to their easy preparation and low cost usually the first method is used. A SAM is simply produced by immersing the substrate in a solution of the corresponding molecule. The molecules anchor to the substrate by their headgroup and laterally assemble to each other, the covering process will end once the complete monolayer is formed. Figure 2.2.1 shows a picture of a self-assembled monolayer formation. We note that this process typically stops at the monolayer formation and does not extend to the formation of multiple monolayers because the headgroup of the SAM is chosen to specifically anchor the substrate atoms but not the surface of the monolayer (the endgroup of the molecule). Typically a thiolate monolayer on gold forms in a few hours, however in many cases for obtaining high quality free of defects films longer immersion times or special preparation condition (as temperature annealing) are necessary. Ethanol is the most used solvent, but depending on the molecule other solvents such as water, acetone, dichloromethane etc are also used.

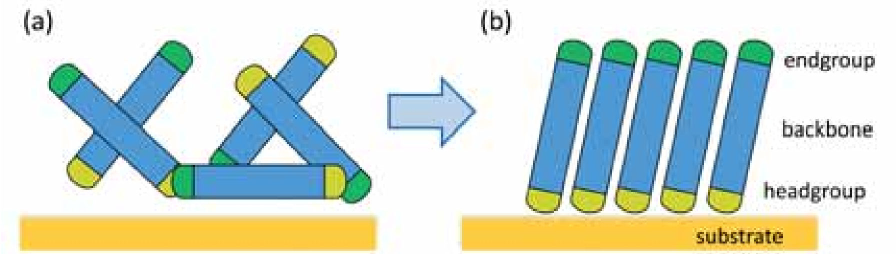

Figure 2.2.1: *Schematic representation of a SAM formation is presented from (a) to (b). The different parts of the molecules have been highlighted on the right.*

When describing the formation and organization of SAMs, it is useful to divide the structure of the molecule into three parts (see figure 2.2.1 b):

i) headgroup: it is the part of the molecule that interacts with the substrate and its bonding (chemisorption) to the substrate is essential in the monolayer formation.

ii) spacer or backbone: this part of the molecule act as a physical barrier between the substrate and the external environment and is responsable of the quality of the packing via cohesion energy. For the simplest SAMs studied, the backbone is formed by an alkyl chain (CH_2 groups) whose length normally varies between 1 and 3 nm, depending on the number of methylene groups. The SAMs backbone provides well-defined thickness (∼backbone length) and alters the electronic conductivity and local optical properties.

iii) terminal group or endgroup: it is the part of the molecule exposed to the external environment and therefore the one determining the SAMs´ surface properties.

The wide range of applicability of these SAMs stems mainly from the flexibility to modify one or several of these parts and thus change the final films's properties. The type of headgroup is typically used to define the individual SAM system and it is choosen in function of the chemistry of the employed substrate. The most investigated SAM-substrate systems include: organosulfur compounds such as thiols ($R-SH$), sulphides (RSR') or disulphides ($RSSR'$) for metallic surfaces (Au, Ag, Hg or Cu), carboxylic acids ($R-COOH$) on oxides (TiO_2, Al_2O_3, etc), organosilanes ($R-SiCl_3$, $R-SiH_3$, $R-Si(OH_3)_3$) and organophosphonic acid ($R-PO(OH)_2$) on hydroxylated surfaces (SiO_2, Al_2O_3, $mica$, $glass$), etc. The variation in the chemical bond between the molecule and the substrate also plays a role in the strength of the interaction and thereby, the stability of the assembly, but also properties as the electron transmission from the molecule to the surface under applied potential and changes in the inner structure and nature of the film affects its innate ability to order. The terminal functional group of a SAM exerts the most direct influence on the surface properties of the film: hydrophobic/hydrophilic character, adhesive and frictional characteristic, chemical reactivity, electrostatic etc. For this reason chemical modification of the endgroup is an active field of research. Some common terminal groups employed in SAMs include CH_3,$-COOH$, $-OH$, $phenyl$, $pyridine$, etc.

SAMs are of particular relevance in a wide variety of fields to improve or modify the characteristics of the materials surfaces. The earlier application of SAMs was based in their lubricant character and their ability to prevent corrosion of the underlying surface. Therefore, they have been employed in relatively conventional electromechanical devices as lubricating layers [7]. Nowadays, the applications range has considerably widened from electronics and spintronics, to biosensors, bio-recognition devices and drug delivery, just to name a few. For a more extended view of the concepts, growth and applications of SAM we refer to [5, 6, 8, 9].

In the present thesis we use thiols for the functionalization of gold surface by solution deposition methods (in chapters 4). The use of sulphur-containing compounds on gold, and in particular of thiols, have attracted most of the research interest because they form densely packed and precisely oriented films and are easy to prepare. Moreover, the use of gold substrates provide additional advantages; firstly it binds thiols with high affinity (the S-Au interaction is of about $\sim 1.3\ eV$ [6]), which promotes the displacement of adsorbed solvent from the gold surface readily. Secondly, it is a reasonably inert metal. When compared with other metals, gold has the lowest tendency to react with air to form oxides; it does not react with atmospheric O_2 ; it does not react with most chemicals. This allows working for relatively long periods of time under ambient conditions.

Moreover, by the appropriate preparation of the Au substrates large extended (∼hundreds of nm) atomically flat $Au(111)$ terraces can be obtained (see section 3.4.1). In addition to thiols, for the work presented in chapter 5 we make use of the stearic acid molecule, containing a carboxylic acid ($R-COOH$) headgroup, for the functionalization of $SrTiO_3$ surface because it is known that the carboxylate function interacts favorably with oxide surfaces.

2.2.2 Small organic molecular layers

The use of small molecules as building blocks for the formation of organic thin film is present in a wide range of applications [10, 11] such as in organic field-effect transistors (OFETs)[12, 13], organic light-emitting diodes (OLEDs)[14], solar cells [15], sensors [16], molecular magnets [17], etc...

The most common methods for obtaining organic thin films formed by small organic molecules are based on the deposition from chemical solution or vapour phase. Each method present some advantage and disadvantages. Vapor phase methods have the advantages of presenting a good control over the growth rate, film thickness and growth temperature of a chemical pure compound on an atomically clean substrate and environment. Those methods give rise to exceptionally high-quality films with well-ordered films. However, vapor-based methods are relatively expensive and may be difficult to scale up to manufacturing processes. On the contrary, those are precisely some the main advantages of the solution based methods, that are easy to prepare, low cost and scalable.

In this work we make use of the vapor-based method organic molecular beam deposition (OMBD) (introduced in section 3.4.4) for the growth of pentacene submonolayers (in section 6.2), and solution methods for the deposition the tetrathialfulvalene derivative 2- (thioacetooctadecylamide)-3-methylthio-6,7- ethyldithiotetrathiafulvalene molecule (TTF-derivative) (section 6.3).

2.3 Nano(micro)-structuration of surfaces: organic and inorganic

The two basic approaches in nanotechnology for structuring matter in a controlled and repeatable manner are the top-down and bottom-up techniques [3, 18]. The top-down approach makes use of methods of lithography to pattern nanostructures, and the bottom up fabrication strategies are based on the spontaneous self-assembly of atoms and/or molecules. In this thesis we present different structured surface sytems obtained by bottom-up and top-down approaches, with nm size structures in the direction normal to the surface and structuration sizes ranging from tens of nm to the μm on lateral dimensions in the surface plane.

Among the bottom-up approaches, we present two examples nanostructuration driven by temperature. In chapter 4 temperature and time controlled supramolecular phase transition yields to the nanostructuration of $Au(111)$ surface with the co-existence of two polymorphic phases of the same molecular unit on top. The ratio between areas covered by each phase is dependent on the precise annealing time employed and can be therefore tuned at while. The molecular domains present sizes ranging from tens to hundreds of nanometers and can be tunned. In chapter 5 the nanopatterning of the $SrTiO_3$ surface with sizes ranging from hundreds of nanometers to micrometers is achieved by the thermal process of the TiO_2 and SrO terminations self-assembly. Moreover, the presented procedure can be employed as a method to fabricate functional oxide nanostructures ordered over the centimeter scale [19]. In addition, these nanopatterned oxide surfaces can be employed as template for the selective chemisorption of SAMs as in shown in section 5.3 what could be extended to other functional molecules, and furthermore, to be used for the controlled growth of 3D nanostructures.

Among the top-down approaches, in chapter 4 we make use of the $\mu-$contact printing (μCP) patterning method to laterally functionalize gold substrates by SAMs in the μm range and in chapter 6 we present examples of tip-induced matter manipulation that yield to the formation of nanostructures of tens to hundreds of nm.

Chapter 3

Instrumentation and sample preparation techniques

The goal of this chapter is to make a brief introduction to the experimental techniques that have been employed through this thesis. The first three sections 3.1, 3.2 and 3.3 are devoted to explain the main experimental characterization techniques in which this thesis is based on, the scanning probe microscopy (SPM) in general, and with particular attention, in the scanning force microscopy (SFM) in ambient conditions. We start by introducing in section 3.1 the SPM techniques. In sections 3.2 and 3.3 we extend and focus the explanation to SFM and scanning tunneling microscopy (STM) techniques respectively. Final section 3.4 is devoted to introduce the main experimental techniques used for the sample preparation, including the main characteristics of the employed gold substrates (section 3.4.1), molecular solutions (section 3.4.2) and μ-contact printing (section 3.4.3) and organic molecular beam deposition (section 3.4.4) techniques.

3.1 Scanning probe microscopy techniques

Scanning probe microscopy (SPM) is a branch of microscopy that uses a physical nanometric-sized probe to measure surface properties of materials by monitoring a certain short-range probe-sample interaction. The sample surface is usually scanned by mechanically moving the probe in a raster scan of the sample, line by line, and recording the magnitude of the probe-surface interaction of interest as a function of position. The collected data are usually arranged as a two-dimensional grid of data points and typically visualized in false color as image. In the different SPM techniques the working principles vary, however as general rule the signal used as feedback source is essentially a certain interaction between the probe and the sample.

The dawn of the SPM came in 1982 with the invention of the scanning tunneling microscope (STM) by Heinrich Roher and Gerd Binnig [20, 21]. STM is based on the quantum tunneling effect, which formulates that a current can flow between two electrodes separated by an insulator or vacuum gap. In this microscope, a sharp metallic tip is brought close to a conductive surface and, upon applying a voltage, a current flows between tip and sample. In a standard experiment the tip is moved in three dimensions over the surface while an electronic controller keeps the tunneling current constant by means of a feedback loop that varies the tip-sample distance. This distance is recorded as a function of the tip lateral position and displayed as an image. The lateral resolution on STM is down the Å range what makes possible true lateral atomic resolution, while the vertical resolution is in the range of ~ 0.1Å. The use of STM however posses a severe limitation, it is restricted to electrically conductive samples.

With the development of the scanning force microscopy (SFM) [22] the possibility to image surfaces independently of their conductive properties was reached, being possible to measure almost any surface. In this case, the metallic tip is replaced by a tip attached to a force sensor, the so-called cantilever, to measure the interaction forces acting between probe and surface. The success of the SFM technique mainly arises from the possibility to image surfaces independently of their conductive properties, but SPM in general and SFM in particular, offer much more than just imaging the surface profile. Besides surface topography, the probe-sample interactions also reveal information about lattice symmetry, adhesion, friction, elasticity, wear, conductivity, electrostatic, piezoelectric, etc...properties of material surfaces with unprecedented nanometric spatial resolution. In the last decades the SPM techniques have become a powerful tool in nanotechnology. Not only to visualize nano scale objects down to atomic details on a wide range of materials in vacuum , ambient air, or liquid, but also to obtain a wide variety of their mechanical, electronic, compositional, etc...properties. Some alternative and outstanding applications of SPM in the field of material science have been collected in [23].

In the following sections we will give a brief description of the SPM techniques with particular attention to those employed throughout this thesis. In the next section 3.1.1 we start introducing the key components shared in SPM techniques, in section 3.2 we will extend and focus on the SFM components and operation modes, and finally, we will briefly introduce the basic operating mode of the STM in section 3.3.

3.1.1 Basic components on Scanning Probe Microscopy

All Scanning probe microscopy (SPM) techniques share some key components which are the base of their great performance. In figure 3.1.1 a schematic representation of a SPM system is shown. The key component in any SPM technique is the nanometric size probe, which is the sensor that enables us to measure a certain tip-surface interaction (f_i) with nanometer spatial resolution. Depending on the technique or/and measuring mode, the specification of the tip varies (composition, shape, etc...) , but typically as a general rule the goal is to have the possible sharpest tip to enhance the lateral resolution of the measurement. All the SPM techniques are based in monitoring a given tip-sample interaction (f_i) that the tip *senses*, to this end, the corresponding physical quantity to this interaction has to be accurately measured. As its name indicates, the physical quantity of interest in STM is the current that flows between tip-sample system which is monitored by low noise amperimeter. And in the case of the SFM, the force acting on the tip is the corresponding monitored physical quantity. A detailed explanation of the operation of the force sensor will be presented in the following section 3.2.

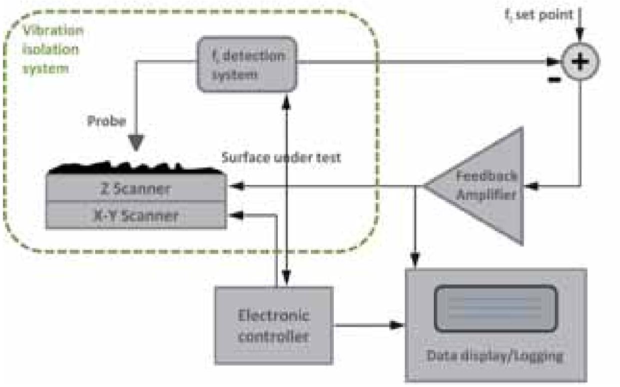

Figure 3.1.1: *Schematic representation of the basic elements shared in SPM techniques: nanometric scale probe, f_i physical quantity detection system, a piezo actuator that acts as scanner (for x,y,z sample motion), a vibration isolation system, an electronic control unit (piezo control and feedback amplifier) and a computer with an internal DSP board.*

Together with the probe, the most relevant component of a SPM instrument is the scanner. In SPM techniques, the probe needs to be positioned with an accuracy of $1\,pm$ if atomic resolution is required. For accurate and sensitive positioning and sample motion, the sample (or tip) is mounted on a piezoelectric (lead-zirconate-titanate, PZT) ceramic tube coated with metallic electrodes in a four segmented fashion (see figure 3.1.2). When a potential difference is applied across the electrodes, the piezoelectric ceramic expands or contracts in a direction that is perpendicular to the applied electric field. The expansion or contraction of the piezoelectric is controlled by the polarity of the applied voltage difference, and its amplitude by the magnitude of the voltage difference. A voltage difference applied between the interior electrode and all the outers causes the vertical (Δz) displacement (figure 3.1.2 a), whereas the lateral motion for 2D scanning ($\Delta x, \Delta y$) is achieved by biasing the opposite external electrodes in the corresponding x or/and y direction (figure 3.1.2 b). In most experimental set ups, the tip is fixed and the sample is attached to a piezoelectric actuator, which moves in three dimensions, while an electronic feedback circuit controls the probe sample distance to keep constant the employed tip-sample interaction magnitude.

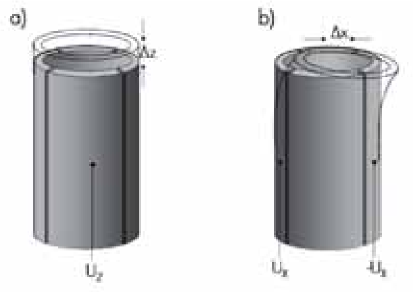

Figure 3.1.2: *Schematic representation of the response of a tube-shaped piezo actuator to an applied voltage between the internal and external electrodes (a) and two opposite external sectors (b). From the PhD Thesis of Carmen Munuera [24].*

For the correct conversion factor between applied voltage and piezo displacements, periodical calibrations are done. Commercial calibration grids with known lateral and vertical dimensions are employed for large piezo scans (figures 3.1.3 a and b) whereas flame annealed gold substrates, exhibiting $Au(111)$ terraces separated by monoatomic steps, are used for small scans calibration (figure 3.1.3 c). The height of these monoatomic steps ($d_{Au}(111) = 0.235\,nm$) provides accurate reference for the vertical calibration (figure 3.1.3 bottom). Moreover, from the lattice-resolved hexagonal periodicity ($a_{Au} = 0.289\,nm$) of $Au(111)$ measured by high resolution lateral force images, the lateral calibration is refined to the atomic level (figure 3.1.3 d) [1]. Two methods for reliably measuring the height in our topographic images are illustrated in the bottom part of figure 3.1.3.

Also home flame annealed gold substrates exhibiting (111) oriented terraces were employed for

---

[1] Detailed description of how this SFM atomic periodicity images are acquired can be found in section 3.2.5.1

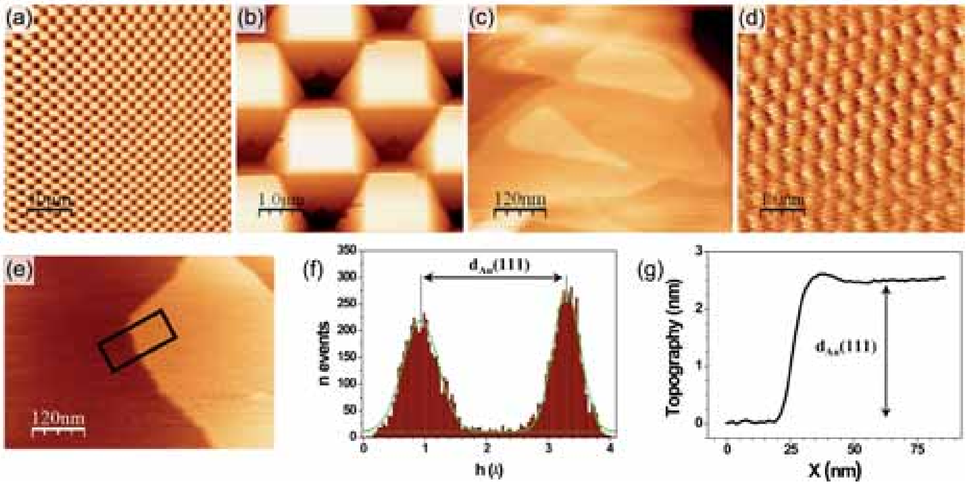

Figure 3.1.3: *Top: (a),(b) Different magnification SFM images of a commercial calibration grating. (c) Topographic and (d) lattice-resolved lateral force images of the Au (111) surface. Bottom: Two different ways of measuring heights (averaged profiles and histograms) from the corresponding topographic image shown in (e). From the selected area marked in (e) the height histogram is calculated (f) and the averaged profile plotted in (g). Lines in the histogram are the corresponding Gaussian fits.*

vertical and lateral calibrations of the STM scanner. In figure 3.1.4 (a) a constant current STM (cc-STM) image of gold substrate exhibiting $Au(111)$ terraces separated by monoatomic steps is presented[2]. Height histograms as the one presented in figure 3.1.4 (b), corresponding to the location marked in (a) with green dashed square containing several $Au(111)$ monoatomic steps are used for vertical calibration. The lateral dimensions of the $22 \times \sqrt{3}$ reconstruction of $Au(111)$ surface [25, 26], visible in enlarged image of figure 3.1.4 (c) corresponding to the location marked by the red square in (a), can be also used for the lateral calibration of the piezo scanner.

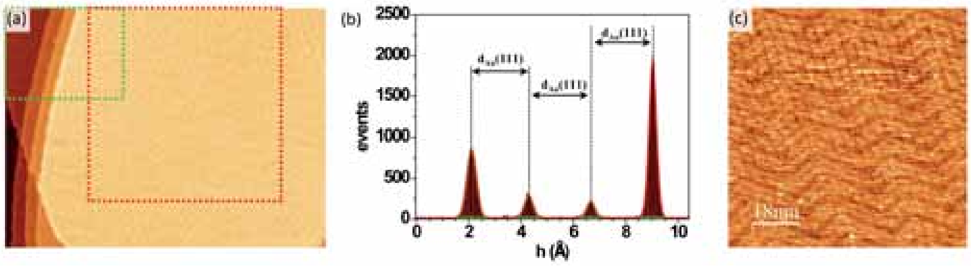

Figure 3.1.4: *cc-STM image (a) of a flame annealed gold substrate, exhibiting Au(111) terraces separated by monoatomic steps (image size:* $150\,nm \ \times 112\,nm$*). (b) Histogram of the z piezo displacement signal of the image region marked by dashed green square in (a) corresponding to* $d_{Au}(111)$ *atomic steps. The* $22 \times \sqrt{3}$ *reconstruction of Au(111) extended over the top most terrace is visible in enlarged image of (c) of the location marked by dashed red square in (a). Total z-scale of (c)* $0 - 1\mathring{A}$. $U = 0.5\,V, I = 530\,pA$.

---

[2] Description of the constant current STM measuring mode can be found in section 3.3

To achieve high resolution in any SPM system an essential requirement is to isolate the system against the mechanical and electromagnetic vibrations. Moreover, to achieve sub-nanometer sensitivity the noise amplitudes should be lowered below the $0.01\mathring{A}$. Typical vibrations in buildings (frequency range between $1-50Hz$) and acoustic noise (frequency range from 10 to $20Hz$) must be eliminated. Many factors have to be taken into account for an efficient vibration isolation, but as general rule, the construction of the tip holder, sample holder and piezo scanner should be as rigid as possible in order to increase the mechanical resonance frequency of the system, and the natural frequency of the isolation system has to be as low as possible. The SFM head used in this thesis is located on top of a granite plate, supported by four springs that act as a low resonant frequency support, as shown in figure 3.1.5 (a). In the case of the STM system, the head is suspended with four bungee cords that act as springs (figure 3.1.5 d). In both SFM and STM systems, a grounded metallic hood covers the scanning force microscope head (tip, sample, detection system and piezo actuator), what provides further acoustic and electromagnetic isolation. SFM systems have an extra hood cover which allows controlling the relative humidity (RH) of the working atmosphere by introducing a controlled dry nitrogen gas flux. The hygrometer used to measure the temperature and relative humidity inside and outside the hood has an accuracy of $\pm 2\%$ RH (in the $2-98\%$ RH range) and $\pm 0.2°C$ (in the $0-70°C$ range).

An electronic control unit connected to a digital signal processor (DSP) inside a PC basically complete the experimental setup (figure 3.1.5 b). The DSP board is mainly in charge of collecting the signal coming from the head and controlling the movement of the piezo. The DSP is also in charge of the so-called feedback loop, a way to control the vertical distance between tip and sample by maintaining a selected magnitude fixed to a preset value during the scanning. By means of the feedback loop, the selected magnitude and the preset set point are continually compared at each point of the image. If they are not equal, a voltage is applied to the scanner in order to move the sample closer or further to the probe, to maintain constant the used physical magnitude in the selected value (set point). This applied voltage is the signal used to generate the SFM image [3].

Three different SFM microscopes systems have been employed to obtain the results presented in this work: two of them are commercial SPM from Nanotec Electronica [27] and the third one is a home-made SFM that follows the design by Kolbe et al. [28] with an electronic unit fabricated in

---

[3] The conversion factor from the applied bias to the piezo to its longitudinal expansion or contraction is known from the corresponding calibration presented above in figures 3.1.3 and 3.1.4.

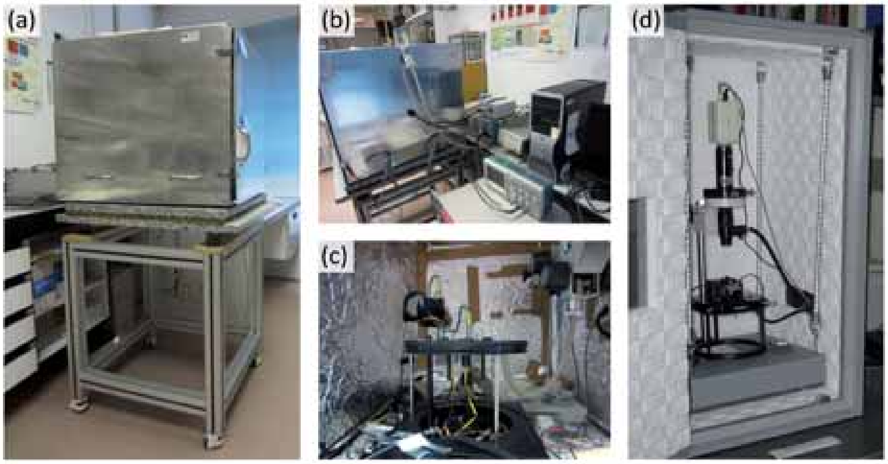

Figure 3.1.5: *The SFM, located in the Institute of Materials Science of Barcelona-ICMAB, is mounted on a granite plate and suspended by a damping table (a), to eliminate building vibrations. Additionally, a metallic box is used to minimize electrical and acoustic noise. In (b) the electronic control unit, the PC, an I-V converter, etc...can be seen. (c) shows a close up of the SFM head. In (d) a Molecular Imaging PicoSPM head suspended with four bungee cords inside of the metallic hood is shown (image from the net). The Molecular Imaging PicoSPM is located in the School of Chemistry of the University of St Andrews (Scotland-UK).*

the *Universidad Autónoma de Madrid-UAM (Segainvex Workshop)*. The software used for SFM data acquisition and image processing is the freeware *WSxM* [27, 29]. The STM measurements presented in this thesis were acquired by the author with a *Molecular Imaging PicoSPM* system [30], under the supervision of Prof. Manfred Buck in the *School of Chemistry* of the *University of St Andrews* in the context of a short stay of two months. STM image processing has been also done with the *WSxM* program.

3.2 Scanning force microscopy

In the scanning force microscope (SFM) a sharp mechanical tip is used to sense the surface of the sample by detecting the forces acting between the tip and sample. It is the sensing of these interaction forces what gives rise to the profile of the surface and from the SFM takes name. These forces are usually in the range from pN to μN and, though atomic resolution can be achieved, typical lateral resolution ranges between 5 to 20 nm, depending on the sharpness of the probe. Vertical distances can be measured with an accuracy lower than one Å. Some outstanding applications of SFM in the field of material science have been collected in [23]

3.2.1 The force sensor

Strictly speaking, the SFM does not measure forces but the bending and torsion of a lever, also called cantilever. These deflections of the cantilever are induced by the forces acting on a nanometer-sized tip attached to one of the lever ends. Because of its good elastic properties, the cantilevers are commonly fabricated from silicon (Si) or silicon nitride (Si_3Ni_4), and most used geometries are triangular and rectangular (see figure 3.2.1). These last ones are generally preferred because they make theoretical calculations easier. Ideally, the stiffness of the cantilever should be below interatomic spring constants (typically in the range of $10-20\,N/m$) and its effective mass has to be as small as possible to prevent the transmission of external vibrations. Typically the cantilevers spring constants are in the $0.01\,N/m$ to $50\,N/m$ range and their dimensions commonly are $100-300\,\mu m$ long, $10-30\,\mu m$ wide and $0.3-5\,\mu m$ thick, while tip dimensions are of $3-15\,\mu m$ high with radius of about $2-100\,nm$. The spring constant of the cantilever plays a crucial role in the sensitivity of the forces to be measured and it has to be as soft as possible to be able to detect forces down the pN range if sensitivity down the atomic forces is desired. The tip can be coated with different materials or even doped to have specific properties (conductive, magnetic, etc...), required for specific SFM techniques. Scanning electron microscopy (SEM) images of uncoated and diamond coated silicon probes manufactured by Nanosensors [31] are presented in figure 3.2.2.

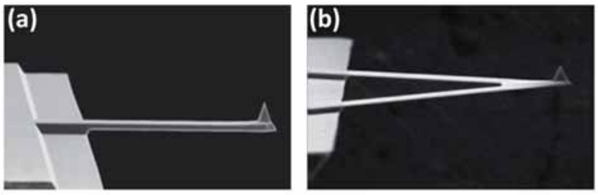

Figure 3.2.1: *Scanning electron microscopy images of silicon rectangular (a) and triangular (b) cantilevers. Images from Micromasch [32].*

If the cantilever spring constant (k_z) is known, it supplies the conversion factor to quantify the force sensed by the tip. The cantilever force constant is usually provided by the manufacturer. However, a small variation in the dimensions and/or the mass of the cantilever affects and introduces deviations on the nominal k_z values for the same kind of cantilevers. Along this thesis the nominal cantilever force constants provided by the manufacturer have been used for quantifying the forces applied for tips mounted in triangular shape cantilevers. For rectangular cantilever, the Sader method [33] has been employed to obtain a more accurate value of k_z.

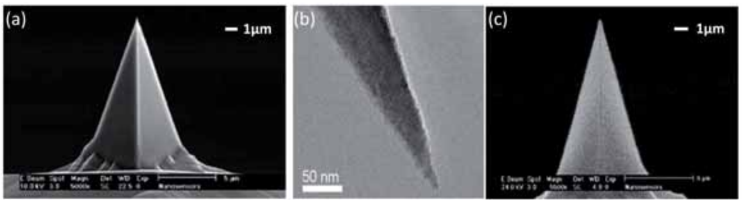

Figure 3.2.2: *Scanning electron microscopy images of some of the employed tips. Different magnification images of PPP type Nanosensors tip are shown in (a) and (b), while (c) corresponds to a diamond coated silicon tip. Images from Nanosensors [31].*

In this work, a variety of tips mounted in different spring constant cantilevers from, Nanosensors [31], Veeco (now Bruker [34]), Olympus [35] and Budgetsensors [36] have been used. Veeco probes with nominal tip radius of 2 nm mounted on V-shaped cantilevers with a nominal force constant $k_z = 0.05 - 0.5\,N/m$ have been mainly used for the contact mode structural and frictional characterization [34]. However, in some experiments Olympus rectangular cantilevers with similar cantilever force constants have been also employed. For dynamic mode measurements, Nanosensors probes with a tip radius of curvature $< 10\,nm$ mounted in rectangular cantilevers with nominal spring constant of $k_z = 2.8\,N/m$ have been used. For the conducting and electrostatic measurement, depending on the sample under study, either diamond doped or Pt/Cr coated tip mounted in rectangular cantilever with typical spring constants on three different ranges ($k_z \sim 0.2,\ 3,\ 40 N/m$) have been used. Diamond coated tips are manufactured by Nanosensors, while Pt/Cr coated ones are from Budgetsensors. The coating on silicon probes increases the tip radius curvature and lowers the lateral resolution (compare the uncoated and diamond coated tips in figure 3.2.2 a and c respectively). The macroscopic radius of curvature for Pt/Cr coated tips is $< 25\,nm$ [36], while for diamond coated tip is between 100 and 200 nm with a roughness of $\sim 10\,nm$ which enhances the lateral resolution [31].

3.2.2 The deflection sensor

The bending of the cantilever is usually sensed by the so-called optical beam detection method, proposed in [37, 38] and found nowadays in most microscopes. A laser beam is focused in the back side of the cantilever (usually gold or aluminum coated to enhance the reflectivity) and reflected into a 4 segmented position-sensitive photodiode (figure 3.2.3). This segmenting of the photodiode makes possible the detection of the deflection in two orthogonal directions, separating and quantifying them as the normal bending and the torsion of the cantilever.

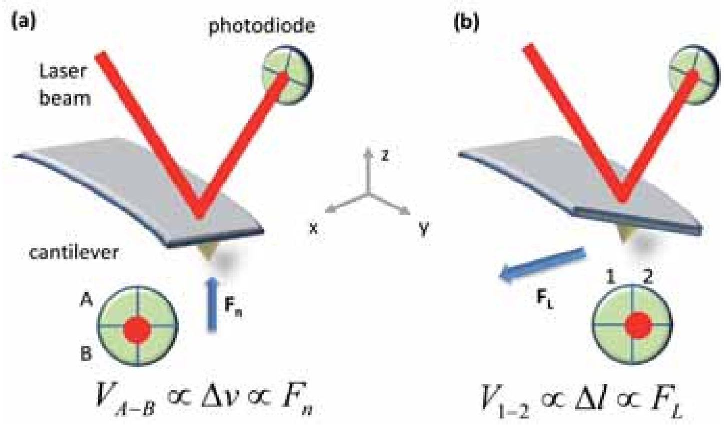

Figure 3.2.3: *Schematics showing the optical detection method used to measure the bending of the cantilever produced by normal (a) and lateral forces (b). Normal forces are proportional to the V_{A-B} signal whereas lateral forces, to V_{1-2}. Image courtesy of Luis Garzón.*

A schematic drawing of the optical beam detection method into 4 segmented photodiode setup is shown in figure 3.2.3. In the absence of force the laser spot is centered, i.e. equal signals are measured in each of the four sectors. When a force acts on the tip, the lever is deflected and the reflected spot is deviated. As depicted in figure 3.2.3 (a), a normal force produces a vertical deflection of the cantilever that is proportional to the signal difference between the upper and lower halves of the detector $\Delta v \propto V_{A-B}$. Similarly, the main effect of the lateral forces is the torsion of the cantilever (figure 3.2.3 b), which is proportional to the signal difference between the right and left halves of the photodiode ($\Delta l \propto V_{1-2}$).

For every cantilever used, a calibration of the photodiode response is required to obtain the conversion from the measured signals, V_{A-B} and V_{1-2}, to the cantilever displacement, Δv and Δl :

$$\Delta v = S_v \, V_{A-B} \tag{3.2.1}$$

$$\Delta l = S_l \, V_{1-2} \tag{3.2.2}$$

where S_v and S_l are the calibration factors for the bending in the vertical and lateral directions, respectively. As it will be explained in section 3.2.3.1 S_v is obtained from the force versus distance curves, by measuring the photodiode signal difference as a function of the piezo displacement, assuming a linear behavior with a slope of 1 for the contact regime. That is, we assume that the measured sample is hard enough to neglect any surface deformation when the tip is in contact, and thus any z displacement is translated to cantilever deflection. For our systems, S_v varies between 20 nm/V and 80 nm/V depending on the cantilever employed. Knowing the value of S_v, the photodiode signal (in Volts) can be translated to deflection of the cantilever (nm) and this to the applied load (in nN) by introducing the cantilever force constant (in N/m). That is,

$$F_n = k\, S_v V_{A-B} \tag{3.2.3}$$

The determination of S_l is rather complicated and requires some assumptions that are not generally fulfilled [39]. These difficulties in determining S_x together with the uncertainties of the torsion spring constant (k^T) pose a severe limitation when trying to obtain absolute values for the lateral force and, consequently, for the friction values. This fact will be discussed in detail in section 3.2.5.1.

3.2.3 Relevant tip sample interactions

The operation principle of a scanning force microscope is the detection of the force acting between the probe and sample. This force can have different origins and contributions and, depending on the tip-sample system under study, the predominant interaction mechanism might vary. In this section, we describe the most relevant forces involved in the SFM measurements performed to obtain the results presented in this work. More detailed information on intermolecular and surface forces can be found in the book [40] and a nice extended description of tip-sample interactions can be found in the review [41].

Van der Waals forces: These are forces attributed to the dipolar interactions of molecules and atoms. In the van der Waals forces, forces between permanent dipoles (Keeson forces), between permanent and the corresponding induced dipoles (Debye forces) and those between instantaneously induced dipoles (London dispersion forces) are included. The most relevant ones are these last London dispersion forces, because they act between dipoles arising from electronic fluctuations and dipoles induced in their electric field and thus, are always present. Their origin can be intuitively understood as follows: consider a non-polar atom with time averaged dipole equal to zero, however, for any instant it exists a finite dipole moment given by the instantaneous position of the electrons with respect to the nucleus. An electric field will be generated by this instantaneous dipole, which will polarize any nearby atom (even if it is neutral). As a consequence of this induced polarization an attractive interaction between these two atoms will be induced. Typically van der Waals forces range a few nanometers, but depending on the conditions they can range between $\sim 0.2\,nm$ to distances greater than $10\,nm$ [40].

In order to model this interaction in SFM, macroscopic bodies rather than individual atoms or molecules are considered. The tip-sample geometry can be well approximated as a sphere approaching a plane and, for such configuration, the interaction of van der Waals interaction has the form:

$$F_{vdW} \approx -\frac{AR}{r^2} \tag{3.2.4}$$

where R is the sphere radius, r is the sphere-plane distance and A is the Hamaker constant. The order of magnitude of this constant, which accounts for the materials involved, is $\sim 10^{-19} - 10^{-20} J$ [40]. This interaction acts between the surface and the mesoscopic tip end, i.e. not only with the end atoms of the tip, and for the typical tip sample systems (e.g. $Si_3N_4 - Au$ in air) and a tip radius $R = 30\,nm$, the van der Waals force at a distance $r = 5\text{Å}$ is of the order of $F_{vdW} = 4\,nN$. In vacuum or air, this van der Waals interaction is always attractive. However, in other media, the interaction can be attractive ($A > 0$) or repulsive ($A < 0$), depending on the dielectric properties (ε) of the tip, sample and media in-between [40].

Short range forces: These forces arise from the overlapping of electron wave functions and from the repulsion of the ion cores. Their range is comparable to the extension of the electron wave functions, i.e. less than one nanometer. They can be either attractive (as for example in bond formation) or repulsive (due to the Pauli exclusion principle). As stated in the compilation work by Meyer and co-workers [42], the magnitude of attractive short-range forces is around $0.5 - 1\,nN$ and the decay length around $0.2 - 0.3\,nm$.

Friction forces: During sliding, a macroscopic object has to overcome an opposing force which results in a loss of kinetic energy and, if no additional energy is supplied, the object finally stops. This force, that opposes the relative motion between objects in contact, is the friction force.

These frictional forces can have their origin in a combined effect arising from various physical phenomena, such as elasticity, adhesion, capillary forces, surface chemistry, phononic and electrostatic interactions etc. In the SFM setup, friction causes the torsion of the cantilever when the tip is scanned over the sample as shown in figure 3.2.3 (b). These lateral forces can be exploited to form an image or map of the dissipated energy, sometimes showing higher contrast than topographic images. This contrast might arise from mechanical and/or chemical differences between regions.

Adhesion forces: Adhesion is the molecular attraction exerted between bodies in contact and can be defined as the free energy change to separate unit areas of two media from contact to infinity in vacuum or in a third medium [40]. Moreover, in SFM working under ambient conditions, there is another important contribution to the adhesion force coming from the water meniscus that forms between the tip and substrate. Due to the unavoidable adsorption of thin water films at surfaces and subsequent capillary condensation [43], the formation of the water meniscus have to be considered even in quite dry conditions. The formation of this meniscus produces an attractive adhesion force that depends on the relative humidity [44], the temperature, the hydrophilicity of the tip and sample, the sharpness and shape of the tip [45, 46]. Depending on all this factors the adhesion forces due to capillary forces can range between a few to hundreds of nN and the meniscus can reach heights up to $\sim 1\ \mu m$ at high humidity conditions ($RH \sim 75-90\%$) as has been shown by environmental scanning electron microscopy [47].

Electrostatic forces: These are long ranging forces that obey the Coulomb´s law and can be attractive or repulsive. Since usually at least either the tip or the sample is conductive and grounded, an image charge generates on both sides of the tip-sample system and as a consequence the net electrostatic force is usually attractive. Usually it is stronger than other interactions such as the van der Waals ones or the magnetic interaction, for a non-magnetic tip. If one considers the tip-sample system as a capacitor, the Coulomb interaction energy of the system is given by:

$$W_{el} = \frac{1}{2}CU^2 \tag{3.2.5}$$

where C, the capacitance, depends on the tip-sample distance, the geometry of the system and the dielectric constant of the medium in-between. z is the tip-sample distance, and U is the potential difference between the tip and the sample. U usually presents two different contributions, the contact potential difference (U_{CPD}) caused by the tip-sample work function difference and a possible potential difference applied between tip and sample (U_{bias}). The resulting force can be then written as:

$$F_{el} = -\frac{1}{2}\frac{\partial C}{\partial z}(U_{bias} - U_{cpd})^2 \tag{3.2.6}$$

Therefore, the force does not only depend on the tip-sample potential difference, but it also depends on the derivative of the capacitance. From equation 3.2.6 it is inferred that a zero bias voltage ($U_{bias} = 0$) does not normally correspond to a minimal electrostatic force, since the contact potential difference is not compensated. Due to the long-range character of these forces, electrostatic interactions act between the sample and the whole cantilever. Only for very small tip-sample distances ($\leq 2nm$), the electrostatic force contribution from the end of the tip dominates over the other terms [48]. This effect limits the resolution of electrostatic force microscopy (EFM) in general, and that of the Kelvin probe force microscopy (KPFM) [49] in particular. By the detection of the electrostatic force gradient instead of the force, this effect can be minimized, as will be discussed in greater detail in section 3.2.5.3.

3.2.3.1 The force versus distance curve

A typical and simple measurement of the tip-sample interaction is recording the variation of normal force as the tip-sample distance is being changed. This is the so-called force spectroscopy mode based on the force versus distance curve [50] analysis shown in figure 3.2.4. During the tip-sample approach (green line), the cantilever deflection is approximately constant until an attractive interaction such as van der Waals, electrostatic or capillary forces provokes a change in the deflection of the cantilever (situation (i) in figure 3.2.4). When these forces are stronger than the cantilever restoring force, the tip suddenly jumps into contact with the surface (ii). After this snap-in point, the cantilever deflects away from the surface approximately linearly with the scanner movement (iii) if the sample is not deformed by the tip. When the full extension of the piezo is reached, the scanner begins to retract (red line) and the cantilever deflection retraces the same curve until a snap-out instability is observed (iv), indicating that the tip is no longer in contact with the sample. In air, capillarity adhesion due to the presence of water holds the tip in contact with the sample bending the cantilever to the surface (iv). This generates an hysteresis in the curve, and the snap-out point is not observed at the same piezo position as the snap-in instability, i.e. extra piezo movement is needed to detach the tip from the surface. The value of the force at the snap-out point is generally denoted as the adhesion or pull-off force.

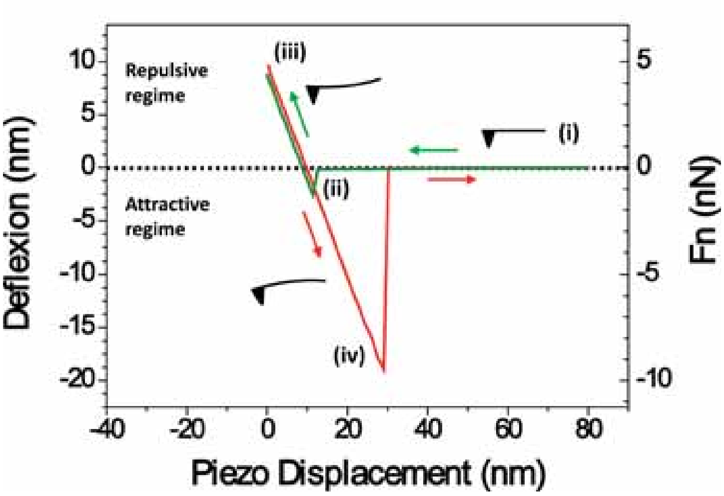

Figure 3.2.4: *Force versus distance curve acquired during an approach-retract cycle of the sample towards the tip: the cantilever deflection is measured as a function of the piezo displacement. The different regions correspond to the different cantilever deflections schematically depicted.*

On the other hand, the value of the adhesion force measured from the force versus distance curve is often used as a direct method to in situ check the tip conditions. For instance, the dependence of this adhesion on the tip dimensions allows correlating sudden changes on the adhesion value to changes in the tip contact area due to damage during the scanning. Typical adhesion forces range between a few and hundreds of nN.

The measured curves are the direct result of the photodiode response (V_{A-B}) versus vertical movement of the piezo actuator (z). To obtain a true force versus distance curve, V_{A-B} and z have to be converted into force and tip-sample distance respectively. As introduced in section 3.2, to convert the photodiode signal into a meaningful quantity as the deflection of the cantilever (equation 3.2.1) or/and normal force (equation 3.2.3) the photodiode sensitivity (S_v) has to be determined. When the sample measured is hard enough to neglect surface deformation S_v is obtained from the FZ curve itself, the measurement of the inverse slope of the repulsive part of the curve (from (ii) to (iii) in figure 3.2.4) yields to the nm/V calibration ratio.

The conversion of the piezo movement into tip-sample distance is more complicated, especially for deformable materials. Generally, the zero tip-sample distance is defined at the point where the sign of the force versus distance curve changes due to repulsive interactions. At this point, the tip contacts the sample surface. If there is no sample deformation, beyond this point further piezo displacement does not change the tip-sample distance but only increases the applied force. When softer materials are under study, tip indentation and elastic/plastic deformation might play a significant role in the conversion of the piezo movement into tip-sample distance. In this case, after the contact with the surface, tip-sample distance can still be reduced due to tip indentation. This topic is extensively discussed in [41, 51].

3.2.4 Basic operating modes

Scanning probe microscopy techniques are classified in two main primary modes, the contact and dynamic modes. In contact mode, the tip is brought in direct contact with the sample and the vertical deflection of the cantilever is used to directly sense the tip-surface interaction force. In the standard dynamic mode, the cantilever is externally oscillated close to its resonance frequency at a given distance from the sample surface. Tip-sample interactions induce frequency, amplitude and phase variations on the cantilever dynamics with respect to the reference oscillation and provide information about sample characteristics. Though further details are given in the next sections on those modes employed throughout this work, a complete description of all of them can be found in general SFM books as [39, 42].

3.2.4.1 Contact mode

Contact mode (cm-SFM) was the first developed SFM mode and as commented above, it is based upon the measurement of the deflection of the cantilever caused by the tip-sample forces when the tip contacts the sample surface. When scanning the tip over the sample surface, this deflection can be kept constant to a given setpoint value by means of a feedback loop which controls the z position of the piezo. A topographic image is generated by plotting, at each point of the scanned area, the vertical piezo movement needed to keep the normal deflection of the cantilever constant. Therefore, all topographic imaging generated by cm-SFM techniques are in fact constant force maps which we interpret as topography. In cm-SFM, the variation of the tip-sample forces are mainly due to changes in surface morphology. Care has to be taken however when heterogeneous samples are measured. Variations in tip-surface interaction (e.g. electrostatic force variations) or/and variations of mechanical properties (e.g. elastic constant of the sample) at different surface locations can give rise to deviations of the measured piezo displacement from the real topography depending on the values of the normal force used when scanning the sample.

As introduced in section 3.2.3.1, the essential measurement to get information about the tip-sample interaction conditions is the force versus distance curve (see figure 3.2.4). Depending on the force set point selected for scanning, two measurement regimes can be distinguished whether the cantilever deflection points away or to the surface, denoted as repulsive and attractive regimes. In air, the presence of water gives rise to capillary adhesion forces which holds the tip in contact with the cantilever deflected to the surface, making possible to scan the surface in the attractive regime and preventing any sample deformation or/and damage of the sample. Contact mode results presented in this thesis have been performed mainly in the attractive regime, as close as possible to the pull-of force. Simultaneously to the surface topography, maps of friction or conductivity, which also require direct contact, can be measured in cm-SFM operation mode. A detailed description of the SPM techniques to obtain friction and conductivity maps will presented in the following, in sections 3.2.5.1 and 3.2.5.2.

Tip-sample contact area

In SFM, one of the main drawback stems from the determination of the contact area of the tip-sample system, A_{true} , which cannot be directly measured. Even they are known to break down as the contact radius approaches to atomic dimensions [52, 53], in general, the continuum models are still used for the mechanics of the tip-sample contact in SFM. The simplest one is to model the tip-sample contact as a sphere-plane contact and apply the Hertz model [54], in which the relation between the contact area and the applied load is given by:

$$A(F_n) = \pi \left(\frac{R\, F_n}{E^*} \right)^{2/3}$$

where R is the sphere radius and E^* is an effective modulus related to the Young´s modulus (E) and the Poisson ratio (ν) of both sphere and plane materials by:

$$\frac{1}{E^*} = \frac{3}{4}\left(\frac{1-\nu_1^2}{E_1} + \frac{1-\nu_2^2}{E_2}\right)$$

The major restriction when using the Hertz model comes from the fact that it neglects any adhesion between contacting surfaces and assumes that there are no attractive forces acting between them: at zero external loads the contact area reduces to zero. However, as commented previously, adhesion plays an important role when SFM measurements are performed under ambient conditions. Adhesive interactions are incorporated in two other contact mechanics models: i) the Johnson, Kendall and Roberts (JKR) model [55] for the case of short-range adhesion forces and ii) the Derjaguin, Muller and Toporov (DMT) model [56] applicable to long-range interactions. The contact area predicted by the former is expressed as:

$$A(F_n) = \pi\left(\frac{R}{E^*}\right)^{2/3}\left[F_n + 3\pi\gamma R + \sqrt{6\pi\gamma R F_n + (3\pi\gamma R)^2}\right]^{2/3}$$

where $\gamma = \gamma_1 + \gamma_2 - \gamma_{12}$, being γ_1 and γ_2 the surface energies of tip and sample and γ_{12} the interfacial energy. This model predicts that a finite negative load is required to separate the surfaces, which is often referred as the critical load, F_c:

$$F_c = -\frac{3}{2}\pi\gamma R$$

The pull-off force measured in force versus distance curves (section 3.2.3.1) is generally identified with this critical load and at this load a finite contact area exists. In the DMT model, the expression for the contact area is similar to the Hertz model except for the presence of an offset to introduce the adhesion forces:

$$A(F_n) = \pi\left(\frac{R}{E^*}\right)^{2/3}(F_n + F_{adh})^{2/3} \tag{3.2.7}$$

In this case, the critical force to separate both surfaces is higher than in the JKR model:

$$F_c = -2\pi\gamma R$$

For studies dealing with SAMs, the JKR and DMT approximations have been used to estimate contact areas and pressure values [57–59], and those are the ones employed throughout this work.

These two models are, of course, limiting cases, and descriptions of intermediate situations between them are provided in different works [60–63].

The uncertainty in the tip-sample contact area is not only dependent on the model used, but also in uncertainties as the real tip radius and shape, or the elastic constant of the materials involved. The impossibility to access to the exact values of those parameters might introduce considerable errors when estimating the contact area, and in consequence, when trying to compare absolute values of physical quantities such as friction or conductivity that depend on it. To overcome this problem, for such kind of measurements we have performed a reliable procedure that consist in the study of relative rather than absolute friction/conductivity characteristics by always using heterogeneous samples.

3.2.4.2 Dynamic modes

Dynamic SFM modes (dm-SFM) are based on monitoring the behavior of the vibrating cantilever when tip is approached close to the sample surface. Tip-sample interactions induce frequency, amplitude and phase variations on the dynamic of the cantilever with respect to the reference oscillation. In principle any of those physical magnitude variation can be employed as a working parameter on a feedback loop to track the sample surface properties, what gives rise to multiple possible operational modes in dm-SFM. The most extended ones and the particular operating modes employed to obtain the results presented in this thesis will be introduced in the following. Further extended discussion of dynamic SFM methods can be found in recent reviews [39, 64, 65].

The cantilever is usually mechanically oscillated by electrically exciting a piezo actuator placed in the cantilever holder. The control of the applied *ac* bias to the piezo actuator allows the control of the exciting force (F_{ext}) and the frequency (w) of the oscillating cantilever ($F_{ext}(t) = F_{ext} sin(wt)$). Depending on the amplitude of oscillation compared to the tip-sample distance, the tip may either not contact the sample (non contact) or intermittently contact the sample surface (intermittent contact or tapping mode). However, before entering in more details it is instructive to analyze the simple case of an harmonic oscillator in order to understand the basic underlying physics involved in dm-SFM. The motion of a forced harmonic oscillator with damping is given by:

$$m\ddot{z}(t) + \alpha\dot{z}(t) + kz(t) = F(z,t) \tag{3.2.8}$$

where m and k are the effective mass and the spring constant of the cantilever respectively, hence the resonant frequency of the free cantilever is given by $w_0 = \sqrt{k/m}$. α is the viscous damping coefficient of the oscillator. In dm-SFM it is common to define the dimensionless quality factor $Q = mw_0/\alpha$ which is inversely proportional to the damping coefficient and in absence of any external excitation, Q describes the number of oscillation cycles after which the damped oscillation amplitude decays to $1/e$. Q is extremely dependent on the environment, it takes values on the range from 10^4 to 10^5 in vacuum, in air it is reduced to 10 to 200 range and in liquid media the values are below 10. $F(z,t)$ is the sum of all the external forces acting on the oscillator, those are, the time dependent external driving force ($F_{ext}(t)$) and the distance dependent tip-sample interaction force ($F_{ts}(z)$). In absence of tip-sample interaction ($F(z,t) = F_{ext}(t)$) , the solution of equation 3.2.8 is a linear combination of a transition state and a steady state:

$$z(t) = A_t e^{-w_0 t/2Q} sin(wt + \varphi_t) + A_0 cos(wt + \varphi) \tag{3.2.9}$$

Where A_i and φ_i are the amplitudes and phase differences of the transient ($i = t$) and steady ($i = 0$) states.The transient regime decreases exponentially with the time constant $\tau = 2Q/w_0$, which means that after a time τ the motion is dominated by the steady state term. The dependence of τ with Q has important implications in the dynamic operational modes that can be applied for each particular environments (vacuum, air and liquid media). For a typical cantilever with resonant frequency of $10^4 - 10^5\ Hz$, τ takes values in the $ms\ to\ s$ range in vacuum, what implies long range times for the $z(t)$ transition state solution and limits the practical application of monitoring amplitude changes for a large number of pixels on a scan grid (typically 512×512 or 256×256) [66]. Evaluating the 3.2.8 differential equation with the steady state solution, the following relations are found for amplitude and phase as a function of w:

$$A = \frac{QF_{ext}/m}{\sqrt{w^2 w_0^2 + Q^2(w_0^2 - w^2)^2}} \tag{3.2.10}$$

$$\varphi = arctan(\frac{ww_0}{Q(w_0^2 - w^2)}) \tag{3.2.11}$$

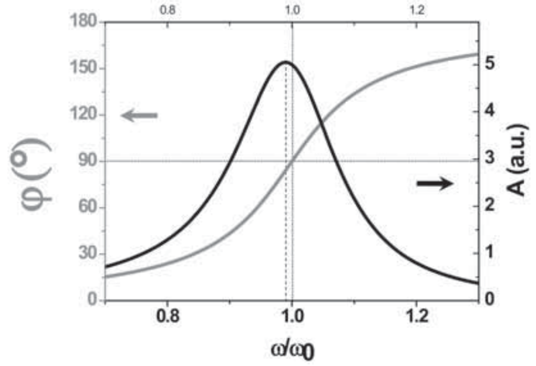

Figure 3.2.5: *Amplitude and phase response of an oscillating cantilever as a function of the frequency (Q=5).*

In figure 3.2.5, we plot those amplitude and phase in function of $^{\omega}/_{\omega_0}$ for the particular case of a quality factor $Q = 5$. By exciting the oscillator at its resonant frequency ($w = w_0$) and in absence of damping, the amplitude takes the form $A_0 = \frac{QF_{ext}}{k}$, i.e. the free amplitude. However, the damping term of the harmonic oscillator causes a shift of the resonant frequency from w_0 to $w_0^* \approx w_0\sqrt{1 - \frac{1}{2Q^2}}$, as appreciated in the figure 3.2.5. In the case of ambient conditions, Q usually is around 100 or higher values, what makes this shift of the resonant frequency negligible. The phase of the oscillation suffers an abrupt change near the resonance, where it takes a value of 90° (figure 3.2.5 left axis). For higher values of Q, the peak of the amplitude becomes sharper and the change in phase more abrupt.

When considering tip-sample interactions for the simplest case of a weakly perturbed oscillator, in which the vibration amplitude is small compared to the influencing forces distance range, and that the force gradient ($^{\partial F_{ts}}/_{\partial z}$) does not vary significantly over one oscillation cycle, we can model the SFM system as a two coupled springs system. The cantilever is represented by its spring force constant (k) and the tip-sample interaction is represented by a second spring (k_{ts}). Therefore, the total spring constant of the SFM system can be written as:

$$k_t = k + k_{ts} = k - \frac{\partial F_{ts}}{\partial z} \tag{3.2.12}$$

Due to the tip-sample interaction, and neglecting any damping effects, it is found that the resonant frequency of the system is shifted by Δw from the resonant frequency w_0:

$$w^2 = (w_0 + \Delta w)^2 = \frac{k_t}{m} = \frac{(k - \frac{\partial F_{ts}}{\partial z})}{m} \tag{3.2.13}$$

If it is assumed that the frequency shift is much smaller than the resonant frequency ($\Delta w << w_0$) , from equation 3.2.13 is found that:

$$\frac{\Delta w}{w_0} \approx -\frac{1}{2k}\frac{\partial F_{ts}}{\partial z} \tag{3.2.14}$$

Thus, the frequency shift of the cantilever is proportional to the force gradient of the tip-sample interaction. As illustrated in figure 3.2.6, a negative shift in the frequency is observed when attractive forces are dominant, and conversely, a positive shift appears when forces are repulsive. As a consequence of this frequency shift, a displacement of both amplitude and phase curves from figure 3.2.5 is induced without introducing any shape or size modification (as is shown in figure 3.2.6).

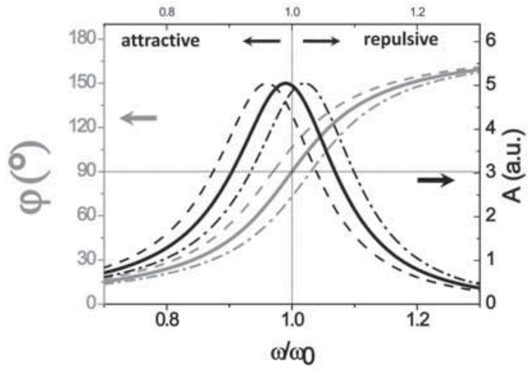

Figure 3.2.6: *Amplitude and phase response of an oscillating cantilever as a function of the frequency. Free cantilever oscillation situation (continuous line) and the frequency shift induced (dashed lines) by an attractive (←) or repulsive forces (→).(Q=5).*

Hence, an important conclusion is that while in contact mode SFM we were sensitive to the tip-sample force itself, the dynamic scanning force microscopy is sensitive to the force gradient sensed by the tip. From equations 3.2.10 and 3.2.14, we can find that the change in amplitude can also be related to the force gradient by:

$$\Delta A \propto \frac{Q}{2k}\frac{\partial F_{ts}}{\partial z} \tag{3.2.15}$$

From equation 3.2.15, we find that the change in amplitude is proportional to the quality factor

Q. Another aspect that have to be in consideration is the distance dependence of the quality factor, $Q = Q(z)$, which has been observed experimentally [67, 68] but is not usually considered in the theoretical models. If Q varies with the tip-sample distance, apart from the variation of the force gradient of the system which induces the amplitude and phase curves shift, there is another factor influencing the variation of the amplitude when the oscillating tip approaches the sample. As it is commented above the quality factor is inversely proportional to the damping coefficient and thus describes the energy dissipated in the tip sample system.

The two main operation modes on dm-SFM are the Amplitude modulation (AM-SFM) and Frequency modulation (FM-SFM) modes, and are based on monitoring the amplitude and frequency shift, respectively, induced by the shift of the amplitude and phase curves presented above (see figure 3.2.6).

In amplitude modulation (AM-SFM) the cantilever is excited at a fixed frequency close to its resonance frequency and the oscillation amplitude of the cantilever is monitored. In presence of any acting force, as a consequence of the shift of the amplitude curve , the amplitude of the oscillation will decrease. The feedback maintains a constant amplitude (always smaller than the free amplitude) by adjusting the relative tip-sample position during scanning and, by recording the relative piezo displacement, the constant amplitude profile map is built. Hence, the topography images obtained by this operation mode are indeed constant amplitude maps of the scanned surface. The long range times (τ) that high Q values impose to the transition states of $z(t)$ (equation 3.2.9) set a severe limitation to the use of AM-SFM in vacuum. That is why AM-SFM operation mode is typically applied in ambient and liquid environments. In AM-SFM non-contact operation can be achieved by employing very small oscillation amplitudes, but typically in air large amplitudes in the range of of $10 - 100\,nm$ are employed, what typically yields to intermittent contact or tapping mode operation. In the tapping mode the tip periodically enters in contact with the sample what, compared to contact mode SFM, minimizes tip–sample contact time avoiding damage not only of the sample but also of the tip. Because it is fairly easy to operate experimentally, it is the most extended operation mode in common surface "visualization" by SFM. However, the underlying Physics of tip-sample interaction in tapping mode is complex and still subject of research [69, 70]. Commonly the direct ascription of constant amplitude map to topography is done, but this direct correlation can yield to unexpected and wrong topographic results in samples that present regions with different chemical composition or/and physical properties. A variety of topographic artifacts including strange shapes contours, wrong height measurements and even contrast inversion have been already observed [71–73]. These artifacts have been ascribed to differences in local elasticity [74], wetting [71, 75], contact potential [76, 77] or to switching between two regimes of tip– sample interaction, one dominated by attractive and other by repulsive interactions [78, 79]. As a result of these possible artifacts in topographic details determination, the dm-SFM topography results obtained along this thesis have been always cross-checked by contact mode SFM (cm-SFM). In AM-SFM, simultaneously to amplitude monitorization the phase shift between the excitation driving force (F_{ext}) and the cantilever oscilation is also recorded . The phase shift is related to energy dissipation in the tip sample contact [80], what usually gives rise to contrast between heterogeneous materials [81].

In frequency modulation SFM [66] the changes in the cantilever's resonant frequency are monitored. The feedback mechanism maintains a constant frequency shift (Δw) by adjusting the relative tip-sample position during scanning and by recording the relative piezo displacement, the constant Δw map is built. Thus, the topography image obtained by this operation mode represents a map of constant frequency shift over the surface. Contrary to the amplitude detection, the change in resonant frequency is simultaneous to a change in the tip-sample interaction, hence, no problems with the long τ time constants associated to high Q factors are involved. This is the reason why FM-SFM is usually the common operation mode in vacuum, although it can be also applied in air [73, 82, 83] and even in liquids [84].

Along this thesis, most of dm-SFM measurements have been performed by a specific operation mode that combines some aspects of both AM-SFM and FM-SFM techniques and is implemented in *Nanotec Electronica* instrument [27]. As in common AM-SFM operation mode, we use the amplitude of oscillation as the physical magnitude for the topography feedback, but in parallel a phase locked loop (PLL) is used to track the frequency of the oscillator and fix the phase [85, 86]. The PLL is basically an extra feedback that works maintaining the phase constant (at resonance, $\varphi = 90°$) by varying the frequency of the external driving force (F_{ext}). In other words, the PLL works shifting the resonance curve (figure 3.2.5) keeping the system always in resonance. Therefore, any change in amplitude corresponding to a variation of the tip-sample force gradient ($^{\partial F_{ts}}/_{\partial z}$), that gives as a result the shift of the amplitude resonance curve, is also automatically corrected by the PLL. In consequence any amplitude variation measured when we work with the PLL is simply associated to a variation of the quality factor (Q), and hence to dissipative interactions. The use of a PLL circuit allows on the one hand to rule out any influence of conservative forces into the topographic signal, and on the other hand permits the direct measurement of the resonance frequency in hertz, and thus the determination of interaction data in physically meaningful units.

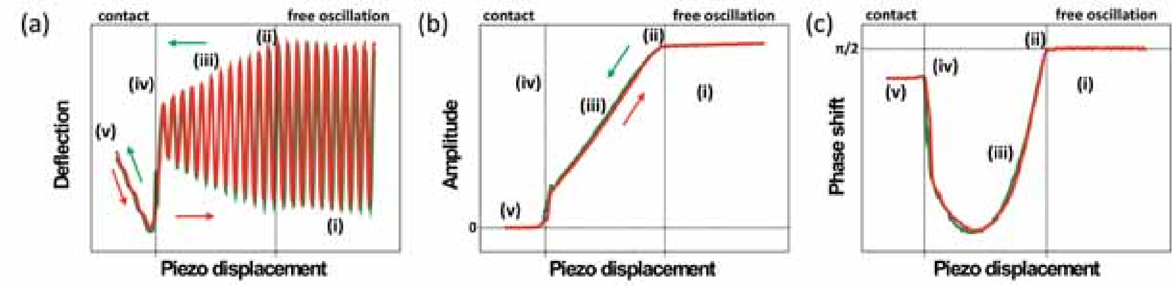

Figure 3.2.7: *Cantilever deflection (a), amplitude (b) and phase shift (c) responses of an oscillating tip as a function of the piezo displacement, approaching to (green curves) and withdrawing from the surface for the case in which attractive forces are dominant all over the tip to sample approach.*

As in cm-SFM mode, the tip-sample interaction conditions can be checked by monitoring the tip dynamics as the tip-sample distance[4] is changed. In the case of dm-SFM the corresponding physical quantities of interest are the oscillation amplitude and phase shift of the probe oscillation. In figure 3.2.7 an example of a so-called amplitude versus distance curve is presented. The deflection (a), oscillation amplitude (b) and phase shift (c) signals response in the tip-surface approach (green line) and retraction (red line) are shown. Far from the surface, the tip-sample interaction forces are negligible and the tip is oscillating at its free oscillation amplitude (region (i)). During the tip approach (green line) the amplitude and phase are nearly constant until an attractive interaction provokes a negative phase shift and an amplitude reduction (ii). The amplitude decreases linearly with the distance (iii) until the attractive forces are such strong that the tip jumps into contact with the surface (iv). After the snap-in point, the cantilever deflects away from the surface linearly with the scanner movement, as in the common force versus distance experiment (see section 3.2.3.1). During the retraction (red line), ones the pull-off force is reached the oscillation of the tip is recovered and the amplitude increases with the increase of the tip-sample distance.

The response of the curve presented in figure 3.2.7 corresponds to the simple case in which the tip-sample interaction is controlled by long-range attractive forces all over the tip sample approach.

---

[4] The tip-sample distance is defined in this case as the distance between sample and the tip's rest position.

However in most of the cases the dynamic of the tip is more complex. When the tip is close to the surface during each tip oscillation cycle both large-range attractive forces and short-range repulsive forces are present and compete to control de cantilever dynamics. Depending on which of those forces is dominant, the attractive and repulsive tip-sample interaction regimes can be distinguished [79]. In the attractive regime a net attractive force dominates the tips dynamic and the average force in one cycle is negative, while in the repulsive regime repulsive forces are dominant and thus the average force is positive [79, 87]. The sign of the phase shift signal is directly related to the sign of the average force that the tip's senses and thus can be employed to identify in which of the regimes are we operating for a certain measuring condition [79].

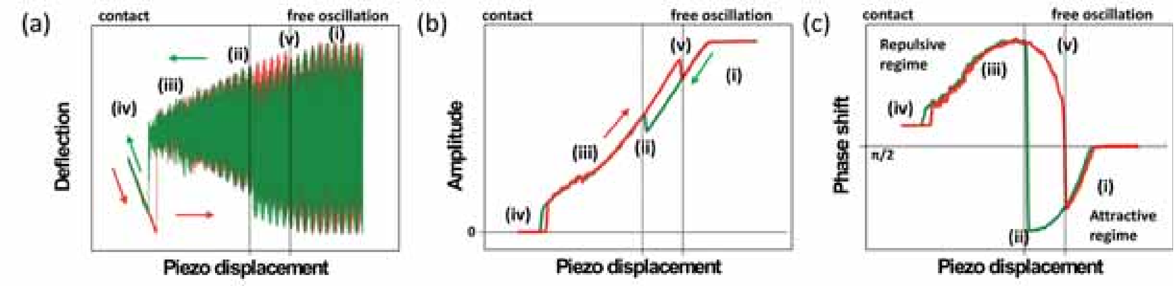

Figure 3.2.8: *Cantilever deflection (a), amplitude (b) and phase shift (c) responses of an oscillating tip as a function of the piezo displacement, approaching to (green curves) and withdrawing from the surface for the case in which both attractive and repulsive regimes are present over the tip sample approach.*

In figure 3.2.8 we present an amplitude versus distance curve performed on top of hexadecanethiol self-assembled monolayer on gold in which both attractive and repulsive regimes are present. As in the previous curve of figure 3.2.7, the tip oscillation deflection (a), amplitude (b) and phase (c) are monitored in the tip approaches to and retraces from the surface. During the tip approach (green line) the long range attractive interactions provoke a negative phase shift and an amplitude reduction (i), but at a certain tip-sample distance (ii) the dominant forces become to be repulsive and the interaction regime suddenly changes as proved by the change on the phase shift sign (see figure 3.2.8 c). The change to the repulsive regime provokes an abrupt amplitude increase and from this point on the amplitude continuous decreasing until the tip holds in contact with the surface (iv). During the retraction (red line), the amplitude increases with the increase of the tip-sample distance until the interaction regime changes from repulsive to attractive, point in which the amplitude suddenly decreases (v). The most important fact that is derived from this experiment, is that an hysteresis is found between the approach and retraction curves. That is, the regime variation point is not the same in the approach and retraction curves and in consequence two stable states with same amplitude coexist for a certain range of tip-surface separations (see figure 3.2.8 b), one in the attractive and the other in the repulsive regime. The coexistence of two oscillation states regime depends on sample and tip properties as well as on the operational parameters employed [64, 88, 89], such as the free oscillation amplitude or cantilever force constant. In the present work is not our objective to go into detail about the underlying theory of AM-SFM, and for further information about it we refer to the extended literature existing on the field [64, 79, 88–91]. However, from a practical point of view it is important take into consideration the attractive and repulsive regime conditions and the bistable region position. On the one hand, the coexistence of two oscillation states typically introduces unstable measuring conditions produced by multiple transitions between regimes if amplitude set point within the bistable region are employed [92], and in consequence those set points have to be avoided. And on the other hand, for surface imaging both attractive and repulsive regimes can be employed, both presenting their own advantage and disadvantages [64]. The attractive regime have been found to result in worse lateral resolution imaging [79], but it also have been proven to minimize the tip-sample contact and its use is recommended to minimize sample or/and tip damage [87] and also for the use of the Kelvin probe microscopy technique (see section 3.2.5.3) [83, 93]. That is why, for the results presented in this work, typically oscillation amplitudes in the range of $10 - 40\, nm$ and setpoints with low amplitude reductions ($^{\Delta A}/_{A} \sim 10 - 20\%$), mainly measuring in the attractive regime, have been used.

3.2.5 Scanning force microscopy techniques

The rich variety of physical quantities that can be detected in SFM has made possible a wide variety of derived SFM techniques. In the following we present the different SFM techniques used along this thesis.

3.2.5.1 Friction force microscopy

As introduced in section 3.2, the use of a 4 segmented position-sensitive photodiode allows to register, simultaneously with the normal cantilever deflection, the torsion of the cantilever due to the presence of a lateral force. In an ideal scenario when the tip is not scanning, there is not any lateral force acting on the tip, and the cantilever torsion is zero. If during a contact mode experiment the fast scan direction (x) is set perpendicular to the long axis of the cantilever, any force acting opposite to the tip motion (F$_x$) is translated to a lateral force (F_l) and a torsion of the cantilever will be induced (figure 3.2.9). Thus, by detecting the torsion of the cantilever, the SFM can be employed to measure the force opposite to the relative motion of the tip-sample nanometric size sliding contact, i.e. the local friction. In this manner, friction force microscopy (FFM) has become a powerful tool to study dissipation mechanisms at surfaces and in ultrathin layers with nanometric lateral resolution [7, 94]. In addition, the capability of SFM to control the applied load allows the quantification of the friction as a function of the normal load, one of the central experiments in tribology. In this way, the friction coefficient (μ) can be determined, which is defined as the proportionality factor between the normal force and friction force ($F_l = \mu F_n$).

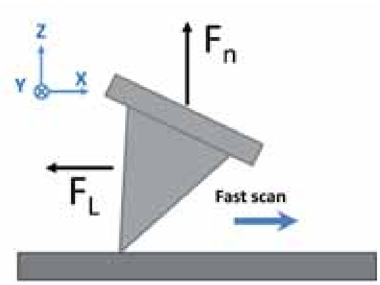

Figure 3.2.9: *Sketch of the SFM tip-cantilever torsion. The probe moves with constant speed along the x axis with controlled load in the z axis (F_n). The generated force on the tip-sample contact opposites the tip motion yielding to the torsion of the cantilever.*

Strictly speaking, the SFM does not measure the lateral force but the torsion of the cantilever. Thus for quantitative FFM, the conversion from cantilever torsion to lateral force value is mandatory. This calibration implies, first, the knowledge of the torsion spring constant of the cantilever (k^T), and second, the determination of the conversion factor between torsion and voltage difference read-out in the photodiode (the S_l factor introduced in section 3.2). The relation between the cantilever torsion and read-out voltage (V_{1-2}) can be established by scanning a known wedge shape surface structure [95]. On the other hand, the determination of k^T is not a simple task. Comprehensive reviews of the different theoretical and experimental approaches proposed to obtain k^T are given in [41, 59, 96, 97]. Due to the difficulties in determining S_l together with the uncertainties in k^T, pose a severe limitation when trying to obtain absolute values for the lateral force. In the present work we have followed a reliable procedure that consist in the study of relative rather than absolute friction characteristics by always using heterogeneous samples. Lateral forces are given in volts, the photodiode output, throughout this thesis.

FFM measurements are typically carried out by completing a trace-retrace scan loop along the fast scan direction, in what is called a friction-loop (see figure 3.2.10). Since the friction force always opposes the tip motion, the torsion of the cantilever will be opposite for forward and backward scan directions and in consequence, will be detected as positive or negative torsions in the segmented photodiode. The lateral force signals presented along this thesis present this scan direction dependence, a higher value of the lateral force on forward scan refers to a higher torsion while the contrary occurs for backward scan direction. This inversion or asymmetry of the lateral force on trace-retrace scans is given by the torsion detection method itself, and has to be clearly distinguished from friction anisotropy and asymmetry effects which are related to the dependence of friction on the sliding direction of the tip in some particular systems. In fact, by definition, friction force is always referred to the direction opposite to the relative motion of the surfaces in contact, thus same absolute values of opposite torsions on trace-retrace scans denote a very same friction force.

Realistically, when scanning a rough surfaces, there is always some cross-talk between the normal bending and the torsion of the cantilever. The topography variations (steps, changes in the surface slope, contact area variations...) can give a significant contribution to the lateral force maps. To obtain chemical or material-specific contrast this non-dissipative part of the lateral force has to be separated. This can be easily done by subtracting the lateral force signal in a forward and backward scans when the tip completes a trace-retrace loop and dividing the signal by two, as shown in figure 3.2.10 sketch. The mean friction signal along the loop can be calculated as:

$$F_{mean} = \frac{1}{2} \mid F_l^f - F_l^b \mid \tag{3.2.16}$$

where F_l^i are the lateral signals in the forward and backward scan directions. A schematic representation of a friction loop is presented in figure 3.2.10. Because normal forces do not depend on the scan direction while lateral forces do, the topography contribution will vanish when calculating F_{mean} (check the corresponding lateral force signals in figure 3.2.10 in the topographic step variations, and the F_{mean} one). The calculation of the friction or/and friction coefficient by this methodology, has also the advantage of correcting any possible asymmetry in the friction loop that arises from imperfect laser alignment (e.g. an offset in the 1-2 alignment, see section 3.2). For simplicity, along this thesis we will refer to the calculated mean friction simply as friction (F). The area enclosed in the loop is equal to the dissipated energy on the cycle and the area divided by twice the scan distance is the mean lateral force, i.e. the mean friction [94]. In this way, when performing FFM experiments as a function of the applied load in order to measure the the friction coefficient (μ), it has to be taken into account that by employing F_{mean} friction values we are actually calculating μ_{mean} instead of μ.

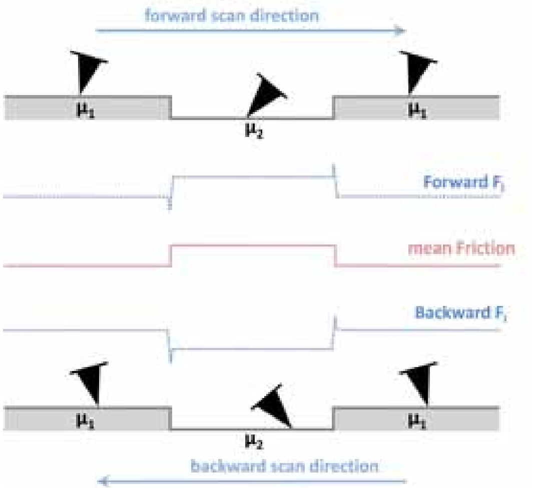

Figure 3.2.10: *Friction loop formed by the trace and retrace lateral signals along the same scan line. The upper and lower pictures represent the torsion movement of the tip as it encounters areas of different frictional properties ($\mu_2 > \mu_1$) or topography changes. Dashed lines are the corresponding lateral force profiles. The solid line is the mean friction force obtained from equation 3.2.16. Reproduced from Bluhm et al. [98].*

The calculation of the friction by this methodology however has to be carefully applied. It has to be considered that for non isotropic friction responses, when the friction response presents an azimuthal orientation dependence, the friction response in trace-retrace direction will vary and the F_{mean} calculated by equation 3.2.16 will be the mean friction value of two different frictional responses. Although the calculation of F_{mean} for non isotropic surfaces may look physically meaningless, the fact is that it can be used to obtain information about locations which hold a 180° symmetry on its frictional response. A clear example of the utility of the combined analysis of the forward-backward lateral forces and the mean friction to disclose structural properties of self-assembled monolayers will be presented in section 4.4.2. The determination of friction differences throughout this thesis is always done by measuring the lateral force forward and backward signals. Several friction loops corresponding to different line profiles are built and in the cases where no relevant deviation is found between forward and backward frictional responses the mean friction is calculated by equation 3.2.16. Applying this line by line procedure to the complete lateral force images leads to a friction map, allowing a direct correlation between the topographical details and the local frictional response.

In addition, the measurement of the lateral force may provide atomic periodicity resolution. When a SFM tip is in mechanical contact with a surface, simple elastic contact mechanics show that, for typical tip radii, elastics constants and loads, the contact is not just a single atom. Therefore, the contact mode SFM can not possess single atom resolution akin to STM. Anyway, these so-called high resolution lateral force images often do display atomic scale stick-slip behavior with the periodicity of the atomic lattice of the sample, and results extremely useful for surface structural characterization. It is well-established that when sliding a SFM tip over a periodic lattice, the so-called phenomenon of atomic stick-slip behavior yields lateral force images exhibiting the two-dimensional (2D) atomic or molecular periodicity of the surface under study. The explanation to this stick-slip behavior has been discussed in numerous experimental and theoretical works [7, 99, 100].

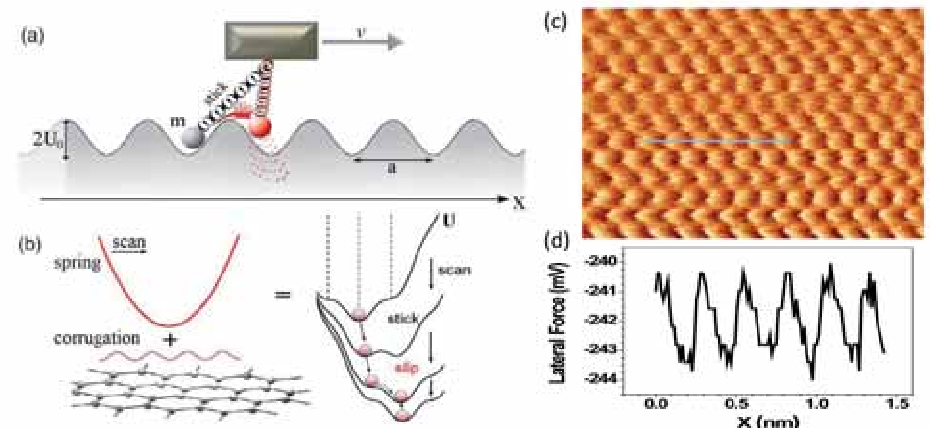

Figure 3.2.11: *Cartoon of the stick-slip behavior is presented in (a). The total potential (harmonic spring + sinusoidal substrate) exhibits different metastable minima (b), giving rise to the stick-slip behavior. (c) High resolution lateral force image measured on HOPG showing the common trigonal pattern with maxima separation of* 2.46Å *visualized by stick-slip experiments [101]. (d) shows the profile marked in (c) where the friction pattern of the stick-slip behavior. (a) and (b) adapted from [100].*

Stick-slip can be intuitively understood considering the combined action of the parabolic potential of the SFM tip (modeled as a spring) and the periodically varying potential of the surface which results in a total potential that presents a series of local minima (see figure 3.2.11 b). At equilibrium, the tip resides in one local minimum. When the tip is pushed laterally, it will remain at that minimum ("sticking"), until the restoring force of the cantilever is enough to overcome the energy barrier and effectively "un-stick" the cantilever, causing the tip to jump or slip to the nearest local equilibrium position, where it is locked again (figure 3.2.11 a). At each jump from one minimum to the next, energy is dissipated, and lateral force images will indeed show the lattice periodicity of the surface. This is not, however, true atomic resolution and, for example, isolated vacancies can not be visualized. However, these lattice-resolved images are extremely useful for surface structural characterization and, as we will show in this work, can be used to differentiate between coexisting domains of specific molecular configurations and an accurate lattice orientation can be determined. In figure 3.2.11 (c) a high resolution lateral force image of highly oriented pyrolytic graphite (HOPG) surface is presented, where the commonly measured trigonal pattern with maximun separation of 2.46Å is visualized [101, 102]. The corresponding friction pattern of the location marked in (c) is presented in (d).

3.2.5.2 Conductive scanning force microscopy

Because nanoscale electrical transport properties have been attracting enormous interest, specially in material science, conductive or current sensing scanning force microscope (CSFM) [103] techniques have been developed over the last decade. They are based in the use of a conductive sharp tip, which allows measuring the current flowing between tip and sample with nanoscale resolution while simultaneously probing the surface morphology thanks to the force control feedback.

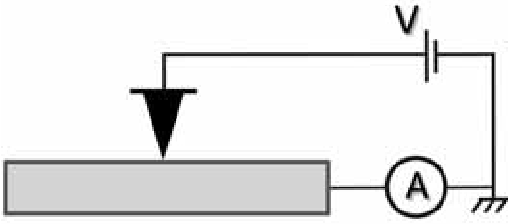

Figure 3.2.12: *Sketch of the CSFM experimental setup. V and A denote the voltage source and ammeter respectively.*

In CSFM measurements a conductive tip is placed in direct contact with the sample surface to attain a stable electrical contact and the electric current flow is measured in function of the position and applied voltage difference between tip and sample. A schematic representation of the experimental CSFM setup is presented in figure 3.2.12. The capability of controlling the cantilever deflection (i.e. the applied load) during the electrical measurements is the main advantage of this technique. This allows the independent but simultaneous topographic and local current flow determination [103]. It should be emphasized that measuring conductivity by means of this technique has the advantage of allowing decoupling between the probe positioning and the conductivity measurements, thus facilitating knowing the tip location. Besides, from the current-applied voltage dependence (I-V curves), the method provides a complementary key to understand the conductive mechanisms. Moreover, the ability to control the applied load permits probing the relation between the mechanical deformation and transport properties. And, in particular, permits avoiding any undesirable tip-induced effect, separating and controlling the mechanical response of the system under study. However, an important aspect to keep in mind is the role of the tip and tip-sample contact conditions on the local conductive measurements. Some parameters such as the tip-sample contact area, the conductive coating conditions of the tip or the possible presence of contamination in both tip and sample are not always controllable, and these phenomena can drastically influence on the local conductivity measured by CSFM. That is why we have followed a reliable procedure that consists in the comparison of the results obtained by the very same tip and using always heterogeneous surfaces to be able to compare the conductive characteristics of each location in a relative way. Besides, the tip conductive conditions have been always cross-checked in freshly cleaved highly oriented pyrolytic graphite (HOPG) prior and after any CSFM experiment.

The conducting probes are highly doped silicon or coated tips, being Au, B-doped diamond, Cr/Pt and Pt/Ir the most common used conductive coatings. In our experimental setup the bias voltage is usually applied to the tip and the current is measured in the grounded sample through a high sensitivity ammeter (see sketch in figure 3.2.12). In our experimental set up we can access to a wide range of compliance currents ($\sim 20\,pA - 10\,mA$) with a level of noise of around $10\,pA$. Whereas for topographic images the color code is the commonly used, bright for high and dark for low, for the current maps it depends on the voltage sign. Thus higher currents appear darker in CSFM images taken at negative V_{tip}. To diminish any possible humidity effect in the CSFM measurements and ensure always the same humidity conditions, the CSFM experiments presented in this work have been always performed under N_2 environment ($RH < 5\%$).

3.2.5.3 Kelvin probe force microscopy

The Kelvin probe force microscopy (KPFM) is a method that measures the contact potential difference (CPD) between the sharp conductive SFM tip and sample with nanometer resolution. It was introduced in 1991 by Nonnenmacher et al. [104] and it is based on the use of a dynamic SFM system, with a nanometric size probe as metallic electrode to apply the vibrating capacitor method [105] into the nanoscale. The vibrating capacitor method was introduced by W. Zisman [105] and is an extension of the Kelvin method [106] invented by William Thomson, more known as Lord Kelvin, who measured the CPD between zinc and copper by nullifying the field between the two plates capacitor of the two materials.

To describe the contact potential phenomena, the concept of work function (ϕ) has to be introduced. The work function (Φ) is defined, for the case of an infinite homogeneous surface, as the difference in energy between an electron in the vacuum state (E_{vac})and an electron at the Fermi level (E_F) [107, 108]. Naturally, for all materials but metals there is not an actual energy level in the Fermi level and actually, by term Fermi level the chemical potential of electron is meant [109]. If we consider two metallic materials with different work functions (figure 3.2.13 a), the two plate capacitors employed by Lord Kelvin or, for example, a conducting SFM tip and a conducting sample, their local vacuum levels are aligned but there is a difference in their Fermi levels. The contact potential difference (CPD) between the two materials, is defined as:

$$CPD = \frac{\phi_{sample} - \phi_{tip}}{q} = \frac{\Delta\phi}{q} \tag{3.2.17}$$

where ϕ_{tip} and ϕ_{sample} are the work functions of tip and sample, respectively, and q is the elementary charge. When the two materials are electrically connected, electrons flow from the material with the smaller work function to the material with higher work function until their Fermi levels align. In this situation, the two materials are charged and a difference in their local vacuum levels is established. As a consequence of the charging of the tip and the sample an electrostatic force develops (figure 3.2.13 b). If an external bias voltage that equals V_{CPD} is applied between tip and sample this force is nullified and the contact potential difference between tip and sample can be directly determined (figure 3.2.13 c).

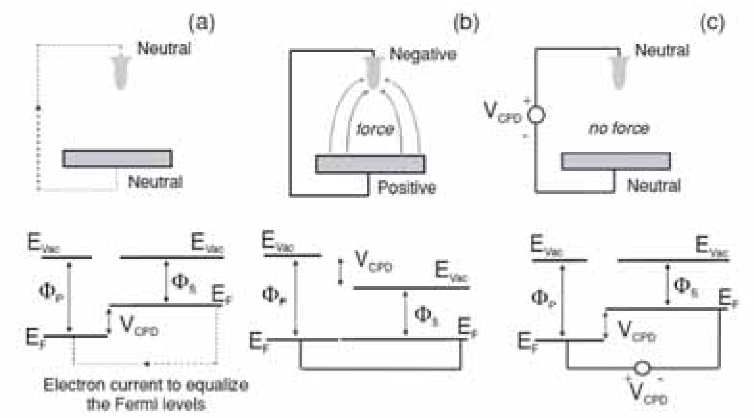

Figure 3.2.13: *Schematics definition and basic measurement setup of contact potential difference (CPD). Energy level diagrams of two different metals, which are assumed to be plates and form a capacitor, with work functions ϕ_p and ϕ_s : In case (a) both metals are isolated. If the are connected, as in part (b), the Fermi levels E_F align with the consequence that a potential drop, the so-called contact potential difference (CPD), in the local vacuum level E_{vac} is generated. The vacuum level can be flattened by a bias voltage V_{CPD}, as shown in part (c). Adapted from Glazel et al. [110].*

The CPD between two materials does not depend only in the work function difference of the materials, but also on a variety of parameters such as adsorption layers, oxide layers, dopant concentration in semiconductors or temperature changes in the sample. Thus the measurement of the CPD can be employed to gain information about a variety of parameters affecting the local CPD in the nanoscale.

As was introduced in section 3.2.3, if the tip-sample system is considered as a plane capacitor, the electrostatic force between tip and sample can be written as:

$$F_{el} = -\frac{1}{2}\frac{\partial C}{\partial z}U^2 \tag{3.2.18}$$

where z is the tip-sample distance, C is the capacitance of the system and U is the tip-sample potential difference. In the SFM system, to measure the electrostatic force separately from other forces (mainly van der Waals and chemical forces), an ac voltage V_{ac} at a frequency w is applied to the conducting SFM tip (or sample) keeping the sample grounded (or tip). Then, the electrostatic force between the two electrodes is given by:

$$F_{el} = -\frac{1}{2}\frac{\partial C}{\partial z}[(V_{dc} - V_{CPD}) + V_{ac}\, sin(wt)]^2 \tag{3.2.19}$$

where V_{dc} is an applied dc bias to the tip. Developing the equation 3.2.19 one finds that the electrostatic force can be separated into three different terms:

$$F_{el} = F_{dc} + F_w + F_{2w} \tag{3.2.20}$$

where,

$$F_{dc} = -\frac{1}{2}\frac{\partial C}{\partial z}[(V_{dc} - V_{CPD})^2 + \frac{1}{2}V_{ac}^2] \tag{3.2.21}$$

$$F_w = -\frac{\partial C}{\partial z}(V_{dc} - V_{CPD})\, V_{ac}\, sin(wt) \tag{3.2.22}$$

$$F_{2w} = \frac{1}{4}\frac{\partial C}{\partial z}\, V_{ac}^2\, cos(2wt) \tag{3.2.23}$$

The F_{dc} component contributes to a static deflection of the cantilever, which in certain operating modes can contribute to the topography signal, see section 3.2.4. As a result of F_w and F_{2w} the tip starts vibrating at the corresponding w and $2w$ frequencies. The term F_{2w} can be used for capacitance force microscopy [111, 112], and the F_w is used to measure the V_{CPD}. The principle of operation of KPFM is based on nullifying the vibration of the tip at this w frequency ($F_w = 0$) by applying an adjustable dc voltage to the tip which equals to V_{CPD}. A feedback loop is used to adjust the dc bias on the tip to nullify the vibration amplitude of the cantilever in the operating frequency (w), and therefore, a quantitative map of CPD can be obtained by monitoring the applied voltage (V_{dc}) by the feedback loop in each scanned location. This operating mode is usually known as amplitude mode Kelvin probe force microscopy (AM-KPFM), since the physical magnitude controlled in the feedback loop is the amplitude of F_w.

An alternative operating mode is the so-called frequency modulation Kelvin probe microscopy (FM-KPFM) which was first proposed by Kitamura et al. [113]. In analogy to the aforementioned AM-SFM and FM-SFM (section 3.2.4), FM-KPFM is based on monitoring the response of the induced frequency shift (Δw) of the mechanical oscillation of the cantilever as a result of the presence of F_w, and thus it is sensitive to the force gradient:

$$\Delta w \propto \frac{\partial F_w}{\partial z} = -\frac{\partial^2 C}{\partial^2 z}(V_{dc} - V_{CPD})\, V_{ac}\, sin(wt) \tag{3.2.24}$$

That is, in FM-KPFM, ∇F_w is used as the physical magnitude for the KPFM feedback loop instead of F_w. FM-KPFM has been proven to improve the signal to noise ratio, avoiding the contribution of the cantilever and the tip cone to the detected electrostatic force and thus enhance the lateral resolution on CPD measurements [48, 114–116]. Due to these reasons, for all the KPFM results presented in this thesis we have used the FM-KPFM technique. A mapping of the contact potential is done simultaneously to topography in the tapping mode (see section 3.2.4), which is sometimes called as single-pass mode. This means that simultaneously to the constant amplitude and PLL feedback (see section 3.2.4), a third feedback is working to keep $\partial F_w/\partial z = 0$ (equation 3.2.24). Depending on the tip-cantilever conditions and characteristics of the sample we reach a lateral resolution of a few tens of nanometers with a noise level around $10 - 20\ mV$. In combination to the single-pass KPFM, the so-called lift mode or retrace mode has also been employed. In this mode, once the topography of each scan line is acquired the amplitude feedback is turned off (the topography feedback) and the tip is lifted from the surface and traced over the same line reproducing the topographic profile at a certain distance with the PLL and KPFM feedback on. By this strategy, the KPFM can be performed in a tip-sample true non-contact condition, discarding any tip-sample contact induced effect in the CPD measurement. The use of the lift mode on KPFM was introduced by Jacobs et al. [117, 118] and takes advantage of the long range of electrostatic interactions (in comparison to van der Waals and chemical interactions, see section 3.2.3) to measure the CPD, preventing undesired cross-talk of non electrostatic interactions into F_w or Δw magnitudes. Typically a $10\,nm$ lift is enough to ensure decoupling any van der Waals interaction. On the other hand, the use of the lift-mode typically has worse lateral resolution of KPFM, because when the tip-sample distance is increased the electrostatic contribution from a wider area is weighted by the tip and the local variation of CPD is averaged over a more extended region.

For the KPFM results obtained along this thesis, the single pass KPFM has been employed simultaneously to intermittent contact (or tapping) mode. However, systematic cross-check of the result obtained in the single pass mode KPFM have been done by lift mode KPFM and/or by the electrostatic force point measurements (making use of the 3D mode, see section 3.2.5.4), which ensure any undesired cross-talk of non electrostatic interactions in the CPD measurement. The 3D modes are an alternative way of acquiring data and can be employed to determine the local CPD as will be introduced in section 3.2.5.4. On another hand, in the present work we have followed reliable procedure that consists in the study of relative rather than absolute CPD measurements by always using heterogeneous samples. As introduced above, our KPFM measurements allow us to measure the local CPD referred to the tip work function. If the work function of the vibrating electrode is ϕ_{tip} and ϕ_s is the one of the sample, then the contact potential difference between tip and sample is $CPD_{sample} = {}^{(\phi_s - \phi_{tip})}/_{q}$. When the sample has two different regions with different CPD, the contact potential corresponding to each region would be given by $CPD_{S1} = {}^{(\phi_{s1} - \phi_{tip})}/_{q}$ and $CPD_{S2} = {}^{(\phi_{s2} - \phi_{tip})}/_{q}$, respectively. Consequently, the contact potential difference between two differentiated regions is going to be $\Delta CPD_{S1-S2} = CPD_{S1} - CPD_{S2} = {}^{(\phi_{s1} - \phi_{s2})}/_{q}$, which is independent of the material the tip is made of. Furthermore, it has to be taken into account that the local CPD does not only depend on the tip work function but also on the specific conditions of the tip. Because small variations in the tip conditions, as possible adsorbates or conductive coating peeling can dramatically influence on the measured CPD, care has always been taken to rule out any tip induced variation on the obtained CPD data.

3.2.5.4 3D modes

In SFM a given magnitude is measured as a function of two others, $f_i(x_1, x_2)$, where the fast scan direction (x_1) and the slow scan direction (x_2) are usually the longitudinal dimensions of the scanned sample area. The so-called three-dimensional (3D) modes are an alternative way for recording data where (x_1, x_2) do not necessarily correspond to these longitudinal magnitudes [27, 43, 119]. Since in common SFM measurements, various physical magnitudes can be simultaneously measured, the dependence of more than one magnitude on the two (x_1, x_2) variables can be simultaneously obtained. In the resulting images the color scale represents the magnitude f_i as a function of the two magnitudes chosen as variables (x_1 and x_2). SFM 3D mode strategies have been widely applied in literature to the study of material properties, including mechanical [24] , conductive [120–123], electrostatic [121, 124] and magnetic [125, 126] properties of variety of systems, as well as to the further understanding and development of SPM techniques [43, 48, 68, 73, 83, 116, 127].

In the present work, the 3D modes are applied for the measurement of local electrostatic and conductive properties of materials. In the following section, we will briefly introduce the basic operation mode and the applications of the 3D modes proposed along this thesis.

3D modes for CPD measurements:

The 3D modes can be applied to measure the contact potential difference (CPD) between the tip and a given surface point as well as to determine tip-sample capacitance dependence with the distance (factor ${}^{\partial C}/_{\partial z}$). As introduced in section 3.2.3, the electrostatic force between between the tip and sample is given by:

$$F_{el} = -\frac{1}{2}\frac{\partial C}{\partial z}U^2 \tag{3.2.25}$$

where z is the tip-sample distance, C is the capacitance of the system and U is the tip-sample potential difference. In absence of external bias, this potential difference is the contact potential difference (CPD) between the tip and the sample. If an external bias is applied to the tip (or to the sample) ($U = U_{ts} - U_{CPD}$), the electrostatic interaction (F_{el}) will present the quadratic dependence given by equation 3.2.25 with the resulting parabola centered in CPD. Thus, by monitoring the quadratic dependence of the normal deflection (normal force, F_n) as a function of the tip-sample voltage difference, the CPD at a given surface point can be obtained. In fact, in analogy to KPFM where the amplitude modulation or frequency modulation can be used to measure the CPD (section 3.2.5.3), not only the normal force but also the frequency shift of an oscillating tip (Δw) can be employed to measure the local CPD by this 3D mode methodology. As the frequency shift of an oscillating probe is proportional to the force gradient ($\Delta w \propto \frac{\partial F}{\partial z}$) (see section 3.2.4), it will also present a quadratic dependence with U_{tip} with the parabola centered in CPD, this is:

$$\Delta w \propto \frac{\partial F_{el}}{\partial z} = \frac{1}{2}\frac{\partial^2 C}{\partial z^2}U^2 \tag{3.2.26}$$

For the application of the 3D mode strategy to this particular measurements, we monitor the normal force ($f_i = F_n$) as a function of the tip–sample applied voltage (fast scan, $x_1 = V$) and

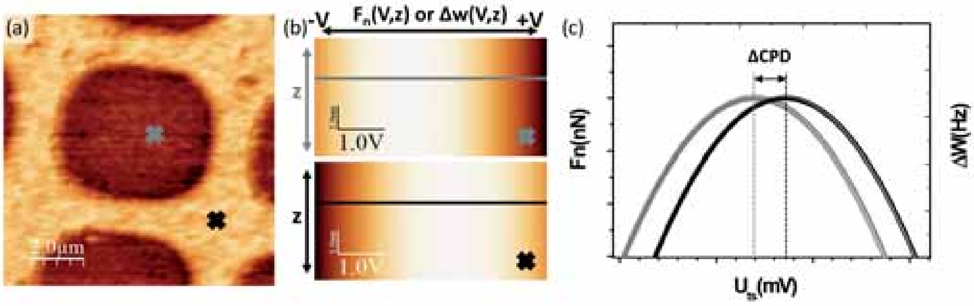

Figure 3.2.14: *KPFM map of a selective growth of MOF presenting differences in CPD. 3D mode $F_n(V_{tip}, z)$ maps obtained in the location marked by crosses in (a) and (c) shows the corresponding parabolas of the profiles marked in (b).*

vertical piezo-displacement (slow scan, $x_2 = Z$), obtaining a $F_n(V_{tip}, z)$ image on a specific point. As expected for the electrostatic force between the tip and sample, horizontal profiles in this F_n image provide the F_n versus U_{ts} parabolic curves centered on CPD. The very same procedure is applied for the force gradient approach, hence, frequency shift ($f_i = \Delta w$) is monitored as a function of (V_{tip}, z) and from horizontal profiles in the $\Delta w(V_{tip}, z)$ image, the parabolic curve of Δw versus U_{ts} is obtained. The main experimental variation between both approaches yields in the requirement of dynamic cantilever conditions for the $\Delta w(V_{tip}, z)$ monitoring, while for measuring $F_n(V_{tip}, z)$ both non-dynamic or dynamic cantilever conditions can be employed. The variation of contact potential difference (ΔCPD) between two locations is directly determined from the relative voltage shift between the parabolas obtained in each location. This is illustrated in figure 3.2.14. Figure 3.2.14 (a) shows a CPD map presenting a clear CPD contrast, obtained by FM-KPFM on a selective growth of metal–organic frameworks (MOFs) over a $COOH$ terminated SAM surrounded by CH_3 terminated SAM. Images in (b) represent the $F_n(V_{tip}, z)$ (or $\Delta w(V_{tip}, z)$) maps obtained by the 3D mode strategy described above on the locations marked in (a). From the parabolas shift shown in (c) the ΔCPD is directly determined.

Along this thesis, 3D modes strategies for CPD determination has been mainly employed to cross-check the results obtained by KPFM measurements. This 3D operation mode presents the advantage of independent but immediate data acquisition while maintaining a precise control over the tip-sample distance, excluding any undesirable artifact in the CPD determination. Both $F_n(V_{tip}, z)$ and $\Delta w(V_{tip}, z)$ measurement approaches have been used to the local CPD determination depending on the specific experimental conditions.

3D modes for electric transport measurements:

In this particular 3D modes we monitor the normal force and current flow ($f_1 = F_n \quad and \; f_2 = I$) as a function of the tip–sample applied voltage (fast scan, $x_1 = V$) and vertical piezo-displacement (slow scan, $x_2 = Z$). As consequence, $F_n(V_{tip}, z)$ and $I(V_{tip}, z)$ images are obtained at a specific point. As in the procedure presented above, the tip voltage varies a certain value for each tip-sample distance while the tip approaches the surface. In this case however, the tip is allowed to enter in contact with the sample and thus the conductive character and the mechanical response of the sample are measured as a function of the piezo displacement. It should be emphasized that measuring conductivity by means of this technique has the advantage of allowing decoupling between the probe positioning and the conductivity measurements, thus facilitating knowing the vertical location of the tip with respect to the sample.

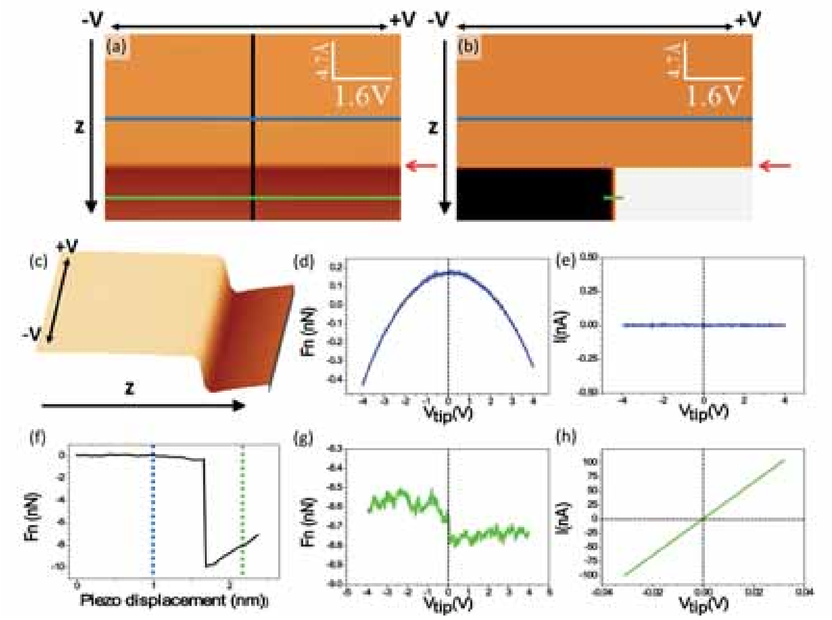

Figure 3.2.15: *Top view (a) and three-dimensional view (c) of the normal force image $F_n(z, V_{tip})$ and the simultaneously acquired current image (b). Vertical line profile marked in (a) that corresponds to the F–z curve at $V = 0V$. The horizontal line profiles marked on each image are the F–V curves (d and g) and the I–V curves (e and h) measured at the z piezo-position of the location marked in the corresponding image. The voltage range is $\pm 4V$ and a total piezo displacement of around $2.5\,nm$. Note: in this particular experiment the current was limited to 100nA, that is why the current signal saturates in (b) for $| V_{tip} | \gtrsim 30mV$ (data not shown in h).*

An example of $F_n(V_{tip}, z)$ and $I(V_{tip}, z)$ 3D mode experiment on top of Au is presented in figure 3.2.15. The simultaneous measurements of the normal force (F_n) and the current (I), both as a function of the bias voltage (V_{tip}) and the vertical piezo displacement (z), are shown in (a) and (b). The $F_n(V_{tip}, z)$ image has been represented as a top view (a) and as a three-dimensional plot (c). Along the fast scan direction, the applied voltage is varied between $\pm 4\,V$ and along the slow scan direction the piezo moves $\sim 2.5\,nm$. From the vertical line profile corresponding to $F_n(0, z)$, the $F - z$ curve presented in (f) is extracted. Two representative points have been selected along the tip approach to the Au surface (marked by blue and green lines). In the first one ($z = z_1$), corresponding to the situation where the tip is still out of contact (in blue color), the horizontal line profile $I(V_{tip}, z_1)$ data in (e) indicate that no current flows between the tip and the sample. Furthermore, from the related $F_n(V_{tip}, z_1)$ profile (d) it can be seen that the force has a parabolic dependence with the applied voltage , indicative of the electrostatic interaction variation between tip and sample when V_{tip} varies. Therefore, both the current and force behavior suggest that the tip is not yet in contact. Note also that the almost constant cantilever deflection in the $F - z$ curve indicates that during this part of the piezo motion the applied force is almost constant while the tip-substrate distance is decreased. The continuous displacement of the piezo approaches the tip to the sample until the Au surface is eventually contacted by the tip (marked by red arrows in a and b images). At this point, the parabolic response of F_n with respect to the applied voltage is lost (g) and a linear behavior of the I-V curve corresponding to the ohmic response of the metallic contact between the Pt coated tip and Au surface is observed from this point until the bottom end of the current image.

3.3 Scanning tunneling microscopy

The scanning tunneling microscope (STM) is based on the quantum tunneling effect, which holds that an electron has a non-negligible probability of crossing an energy barrier. In the STM, an atomically sharp conductive tip is brought close to the conductive surface (typically $< 1\,nm$). The proximity is such that the electrons wave functions of the tip and the sample overlap and by applying a tip-sample potential difference the electrons tunnel through the vacuum from one to the other. Typically the gap between the tip and sample is of the range of a few Å and for a potential difference (also called *bias*, V) of the range of hundreds of mV a tunneling current (I) of the range of hundreds of pA to a few nA is measured. This applied voltage results in a large electric fields

($\approx 10^{10}\ V/m$) localized near the tip apex, what make the electrons to flow mainly through the very last atoms of the tip apex to the single atom below. This means that the tunneling current is highly localized, and is the reason why STM inherently provide atomic lateral resolution. On the other hand, the tunneling current that flows through the small gap between tip and sample presents an exponential dependence with the tip-sample distance (z):

$$I \propto e^{-2\kappa z} \tag{3.3.1}$$

where κ is the so-called decay factor $\kappa = \frac{\sqrt{2m\phi}}{\hbar}$, being ϕ the effective barrier height (which for low voltages corresponds in good approximation to the average work function between the tip and surface), m is the mass of the electron and $\hbar$ is the reduced Planck constant. This exponential dependence of the tunneling current is the key point in the success of STM in terms of vertical resolution, since it gives rise to significant current variations when topographic small corrugations are found during the tips scan. For a typical work function around $4\,eV$, $\kappa \approx 1\text{Å}^{-1}$, by equation 3.3.1 is deduced that the current varies by one order of magnitude when z is changed by 1Å. If the current is kept constant to within, e.g. 2%, then the gap z remains constant to within 0.01Å. This is the reason why the STM has such a good vertical resolution even in ambient conditions [128]. The exponential dependence of the tunneling current with the tip-sample distance described by equation 3.3.1 helps understanding the general working principle of the STM. However, a more complex formalism is necessary to understand the meaning of the images obtained by STM. Most of the tunneling theories are based on the *perturbative transfer Hamiltonian* formalism introduced by Bardeen [129]. For further understanding of the theory and the interpretation of the STM measurements we refer to the work by Tersoff and Hamann [130, 131] and to the extended literature on the field [132–134].

In STM, there are two main operating modes, the constant height mode and the constant current mode. In the constant height mode the surface is scanned with a fixed bias and height and the resulting image is the tunneling current signal in each $x - y$ position. This measuring mode is typically employed for spectroscopic measurements because it presents the problem that only very flat surfaces can be scanned with it and the alignment of the surface and the tip *constant z* scan plane have to be extremely accurate to avoid any tip crashing or non desired influence of the topographic variations into the current signal.That is why the most common measuring method is the constant current mode (cc-STM). In cc-STM the tunneling current and bias are set fixed and during scanning over the surface the tip vertical position is adjusted by a feedback loop at each surface point to keep constant the measured tunneling current, e.g. in those positions where the tunneling current is higher (higher electronic density) the tip retracts to keep the set current value. The piezo z displacement is registered over the $x - y$ position and the constant current map is build. This means that the tip motion follows a profile of constant current and the vertical displacement of the tip gives the so called topography, which corresponds to a constant electronic density profile. Consequently, a constant current map reflects the relative tip height, also known as the apparent height because it is in fact the convolution of the electronic and physical structures of both the tip and the surface sample. The tunneling tip is typically prepared from a wire that is sharpened by chemical etching or mechanical grinding, and W, Pt- Ir, or pure Ir are usually chosen as tip material.

The STM measurements presented in this thesis were made using a Molecular Imaging PicoSPM microscope [30]. Tips were prepared mechanically by cutting a 0.25 mm Pt/Ir alloy wire ($8:2$, Chempur). Measurements were carried out under ambient conditions in cc-STM mode, using tunneling currents between $100\,pA$ and $1\,nA$ and sample bias between 0.6 and $1\,V$.

3.4 Sample preparation

3.4.1 Gold substrates

Two kind of gold substrates have been employed along this work, polycrystalline gold surfaces with low surface roughness ($< 4\,nm$) over large areas of thousands of μm^2 with gold grains of a mean diameter of $60\,nm$, and gold surfaces with considerably larger overall surface roughness but with grains that consist of extremely flat terraces of some thousands of nm^2 separated by monoatomic steps.

Two different polycristalline gold substrates have been used, polycristalline gold on glass and on silicon, being their main difference the overall surface roughness that they present. Polycrystalline gold on glass substrates were purchased from $Arrandee^{TM}$ [135]. They consist of a gold film of $200 - 300\,nm$ in thickness on top of a chromium layer ($1 - 4\,nm$ thick) over a borosilicate glass surface. The chromium layer plays the role of improving gold adhesion to the glass substrate, avoiding bubbles and undesired film pill off. The surface roughness of those substrates is of $\sim 3nm$ over large areas. Polycristalline gold on silicon substrates present a lower surface roughness ($\sim 2\,nm$), and they consist of a gold film of $50 - 100\,nm$ in thickness on top of a titanium layer of $5\,nm$ over a Si wafer with a native SiO_2 layer on top. Because it presents a lower surface roughness, gold on silicon substrates have been employed when possible rather than the gold on glass ones. Figure 3.4.1 (a) and (b) shows the topography of the gold on silicon sample surface. The surface roughness of image (a) is calculated by plotting the height histogram (c) and is found to be $\sim 2nm$. Prior to the formation of the self-assembled monolayers, these kind of gold substrates are cleaned by immersion in a piranha solution ($1:3$; $H_2O_2 : H_2SO_4$) for $10 - 15$ minutes, in order to remove any possible contaminant, mainly of organic nature. Afterwards, the samples are thoroughly rinsed with deionised water (Mili-Q) and dried under N_2 stream. The more hydrophilic the surface appears, the cleaner it is.

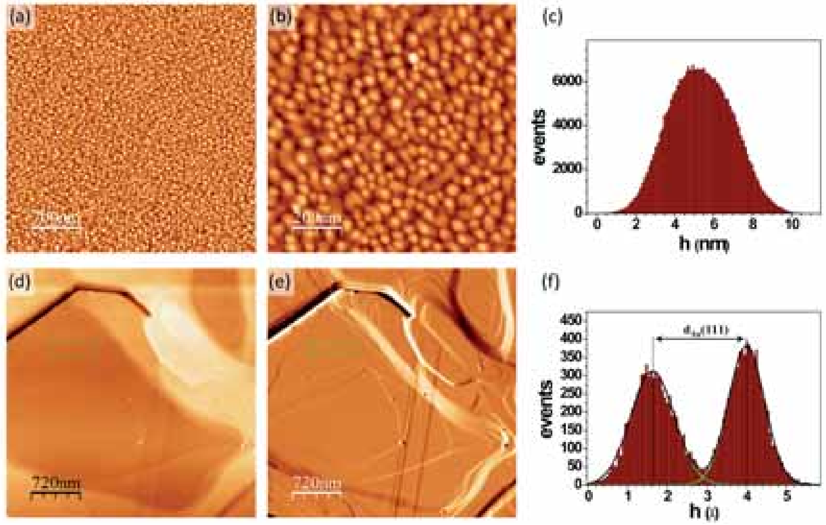

Figure 3.4.1: *Two different magnification SFM topographic images of gold on silicon substrates are presented in (a) and (b). The topographic distribution of image (a) with a rms* $\approx 2.5\,nm$ *is plotted in the height histogram of (c). Topographic (d) image of the gold on mica surface after a good annealing procedure. The large Au(111) atomically flat terraces are better distinguished in the derivative image in (e). The topographic height histogram of (f), corresponding to the location marked in (d), shows the* $d_{Au}(111)$ *atomic step height of* $\approx 2.35\AA$ *measured between to adjacent terraces. The total z-scale of (d) is of* $0 - 22\,nm$.

Two different type of substrates presenting large $Au(111)$ atomically flat terraces have been employed. The gold on glass substrates can be flame annealed in air with a small butane torch set for conical blue (i.e. “reducing”) flame. Good annealing is normally achieved for $1\,min$, when samples are heated to the point where a dim reddish/orange glow is visible. A good flame annealing induces the formation of large grains with atomically flat $Au(111)$ terraces of cents of nm in width. Substrates from *Georg Albert PVD* [136] consisting in 300 nm gold films evaporated onto mica were also used. The as-received substrates already present relatively large Au(111) terraces, but a flame annealing treatment enhances the size of the terraces and eliminates adsorbed contaminants. A lower intensity butane torch is employed for this second type of substrates and a good annealing is obtained by employing subsequent short exposures of the substrates to the flame until the substrates gets an orange like color tone. The flame annealing process does not oxidize the gold nor deposit soot on the surface. In fact, it has been reported that, apart from increasing the grain size and providing large terraces with the lowest energy (111) orientation, it can also contribute to eliminate contaminants [137]. The overall surface roughness considerably increases in these annealed samples due to the deep grain boundaries formed (tens to hundreds of nanometre deep). However, the surface of the grains consists of extremely flat terraces separated by monoatomic steps as the ones seen in figure 3.4.1 (d) topographic image. In the corresponding derivative image presented in (e) the monoatomic steps separating the Au terraces are better seen. A height histogram is depicted in (f), showing the $d_{Au}(111) \approx 2.35$Å height difference between the terraces of the location marked in (d) and (e).

3.4.2 Molecular solutions

In this thesis self-assembled monolayers formed by different molecules have been used. For the results presented in chapters 4 the $\omega-(4'-methylbiphenyl-4-yl)butane-1-thiol$ (BP4, provide by Prof. Manfred Buck from the University of St Andrews) molecule have been employed. In chapter 5 the stearic acid $(n-C_{17}H_{35}COOH)$ molecule was used.

All SAM samples have been prepared by immersion in ethanolic solution. Absolute ethanol provided by both Panreac (PRC, 99.5%) and Romil (SpS, 99.8%)[138] were employed. Prior to solution preparation, the laboratory glassware (Petri dishes, flasks...) were cleaned with an alkaline concentrate (Hellmanex II)[139], to remove any possible contamination, and rinsed with deionised water. Special care was taken to use a set of recipients for each type of molecule. Solutions in the micromolar to milimolar ($\mu M - mM$) range were prepared in two or three consecutive dilution steps of the corresponding molecule in ethanol. Magnetic stirrer with additional heating ($\sim 50°C$)

or sonication in ultrasonic bath were employed to obtain homogeneous solutions.

3.4.3 µ- contact printing

μ-contact printing (μCP) is a soft lithography techniques that forms patterns of self-assembled monolayers (SAMs) on surfaces. μCP uses the relief patterns on a master of polydimethylsiloxane (PDMS) stamp to transfer the molecules to the surface on the desired locations to obtain a pattern. This procedure was firstly developed in Whitesides's group [140–143] and have been extensively used not only for patterning organic molecules, but also for selectively deposit inorganic and biological materials [143]. The elastomeric stamp are molded against a master mold which is fabricated by photolithography or e-beam lithography. The pattern size obtained by this technique are in the range of hundreds of nm to μm [144] and the main advantage of the μCP in comparison to other lithography techniques is that is a versatile, relatively simple and inexpensive technique for patterning surfaces. The PDMS stamps employed in this work were kindle provided by Prof. Andreas Terfort group from the Goethe Universität of Frankfurt within the SURMOF european project (reference NMP4-CT-2006-032109).

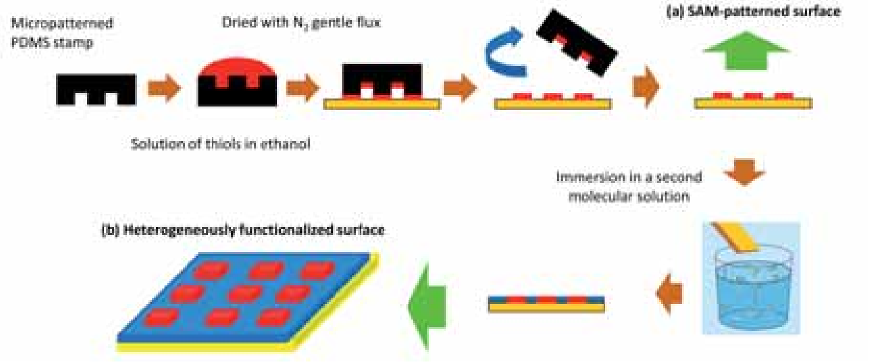

Figure 3.4.2: *The μCP technique procedure is described in the figure.*

For the studies presented in this thesis, we make use of the μCP technique to obtain laterally heterogeneously functionalized surfaces by SAMs. In figure 3.4.2 a schematic representation of the μCP procedure is presented. The stamp is inked in the molecular solution for a few minutes, dried under nitrogen flow, placed on the clean substrate and pressed via mechanical contact. The molecules are transferred from the stamp to the surface where they self-assembly into patterns determined by the relief pattern of the stamp. After a few minutes of contact time, the stamp is carefully removed and the patterned surface is gently rinsed with ethanol to remove non chemisorbed and excess material. At this point the bare substrate is laterally functionalized by a SAM and bare substrate locations (situation a in figure 3.4.2). If the substrate is reimmersed in a second molecular solution, this molecule chemisorbs on the non covered surface regions and a patterned surface with regions of two different functionalities is obtained (situation b).

As for the preparation of SAMs, the ethanol has been the solvent of choice for the preparation of the molecular ink solutions. The mechanical properties of the PDMS are minimally affected by the ethanol [142, 143, 145, 146] and because it rapidly evaporates, the thiol ink rapidly concentrates in the stamp [146]. Typical ink solution concentrations employed for the results presented in this thesis were in the range of 0.1 mM to 5 mM.

For further information about the μCP technique we refer to the literature [147].

3.4.4 Organic molecular beam deposition

Organic molecular beam deposition (OMBD) is a widely used growth technique. Its main advantage is that it offers the growth of a chemically pure compound in a clean substrate and environment with a perfect control of the film thickness, growth rate and substrate temperature. In OMBD the substrate is hold in a ultra-high vacuum (UHV) chamber and is exposed to a molecular beam in vapor phase. The molecular beam is generated in the so-called Knudsen cells, which is composed by a crucible, that contain the organic molecules, surrounded by a heating filament and a thermal shielding. The crucible temperature is measured by a thermocouple and the heating current which fixes temperature is controlled by a Eurotherm [148]. The growth rate and film thickness are controlled by a quartz crystal micro balance (QCM) positioned close to the substrate, making possible the deposition of sub-monolayer films with low deposition rates. For further understanding of the OMBD technique we refer to [149–151].

Two different equipments were employed for the samples prepared by OMBD in this thesis. During my stay in the Max Planck Institut für Metallforschung (Stuttgart-Germany) the thin films were grown in a commercial Omicron UHV system as well as in a home made UHV evaporation chamber. Currently this second home made UHV chamber is located in the ICMAB and has been used to grow new organic films.

Chapter 4

Self-assembled monolayers of BP4 thiols on Au(111) : influence of structural arrangement into the local surface properties

4.1 Motivation

The properties of a surface functionalized by self-assembled monolayers (SAMs) are directly influenced by the chemical composition and the molecular conformation of the molecular units that form the SAM. Among the different parameters that constitute the conformational properties of an organic thin film we can distinguish two main groups based in their origin: the ones related to the molecular structure itself (such as the molecular arrangement, packing density, molecular tilt angle, etc...) and the ones related to the quality of the molecular layer (the coverage, domain sizes, domain boundaries, presence of defects, pinholes, gauche defects, etc...). In this chapter we focus and investigate the influence of the supramolecular structure of a SAM into the morphological, electrostatic and conductive properties of the surface.

For this purpose we have chosen the $\omega-(4'-methylbiphenyl-4-yl)butane-1-thiol$; $(CH_3(C_6H_4)_2(CH_2)_4SH)$ $(BP4)$ molecule that has been shown to form different supramolecular arrangements on $Au(111)$ [152, 153]. Those structurally different phases exhibit a high degree of crystallinity while forming a continuous film and their coexistence can be achieved by an optimal sample preparation. This BP4 system consisting in SAMs with two phases coexisting constitutes an ideal scenario to perform an in situ comparative scanning tunneling microscopy (STM) and scanning force microscopy (SFM) study to demonstrate how different supramolecular arrangements formed out of the same molecular unit influence the morphological, electrostatic and conductive properties of $Au(111)$. We will show how the supramolecular arrangement of the SAM is a decisive factor influencing such surface properties, and thus deserves a deep investigation. In addition, the goal of this study was to correlate and compare the structure of each molecular phase with their mechanical, conductive and electrostatic responses. Besides, we show how FFM can be employed to differentiate SAM domains with different orientation, information that is not accessible by common STM or SFM topography images. In addition, thanks to the combined study of SFM and STM techniques we discuss and correlate the influence of the electrostatic and conductive properties variation in the height differences measured by STM or SFM.

4.2 The BP4 molecule on Au(111) surface

The $\omega - (4' - methylbiphenyl - 4 - yl)butane - 1 - thiol$ $(BP4)$ is a biphenyl based thiol with an alkane chain of four carbons between the thiol headgroup and the aromatic moiety and with a methyl endgroup (see figure 4.2.1). The BPn $(CH_3 - (C_6H_4)_2 - (CH_2)_n - SH)$ $(n = 0 - 6)$ family of biphenyl aromatic thiols containing an alkane spacer have been shown to result in high structural quality SAMs in comparison to the pure aromatic thiols [152–155], that in general present fairly low quality SAMs [156–161]. The number of methylene groups in the alkane spacer chain has been shown to influence on the structure of the SAM layers. The BPn SAMs exhibit a pronounced molecular orientation and coverage alternating variation between n odd and even numbers of alkane groups [154, 155, 162, 163]. Molecular layer properties such as electrochemical stability [164, 165], stability against exchange by other thiols[166] or resistance to electroninduced modification of the film structure[167] are also affected with the odd-even number of alkane groups. In addition and interestengly, the biphenyl thiols containing an even-numbered alkane spacer (that is, $n = 2, 4, 6$) systems upon the preparation conditions present a phase transition that result in supramolecular structures of significantly lower density [152, 153, 168]. Under optimal temperature and time conditions, the coexistence of these different polymorphic phases can be achieved, what constitutes an ideal scenario to perform an in situ comparative study by SFM techniques. For the purspose of this investigation the $BP4$ molecule was chosen because, among the even-numbered BPn-s, is the one presenting the higher structural variation upon the phase transition.

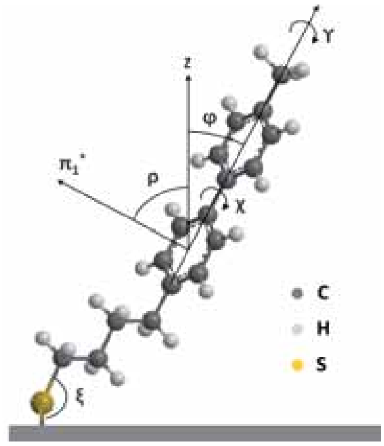

Figure 4.2.1: *Sketch of the BP4 molecule on surface. The angles that describe the Au-S-C bond angle* (ξ) *and the orientation of the aromatic moiety* ($\rho, \varphi, \gamma, \chi$)*. Reproduced from [153, 154].*

The structure of $BP4$ monolayers on $Au(111)$ as obtained by STM has already been reported in detail [152, 153, 155]. Below $343K$, the molecules arrange in a rectangular $5\sqrt{3} \times 3$ lattice, the so-called α-phase, with eight molecules within an unit cell of $24.94 \times 8.64\text{Å}^2$, in such a way that the area per molecule (27.05Å^2) is significantly larger than that of the $\sqrt{3}\times\sqrt{3}$ of alkanethiols (21.55Å^2) [169]. Upon annealing at $373K$, this phase coexists with the β-phase which has been described by an oblique $6\sqrt{3} \times 2\sqrt{3}$ structure with the same number of molecules per unit cell but due to its larger size of $29.93 \times 9.98\,\text{Å}^2$ resulting in a even larger area per molecule ($32.4\,\text{Å}^2$). The unit cells of each molecular phase are schematically presented in the bottom panel of figure 4.2.2. It has to be mentioned that STM results from Su et al. [170] point to a slightly different structure of the β-phase with a commensurate $5\sqrt{3} \times 2\sqrt{3}$ structure. In section 4.4.1 we refer to this discrepancy and point that our SFM results are in agreement with a $6\sqrt{3} \times 2\sqrt{3}$ structure of the β-phase reported by Cyganik et al. [152, 153]. Upon annealing for slightly higher temperatures ($383K$) longer times an additional structure (γ-phase) emerges, which presents and oblique $2\sqrt{3} \times \sqrt{13}$ structure with and area per molecule of (25.2Å^2).

The structural arrangement variation between phases results also in a variation of the molecular tilt angle of the molecule (θ) and thus, on the molecular layer thickness between phases [153]. The thickness of the BP4 fims evaluated from X-ray phoelectron spectroscopy (XPS) data [153] results to be $16.2 \pm 0.7\,\text{Å}$ and $14.4 \pm 0.7\,\text{Å}$ for α and β-phases, respectively. The molecular film thickness of the BP4 α-phase is in agreement with previous ellipsometry results $\sim 1.65\ nm$ assuming a refractive index of 1.47[154]. This difference in molecular thickness has as a result a different molecular tilt angle between α and β-phases. The reported molecular tilt angle for the α-phase (θ_α) is around 40° with respect to the surface normal [154, 155].

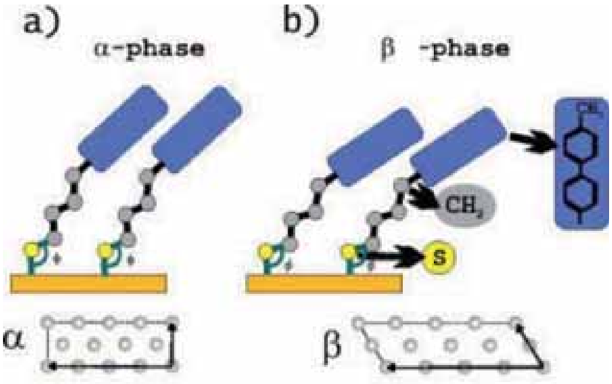

Figure 4.2.2: *Schematic illustration of BP4 molecules on Au(111). (a) shows the room-temperature α-phase with the rectangular $5\sqrt{3} \times 2\sqrt{3}$ structure and (b) the high-temperature β-phase with the oblique $6\sqrt{3} \times 2\sqrt{3}$ structure and higher molecular tilt angle. Adapted from Vervaecke et al. [171].*

The molecular orientation on surface can be described by the angles shown in figure 4.2.1. The orientation of the aromatic moiety is determined by the angles ρ and φ, which are related through the twist angle γ according to $\rho = arccos(sin\varphi\, cos\gamma)$. χ defines the dihedral angle between phenyl rings and ξ the metal-sulfur-carbon angle. Works by M. Buck and co-workers [153, 154, 172] based in near-edge X-ray absorption fine structure spectroscopy (NEXAFS) and infrared reflection absorption spectroscopy (IRRAS) measurements tried to elucidate the difference on the molecular orientation between the two BP4 polymorphic phases. The exact biphenyl moiety orientation however is complicated to evaluate. From their work it can be concluded that the three angles (ρ, φ and χ) that determined the orientation of the phenyl rings change between both polymorphic phases. Combined data of NEXAFS and IRRAS gives rise to an estimation of twist angle $\gamma \approx 60°$ for the α-phase. By assuming a coplanar orientation of the rings they got values of 64 and 68 for the ρ angle of the α and β-phases respectively. However, from the fact that the molecular density is lowered in the β-phase it is concluded that γ have necessarily to change from phase to phase [153], what makes difficult to evaluate φ. In addition, because the dihedral angle χ between the phenyl rings in biphenyl is known to be very sensitive to its environment due to the relatively low energy barrier for rotation (about 63 meV/molecule)[153], it is reasonably to think that the change in ρ ,

γ and the packing density is accompanied by a change in the the dihedral angle (χ). Limited by the integration character of the NEXAFS and IRRAS techniques it cannot be determined whether the measured ρ and γ angle changes were due to uniform changes of both phenyl rings and/or by change of the dihedral angle.

4.3 Sample preparation and experimental procedure

Self-assembled monolayers of ω-(4'-methylbiphenyl-4-yl) butane-1-thiol [154, 173] ($BP4$) on gold with the presence of both α and β-phases were prepared as previously detailed in the literature [152, 155]. Gold on mica substrates (300 nm gold film evaporated onto mica from Georg Albert PVD, Germany [136]) were flame annealed in air for a few minutes in order to obtain large and atomically flat (111) oriented terraces. Complete monolayers exhibiting exclusively the so called α-phase were prepared by immersing the substrate typically in $0.1-1mM$ range ethanol solution of $BP4$ molecule at $338K$ for $12-24\,h$, neither the concentration nor the immersion time are critical for this preparation [152]. The transition to β-phase was induced by post annealing the α-phase monolayer sample at $373K$ in nitrogen atmosphere [152]. The coexistence of the two phases is achieved by annealing times typically on the range $15-18\,h$. The ratio between areas covered by each phase is dependent on the precise annealing time employed and can be therefore tuned at while. For $BP4$ patterned samples soft lithography μ-contact printing (μCP) technique (see section 3.4.3) was employed into flame annealed gold on mica substrates at room temperature. Long printing times (around ~ 5 minutes) were employed in order to obtain SAMs of $BP4$ molecules. No post annealing process was applied to those samples since the goal was to perform a direct comparison between an α-phase monolayer and bare gold.

Scanning tunneling microscopy (STM) measurements were made using a Molecular Imaging PicoSPM microscope under ambient conditions. Tips were prepared mechanically by cutting a $0.25\,mm$ Pt/Ir alloy wire (8 : 2, Chempur). Measurements were carried out at ambient conditions in the constant current operating mode, using tunneling currents between 100 and $800pA$ and sample bias between 0.6 and $1\,V$. Sample electric contact was established through a metallic clamp. Scanning force microscopy (SFM) measurements were performed at room temperature and under N_2 environment (with a relative humidity $RH < 5\%$). Either Si or Si_3Ni_4 tips mounted in low nominal force constant ($k = 0.05 - 0.5\ N/m$) cantilevers were employed to perform contact mode topography and friction force microscopy (FFM) measurements while Pt/Cr coated Budgetsensors tips with nominal force constant cantilevers of $k = 0.2\ N/m$ and $3\ N/m$ were used for conductive scanning force microscopy (CSFM) and Kelvin probe force microscopy (KPFM) experiments. Sample electric contact was established through silver epoxy drop on the sample corner.

Different set of samples of $BP4$ SAMs containing the coexistence of the α and β-phases were used for the SFM and STM characterization. The samples were prepared in Prof. Manfred Buck's group at the University of St Andrews. SFM characterization was carried out at the ICMAB.

4.4 Measurements and results

In the following section we will present and discuss the SFM and STM results obtained in the coexisting polymorphic α and β-phase structures of $BP4$ on $Au(111)$. We start by describing the two polymorphic phases arrangements and their morphology by a combined study of SFM and STM. We will disclose fine structural order by using friction force microscopy. Then the focus will turn to study the influence of the molecular arrangement of the BP4 SAM into the electrostatic and conductive properties of the surface. Finally, we will collect and conciliate the obtained SFM and STM results, discussing and completing them as an instructive "academic example" of the physical quantities measured by each SPM technique.

4.4.1 Structural and tribological properties of the BP4 on Au(111)

In the large scale constant current scanning tunneling microscopy (cc-STM) image of figure 4.4.1(a), the morphology of atomically flat $Au(111)$ terraces separated by monoatomic steps ($d_{Au} = 2.35$Å) is visible. On each terrace, the two distinct phases are clearly discernible which differ in brightness, being the α-phase brighter than the β. In addition darker appearing rounded pits are seen which are the so-called vacancy islands, labeled VI in figure 4.4.1 (b). These one layer deep depressions in the gold substrate arise from the restructuring of the Au surface upon thiol adsorption [174], and are typical for SAMs where an aliphatic chain is attached to the sulfur head group [163, 175]. As it will be shown below, the dark rounded pits exhibit the α-phase covering the one layer deep depressions or vacancy islands in more than a 99% of then. The rippled appearance of the α-phase, more clearly seen in figure 4.4.1 (b), is due to the already reported solitons or domain walls, which appear to release the stress and stabilize the adlayer [153, 163, 176]. Due to small deviations from the preferred molecular packing, the STM contrast at the boundaries could, in principle, arise from resulting changes in the electronic structure of the molecules and their coupling to the substrate. However, as will be presented in more detail in the following, SFM measurements is concluded that most of the contrast in the solitons is due to a geometrical corrugation of the adlayer.

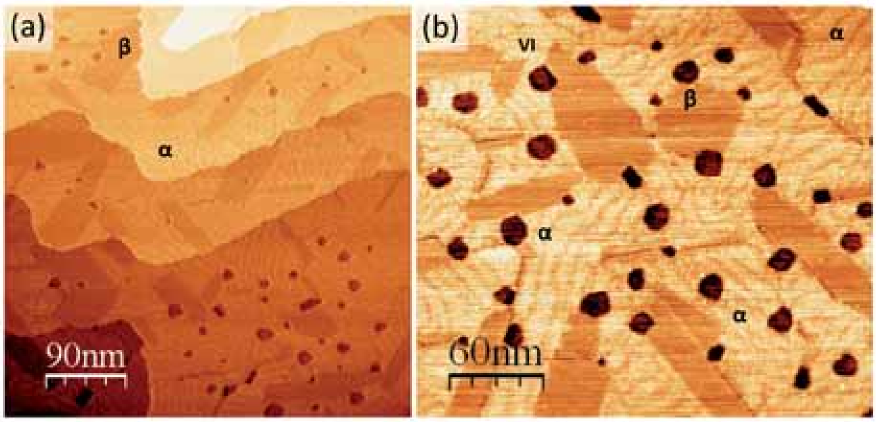

Figure 4.4.1: *cc-STM images of a BP4 SAM on Au(111). Images (a) and (b) at different magnifications show the two coexisting structures with the* α*-phase appearing brighter than the* β*-phase. One* β *domain and three rotated domains of* α *have been labeled. Dark pits are the vacancy islands (VI) typical for SAMs on Au(111).* $U = 0.9\,V$, $I = 100\,pA$.

Different orientations of the domain walls seen in the α-phase are clearly discernible in figure 4.4.1 (b). Running preferentially along the $< 11\overline{2} >$ directions [153] they reflect the symmetry of the substrate and, thus, facilitate to identify the orientation of α-phase domains not only in STM but also in SFM images as will be seen below. Similarly, three orientations of the smoother β-phase can be identified already on the large scale due to the anisotropic shape of the domains. While only three different domain orientations are seen in the STM images, up to twelve equivalent domains for both α and β-phases are expected due to the asymmetry of the SAM domains arising from the tilt of the molecules. The use of specific SFM techniques to differentiate between these equivalent will be presented in detail in section 4.4.2.

In the higher magnification STM image presented in figure 4.4.2 (a) an atomically flat $Au(111)$ terrace location mainly covered by the α-phase arrangement is shown. The corrugation due to domain boundaries of the α-phase domains is visualized in more detail and the resolved molecular periodicity over the α-phase domain seems to be extended into the vacancy islands confirming their

α-phase nature. By zooming into the location marked by dashed lines, the unit cells of each phase have been depicted in the high resolution images in figures 4.4.2 (b) and (c). Though depending on tip end details, individual molecules can be resolved or not, the existence of non-equivalent positions is clear. In the present work, it was not our aim to resolve in detail the molecular arrangements of the molecules in the corresponding polymorphic phase, since the structure of BP4 monolayers on $Au(111)$ as obtained by STM has been already reported in detail , however we notice that our measurement agree well with the rectangular $5\sqrt{3} \times 3$ and oblique $6\sqrt{3} \times 2\sqrt{3}$ structures reported by Cyganik et al. [152] for the two α and β polymorphic phases.

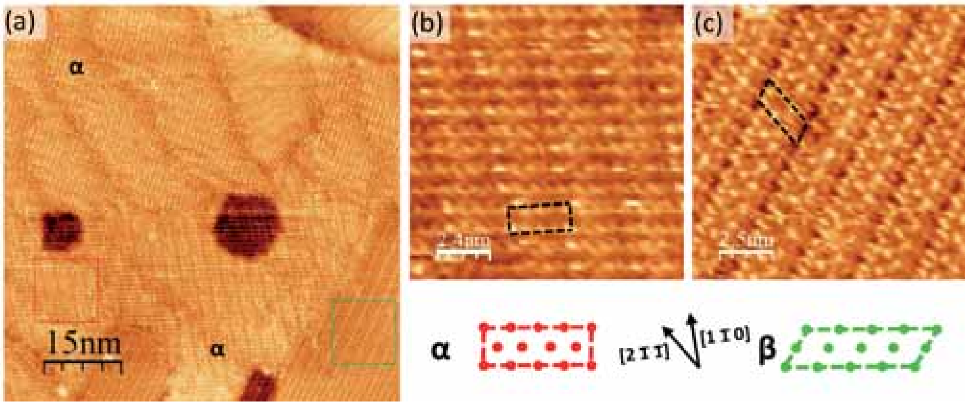

Figure 4.4.2: *STM constant current image of BP4 SAM on Au(111). The dark rounded pits are the typical one layer substrate depressions of SAMs on Au(111) (see text). High magnification (b) and (c) images on the locations marked in (a) show the rectangular centered* $5\sqrt{3} \times 3$ *(*α*) and oblique* $6\sqrt{3} \times 2\sqrt{3}$ *(*β*) lattices, respectively.* $U = 0.8\,V, I = 100\,pA$.

As commented in section 3.3 a cc-STM map reflects the relative tip height, also known as the apparent height because it is in fact the convolution of the electronic and physical structures of both the tip and the surface of the sample. The difference in height between the two polymorphic phases can be accurately measured thanks to the presence of $d_{Au(111)} \approx 2.35$Å height substrate steps. In figure 4.4.3 two cc-STM profiles (b and e) are presented where the difference in height between molecular phases can be determined in direct comparison with $Au(111)$ monoatomic steps. For accurate and statistical $\alpha - \beta$ height difference determination, height histograms of several locations containing both polymorphic phases and $Au(111)$ monoatomic steps where analyzed. Two examples of height histograms corresponding to the location marked with red dashed lines in figures 4.4.3 (a and d) are presented in 4.4.3 (c and f). In spite of the rumpled appearance of α-phase, from the topographic height histograms a difference in height of $h_{\alpha-\beta} \simeq 0.8 \pm 0.2$ Å between α and the featureless β-phase can be accurately measured. The error in height difference between α and β-phases is estimated from the standard deviation of the mean value calculated in more than ten locations [177].

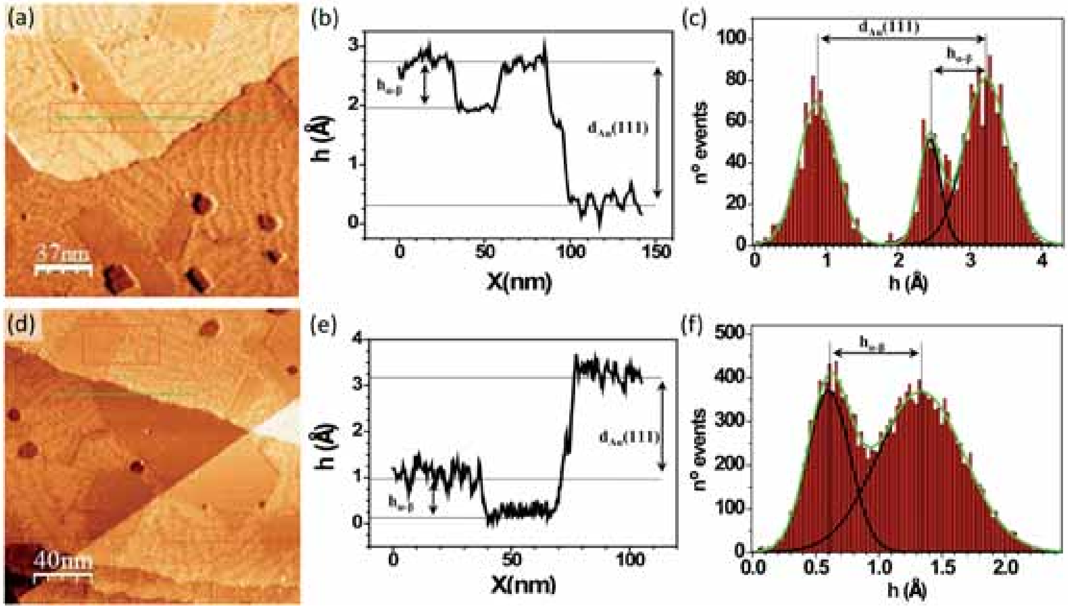

Figure 4.4.3: *cc-STM images of BP4 SAM on Au(111). The height difference between the phases is determined by direct comparison to $d_{Au(111)}$ monoatomic step height, as can be seen in the height profiles (b) and (e). The height histograms (c and f) of the locations marked with dashed lines in (a and d) are used for statistical determination of the height difference. (a) $U = 0.9\,V$, $I = 100\,pA$. (d) $U = 0.6\,V$, $I = 100\,pA$.*

It has to be noted however that, as commented above, cc-STM gives a constant electronic density profile which might be different from the true topographic relief if differences in electronic properties of the two polymorphic arrangements exist. We notice that the measurement conditions for the two images presented in figure 4.4.3 were varied, tunneling current was set constant ($100pA$) for both of them, but the tip-sample potential difference was changed from $0.9V$ to $0.6V$ in images (a) and (d) images respectively. This supports that the height difference by STM is constant at least for a wide range of potential difference for low current regime.

In spite of the obvious advantages of STM to unravel the structural and electronic details of organic monolayers, gaining insight on the mechanical response of the organic layers at the nanoscale needs of the fine measurement of forces provided by scanning force microscopy (SFM). When measuring organic compounds by contact mode SFM (cm-SFM), to avoid any film compression or damage and obtain accurate height values, it is important to keep the measurement conditions in the attractive range and as close as possible to the pull-off force. To check the tip-sample conditions, the adhesion force is systematically determined from force versus distance curves (see sections 3.2.3.1 and 3.2.4.1). When large scan areas of BP4 on $Au(111)$ are scanned by cm-SFM, the underlying $Au(111)$ surface topography variations are reproduced. Figure 4.4.4 (a) topographic image shows a $4 \times 4\ \mu m^2$ area scan reproducing the Au substrate morphology with a total vertical scale of 18 nm from black to white. In the derivative image presented in (b) the topographic changes are better distinguished and the $Au(111)$ surface terraces separated by monoatomic steps are reproduced. The α and β-phases however are not easily distinguished for those large scanned areas in topography signal.

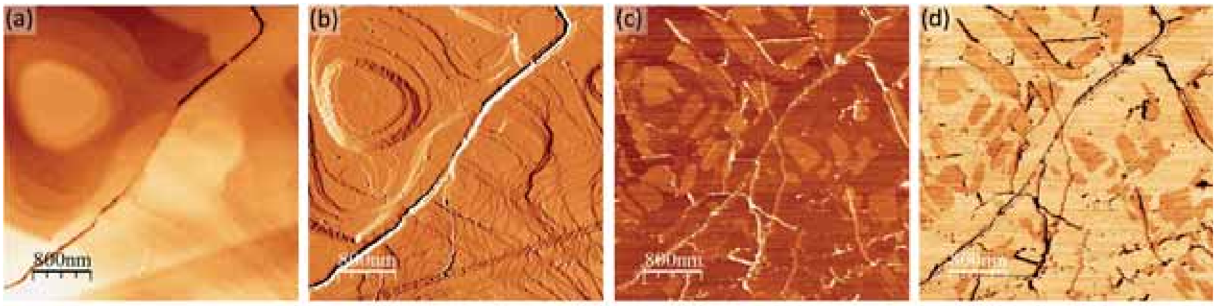

Figure 4.4.4: *Simultaneous contact SFM topographic (a), its derivative (b) and forward-backward lateral force images (c and d) of BP4 SAM on Au(111). On large scanned areas, differences in friction between the two polymorphic arrangements provide an enhanced contrast in lateral force images rather than in topographic ones. Total z-scale for (a) is* $0 - 18\ nm$.

During tip scanning, in addition to cantilever normal deflection (which gives rise to the topographic signal), the cantilever torsion is also monitored what yields to the lateral force imaging. The measured lateral force is directly related to the frictional response between the tip and surface sliding contacts. This is the so-called friction force microscopy technique (FFM) introduced in section 3.2.5.1. As already reported by Mc Carthy et al.[178], differences in friction between the two polymorphic BP4 α and β phases provide an enhanced friction contrast. In figure 4.4.4, the lateral force trace (c) and retrace (d) images simultaneously measured to the topography signal of (a) are presented. Since the friction force always opposes the tip motion, the tip twist reverses when the scan direction is inverted. That is why the lateral force forward (c) and backwards (d) images contrast is inverted, a higher contrast in forward meaning a higher friction and the opposite (for further details related to FFM see section 3.2.5.1). In the lateral force images of figure 4.4.4, an enhanced contrast is detected that enables the localization of the α and β-phases emplacements.

Focusing on the left-upper location of figure 4.4.4, the higher magnification topographic image of figure 4.4.5 (a) shows a surface region containing a pancake-like structure terminated by an extended atomically flat terrace where α and β-phases coexist. As in the STM images described above, each phase is identified thanks to the difference in height and the rough appearance (solitons) of the α-phase as highlighted by the point marked by the arrow in figure 4.4.5 (a) where three differently orientated domains meet. A noticeable resolution of the α-phase solitons is achieved also with SFM measurements that confirms the real and independent nature from electronic coupling of the corrugation measured by STM. In the last part of this section we will focus in more detail in the topographic corrugation of these α-phase solitons. Note that three orientations of the domain walls of this relaxed layer meet at the upper right side of the terrace running along the different $< 11\bar{2} >$ family directions (see arrow pointing to a meeting point of domains).

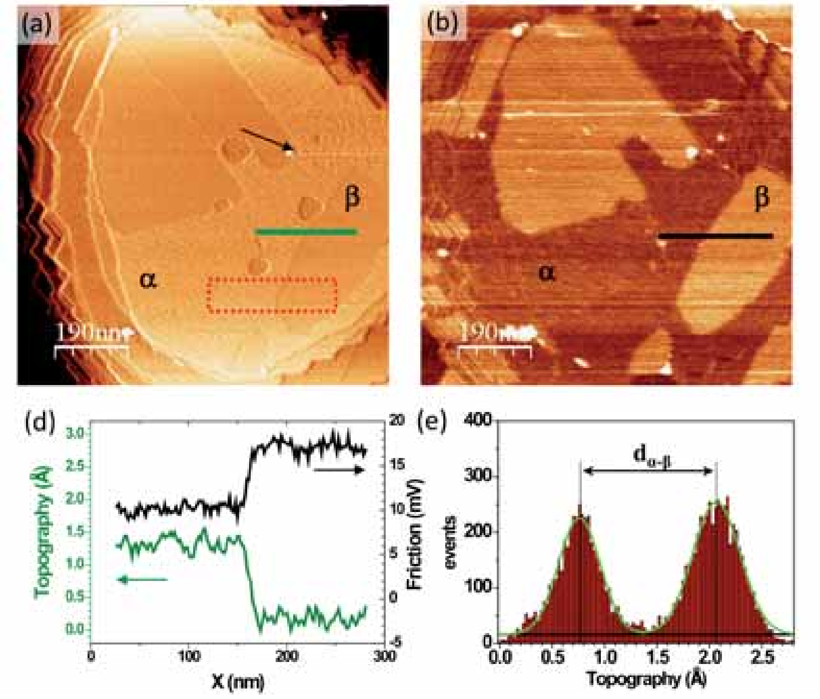

Figure 4.4.5: *cm-SFM topographic image (a) and the corresponding friction map (b) of a BP4 SAM on* Au(111) *(see text and figure 4.4.6 for details of determining friction). Note that different regions of a and* β *phases coexist on the same atomically flat terrace. Line profiles in (c) show the topography (left axis) and friction (right axis) signals in areas of the a and* β *phases. Height histogram as the one presented in (e) are used to determine the height difference between phases.*

The topography difference between the α and β-phases is appreciated in the line profile presented in 4.4.5 (c) (in green) of the location marked in (a), and is determined by different topographic height histograms as the one presented in figure 4.4.5 (d) (corresponding to the location marked by dashed square in a). By the detailed inspection of the height difference over several locations, the α-phase is found to present a $d_{\alpha-\beta} \approx 1.2 \pm 0.2 \AA$ higher topography than the β-phase. Even though the unit cell of the α-phase is less corrugated than the one of the β-phase, overall, α presents a surface roughness larger than β ($rms(\alpha) \approx 0.40 \pm 0.05$Å and $rms(\beta) \approx 0.25 \pm 0.05$Å) due to the presence of the solitons. The estimation of the error in height difference between phases is done, as in the STM case, by the standard deviation of the mean value calculated in more than ten locations. It has to be noticed that the height difference determined by SFM ($d_{\alpha-\beta}$) is a 50% higher than the one obtained by cc-STM ($h_{\alpha-\beta}$). This result suggest that the “height” measured by STM had a non negligible contribution of electronic nature and points the importance of applying each SPM technique for each correct purpose. Taking advantage of the conductive data that will be presented in section 4.4.4, the understanding of the different heights measured SFM and STM will be discussed in section 4.4.5 by mean of the deconvolution of the topographic and electronic contributions to the height difference measured by STM. Besides, the measured $d_{\alpha-\beta}$ by SFM is a 33% lower than the the thickness difference derived by Cyganik et al. [153] from X-ray phoelectron spectroscopy (XPS) data, but within the confidence range of their error (layer thickness of 16.2 ± 0.7 Å and 14.4 ± 0.7 Å for α and β-phases respectively). Here we point the more accurate and confident determination of the height difference by SFM technique in comparison to its estimation from the attenuation length of the photoelectron signal of the substrate in XPS.

The reported molecular tilt angle for the α-phase (θ_α) is around 40° with respect to the surface normal [154, 155]. For the β-phase a larger tilt between $\theta_\beta \approx 49°$ and 45° is obtained depending on the estimation procedure used. Azzam et al. [155] estimated the tilt angle by considering the van der Waals dimensions of the molecule (a cross-sectional area of 21.1 Å^2 for phenyl rings) and the area per molecule (32.4 Å^2), what gives as a result a molecular tilt angle of $arccos(21.1/32.4) \approx 49°$ for the β-phase (θ_β). θ_β can be also extracted from the combination of the topography difference obtained by SFM, the reported θ_α data and a molecular longitude of $BP4$ equal to $1.52\,nm$ (by assuming atomic distances of the rigid molecule and calculated by the ChemDraw program [179]). By this methodology a molecular tilt angle for the β-phase of $\theta_\beta \approx 45°$ is obtained. Independently to the exact value, the difference in topography between phases directly points to a larger tilt angle around $47 \pm 2°$ of the $BP4$ molecules in the β-phase.

In cm-SFM measurements, simultaneously to the topographic signal the torsion of the cantilever

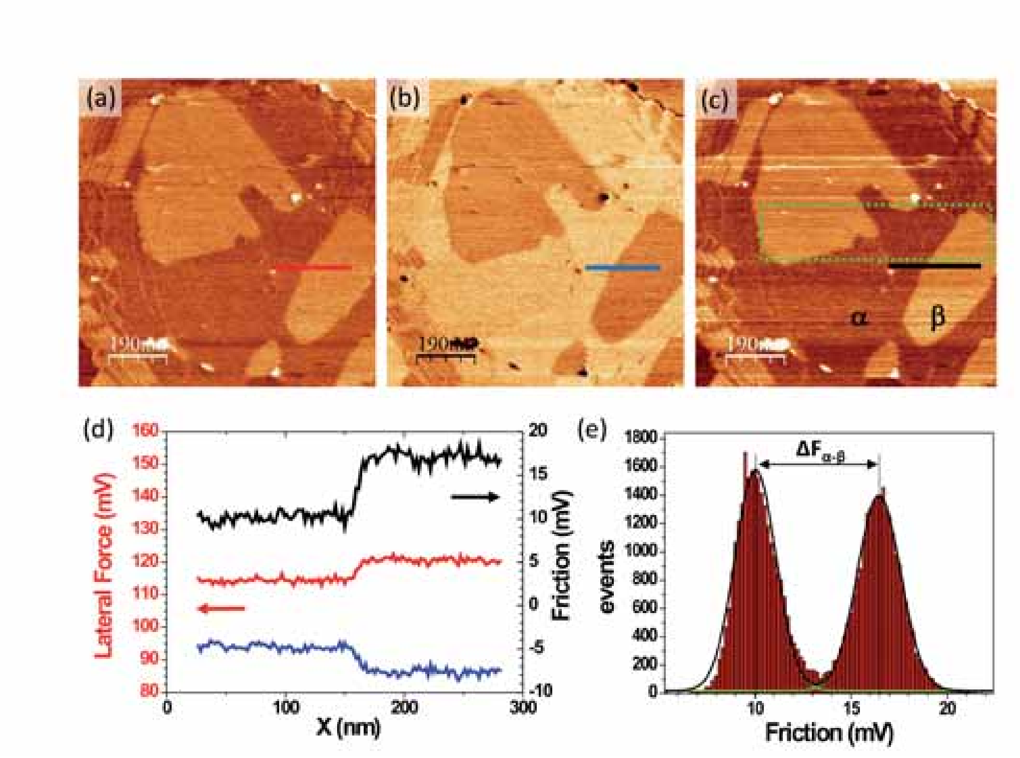

Figure 4.4.6: *Simultaneous recorded lateral force forward (a) and backward (b) images corresponding to the same simultaneous acquisition of topographic signal of figure 4.4.5 (a). The mean friction image (c) generated by calculating the half of the subtraction of (a) and (b)* $(|(a)-(b)|/2)$. *Profile lines in (d) presenting the corresponding lateral forces and mean friction signals of the location marked in (a,b,c). The calculation of the friction difference between phases is performed by plotting the friction histogram (e) of the area marked by dashed green square in (c).*

that gives rise to the local friction can be also measured. In figure 4.4.5 (b) the corresponding mean friction map of the very same location of the topography of (a) is presented. The friction image is build from the lateral force trace and retrace signals recorded simultaneously to the topographic trace and retrace signals acquisition. The calculation of the mean friction image procedure is presented in figure 4.4.6. Images 4.4.6 (a) and (b) present the lateral force forward and backward images correlated to the local frictional response of the SAM and simultaneously measured to the topography image of figure 4.4.5 (a). The local mean frictional signal is defined as half the amplitude of the so called friction loop, $F = \frac{1}{2} \mid F_l^f - F_l^b \mid$ where F_l^i $(i = f, b)$ denote the lateral force forward and backwards signals. When this formula is applied over the profiles marked in figures 4.4.6 (a and b), blue and red lines in (d) corresponding to trace and retrace lateral force signals respectively, it gives rise to the mean friction signal profile presented in black in (d, right axis). As introduced in section 3.2.5.1, applying this line by line procedure to the complete lateral force images (a and b) leads to the mean friction map presented in (c, same image of 4.4.5 b). The friction map allows the direct correlation of frictional response with the topographical details and the direct quantification of the friction signal difference between locations. As seen in figure 4.4.5 (b), a notable friction contrast between regions covered by each phase is clear. By the comparison of figure 4.4.5 (a) and (b) the correlation between height difference and frictional contrast of the two polymorphic phases is established. From the corresponding profiles of topographic and friction signal presented in figure 4.4.5 (c) a direct correlation between higher topography-lower friction for the α-phase is established. The independent analysis of the lateral force images and its correlation to the mean friction map can be used to gain information about fine structural details of the molecular domains as will be seen in next section 4.4.2.

From the combined characterization of adhesive and frictional properties under water conditions, Mc Carthy et al. found a large difference in resistance to shearing but a similar friction coefficient (μ) between α and β phases [178], thus, pinpointing the importance of structural effects of these phases on the tribological properties of the SAMs. Relative friction coefficients of friction forces at zero load (F_0) were obtained by fitting the experimental data to the expected linear behavior $F = F_0 + \mu F_n$ with F denoting the average friction force along a trace-retrace loop. Adopting a more detailed approach here, we will try to unravel the influence of structural differences impossible to be uncovered in previous studies [178] due to the averaging method employed. This is achieved by direct in-situ quantification of ${}^{F^\beta}/_{F^\alpha}$ under controlled humidity conditions ($< 5\%RH$) while providing true topographic details of the monolayer surface by imaging at the pull off force and, thus, safely excluding any film deformation.

In our present work, the determination of the friction forces at zero load is statistically performed in different location, by histogram plots as the one as presented in figure 4.4.6 (e) of the location marked in (c), and yields to a ratio of ${}^{F^\beta}/_{F^\alpha}$ around $\sim 1.6 \pm 0.2$ which is inverted compared to the ratio of the molecular packing densities (${}^{\sigma^\alpha}/_{\sigma^\beta} \approx 1.2$). The friction being higher for the β-phase than for the α-phase is rationalized by the fact that conformational changes in the SAM are affected by the packing density and intermolecular interactions. Even though the trend observed here is in line with the studies under water [178] a much lower ratio is measured at the low RH values employed in this work. This quantitative difference is not too surprising as it is well known that dissipation is not only dependent on the film structure but is also influenced by

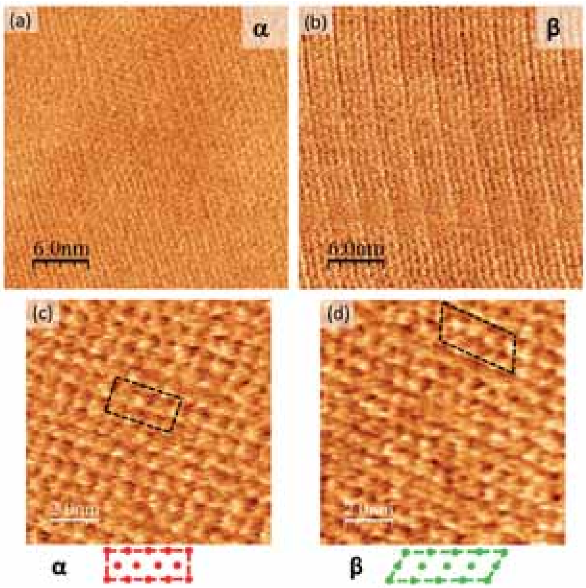

Figure 4.4.7: *High resolution lateral force SFM images of α (a) and β (b) phases. Molecular periodicity resolution images of BP4 regions of a and β-phases .*

interactions of the SAM molecules with the environment. Consequences of these interactions are changes in the conformational energy landscape and additional dissipation channels opening up due to the presence of a condensed phase in contact with the SAM, thus making its exact friction properties dependent on the relative contribution of these factors.

In addition to the tribological characterization of the samples, the lateral force imaging provides high resolution molecular periodicity imaging by the so-called stick-slip phenomena introduced in section 3.2.5.1. Lattice resolved molecular periodicity images of the corresponding polymorphic phases are shown in figures 4.4.7 (a) and (b). Though obviously not so well resolved as in true molecular resolution on STM, the $5\sqrt{3}\times 3$ and the $6\sqrt{3}\times 2\sqrt{3}$ unit cells of α and β-phases, respectively, are clearly recognizable in the higher magnification images (c) and (d). Like STM, conventional SFM imaging is not sensitive to the tilt direction of the molecules and, therefore, can only differentiate between domains orientated along the symmetry equivalent directions of the substrate. However, as will shown in the following section 4.4.2, FFM can also be employed to distinguish molecular domains with different azimuthal orientation and discriminate between opposite tilted directions. Besides, in the medium magnification images of figures 4.4.8 (a) and (b), some details like a thin and elongated α-phase domain (arrow in 4.4.8 a) or disordered narrow boundaries a few molecules wide and separating α and β phase areas (arrow in 4.4.8 b) are discernible. Furthermore, the stress induced long range corrugation (solitons) of the α-phase (bottom figure 4.4.8 b) is seen to persist right up to boundaries between phases.

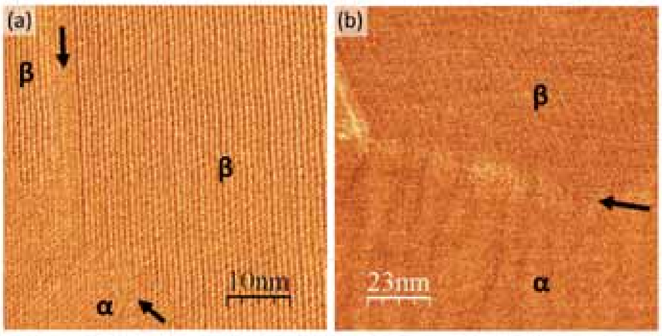

Figure 4.4.8: *Lateral force images of BP4 regions of coexisting a and β-phases containing different types domain boundaries: β − β and β − a (marked by arrows). The visible rough appearance due to solitons in the a-phase (b) is responsible for a larger rms of the a-phase* (≈ 0.4 Å) *compared to the β-phase* (≈ 0.25 Å).

A closer look to the solitons reveals that their topographic difference can be determined by cm-SFM. STM measurements presented by Cyganik and co-workers [163, 176] showed that the stripes present lower apparent height in an amount ∼ 0.5Å. However as commented above both real topographic and electronic properties of the surface appear mixed in the STM measurements. In figure 4.4.9 (a) and (b) a higher magnification cm-SFM images of the same region presented in figure 4.4.9 is presented. The topography variation in the soliton depressions is clearly discernible in the topographic images of 4.4.9 (a) in comparison to the topography difference with the β polymorphic phase. In image (e) and (c) higher magnification topography images of the soliton structures are presented. As can be observed in the topographic profiles depicted in (g, in black) and (h) of the locations marked in (d) and (f), the topographical difference is in the sub Å range and thus, in the limit of the SFM resolution. The corrugation of the solitons and such a small height difference make it difficult to set the exact determination of the topographical difference, but in any case, we found that the mean value of the difference in topography is also around 0.5Å. The fact that the same range of corrugation is found by STM and SFM techniques points to an homogenous electronic density over the different location of α- phase solitons. However as will be seen in section 4.4.4, a difference conductive response is also found in the depression locations by conductive SFM what rules out the previous conclusion and means that upper and lower location do in fact present different electronic nature. Further discussion about the different conductive response over the solitons will be presented in section 4.4.4. In addition, from the simultaneously measured frictions maps it is found that the soliton depression location present a higher friction contrast in comparison to the higher soliton locations. This friction contrast is clearly seen in the friction map presented in figure 4.4.9 (b), where the higher friction thin stripes are directly correlated to the height differences of the solitons in the topographic image of (a). In the simultaneous topography and friction profiles presented in figure 4.4.9 (g) corresponding to the location marked in (e) and (f), the low topography and high friction responses are correlated. As for the height difference over the solitons corrugation, the exact quantification of the friction difference is also rather difficult. On the one hand the solitons corrugation do not present an homogenous friction contrast over different locations, as is seen in figures 4.4.9 (b) and (f), and on the other hand the friction differences are close to the resolution we have. We can estimate that the friction quotient is around ∼ 1.1, been the friction higher in the lower location of the corrugation. From STM measured reported by Cyganik and co-workers [163] the structural quality of the molecular layer of the stripes was found to be excellent and defect free. Although not comparable to the true atomic resolution obtained by STM, the high resolution lateral force molecular periodicity image presented in figure 4.4.9 (d, simultaneously adquired with topography image c) shows a high degree of crystallinity over the solitons structure.

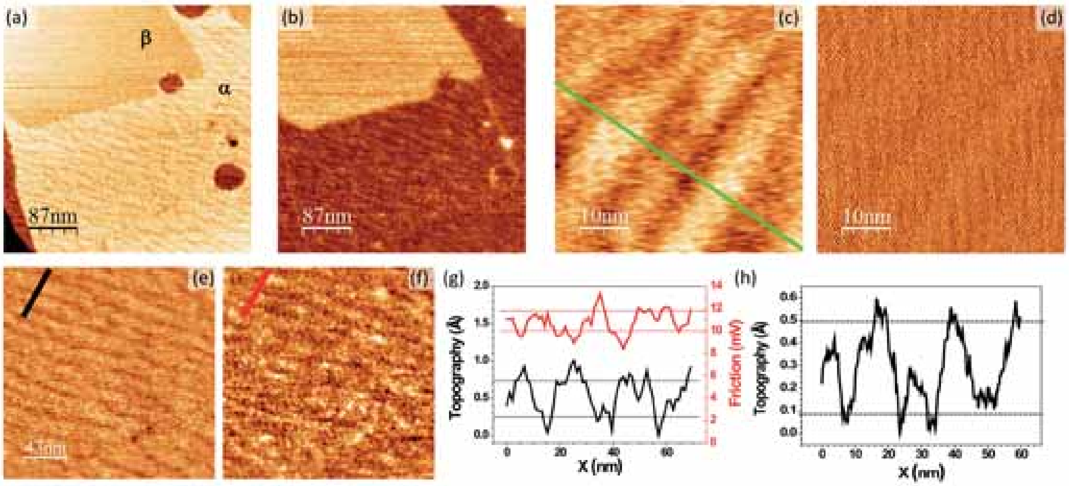

Figure 4.4.9: *cm-SFM topography (a) and friction (b) signal of* α *and* β*-phases coexisting in the same atomically flat Au(111) terrace. Magnification topographic and friction signals on top of the* α*-phase are presented in (e) and (f) where the topographic difference over the solitons is observed. Topographic and friction signal lines profiles of the locations marked in (e) and (f) are depicted in (g). High resolution simultaneous topography (c) and lateral force molecular periodicity (d) images show the the excellent structural quality of the molecular layer over the solitons corrugation. Topography line profile on (h) showing the topography difference of the location marked in (c).*

We now focus in the vacancy islands (VI). As commented above, most of the VI islands reveals are covered by the α-phase. This is not only proven from the larger VI on the upper terrace in the STM image of figure 4.4.10 (a) which exhibits the same rippled structure as the α-phase area, but also from the depth of the VIs which is identical to the step height $d_{Au}(111)$ of a $Au(111)$ surface (figure 4.4.10 b), i.e., the height difference between adjacent terraces covered by the same phase of the $BP4$ SAM. Another example of the α-phase covered VI is presented in the central column of figure 4.4.10. Figure 4.4.10 (d) and (e) show the topography and friction signals of the two polymorphic phases covering the same $Au(111)$ terrace. Both the height difference and friction contrast profiles depicted in (f) confirm the α-phase nature of the SAM covering the VI. The VIs are formed by Ostwald ripening during molecular self-assembly [175] from solution at low temperature. β-phase covered VIs very rarely occur ($< 1\%$ in agreement with SAMs fully converted to the β-phase where VIs as essentially eliminated [152, 153]. The absence of β-phase VIs can be explained by an extended Ostwald ripening and/or a restructuring of the SAM-substrate interface upon the phase transition. Only in a few cases VI covered by the β-phase were found, two different examples are presented in the STM and SFM data in figure 4.4.10 (left and right columns respectively). In the right part of figure 4.4.10 (c) a β covered VI is found, as proved by the height difference measured in the STM profile of (c). A zoom in the region containing the VI (marked by dashed lines in a) is present in (c). The second β-phase covered VI example is presented in the SFM topography and friction images of figure 4.4.10 (g) and (h). The topography difference shows a $d_{Au}(111)$ height difference and same friction contrast of the VI with respect to the β-phase locations, as can be seen in the corresponding profiles of (i), confirming that is covered by the β polymorphism phase.

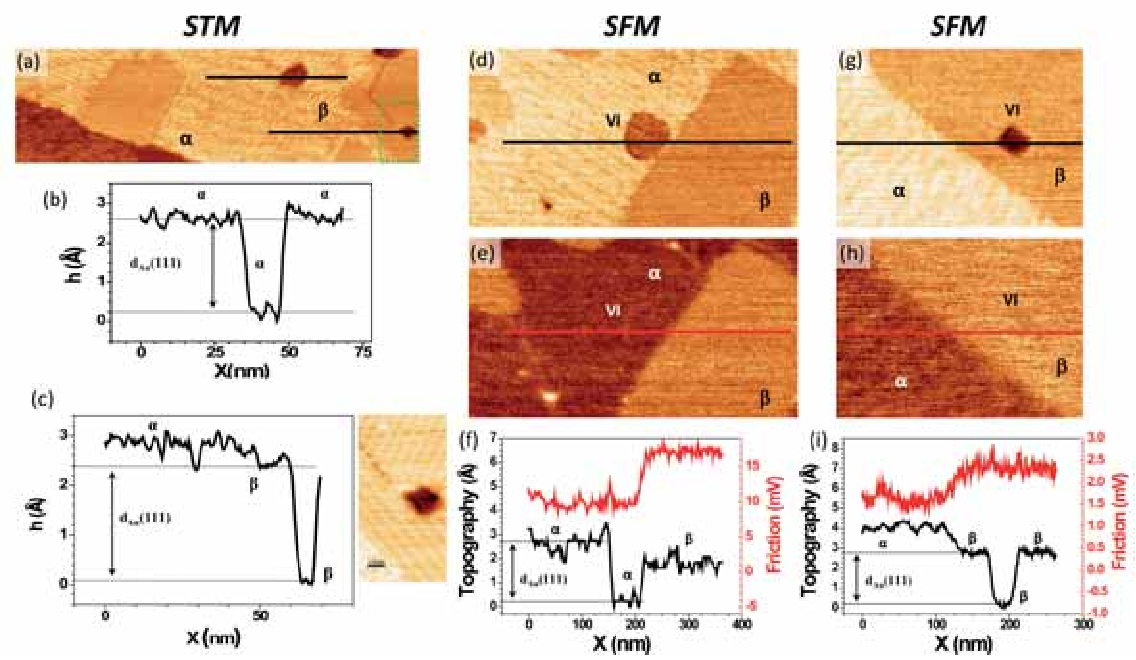

Figure 4.4.10: *STM and SFM measurements of BP4 SAM on Au(111) containing α-phase, β-phase and vacancy island (VI). α and β-phases covered VI cc-STM data is presented in the left column, whereas cm-SFM data of α and β-phase covered VI are presented in the central and right columns respectively.*

4.4.2 Disclosing fine structural supramolecular order of BP4 phases by FFM

SFM is ideally suited for non-invasive friction studies since forces can be measured with high sensitivity and different types (e.g. local lateral force, see) can be monitored simultaneously (see section 3.2.5.1). Commonly, surface properties such as chemical composition and/or structural order which are reflected in the local frictional properties are assessed. However, FFM measurements can provide even more detailed information, for example, on non-isotropic packing of molecules or molecular tilt in self-assembled monolayers (SAMs) [180–182]. These details can be revealed by friction anisotropy (AN) and friction asymmetry (AS) both of which are related to the dependence of the mechanical response on the sliding direction. Since AN and AS are of central importance for the present study we briefly introduce them, in particular because the terms are not unambiguously defined in the literature.

The term friction anisotropy (AN), on the one hand, refers to the variation of the friction coefficient (μ) with the relative orientation of sliding surfaces and is commonly correlated with the azimuthal orientation (γ) of a crystalline surface. Though it has been reported for inorganic quasicrystal surfaces [183–185], generally, friction anisotropy has been observed in crystalline and non-isotropic organic surfaces, i.e. when the periodicity varies with direction within the surface plane [180, 186–189]. Anisotropic friction is revealed by differences in FFM contrast and typically gives variations in $\mu(\gamma)$ lower than a factor of two, even though higher ratios have been observed in the case of organic monolayers on mica [188]. By definition $|\mu_{mean}(\gamma)| = |\mu_{mean}(\gamma + 180°)|$, i.e., AN vanishes when the sliding direction changes by 180°[1]. On the other hand, friction asymmetry (AS), arises from a direction dependent (asymmetric) surface potential and has been also called *directional dependence of friction* [190] to differentiate it from AN as defined above. As a consequence, AS occurs when the sliding direction is changed by 180° with respect a specific symmetry axis of the surface. Given that $|\mu_{mean}(\gamma)| = |\mu_{mean}(\gamma + 180°)|$, AS does not involve different values of mean friction coefficient. Being rarely observed, some illustrating cases of AS have been reported for surfaces of organic single crystals exhibiting an asymmetric arrangement of [98, 189, 190] or for organic layers where a difference in friction is observed between directions parallel or anti-parallel to the tilt direction of molecules [180, 186].

The BP4 system consisting in SAMs with the two α and β-phases coexisting is a particularly interesting system of choice for benchmarking the heterogeneity of nano-tribological properties, because of the occurrence of structurally different phases which exhibit a high degree of crystallinity while forming a continuous film. Complementary to the study of McCarthy et al. [178] and the FFM results presented in the previous section 4.4.1, here we expand the investigations to high resolution FFM to reveal frictional details which were not differentiated in Mc Carthy et al. work because of the averaging methodology employed. The approach taken here permits us to reveal fine differences in mechanical properties arising from crystallographic details of the SAM and tip–SAM sliding geometry, namely friction asymmetry and anisotropy, while avoiding problems derived from tip structure (tip terminating atoms and geometry) [180]. With domain sizes ranging from tens to hundreds of nanometers, i.e., approaching or even exceeding the lateral dimensions of nano-mechanical contacts in devices, our findings give insight into the importance of lateral structural homogeneity in boundary lubricants.

On a large scale the contrast in the topographic SFM images is dominated by numerous monoatomic steps in the $Au(111)$ substrate (figure 4.4.11 a). Using them as internal reference ($d_{Au(111)} = 2.35$Å) the more subtle topographical features such as the sub-Angström corrugation

---

[1] $\mu_{mean}$is defined as the friction coefficient (μ) calculated along a friction loop (see section 3.2.5.1)

of the SAM and the height differences between the phases can be straightforwardly quantified as exemplified by the two line profiles depicted in figure 4.4.11 (d) and (e). Analogous to figure 4.4.5, profiles across a step (figure 4.4.11 d) and on a single terrace (figure 4.4.11 e) illustrate the ∼ 1.2Å topographical difference between the two polymorphic phases. However, even more details are revealed by lateral force imaging which, in general, is especially useful to get insight into the dissipation mechanisms occurring at surfaces and their relationship to structural features. From both line profiles shown in figure 4.4.11 (d) and (e) it is obvious that the α-phase exhibits a lower friction than the β-phase in agreement with previous measurements at water/SAM interface [178] and the result presented in the previous section 4.4.1. Comparison of both profiles reveals a most interesting difference. While the same friction value is observed for the β-phase domains on the upper and lower terrace (figure 4.4.11 d), two distinctly different values are measured for the β-phase domains on the same terrace captured by the profile of figure 4.4.11 (e). The one labeled β_1 has higher friction than the α-phase by a factor of 1.8 whereas for the other one labeled β_2 friction is only 1.4 times higher.

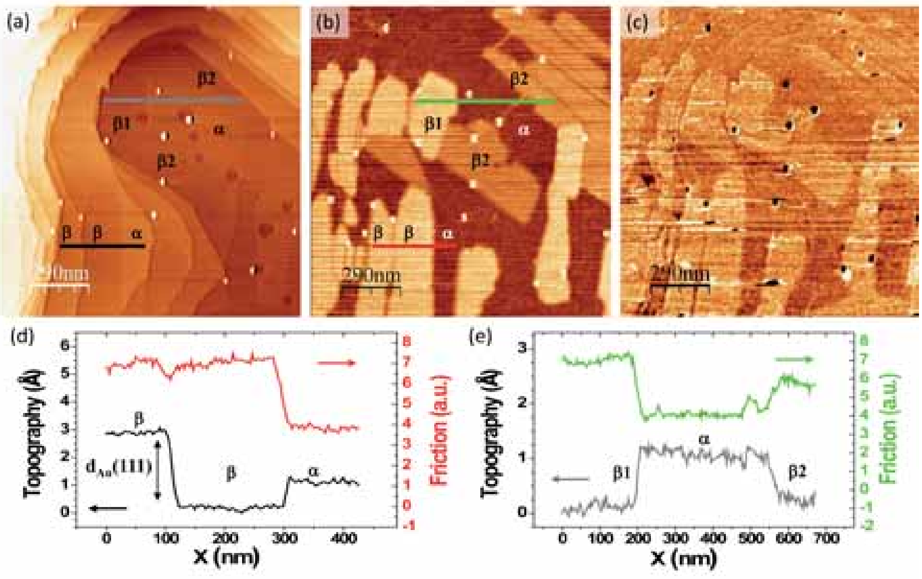

Figure 4.4.11: *(a) Contact SFM topographic image of a BP4 SAM on Au(111) containing several α and β phase domains and (b) the corresponding mean friction and (c) adhesion force (AF) maps (c). In (b) dark friction contrast corresponds to α-phase domains while intermediate and bright contrasts labeled β_1 and β_2 are ascribed to rotated β-phase domains of different azimuthal orientation. (d and e) Topography (black and gray curves) and friction profiles (red and green curves) along lines indicated in (a) and (b). The AF contrast between α and β locations is found to be $\approx 0.1\,nN$. Small spots appearing bright in (a,b) and dark in (c) originate from small particles not intrinsically related to the BP4 SAM.*

This observation can only be attributed to friction anisotropy [186, 191], i.e., a different resistance to sliding for different azimuthal orientations of the β-phase domains and, thus, different angles with the fast scanning direction of the SFM tip. Coming back to this point we note here that in the present acquisition friction anisotropy is only sufficiently large for the β-phase. Even though the α-phase also consists of domains of uniaxially aligned molecules any difference seems to be below detection threshold in this image.

In contrast to friction forces which are sensitive to domain orientation, the interfacial energy of the molecular phases and, thus, adhesion forces should not depend on it (provided the tip is not asymmetric). This can be verified by adhesion force spectroscopy where adhesion hysteresis is estimated from the area enclosed between approach and retraction force *versus* distance curves performed at selected surface positions (monitoring the F_n, no the lateral force). However, apart from a high positioning accuracy, this method requires excellent statistics and, thus, sampling of a large number of curves in order to yield meaningful sets of data for each phase. An alternative simpler approach taken here is a less quantitative but reliable method of generating adhesion force (AF) maps which is based on the direct determination of the pull off force at each point of the scanned surface by withdrawing the tip until it snaps out of contact [192]. By withdrawing the SFM tip along the direction normal to the surface until the tip went out of contact, the pull off force (from now on called AF for simplicity) was determined and recorded at each surface point in a second pass image to get AF maps on the very same surface locations as morphology and lateral force images. Normal deflection (topography) imaging was continuously recorded to detect any possible change or damage during measurements. Though different AF values are expected for the two phases, i.e., $AF(\beta) \neq AF(\alpha)$, only one should be observed for each phase, i.e., $AF(\beta_1) = AF(\beta_2)$, as adhesion does not depend on the azimuthal orientation of a domain. This is fully confirmed by the AF map shown in figure 4.4.11 (c) which exhibits a clear difference between the phases but, in contrast to the friction map (figure 4.4.11 b) does not discriminate between different domain orientations. The AF contrast between α and β locations in figure 4.4.11 (c) is $\approx 0.1\, nN$, being $AF(\beta) \approx 1.07\, AF(\alpha)$. The result $AF(\beta) > AF(\alpha)$ is in agreement with previous results and the expected lower surface energy of the α-phase due to its denser packing [178].

Before analyzing this fact further we address the relationship between the symmetry of the

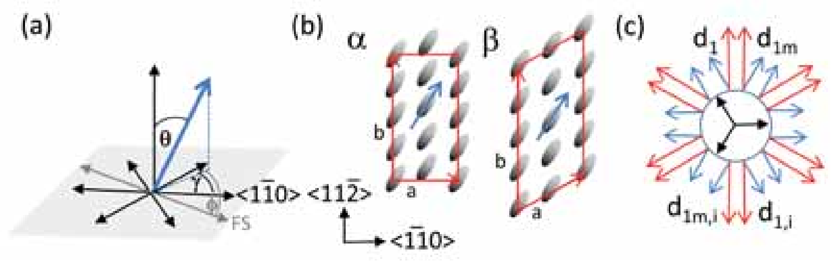

Figure 4.4.12: *(a) Definition of tilt θ and azimuthal alignment γ of SAM molecule and its angle ϕ to the fast scanning direction. (b) Schemes of the unit cells of α and β-phase with ellipses indicating the alignment of the molecules. (c) Equivalent domains for the case of the tilt direction not parallel to the unit cell vector. Red and blue vectors represent b-vector of unit cell and molecular alignment, respectively.*

substrate, the SAM structure and friction properties by referring to figure 4.4.12. Considering the C_{3v} symmetry of the substrate there are six possibilities to orient e.g. the $b-$vector of the unit cells along the $< 11\bar{2} >$ directions. If the molecular alignment, conveniently defined by the orientation of the biphenyl moieties and expressed by angles θ and γ (see figure 4.4.12 a), is not parallel to the unit cell vectors, the symmetry of a domain is reduced to C_1. As indicated in figure 4.4.12 (c) this results in twelve equivalent domains grouped into three sets of four domains which are related to each other by mirror and inversion symmetry as exemplified by the sets of arrows labeled d_1, d_{1i}, d_{1m} and $d_{1m,i}$. Two points are worth noting. Firstly, for both phases of the $BP4$ SAM γ is not known and in the representation in figure 4.4.12 (c) the tilt direction found for bulk biphenyl is adopted which is towards the next nearest neighbour [193]. In the case of alignment of the molecules along a unit cell vector the number of equivalent domains reduces to six. Secondly, the same friction is measured for domains which are related by a rotation of 180° such as d_1, d_{1i}, d_{1m} and $d_{1m,i}$. Differentiation between these cases requires measurement of the friction asymmetry, i.e., a separate analysis of forward and backward scans.

The additional information obtained from the friction asymmetry is demonstrated in figure 4.4.13. Figure 4.4.13 (a) shows the map of the friction (F) obtained from the recorded forward (b) and backward (c) lateral force images of a surface area large enough ($\approx 1.5 \times 1.5\,\mu m^2$) to contain several domains of each phase, α and β. As already seen in figure 4.4.11 (b) up to three different contrast levels are distinguished in friction figure 4.4.13 (a) which can be correlated to the SAM structure by the high resolution images shown in figures 4.4.13 (d-f). Low friction values correspond to regions covered by the α-phase (figure 4.4.13 d) whereas high and intermediate values arise from differently orientated domains of the β-phase (see figures 4.4.13 e and f) as evidenced by the 60°

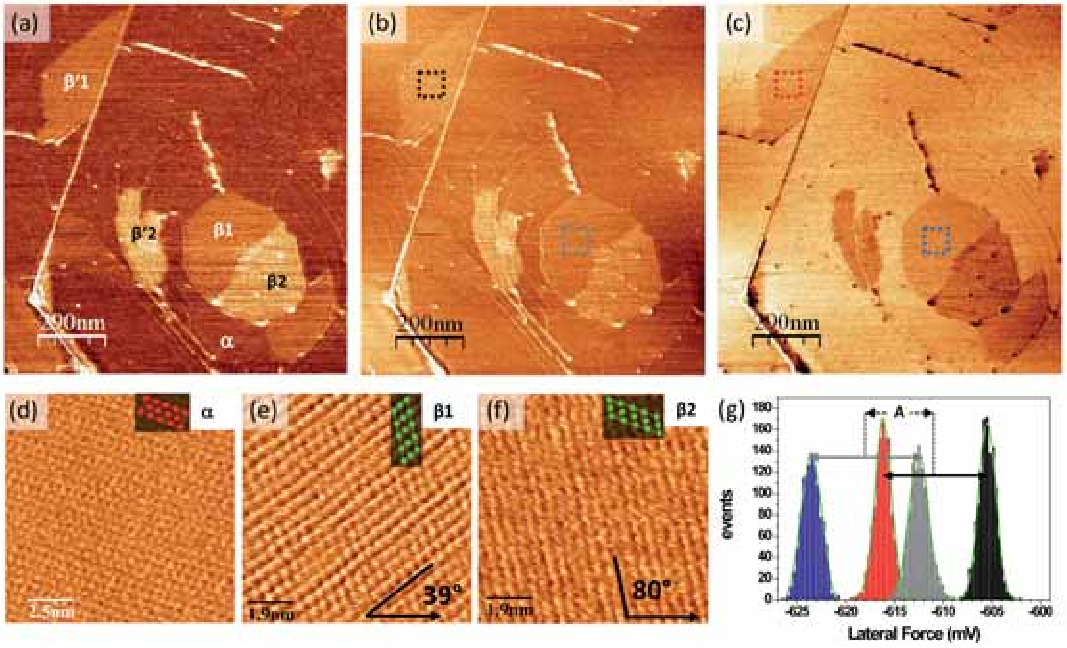

Figure 4.4.13: *Friction map (a) of a BP4 SAM on Au(111) containing divers a-phase and* β*-phase regions. As in figure 4.4.11, dark contrast corresponds to* α*-phase domains while intermediate and bright contrasts arise from rotated domains of the* $\beta - phase$*. Original forward (b) and backward (c) lateral force images. High magnification images taken on the locations labeled in (a) as* α*,* β_1 *and* β_2 *are presented in (d), (e) and (f) respectively. The lattice unit cells are included. The orientation of domains with different friction values (*β_1 *and* β_2*) is marked with respect to the tip scan direction. (g) Histograms of lateral force values obtained out of the squared regions in (b) and (c) with same color code. Equal* $\mid F_l^f - F_l^b \mid$ *values for both domains (double headed arrows between Gaussian fits) indicate same friction,* $F(\beta_1) = F(\beta_1')$*, while the lateral displacement between couple of Gaussians (A) is due to friction asymmetry (see text and figure 4.4.14). The straight lines on the images are defects on the gold substrate and do not affect neither the results nor the discussion.*

difference in the angles between the fast scan direction and the unit cell vectors for β_1 and β_2. The different orientation of β_1 and β_2 domain (shown in e and f), demonstrate that friction anisotropy is due to azimuthal variations between β-phase molecular domains. While $F(\beta_1) \neq F(\beta_2)$ is a clear signature of friction anisotropy, there are also regions labeled as β_j' $(j = 1, 2 \ldots)$ which exhibit the same friction values as their β_j counterpart, i.e., $F(\beta_j) = F(\beta_j')$, indicating the same tip-surface sliding relationship, in other words β_j and β_j' should be domains rotated by 180°. To corroborate this lateral force images have to be analyzed for friction asymmetry (AS) by comparing images of opposite scan directions (figure 4.4.13 b and c). For higher accuracy, instead of using conventional friction loop profile analysis, mean values of the lateral forces F_l^f and F_l^b of each domain are obtained from histograms (figure 4.4.13 g and h) compiled from the $100 \times 100\, nm^2$ sized areas indicated by squares in the images (b) and (c) of figure 4.4.13. Note that, on the one hand, $|F_l^f - F_l^b|$ (modulus marked by the double-headed arrows between Gaussian fits in figure 4.4.13 g) is the same in both cases, confirming that $F(\beta_j) = F(\beta'_j)$ $(j = 1, 2)$ and, on the other hand, the Gaussian fits for β_j are shifted with respect to those for β'_j by an amount A well beyond the experimental error. This result means that the lateral force is asymmetric, i.e., the torsion of the cantilever is not fully reversed within each domain when the sliding direction is changed by 180°. The schematic of the setup detailing the cantilever scanning direction and sample orientation (Φ) with regard to the torsion and deflection responses in the quadrant detector is shown in figure 4.4.14 (a).

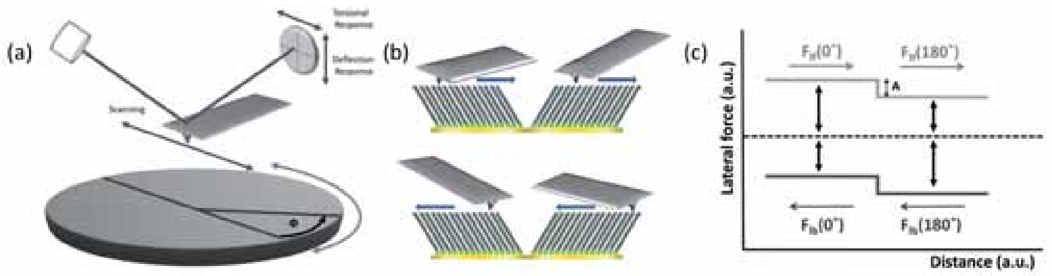

Figure 4.4.14: *(a) Schematic of the tip-sample sliding geometry and deflection and torsion detection modes. (b) Cartoon illustrating the friction asymmetry observed for the reversed scan direction due to molecular tilt. (c) Schematic drawing of the lateral force loop expected for the* 180° *rotated domains in (b).* F_l^f *and* F_l^b *represent the lateral force signals along the forward and backward scan directions, respectively, and A stands for the friction asymmetry (see figure 4.4.13). Dimensions of the vertical double arrows in (c) are scaled to illustrate that* $|F_l^f(0°)| = |F_l^b(180°)|$ *and vice versa.*

As already reported for other systems[180, 186] the origin of this AS is an asymmetric surface potential arising from the out of plane molecular tilt and which is revealed by the tip scanning direction (forward or backward) relative to the azimuthal alignment. This effect has been illustrated in figure 4.4.14 (b) by schematically drawing two equivalent domains rotated 180° with respect to each other. The cartoon makes it easy to understand that during forward and backward scans, the cantilever torsion will behave asymmetrically when sweeping across each domain (along or opposite to the molecular inclination). The schematic drawing of figure 4.4.14 (c) represents the corresponding lateral force signals that would be measured along the reversed scans depicted in figure 4.4.14 (b). Provided $\mid F_l^f(0°) \mid = \mid F_l^b(180°) \mid$ and $\mid F_l^b(0°) \mid = \mid F_l^f(180°) \mid$, it holds that $F(0°) = F(180°)$ (AN is 0) while the reversed alignment of the molecular tilt respect to the sweeping action of the tip is reflected in the vertical displacement of the separated friction loops.

In most measurements no friction differences were detected between different orientation α-phase molecular domains, thus those differences seemed to be below detection threshold. This is not surprising, since the $BP4$ molecules present a lower tilt angle in the α-phase with respect to the β-phase and in consequence a less pronounced influence of the relative orientation of the domains with respect to the tip scan direction is expected. In fact, by making use of softer cantilevers ($k \approx 0.01 - 0.05\ N/m$) in some cases AS effect was also detected for the α-phase.

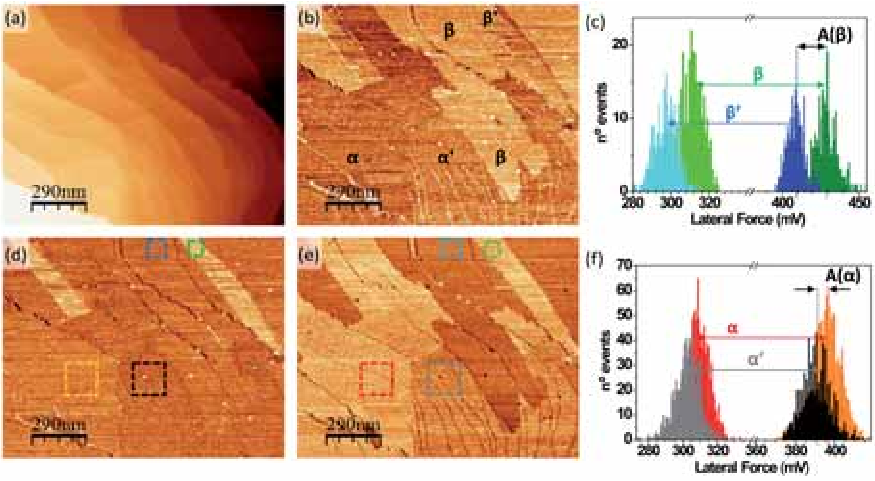

Figure 4.4.15: *cm-SFM topography (a) and mean friction map (b) of a BP4 SAM on Au(111) containing divers α and β-phase regions. As in previous figures , low friction location corresponds to $\alpha - phase$ domains while bright contrast corresponds to the $\beta - phase$. Original forward (d) and backward (e) lateral force images. Histograms of lateral force values obtained out of the squared regions for β and α phase domains presenting same friction in (b) are shown in (c) and (f) respectively. While equal friction is found between $\alpha - \alpha'$ and $\beta - \beta'$ domains, i.e. $F(\alpha) = F(\alpha')$ and $F(\beta) = F(\beta')$, the friction asymmetry (AS) found for different domains of α is less than the half than the one presented by the β.*

Figure 4.4.15 (a) shows the topographic signal of a surface region where AS is measured for both α and β-phases. The two polymorphic phase regions are well differentiated in the corresponding friction map of figure 4.4.15 (b). By analyzing the lateral forward (d) and backward (e) images, it is found that while nearly equal friction is found between $\alpha - \alpha'$ and $\beta - \beta'$ domains, i.e. $F(\alpha) = F(\alpha')$ and $F(\beta) = F(\beta')$, the corresponding lateral forces show a different contrasts for those locations. This is a clear indicative of AS effect between different locations of both α and β-phases. In figure 4.4.15 (c) and (f) the lateral force values of the locations marked in (d) and (e) are represented in histogram plots. From the AS found for the α and β domains (denoted by $A(\alpha)$ and $A(\beta)$), we found that the amplitude of $A(\alpha)$ is of $\sim 5mV$, whereas a quantity four times higher is found for $A(\beta)$, which is of around $\sim 20mV$. The measured small $A(\alpha)$ difference in the lateral force signal is close to our detection threshold, what explains the difficulties we had to detect such a small AS effect for differently oriented α-phase domains. As mentioned above this difference in the measured AS between phases, i.e. $A(\beta) > A(\alpha)$ is not surprising. The lower tilt angle presented by the $BP4$ molecules in the α-phase decreases the magnitude of the anisotropic effects measured over molecular domains with different orientation and in consequence, making also less pronounced the friction asymmetry effect.

In general, the present results show and consolidate that lateral force imaging is a powerful method not only for the accurate tribological characterization of ultrathin crystalline soft layers, but also for gaining information about structural details as the azimuthal orientation of the molecular domains on surface, information not accessible by common STM and SFM measurements providing 2D information.

4.4.3 Influence of the supramolecular arrangement of BP4 molecules on the surface electrostatic properties

In this section we move on to the study of the electrostatic properties of the two polymorphic α and β-phases, with the goal of studying the influence of the molecular arrangement on the electrostatic properties of the surface. In the last years, with the development of organic electronics, the study of the SAM adsorption influence on the surface electrostatic properties has gain attention as a way to improve the properties and performance of organic-inorganic interfaces [194]. It is well established, for instance, that by the adsorption of organic molecules in metals surfaces the local work function of the surface is modified [195–197]. The SAM acts as an array of oriented dipoles that modifies the local surface potential and hence changes the local work function of the surface. In a simplified model, in such chemisorbed systems the work function modification can be decomposed as the sum of the intrinsic dipole moment of the molecules and the interface dipoles generated by the charge rearrangement induced by the chemical bond [196, 198, 199]. This interface dipole is found to strongly depend upon the surface [200, 201] and the adsorption sites of the molecule, but it has been shown that usually its contribution is much lower than the molecular dipole itself [202–204]. In addition to the magnitude of these dipoles, the work function shift is influenced by the density of molecules on surface, that is, the density of dipoles, the permittivity of the layer and the polarizability of the molecules. Structural variations, such as the presence of defects or molecular domains sizes and boundaries also have an impact on the effective work function variation induced by the SAM.

In previous studies related to the work function modification by adsorption of organic molecules, much of the attention has been focused on the impact of the chemical composition and structure of the molecules themselves [196, 199, 200, 205–210], the different influence of the same molecular layer on different metal surfaces [201] or the coverage dependence [211–213] on the work function modification induced by the SAMs. However, a detailed understanding of the role of the different supramolecular arrangement parameters affecting the work function modification is still scarce. Previous investigations on the molecular orientation and arrangement dependence of the work function shift include studies on organic semiconductor molecules physisorbed on different substrates [214–219] and few on chemisorbed SAMs [220].

The coexistence of the two polymorphic arrangements varying in molecular conformation, packing density and structural array of the same $BP4$ molecular unit presents an ideal scenario where the influence of the SAM structural parameters into the work function change can be studied by Kelvin probe force microscopy (KPFM). In order to explore the influence of the supramolecular order on the local work function, here we present contact potential difference (CPD) measurements over the two polymorphic phases using KPFM. Our first goal was to measure the difference of work function change induced by the so called α and β phases in $Au(111)$, and second, thanks to the extended information we have about the two supramolecular phases (see section 4.2 and 4.4.1), try to disclose the relative significance of each particular contribution to this work function change.

Experimental Procedure

All the measurements presented in this section were done using the following procedure. Surface regions with large enough $Au(111)$ terraces where selected by using the dynamic SFM mode (dm-SFM, see section 3.2.4.2). The tip was then placed in direct contact with the sample (cm-SFM mode, see section 3.2.4.1) and taking advantage that the two α and β polymorphic phases present different friction contrast (proven in section 4.4.1) each phase location was determined. By changing back to the dynamic mode, surface potential data were acquired using both KPFM images and 3D mode strategies (techniques introduced in sections 3.2.5.3 and 3.2.5.4 respectively). All the measurements were performed by using Budgetsensors Pt/Cr coated probes mounted in cantilevers with a nominal spring constant $k \approx 3N/m$. The choice of cantilevers with appropriate (intermediate) stiffness and the capability to pass from cm-SFM to dm-SFM measurements, under controlled conditions without changing surface location, has allowed us to correlate each polymorphic phase with its electrostatic response. cm-SFM measurements were performed in the attractive regime as close as possible to the pull off set point, thus preventing any tip induced layer deformation. For KPFM measurements, oscillation amplitudes in the range of $10 - 20\,nm$ and ac bias of $0.5 - 0.6\,V$ and $7\,KHz$ were employed.

Results and discussion

In figure 4.4.16 a complete SFM data series of cm-SFM and dm-SFM mode measurements over a region containing α and β-phases coexisting is presented. The cm-SFM topographic image of 4.4.16 (a) shows two adjacent $Au(111)$ terraces, the one on the left is covered by α-phase and the adjacent terrace presents coexistence of both α and β-phases. Even if the topographic details are not well resolved in this case, the corresponding profile presented in 4.4.16 (b) reproduces the $\sim$ 1.2Å height difference between both phases (found in previous section 4.4.1) in direct comparison to the $d_{Au}(111) = 2.35\mathring{A}$ between adjacent terraces covered by the α-phase. Further evidence of the α and β-phase regions locations is gained by the lateral force forward and backward signals shown in 4.4.16 (d) and (e), where the higher friction contrast is correlated to the lower topography location of β-phase as described in sections 4.4.1 and 4.4.2. By changing from cm-SFM to dm-SFM mode in the very same surface location the KPFM measurements were performed, that enables us to correlate the contact potential difference (CPD) signal (figure 4.4.16 f) with each polymorphic phase. From the faint contrast detected in the CPD map presented in figure 4.4.16 (f), the CPD between α and β-phases locations is found to differ in about $\Delta CPD_{\alpha-\beta} = CPD_{\alpha} - CPD_{\beta} \approx 30 \pm 10\,mV$ as can be appreciated in the profile depicted in (g) from the location marked in (f). The error is estimated from the quadratic sum of the standard deviations of the mean values found for α and β locations in multiple profiles as the one shown in (g). This result was verified by measuring the CPD with the 3D mode strategy (introduced in section 3.2.5.4) which can be use as an alternative mode to measure the local CPD and has the advantage of independent but immediate data acquisition while maintaining a precise control over the tip-sample distance. In this case the normal force (F_n) versus tip-sample voltage (V) is measured in a certain position of the surface, which provides the electrostatic force dependence upon voltage, $F_n \propto (V_{tip-sample} - V_{CPD})^2$, with the resulting parabolic curve centered in CPD. The CPD variation between locations is determined from the relative displacement of the centers of the parabola obtained over each region. In figure 4.4.16 (h) the experimental parabola curves obtained by an average of ~ 250 curves recorded over each region are plotted. From the corresponding parabolic fit of each curve and the determination of the parabola center displacement a $\Delta CPD_{\alpha-\beta}$ of $\sim 30\,mV$ is also found, confirming the $\Delta CPD_{\alpha-\beta}$ value measured by KPFM.

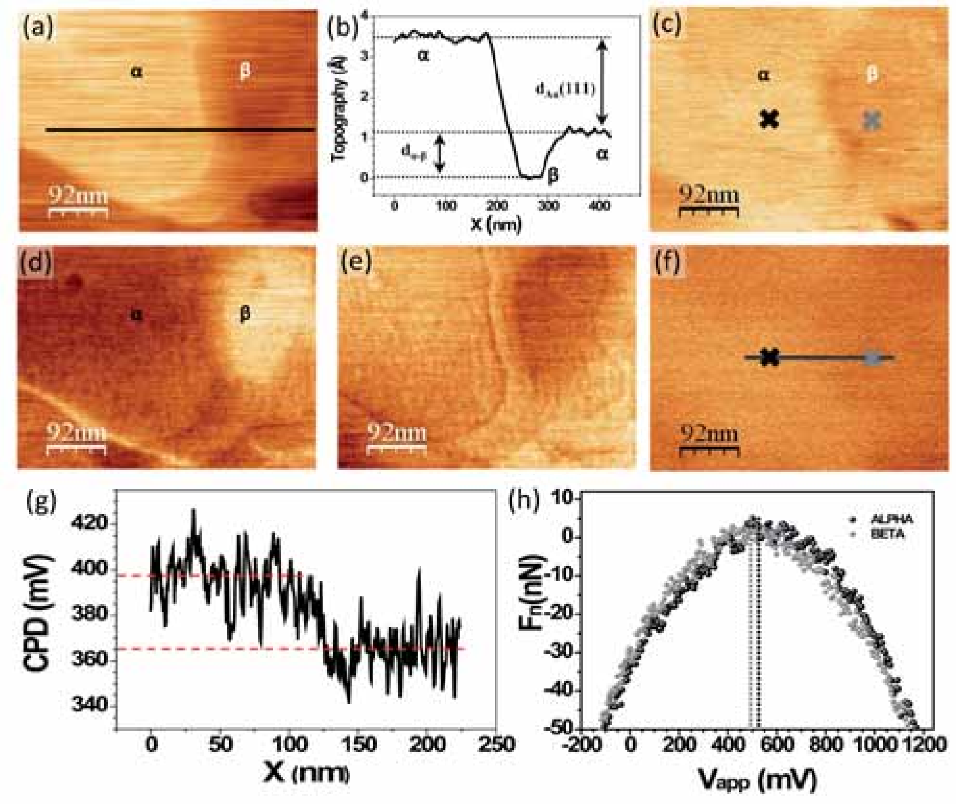

Figure 4.4.16: *cm-SFM topography (a) and simultaneous forward (d) and backward (e) lateral force images of a surface location containing the a and β phases of BP4 on Au(111). The topographic line profile marked in (a) is presented in (b). dm-SFM topography (c) and CPD (f) maps of same surface location. A line profile of CPD signal is depicted in (g). Normal force versus bias voltage parabolas measured on the two locations (black and grey are used to indicate a and β phases locations respectively) confirming KPFM data are presented on (h).*

A supplementary 3D mode experiment is presented in figure 4.4.17. In this case, several surface steps covered by BP4 can be seen in the contact mode topography (a) and the two supramolecular phases locations can be distinguished in the corresponding lateral force forward and backward signals (figure 4.4.17 (b) and (c)). Each phase is identified at the same terrace level in FFM as pointed in (b), and the topographic line profile presented in (d) (of the location marked in (a)) corroborates the already determined topographic height difference of $\sim 1.2\text{Å}$ between α and β phases. In figure 4.4.17 (e) the normal force versus tip bias parabolas centered in CPD obtained by the 3D mode strategy on top of the locations marked in (c) are presented. In spite of the overlap between experimental parabolas, a magnification of the relevant region around the maxima of the corresponding fits is presented in figure 4.4.17 (f), clearly showing a similar CPD difference ($\sim 25mV$) as that of the previous example, supporting the accuracy of the result. Therefore, we can conclude that even if the two phases are made out of the same molecular unit, the supramolecular arrangement influences the change in surface potential (local work function) in a non-negligible extent.

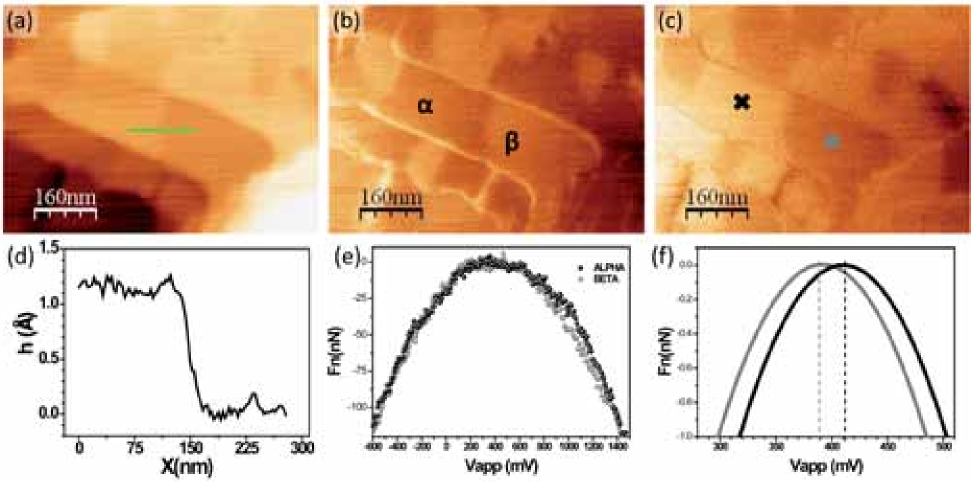

Figure 4.4.17: *cm-SFM topography (a) and simultaneous lateral force forward (b) and backward (c) measurements. The height difference between phases is* 1.2Å *as determined from the topographic profile of (d) taken along the segment marked in (a). The 3D mode experimental parabolic data performed in the location marked with crosses in (c) are shown in (e). A magnification of the near maxima region of the corresponding parabolic fits can be seen in (f).*

From the above results we could naturally wonder if the measured $\Delta CPD_{\alpha-\beta}$ is in agreement with the work function shift ($\Delta\varphi_{\alpha-\beta}$) that one should expect between two polymorphic α and $\beta-$phases of the same BP4 molecular unit. In the following we are going to try to face this question by evaluating and comparing the different contributions that play a role in this work function variation.

The change in work function of the metal upon a specific SAM adsorption is commonly described in first order approximation by the Helmholtz classical electrostatic equation [195]:

$$\Delta\varphi = -\frac{\mu}{\varepsilon_0 \varepsilon A} \tag{4.4.1}$$

Where μ is the normal component of the dipolar moment of the molecule chemisorbed, ε_0 the vacuum permittivity, ε the permittivity of the organic layer and A_i the area per molecule within each specific packing, that is the inverse of the density of dipoles on surface. In our KPFM measurements, the magnitude measured is the contact potential difference (CPD), which for our experimental set-up is related to the work function shift as $\Delta CPD_{i-j} = CPD_i - CPD_j = \varphi_j - \varphi_i$ (see section 3.2.5.3). On the present case, for the two different supramolecular arrangements of the $BP4$ molecule, the Helmholtz equation 4.4.1 would present the form:

$$\Delta\varphi_{\alpha-\beta} = -\left(\frac{\mu_\alpha}{\varepsilon_0 \varepsilon_\alpha A_\alpha} - \frac{\mu_\beta}{\varepsilon_0 \varepsilon_\beta A_\beta}\right) \tag{4.4.2}$$

where μ_i denotes the normal component of the dipolar moment of the molecule chemisorbed in each molecular phase ($i = \alpha, \beta$), ε_0 the vacuum permittivity, ε_i the dielectric constant of the SAM and A_i the area per molecule within each specific packing (been $i = \alpha, \beta$). In equation 4.4.2 we are considering that the two polymorphic phases present a different dielectric constant. Commonly the dielectric constant of SAMs is assumed to be in the range of 2-4 [196, 221–223]. In spite of being formed by the same molecular unit, along this section we will deduce that both polymorphic phases present different dielectric constants and we will discuss the nature of this difference. In addition, by modeling our system with equation 4.4.2, we are implicitly performing a series of approximations. We are assuming that in each phase all of the chemisorbed molecules present the same normal component of the electric dipole. However this is not necessarily true for each supramolecular arrangement formed by the BP4 molecule. Both α and β-phases present incommensurate structures with $Au(111)$, and thus in both cases the BP4 molecules present different sulfur adsorption sites on the $Au(111)$ [155, 162, 163, 176]. In fact, in the STM results of Azzam et al. [155] three different heights of the BP4 molecules were observed in each unit cell of the α-phase. The nature of those differences in heights can be either of topographic or electronic nature, but in any case it will directly influence the individual molecular dipole moment. Moreover, these variations in the adsorption sites could be responsible of $S - Au$ bond angle variations [224] and in consequence of its contribution to the vertical component of the dipolar moment. In any case, we consider reasonable to assume a same normal component of the dipolar moment for all the molecules in each polymorphic phase, because in most of the chemisorbed thiols on Au the Au-S bond have been found to make a small contribution to the measured surface potential in comparison to the molecular dipole[203, 204, 225]. In addition, we are assuming that the $Au(111)$ surface remains flat and defect free with the α and β-phases SAMs on top, ruling out any possible underlying gold reconstructions difference from one phase to the other that could contribute to variations of $\Delta\varphi$ of a few mV[226]. In fact, recent works on the thiol-$Au(111)$ interface evidence a much more complex landscape in the alkanethiols adsorption on $Au(111)$ [227] , with a important dependence on the particular thiolate. However, in our incoming analysis we assume that the $Au(111)$ surface remains unchanged from one phase to the other, flat and defect-free with the chemisorbed α and β-phases SAMs on top. Besides, as introduced in section 4.4.1, the structural quality of the two phases is rather different. While the β-phase is characterized by an exceptional structural quality, the presence of defects and domain boundaries is much more extended in the α-phase, in addition to the presence of the solitons. However, for the following analysis we obviate these differences in the structural quality of the layer and assume a perfect structure of both polymorphic phases.

From equation 4.4.2 and assuming a same molecular dipole along the molecule for both molecular arrangements, equation 4.4.2 can be rewritten as:

$$\Delta\varphi_{\alpha-\beta} = -\frac{\mu_0}{\varepsilon_0}\left(\frac{cos\theta_\alpha}{\varepsilon_\alpha A_\alpha} - \frac{cos\theta_\beta}{\varepsilon_\beta A_\beta}\right) \tag{4.4.3}$$

where θ_i is the molecular tilt angle in the corresponding supramolecular phase. As previously seen in sections 4.2 and 4.4.1 the molecular tilt angles (θ_i) and the areas per molecule (A_i) of the corresponding phases are known from previous STM, NEXAFs, ellipsometry [152–155] and our SFM data (section 4.4.1), thus in principle only the dipolar moment of the chemisorbed molecule (μ) and the dielectric constant of the organic layer (ε_i) in each molecular phase remain unknown. Equation 4.4.3 can be rewritten in the following form:

$$\Delta\varphi_{\alpha-\beta} = \Delta\varphi_\alpha\left(1 - \frac{cos\theta_\beta}{cos\theta_\alpha}\frac{A_\alpha}{A_\beta}\frac{\varepsilon_\alpha}{\varepsilon_\beta}\right) \tag{4.4.4}$$

The form of equation 4.4.4 offers us two main advantages: On the one hand it enables us to derive and compare the relative influence of each factor, i.e. molecular tilt angle, packing density of the layer and layer permittivity, in the local work function change, and on the other hand it overcomes the uncertainty of the molecular dipole moment of the molecule if the work function change induced by the BP4 molecule in the α-phase ($\Delta\varphi_\alpha$) configuration on gold is known. Heimel and co-workers [228] calculated the work function shift induced by the $BP4$ monolayer on $Au(111)$ using density-functional theory (DFT) calculation, and obtained a $\Delta\varphi_\alpha \approx -1.4\, eV$ [228]. For their calculations instead of considering the $5\sqrt{3}\times 3$ structure with eight molecules in the unit cell reported by Azzam et al. [155], which implies different adsorption sites for the molecules within the unit cell, they use a $2\sqrt{3}\times 2$ with two molecules in the unit cell with the sulfur located between the fcc-hollow and the bridge sites on top of perfect atomically flat $Au(111)$ surface. In addition, they do not consider any presence of solitons or defects on the layer. An alternative procedure to using the DFT calculated value is to measure the $\Delta\varphi_\alpha$ induced by BP4 α-phase with respect to gold. For this purpose a reference sample consisting of stripes of BP4 (α-phase) surrounded by bare gold was prepared using soft lithography $\mu-$contact printing (μCP) technique (see section 4.3) using a polydimethylsiloxane (PDMS) stamp with a stripped pattern ($3\, \mu m$ wide). Since the samples are not thermally treated, no phase transition to the β-phase occurs and the patterned SAM are assumed to be formed by the α-phase. This samples were also prepared on the same gold on mica substrates employed for the BP4 α and β coexisting phases samples.

In figure 4.4.18 the SFM measurements of the patterned surfaces by BP4 SAM are presented. Though no distinguished in the contact mode topographic image (figure 4.4.18 a), the contrast on the friction image (figure 4.4.18 d) confirms the presence of BP4 SAM areas (see the stripe at the right part of the lateral force image) coexisting with regions of bare gold. The BP4 surface locations presents a lower friction response with respect to the bare gold surface as expected for methyl terminated SAMs and in agreement with previous FFM studies of BP4 and alkanethiols SAMs on gold [178, 180]. Dynamic mode simultaneous topography and CPD maps of a slightly shifted location are shown in figure 4.4.18 (b) and (e) respectively. The change in work function is estimated from the histogram (figure 4.4.18 f) of the whole CPD image (figure 4.4.18 e) and is found to be $\Delta\varphi_\alpha = -220 \pm 20\, mV$ between bare gold surface and BP4 ($\alpha - phase$) functionalized location. The error is estimated from the add in quadrature of the standard deviations of the peaks in figure 4.4.18 (g). The measued $\Delta\varphi_\alpha$ was cross-checked by the so called 3D mode experiments,

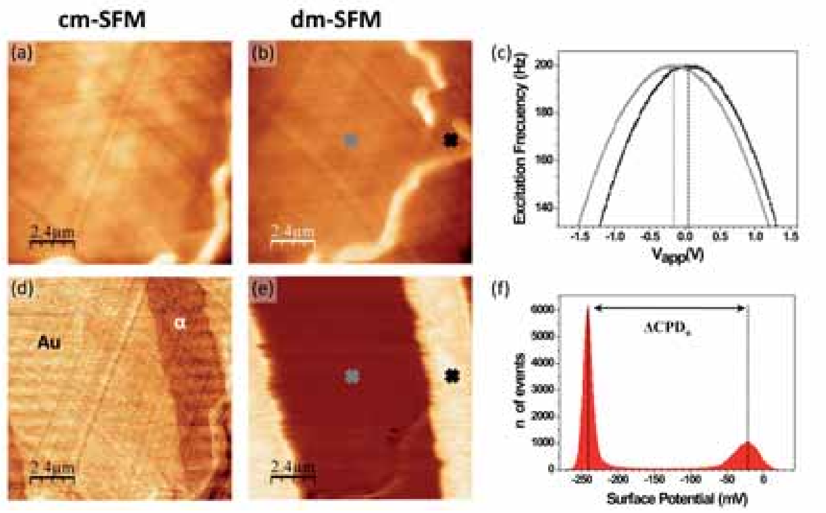

Figure 4.4.18: *cm-SFM and dm-SFM measurements of BP4 stripes are presented in the left and central columns respectively. Topography images of two different locations are presented in (a) and (b). Contact mode friction image showing the lower contrast of the BP4 locations (c). The ΔCPD_α is determined by the histogram plot (f) of the CPD map (e) and the 3D mode experiments (c) performed in the locations marked with crosses in (b) and (e). The topography color scale is of 23 nm from dark to bright.*

by recording the frequency shift of the oscillating tip in function of the tip voltage in this case and presented in 4.4.18 (d). By determining the parabolas maxima shift measured on top of the locations marked by crosses in 4.4.18 (a) and (c), the CPD difference ($\Delta CPD_\alpha = CPD_\alpha - CPD_{Au} = 220\, mV$) between the BP4 ($\alpha$-phase) and the bare gold regions is measured. Our experimental result is far from the calculated $\Delta\varphi_{\alpha-\beta}$ by Heimel and co-workers [228]. However, we consider that our result yields in the range of other ΔCPD measured between bare gold and different SAMs (such as hexadecanethiol) and that the a ΔCPD of $\sim 1.5\, V$ would be unstable in laterally functionalized gold surface by a SAM. By comparison of the $\Delta\varphi_{\alpha-\beta}$ and $\Delta\varphi_\alpha$ experimental values, the influence of the different supramolecular arrangement into the work function shift difference between phases can be inferred, resulting that the supramolecular change modifies it in nearly a 14% the work function change on gold.

The determination of ΔCPD_α allows us to estimate the dipolar moment of the chemisorbed molecule (μ) by introducing in the Helmholtz equation (equation 4.4.1) ($\Delta\varphi = -{}^{\mu_\alpha}/_{\varepsilon_0\varepsilon_\alpha A_\alpha}$) the corresponding area per molecule of the α-phase and the experimental $\Delta\varphi_\alpha$ result and the dielectric constant of the molecular layer. Typical dielectric constants of SAMs range between 2 to 4 [196, 221–223]. From electrochemical experiments performed on different biphenyl based thiols on gold, Felgenhauer et al. [166] got a value of 5 and 2.5 for the dielectric constants of the biphenyl aromatic unity and aliphatic part respectively. Combining those values with an approximation of the thikness of the aliphanic and biphenyl moiety we can estimate the dielectric contant of the BP4 molecule to be in a confident limit of $3-4$. This yields to a value in the range of $0.6-0.8\,D$[2] for the dipole moment of the BP4 molecule along the molecule. Though lower, are reasonable values compared typical dipolar moments of thiols reported in the literature, such as hexadecanethiol ($\mu \approx 1.5D$) [201, 229] or benzyl mercaptanthiol ($\mu \approx 1.0D$) [203].

With the experimental values of $\Delta\varphi_{\alpha-\beta}$ and $\Delta\varphi_{\alpha}$, introducing the structural data (presented in table 4.1) and considering as a first approximation that the permittivity is exactly the same in both supramolecular arrangements ($^{\varepsilon_\beta}/_{\varepsilon_\alpha} = 1$), we can estimate from equation 4.4.4 a difference in work function change between phases of $\Delta\varphi_{\alpha-\beta} \simeq -60\,mV$. Though $\Delta\varphi_{\alpha-\beta} < 0$ is consistent with the relative ratio between areas per molecule ($^{A_\alpha}/_{A_\beta} \approx 0.83 \pm 0.01$) and tilts ($^{Cos\theta_\beta}/_{Cos\theta_\alpha} \approx 0.88 \pm 0.09$) in each phase (assuming $\delta A_{\alpha,\beta} = 0.1\text{Å}^2$ and $\delta\theta_{\alpha,\beta} = 3°$), the absolute value results however nearly twice the experimental value ($\Delta\varphi^{exp}_{\alpha-\beta} = -\Delta CPD_{\alpha-\beta} \simeq -30\,mV$).

However, in the above description the dielectric constant of the two phases have been considered to be the same, that is far from being true. On the one hand, the difference on structural conformation and layer thickness in the two phases should yield to a difference in permittivity. And on the other hand, the electrostatic interaction between molecules forming the organic layer has not been yet considered. This interaction induces an additional dipole (μ_{depo}) in the molecules that points opposite to μ and provokes a decrease in the effective surface dipole of the molecular layer. This is the so-called depolarization effect, which can significantly contribute to the otherwise small differences in local work function. The impact of this effect has been commonly considered in Helmholtz equation via an effective permittivity parameter [195, 230]. As it will be detailed below, the depolarization effect is also dependent on the polarizability and structural arrangement of the molecules [222, 223, 231]. The polarizability of a molecule in general, and of the biphenyl moiety in particular is rather anisotropic, thus a difference of the molecular orientation between phases will directly influence the permittivity of the molecular layer and a difference in the effective permittivity of the molecular layer is expected depending on the polymorphic phase.

In fact, it is worth to note that a ratio of $^{\varepsilon_\alpha}/_{\varepsilon_\beta} = 1.18 \pm 0.11$ is sufficient to conciliate equation 4.4.4 with the $\Delta\varphi_{\alpha-\beta}$, $\Delta\varphi_\alpha$ experimental values and θ_i, A_i ($i = \alpha, \beta$) (values resumed in table 4.1.

---

[2] Electrical dipolar moment has the SI units of $C \cdot m$ but for molecular dipoles is more often used the CGS Debye (D) unit, which is defined as $1D \approx 3.33564 \times 10^{-30}\ C \cdot m$.

We notice that the obtained large error for the permittivity ratio ($\delta(\varepsilon_\alpha/\varepsilon_\beta) = 0.11$) is a combination of the experimental errors of $\delta(\Delta\varphi_{\alpha-\beta})$ and $\delta(\Delta\varphi_{\alpha-Au})$ and the error on the molecular tilt angles (we consider a $\delta\theta = 3^\circ$ and $\delta A = 0.1\text{Å}^2$).

	$\theta_i(^\circ)$	$A_i(\text{Å}^2)$	$Cos\theta_\beta/Cos\theta_\alpha$	A_α/A_β	$\varepsilon_\alpha/\varepsilon_b$
$\alpha - phase$	39	27.05	0.88	0.835	1.2
$\beta - phase$	47	32.40			
δ	3	0.1	0.06	0.004	0.1

Table 4.1: *Molecular tilt angle and area per molecule for each supramolecular phase and the ratios between magnitudes in equation 4.4.4. The corresponding errors* (δ) *are given in the bottom line. Note:* $\delta\theta_i$ *and* δA_i *are an assumed errors for calculating the error of the ratios.*

Provided that $\varepsilon_\alpha/\varepsilon_\beta > 1$, while both A_α/A_β and $Cos\theta_\beta/Cos\theta_\alpha$ are <1 (see table 4.1), we deduce that the depolarization effect and the structural factors have an opposite influence on the work function difference ($\Delta\varphi_{\alpha-\beta}$). Equation 4.4.4 has the particular form $\Delta\varphi_{\alpha-\beta} \propto (1 - \prod_{i=1}^{3} X_i)$, where the different $\varepsilon_\alpha/\varepsilon_\beta$, A_α/A_β *and* $Cos\theta_\beta/Cos\theta_\alpha$ ratios are denoted by X_i ($i = 1, 2, 3$). The form of this equation implies on the one hand that the higher X_i factor deviation from unity is the more it contributes to a higher $\mid \Delta\varphi_{\alpha-\beta} \mid$, and on the other, that a $X_i < 1$ gives rise to a more positive $\Delta\varphi_{\alpha-\beta}$ and vice versa. In consequence, for the present case the relative contribution of the corresponding factors are estimated by the variation from unity of the corresponding ratios in equation 4.4.4. The are per molecule (A) and effective permittivity ratios seem to contribute nearly the same but in an opposite sign to $\Delta\varphi_{\alpha-\beta}$ (note that $|A_\alpha/A_\beta - 1| \simeq |\varepsilon_\alpha/\varepsilon_b - 1|$), while the difference on molecular tilt angle contributes around 30% less than the two others.

In the following we are going to focus in discussing the different factors affecting the variation of the dielectric constant from one polymorphic phase to the other.

Dielectric constant of BP4 as a function of the supramolecular arrangement

The dielectric constant is defined as the relative permittivity of a material in presence of a static electric field, being the permittivity a measure of how an electric field affects and polarizes a given medium. In molecular arrangements such as SAMs, each molecular unit is influenced by the electric field generated by the SAM itself and due to the molecular polarizability an opposite dipolar moment is generated. In consequence, the total dipolar moment (μ) of the molecular layer is the sum of the dipolar moment of molecule chemisorbed (μ_0) and the opposite dipole (μ_{depol})

induced by the polarization of the other molecules [195, 222, 232, 233]:

$$\vec{\mu} = \vec{\mu_0} + \vec{\mu}_{depol} = \vec{\mu_0} + \alpha\, \vec{E}_{depol} \tag{4.4.5}$$

where E_{depol} is the electric field inside the monolayer induced by the monolayer molecular dipole array and α is the molecular polarizability. The polarizability of a molecule is defined as the tendency of the molecular charge to redistribute in presence of an external electric field. The electric field generated by an array of point dipoles can be expressed as [195]:

$$\vec{E}_{depol} = -\frac{\mu}{4\pi\varepsilon_0} \sum \frac{1}{R_{lm}^3} \hat{\mu} = -\frac{\mu}{4\pi\varepsilon_0}\, F\, A^{-3/2} \hat{\mu} \tag{4.4.6}$$

$$F = \sum_{l,m} \frac{1}{R_{lm}^3} \tag{4.4.7}$$

where R_{lm} refers to the distance between a given molecule and its l, m neighbors, F is a dimensionless structural factor characteristic of the dipolar array geometry distribution and A denotes the area per molecule. The influence of this local electrostatic field into de dielectric properties of the layer has commonly been accounted by introducing a so called effective dielectric constant (ε^{eff}) factor into the Helmholtz equation. From equation 4.4.5 & 4.4.6 and by the definition of the effective dielectric constant of the organic layer as the ratio between the original dipole and total dipole ($\varepsilon^{eff} = \mu_0/\mu$) [195, 230] the following expression for ε^{eff} is derived [195, 222, 232]:

$$\varepsilon^{eff} = 1 + \frac{\alpha}{4\pi\varepsilon_0} F\, A^{-3/2} \tag{4.4.8}$$

This means that the dielectric constant of the layer depends on the molecular polarizability (α) on the one hand and on the molecular structural configuration on the other (that is given by F and A). Because the structure of the two supramolecular phases are known and the ratio between effective permittivities has been derived by our experimental results, the estimation of the difference between molecular polarizabilities on the two phases should be possible. Using equation 4.4.8 for the permittivity of each molecular phase and with η grouping all structural details (that is, defining $\eta = F\,A^{-3/2}$), the ratio between α and β phases permittivity can be rewritten as [3]:

$$\frac{\varepsilon_{\alpha}^{eff}}{\varepsilon_{\beta}^{eff}} = \frac{1+\alpha_{\alpha}\eta_{\alpha}}{1+\alpha_{\beta}\eta_{\beta}} \tag{4.4.9}$$

Concerning the structural factors η_i ($i = \alpha, \beta$), the area per molecule of α and β phases are known to differ (table 4.1) and a variation on F_i factors is also expected since the two supramolecular phases present a different molecular array distribution (section 4.2). For hexagonal packing geometries F has been previously calculated by Topping [234] by evaluating the double summations as second order Zeta-functions, and is found to be 8.8927. In our present case both packing geometries slightly differ from a hexagonal packing as can be appreciated in figure 4.4.19, where the primitive cells of α (in red) and β (in green) phases are compared with two hexagonal arrays (dashed lines) presenting same a_i primitive vectors of the corresponding phase. In comparison to the values calculated by Topping for hexagonal and rectangular lattices, in our case the primitive vectors obey $a_i \neq b_i$, consequently an area per molecule parameter ($A_i^{3/2}$) has to be included into equation 4.4.7 to maintain the dimensionless character of F_i.

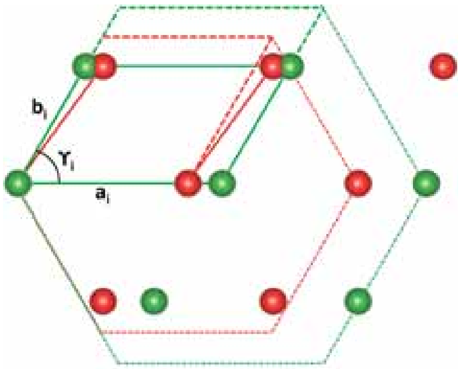

	a_i(Å)	b_i(Å)	γ_i(°)
$\alpha - phase$	6.24	5.33	54.18
$\beta - phase$	7.48	4.99	60

Figure 4.4.19: *The primitive cells of α and β phases are shown in red and green lines respectively, while dashed lines correspond to hexagonal lattices with same a_i primitive vectors of α and β phases respectively. Primitive cells structural data is presented in the table.*

In order to obtain the geometrical factors of each molecular phase a finite numerical calculation

---

[3] Polarizability has the SI units of $C \cdot m^2 \cdot V^{-1}$but is more often expressed as polarizability volume with units of $Å^3$. In the following it will expressed in $Å^3$ units, been $\alpha(Å^3) = \frac{10^{30}}{4\pi\varepsilon_0}\alpha(C \cdot m^2 \cdot V^{-1})$ the conversion factor to SI units.

has been performed using the Matlab program [235] and the following equation extended from equation 4.4.7:

$$F_i = \sum_{l,m} \frac{A_i^{3/2}}{R_{lm}^3} = \sum_{l=-n}^{n} \sum_{\substack{m=-n \\ (l,m)\neq(0,0)}}^{n} \frac{A_i^{3/2}}{\left(a_i^2\, l^2 + b_i^2\, m^2 + 2\, a_i\, b_i\, l\, m\, \cos\gamma_i\right)^{3/2}} \tag{4.4.10}$$

where a_i and b_i denote the primitive vectors of the corresponding molecular phase ($i = \alpha, \beta$), γ_i is the angle between the primitive vectors and n denotes the number up to we are extending the double summation, thus it is the number of neigbour molecules that are considered to contribute to the E_{depol} electric field. In order to estimate the n value necessary to obtain a good enough approximation to F value, preliminary calculation were performed for hexagonal packing geometry ($a_i = b_i$,$\gamma_i = 120°$) varying n and comparing the obtained $F_{hexa}(n)$ with Topping's result. For n=10^3 a value of 8.8869 (F_{hexa}) has been obtained, which presents a deviation of a 0.07% with respect to Topping's result. Taking into account that a summation extended to n=10^3 would yield to molecular domain sizes larger than 1 μm^2, which is larger than the ones in our case, we think that $n = 10^3$ is a reasonable value for the calculation and comparison of both phases F_i factors.

Expression 4.4.8 however, has been only found to successfully model the dielectric constant of monolayers with short molecular lengths compared to the intermolecular distances, since it approaches the molecules by polarizable single points. This is not clearly our case since in both α and β phases the layer presents a well packed structure with intermolecular distances shorter than the molecular layer length. Romaner and co-workers have recently shown by DFT calculations [222] the validity of the corrected model introduced by Taylor et al. [195] where the finite size effects are taken into account by including an extra effective finite size parameter (g) into the F geometrical factor calculation $F_i^g = \sum_{l,m} \frac{A_i^{3/2}}{\left(R_{lm}^2+g^2\right)^{3/2}}$ ($i = \alpha, \beta$). Notice that for g equal to cero the point dipole approximation is recovered ($F_i^0 = F_i$). The choice of an appropriate g has been also discussed in Romaner et al. work [222] which depending on the system under study can take values between L/2 and L, being L the molecular length. Taylor and Bayers [195] recommended to use g=L/2 value and Natan et al. [223] found that the use of this value gave them excellent agreement with their DFT calculations on oligophenyl arrays with phenyl rings planes perfectly aligned normal to the surface. In consequence we calculate the corresponding F factor for $g = 0$ (point dipole approximation) and $g = L/2$, choosing L as the thickness of the molecular layer in each molecular phase[4].

The F_i^g values calculated for the corresponding phases and the grouped structural paramater η, defined as $\eta_i^g = F_i^g\, A_i^{-3/2}$ (for $i = \alpha, \beta$), are presented in table 4.2. As expected from the comparison to hexagonal lattices sketched in figure 4.4.19, because the packing geometry of the β-phase differs more from an hexagonal packing than the one of the α-phase, F_α^0 value is closer to F_{hexa} than F_β^0. The calculation of F_i^g enables us to distinguish between the two structural parameters influencing the effective dielectric constant of the layer, the dipolar array geometry in one hand (F_i^g) and the relative dipole-dipole distance factor summarized as the molecular density factor in the other ($A_i^{-3/2}$). The numerical values of each contribution and their ratio as a function of the molecular phase are resumed in table 4.2.

	F_i^0	$F_i^{L/2}$	$A_i^{-3/2}$(x10^{-3}Å^{-3})	η_i^0(Å^{-3})	$\eta_i^{L/2}$(Å^{-3})
$\alpha - phase$	8.9433	3.6983	7.11	0.0636	0.0265
$\beta - phase$	9.3263	4.2593	5.42	0.0506	0.0232
ratio	0.96	0.87	1.31	1.26	1.14

Table 4.2: *Structural details factors influencing the effective permittivity of the layer of each molecular phases and their ratios are presented in the table.*

Although equation 4.4.9 form $(\frac{1+\alpha_\alpha\eta_\alpha}{1+\alpha_\beta\eta_\beta})$ does not permit a direct comparison between the geometrical and packing factors influence in the permittivity ratio, the fact that $F_\alpha^g < F_\beta^g$ and $A_\alpha^{-3/2} > A_\beta^{-3/2}$ means that both factors tend opposite in their contribution to the dielectric constant of each phase. While the geometrical factor ratio favors a higher permittivity of the β-phase $({}^{F_\alpha^g}/{}_{F_\beta^g} < 1)$, the packing factor ratio $({}^{A_\alpha^{-3/2}}/{}_{A_\beta^{-3/2}} > 1)$ tends to the opposite. The packing factor however seems to have more relevance in the present case since $|\eta_\alpha^g| > \left|\eta_\beta^g\right|$, that is, the packing density factors seem to govern the grouped structural factors (η_i^g) variation, obtaining a 1.14 higher value for the α-phase when finite size effects are considered. The fact that $\eta_\alpha^{L/2} > \eta_\beta^{L/2}$ means that the difference on supramolecular structure, governed by the difference on density of molecules, favors a higher effective dielectric constant of the α-phase in comparison to the β. But, is this structural difference enough to conciliate the permittivity ratio $({}^{\varepsilon_\alpha}/{}_{\varepsilon_b} = 1.2)$ derived from our experimental results? or does the polarizability of the molecule play a role itself on the dielectric constant difference between phases?

---

[4] We use the thickness of α phase determined by ellipsometry measurements [154] (16.5Å) and for β-phase the determined by the difference measured by SFM (15.3Å) (section 4.4.1).

In the case of the $BP4$ molecule the larger contribution to the polarizability tensor is expected to come from the phenyl units [40]. The fact that both, the biphenyl moiety tilt, twist and dihedral angle (φ , γ and χ angles of figure 4.2.1) change from α to β phases make difficult to estimate the expected polarizability difference [153]. However, as a rough qualitative approximation we can guess a higher polarizability of the molecule in the α-phase configuration since it presents a lower tilt angle of the biphenyl moiety (θ), that is, a lower tilt of the in plane direction of the phenyl rings that is the one which corresponds to the higher polarizability component of the ring [236, 237]. By combining $\eta_i^{L/2}$ values with $\varepsilon_\alpha^{eff}/\varepsilon_\beta^{eff} = 1.2$ into equation 4.4.9 a linear relation between supramolecular polarizabilities is found, $\alpha_\alpha = 6.8 + 1.033\,\alpha_\beta$, which implies that the polarizability of the molecule in the α-phase arrangement is higher than for the β-phase, in agreement with what we expected. Thus we can conclude that not only the structural factors but also the polarizability of the molecule in each supramolecular phase is playing a role in the variation of the local dielectric constant of the layer. Because $\alpha_\alpha > \alpha_\beta$, the polarizability difference tends in the same sign of the grouped structural factor (η) and favors a higher permittivity of the α-phase layer. By combining the liner relation that relate the polarizabilities of the two polymorphic phases and equation 4.4.9, we can estimate the polarizability values of the $BP4$ molecule to be in the range of $50 - 150$ Å^3. Natan et al. have obtained by DFT calculations an in plane polarizability around 30 Å^3 for an isolated biphenyl moiety [223], thus such values are in the range of what would be expected for the polarizability of a biphenyl thiols molecules.

In summary, we have demonstrated how different supramolecular arrangements formed out of the same molecular unit influence the electrostatic properties of $Au(111)$. The difference in work function modification due to differences in supramolecular arrangement of BP4 molecules has been directly measured by the KPFM technique, and the relative influence of each factor influencing the surface work function change has been derived and discussed. In addition, we have derived the difference on the dielectric constant and polarizability of the molecules in each polymorphic phase.

4.4.4 Transport properties dependence on the supramolecular arrangement

In addition to structural, tribological and electrostatic properties of the BP4 α and β-phases, the electrical transport properties of the two polymorphic phases were investigated by the use of the conductive scanning force microscopy technique (CSFM, introduced in section 3.2.5.2). In CSFM the conducting tip is in contact with the sample, acting as a movable electrode and the electric current flow is measured in function of the position and applied voltage difference between tip and sample. The CSFM measurement give the electronic current through the molecular film, the gold substrate being the counter-electrode. As it is well known, the electrical contact between molecules and electrodes as well as the electronic nature of the molecule itself are relevant factors determining the final conducting response of the whole tip-SAM-gold system. To overcome unknown details, only comparison between supramolecular orders, coexisting and adopted by the same BP4 molecule are studied.

The conducting response of the sample surface was obtained by following different CSFM strategies:

i) Simultaneously acquiring topographic images $z(x, y)$ and current maps $I(x, y)$ over a given region at different voltages, what allows performing current versus voltage "movies" avoiding mechanical invasion (no film indentation) by using the contact operation mode at the lowest possible applied load needed, which is previously determined from force spectroscopy curves by method.

ii) Using the so called 3D modes, which are an alternative way of acquiring data (introduced in section 3.2.5.4), in the electrical transport measurement mode. This is, in this particular 3D modes we monitor the normal force and current flow ($f_1 = F_n \quad and\ f_2 = I$) as a function of the tip–sample applied voltage (fast scan, $x_1 = V$) and vertical piezo-displacement (slow scan, $x_2 = Z$) while the tip approaches and loads the SAM surface. As consequence, $F_n(V_{tip}, z)$ and $I(V_{tip}, z)$ images are obtained at a specific point. From the $I(V_{tip}, z)$ image the so-called $I-V$ characteristics corresponding to different z values can extracted. This approach permits quantifying force induced effects (as film deformation or indentation) and separating them from the voltage induced effects under investigation.

The Simmons model

The tunneling behavior of the transport through SAMs has frequently been roughly approximated as tunnelling through a rectangular barrier. The current can thus be modeled with the simple Simmons relation [238]:

$$I = \frac{\Lambda e}{4\pi^2 \hbar d^2} \left\{ \left(\Phi_B - \frac{eV}{2} \right) e^{-\frac{2\sqrt{2m}}{\hbar} \cdot \lambda \cdot d \cdot \sqrt{\Phi_B - \frac{eV}{2}}} - \left(\Phi_B + \frac{eV}{2} \right) e^{-\frac{2\sqrt{2m}}{\hbar} \cdot \lambda \cdot d \cdot \sqrt{\Phi_B + \frac{eV}{2}}} \right\} \qquad (4.4.11)$$

where Λ is the tip-sample contact area, m is the electron mass, d is the barrier width (the molecular layer thickness), ϕ_B is the barrier height in energy, V is the applied voltage and $\hbar$ is the reduced Planck's constant. To obtain more accurate fittings to the experimental data, for SAM junctions the Simmons model has been modified with a parameter λ[239, 240]. This parameter provides either a way of applying the tunnelling model of a rectangular barrier to tunneling through a nonrectangular barrier [239] or and adjustment to account for the effective mass of the tunnelling electrons through a rectangular barrier [240]. The success of this model in describing the current versus voltage characteristics of SAMs has been proven in different works.

Particularly, in the low bias regime, equation 4.4.11 can be approximated as

$$I = \left(\frac{\Lambda \sqrt{2m\Phi_B} e^2 \lambda}{h^2 d} \right) \cdot V \cdot e^{-\frac{2\sqrt{2m}}{\hbar} \cdot \alpha \cdot d \cdot \sqrt{\Phi_B}} \qquad (4.4.12)$$

and a tunneling decay coefficient, κ[5], can be defined from $I \approx (1/d) e^{-\kappa d}$ as:

$$\kappa = \frac{2\sqrt{2m}}{\hbar} \lambda \sqrt{\Phi_B} \qquad (4.4.13)$$

This κ parameter is a structure-dependent factor that has emerged as a characteristic parameter of the junction and can be used to classify the ability of molecular structures to provide a medium that facilitates tunneling form one electrode to the other.

Measurements and results

Prior to any current versus voltage measurement ($I-V$ characteristics) the tip conditions and the conductive response of the $BP4$ SAM were tested by mean of current maps. Each polymorphic phase is localized thanks to their different contrast on the friction signal (figure 4.4.20 d) as well as their difference in height in the topographical image (figure 4.4.20 a). We localize regions of coexisting α and β- phases to comparatively investigate the electronic conduction through them by

---

[5] The tunneling decay coefficient is usually denoted by β, here however in order to avoid any confusion with the $BP4$ β-phase we denote it by κ.

recording series maps i.e., simultaneous topography, lateral force and current maps (figure 4.4.20).

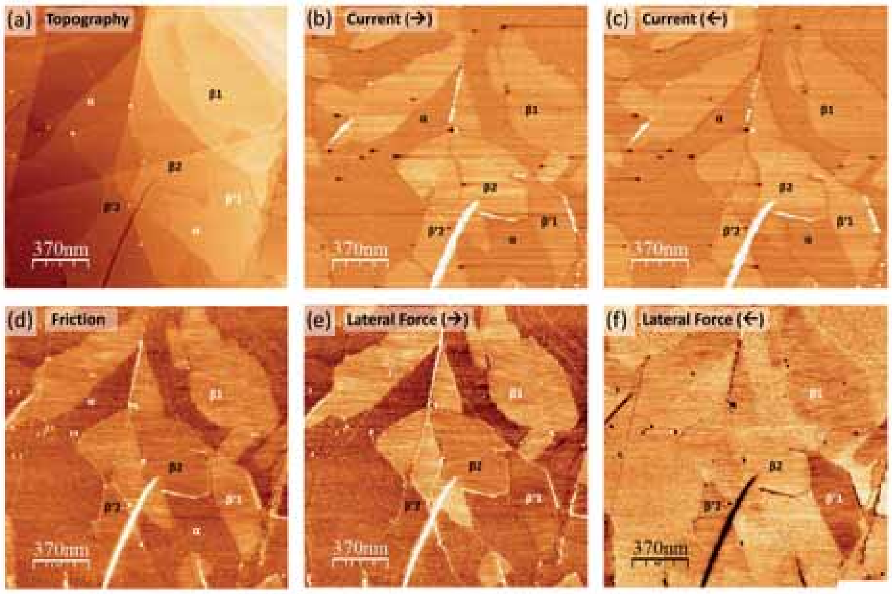

Figure 4.4.20: *Simultaneously measured topography (a), current map (trace (b) and retrace (c)) and lateral forces (trace (e) and retrace (f)) for tip-sample voltage difference of* $100\,mV$. *Calculated friction map is presented in (d). Colo scale in (b) and (c) is of* $0-2\,nA$ *from black to white.*

Figure 4.4.20 presents a complete data series of topographic, lateral force, friction and current maps corresponding to a tip-sample voltage difference of $100\,mV$. As can be seen in the top panels of the figure 4.4.20, the forward (b) and backward (c) current maps show that the thinner β-phase ($d_\beta < d_\alpha$) presents a clear higher conducting response than the α-phase. By consecutively scanning the same location with different applied voltages the conductive response in function of the applied voltage of different α and β-phase locations can be determined. This not only allows the direct comparison of the conductive response of different locations, but also enables the statistical analysis of the conductive response over each molecular phase. Topographic, lateral force and current movies are built by computer-aided monitoring of the same area at constant voltage intervals. In this case the complete topographic, lateral force and current movies consisted of 33 frames and a total duration of about 3.3 hours obtained at constant voltage intervals, from frame to frame, of $\Delta V_{tip} = 10mV$, ranging from 0 to 300 mV. The complete movies are available in the supporting information 6.3.5 (Movies 4-4-4-a to f [6]).

As was the case in series of images presented in figure 4.4.13, from the simultaneous study

---

[6] Movies 4-4-a to f correspond to topography forward and backwards, lateral force forward and backward, current forward and backward

of the lateral force forward and backward images (figure 4.4.20 e and f respectively) and the friction signal (figure 4.4.20 d) the friction anisotropy and asymmetry effects are detected which are indicative of the presence of rotated molecular domains with respect to the fast scan direction of the tip. In figure 4.4.20 some β-phase domains presenting friction anisotropy (differentiated as $\beta_i\ for\ i = 1, 2$) and friction asymmetry (differentiated as $\beta_i\ and\ \beta_i'$) have been labeled. As was explained in section 4.4.2 friction anisotropy is referred to rotated molecular domains while friction asymmetry is detected between domains that present mirror like symmetry. This makes us wonder if the relative orientation of the molecular domains could somehow affect to the conductive response detected by CSFM, because since the tip that acts as a mobile electrode confronts the molecular domains by different azimuthal orientation with respect to their molecular tilt angle direction. In order to investigate the possible effect of the fast scan direction with respect of the molecular orientation, analysis of the detected current over the $\beta_i, \beta_i'\ i = 1, 2$ location was performed and no direct correlation was found. However, a general direction dependence over all the scanned area of the detected current was found in all the measured current maps. In this particular case, a higher current was detected for the backward direction of scan with a proportion factor of around ${}^{I_{\leftarrow}}/_{I_{\rightarrow}} \approx 1.5$. The most probable explanation to this divergence on the detected current could be related to a variation of the effective conductive contact area of the tip-sample system in the two different scan directions. Small inhomogeneities on the conductive Pt coating conditions, the tip shape, etc... could be responsible of such a variation and of the absolute current measured in the experiment. This result emphasize the extreme care that has to be taken when interpreting CSFM transport measurements and the difficulty to get confidence absolute values results by SPM techniques of physical quantities that depend on the probe contact area. This result highlights the importance of always performing comparative studies with the presence of in situ references in such type of measurements.

The comparison of the conductive response of the two polymorphic phases was determined by histogram plots of the conductive response over different locations. A resume of the results is presented in figure 4.4.20. Some selective current maps are depicted in (a-d) with examples of the α and β-phases current response difference determination by histogram plots. The conductivity results for the α (in red) and $\beta-$phases (in green) in function of the applied voltage are shown in figure 4.4.21 (e). The errors are estimated from the standard deviation of the mean value calculated

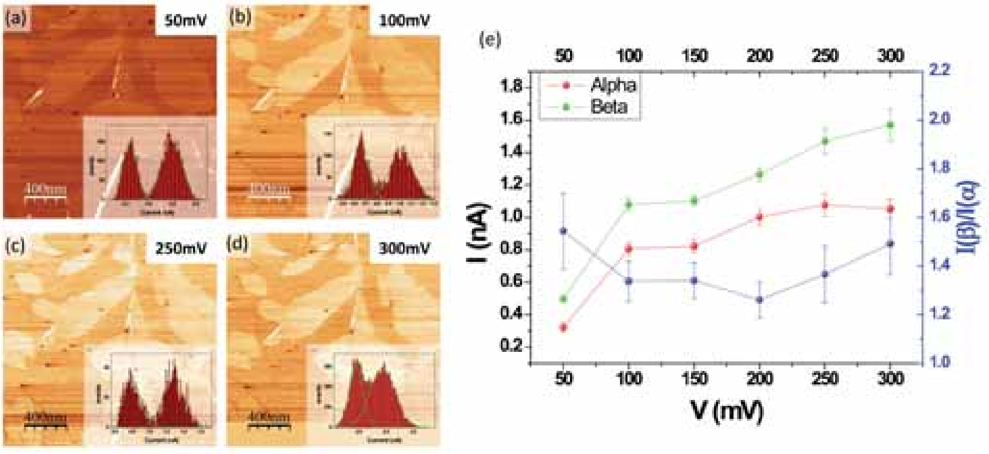

Figure 4.4.21: *Some selected current maps obtained for different applied voltages are presented in (a-d) with the measured current difference represented as histogram plot in the insets. The calculated current differences as well as the quotient represented as a function of the applied voltage is presented in (e).*

in more than ten locations[177]. Interestingly, the ratio $^{I_\beta}/_{I_\alpha}$ results to be a rather constant value of about ≈ 1.35 (presented in blue in e). By taking into account the molecular density on surface, this results means that, in spite of its lower molecular density ($^{\sigma_\beta}/_{\sigma_\alpha} = {}^{A_\alpha}/_{A_\beta} \approx 0.83$), the β-phase presents a higher conducting response per molecule ($^{I_\beta}/_{I_\alpha}\,|_{molec} \approx 1.6$).

In some cases, the lateral resolution is good enough to reach detailed conductive response of the α-phase soliton structures. In figure 4.4.22 the simultaneous topographic (a), friction (b) and current (c) signals with a tip bias of $300mV$, of a location with α and β-phases coexisting is presented. The higher topography, lower friction and lower current response of the α-phase with respect to the β-phase is distinguishable and also slight differences of the three signals are seen in the soliton structures of the α-phase. A clear sign of the good lateral resolution of the tip conditions is also derived from the conductive response of the β-phase. In the magnification current image (d) of the location marked with dashed green lines in (c) a certain molecular periodicity can be distinguished. We notice that rather than molecular periodicity from the distance between rows (~ 3 nm) seems that this periodicity could be associated with the dimension of the β-phase unit cell or simply could be directly related to the lateral resolution we have in this image. In any case, it is a clear indication of the good condition of the tip for conductive experiments.

Although the topographical and frictional differences in the α-phase soliton structures are not as clear as the one presented in figure 4.4.22, the contrast in the current signal over the top and bottom sides of the solitons is clear in figure 4.4.22 (c) and the direct correlation between higher topography

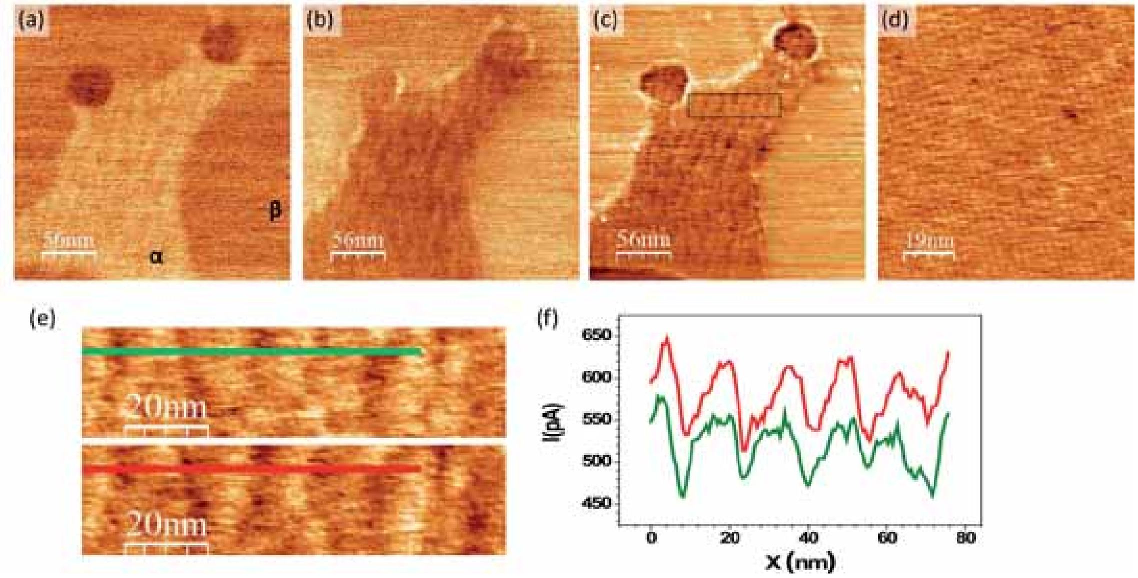

Figure 4.4.22: *Simultaneously measured contact mode topography (a), friction (b) and current (c) images of BP4 on Au(111). (d) shows a magnification of the current image of the location marked by dashed green lines in (c). Magnification current forward and backward images of the location marked by dashed black lines in (c) is presented in (e), with the corresponding line profiles in (f).*

and higher current response can be established. In figure 4.4.22 (e) the current response signal of the location marked by dashed black line in (c) corresponding to the forward (top) and backward (bottom) scan directions are presented (here we notice that both a and c images correspond to the forward scan direction). The similarity of both current signals for opposite scan directions is an additional evidence of the real nature of the measured conductive difference. From the current profiles depicted in (f) we quantify the difference in conductivity to be ~ 1.12 times higher in the high topography locations. The higher conductivity measured in backward scan direction is not surprising, since as commented above, a current response dependence with the scan direction was also found in the case of figure 4.4.20. we used the same tip for the two experiments. The fact that the higher topography locations present a higher conductivity is surprising.

In addition, high resolution stick-slip molecular periodicity experiments were performed with an applied tip bias of $300mV$. Figure 4.4.23 (a) and (b) present the simultaneously recorded lateral force and current signals over the α-phase, whereas (c) and (d) shows the ones corresponding to the β-phase. Even though in the current signal (b) a high conductive contrast is dominant, probably related to the soliton variation in height, a certain periodicity pattern is also distinguished. Interestingly, the same molecular periodicity of the one measured by the common stick-slip behavior

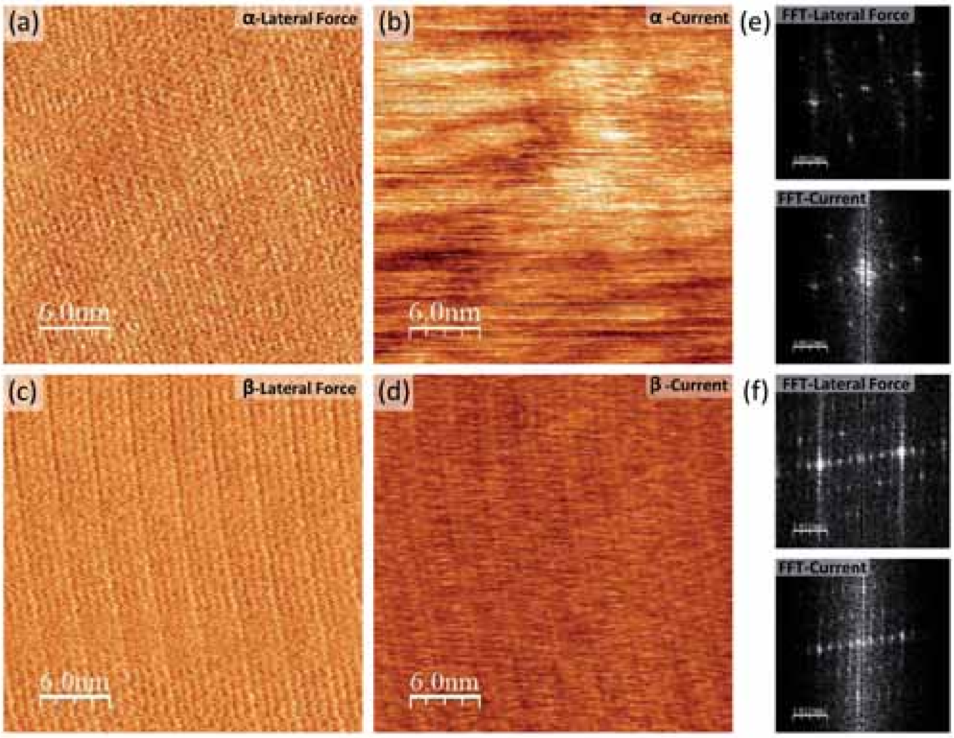

Figure 4.4.23: *Simultaneously measured high resolution lateral force (left column) and current (central column) images of* α *and* β*-phases are presented in top and bottom lines respectively .(e) and (f) show the FFT signals of the lateral force and current images of the* α *and* β*-phases of (a-d).*

in the lateral force signal is reproduced also in the current signal. This is confirmed by the FFT analysis presented (e) where the FFT signals of the lateral force and current are presented on top and bottom respectively. The correlation of the lateral force and current signals is even more clear is the case of the β-phase (bottom line of figure 4.4.23). Because the conductive area of the tip in contact with the SAM is much larger than the area that a molecule occupies, the contrast measured in the current signals can not be related to the conductivity through a single BP4 molecule. We hypothesize that the molecular periodicity signal recorded in the current image is consequence of the stick slip non constant motion of the tip. As explained in section 3.2.5.1, in this kind of experiments the tip moves over a potential, convolution of the surface periodic potential and tips potential, that presents a series of local minima. When the tip is pushed laterally, it will remain at that minimum (“sticking”), until the restoring force of the cantilever is enough to overcome the energy barrier and effectively “un-stick” the cantilever, causing the tip to jump or slip to the nearest local equilibrium position, where it is locked again. In consequence, the motion of the tip is not constant neither the efficiency of the tip-sample contact. On the one hand, when the tip holds in those local minima the tip-sample contact is suppose to be better than in process of un-stick. And on the other hand, the jumps from minima to minima are non stable situations of the tip motion and in consequence one could think that shorter integer times would be associated to those positions, that is, lower currents.

In addition to the current maps, local conductive response of the $BP4$ layer was measured by mean of performing current versus voltage characteristic (so called $I-V$ curves) on top of each polymorphic phase. For that purpose we make use of the 3D mode strategy in the electric transport approach (see section 3.2.5.4). In such a way, we are able to establish the comparison between conductivity measured not only for the same applied force but also for the same piezo displacement for both SAMs. The transport measurements were performed over a single point on the surface, avoiding gold grain boundaries and defects within the monolayer. By combining the information extracted from the simultaneously acquired $F_n(V,z)$ and $I(V,z)$ images, the I–V characteristics at different applied loads and different piezo displacements can be obtained; while separating and controlling the mechanical response of the organic layer.

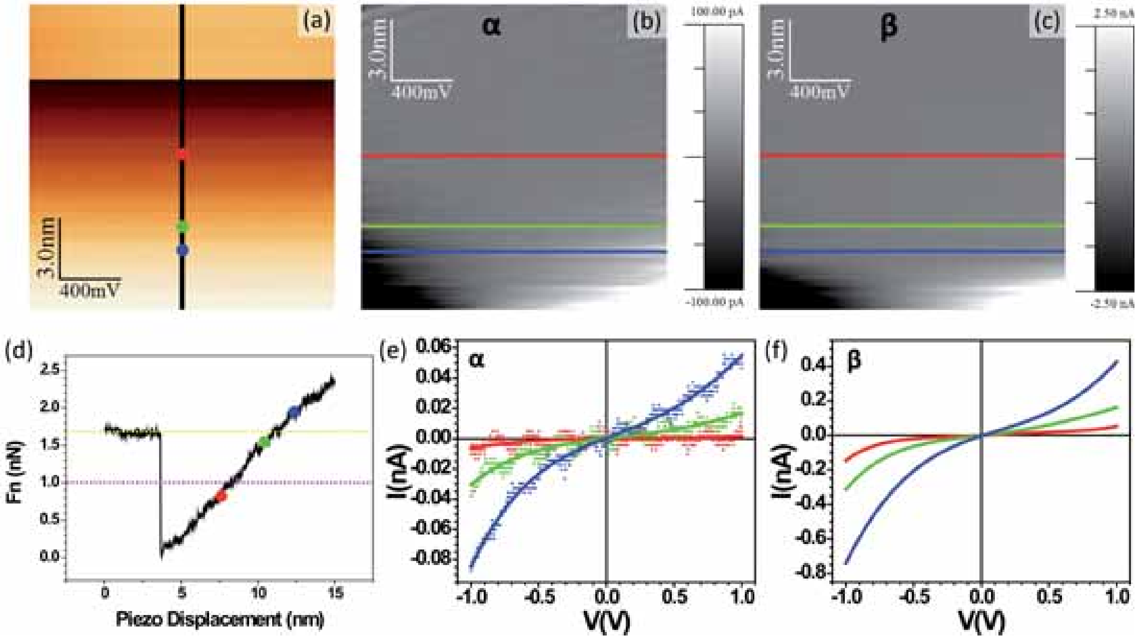

Figure 4.4.24: *Normal force image (a), $F_n(V,z)$, acquired in 3D CSFM operation mode on top of the α-phase. The voltage range is $\pm 1V$, and the total piezo displacement is $15\,nm$. Current images, I(V,z), acquired on the α and β-phase layers. (d) shows the FZ curve corresponding to the black line in (a), that is $F_n(0,z)$. The $F_n(0,z)$ corresponding to the β-phase presents the same slope and slight variation on the adhesion force ($\sim 1\,nN$). (e) and (f) show some selected horizontal line profiles extracted from images in (b) and (c) at different applied loads.*

The simultaneous measurements of the normal force $F_n(V,z)$ and the current $I(V,z)$ performed by mean of the 3D mode strategy for both polymorphic phases are presented in figure 4.4.24. The normal force image measured on the α-phase is shown in (a). The different regions of the tip-sample approach can be identified in the FZ curve depicted in figure 4.4.24 (d) corresponding to $F_n(0,z)$, the vertical profile in (a). For simplicity only the normal force image measured on the α-phase is shown, the FZ curve corresponding to the β-phase present the same $F_n\ vs\ z$ slope and a small variation of $\sim 0.1\,nN$ in the adhesion force. As is seen in (d), initially ($z = 0$) the tip is not in contact, the cantilever deflection is almost constant for a few nm travel and at around $z \approx 3.5\,nm$ the tip jumps to contact. F_n increases with z along the attractive regime (see section 3.2.3.1) and changes to repulsive regime around $z \approx 11\,nm$.

The grayscale is used to depict the current $I(V,z)$ as a function of both the applied voltage (fast scan or horizontal axis), which is varied between $\pm 1\,V$, and the total piezo movement (slow scan or vertical axis), which corresponds to a 15 nm travel. The $I(V,z)$ images corresponding to the α and β-phases are shown in (b) and (c) respectively. Horizontal profiles performed in the $I(V,z)$ image are $I-V$ characteristics corresponding to each piezo displacement value, which combined with the $F_n(V,z)$ image, allows us to extract the value of the applied load at which each $I-V$ curve was measured. Straightforward comparison between $I-V$ curves at different applied loads for the α and β polymorphic phases is therefore possible. Because the current measured for the α-phase are close to our resolution limit (we have a level of noise of $10\,pA$) the original data (presented by points) was fitted by a fifth degree polynomial (presented by solid lines). Both, the original data and polynomial fits are superimposed in figure 4.4.24 (e), and shows how the fits nicely reproduce the conductive behavior of the original data. The reason for performing such a fit is twofold: on the one hand it allows a better visual comparison with the $I-V$ characteristics of the β-phase and on the other hand and more importantly, enables an easier analysis of the data that is presented below.

In figure 4.4.24 (e) and (f) the $I-V$ curves of α and β-phases corresponding to the applied loads marked in the FZ curve of (d) are presented (notice the color code). The $I-V$ curves show a sigmoidal shape over the $\pm 1V$ range, with a linear response in the low bias region. This is in good agreement with the tunneling mechanism modeled by Simmons. However, we notice that Simmons model is symmetric model. However, in the present case a noticeable asymmetry in the $I-V$ curves with respect to the voltage sign is observed for both polymorphic phases. In fact, more current is consistently measured when the tip is biased negatively relative to the substrate. This asymmetry in the $I-V$ characteristics could be associated to different factor: on the one hand the coupling is different at the two metal-molecule interfaces: one end of the molecule is bonded to the Au substrate whereas the other end is physically in contact with the tip [241]. In addition, the asymmetric chemical structure of the BP4 molecule, with the alkyl chain and biphenyl moiety could also play a role, since the efficiency of electron injection is not going to be the same in the two of them. For comparison of the current asymmetry for each polymorphic phase we use the rectification ratio (RR) concept. RR is a figure of merit, defined as the current ratio between positive bias and the absolute value of the current at negative values [242]. Defining it by $RR = \frac{|I(-V)|}{I(V)}$ and calculating RR over a confident range of $0.8-1V$, we have that $RR_\alpha \approx 1.6$ whereas $RR_\beta \approx 1.9$. That is, the conductive characteristic on the $\beta-$phase is more asymmetric than in the α-phase.

After the jump into contact point, the central bottom region of the $I(V, z)$ images for both molecular phases narrows, leading a triangular shape typical of monotonous pseudogap reduction. The observed behavior can be more clearly observed and even quantified in the selected representative I–V profiles presented in figure 4.4.24 (e) and (f) (notice the color code of the horizontal profiles in (b) and (c)). But, which are the reasons for the current increase as the load is increased? Some plausible effects of the applied load are, for instance: (1) increase in the junction contact area which in turns affect the number of molecules contributing to the current signal; (2) compression of the film either due to molecular tilting or elastic deformation; (3) changes in electronic properties as a result of film deformation. We have tried to discern among these possible effects by analyzing the behavior of the junction resistance as a function of the applied force.

At low bias, equation 4.4.12 can be used to determine the resistance (R_c) of the junction, defined as the inverse defined as the inverse slope of the low voltage linear region ($\pm 0.2\ V$ in this particular case) around $V = 0V$, that is, $R = {}^{V}\!/_{I}$. We calculate R_c all over the tip-sample approach for α and $\beta-$phases and correlate each $R_c(z)$ to its corresponding $F_n(0, z)$. The results are plotted in semi logarithmic and logarithmic scales in figure 4.4.25 (a) and (b).

For low F_n values ranging from 0 to $\sim 0.3nN$ it can deduced that the tip-sample electric contact is not yet well established and the R_c values present some dispersion. From $F_n \sim 0.3nN$

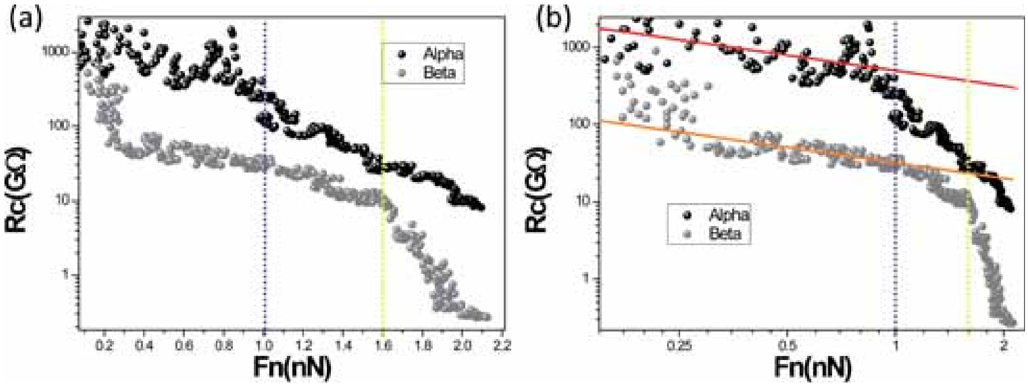

Figure 4.4.25: *Calculated contact resistance values on function of the normal force in semi logarithmic (a) and logarithmic scales (b) for the α and β-phases are shown in black and gray respectively.*

on, a nearly linear decrease of R_c with F_n is found in the log-log plot of figure 4.4.25 (b). If the reduction in the junction resistance values were mainly due to an increase in the contact area, R_c would be expected to scale as $F_n^{-2/3}$, because the relation between contact area and applied load is $\Lambda \propto F_n^{2/3}$ (equation 3.2.7) and the resistance is inversely proportional to the contact area. In order to test if we have a contact area dependent R_c scaling we fit our data with the $R_i \propto F_n^{-2/3}$ relation in figure 4.4.25 (b). That is, in a log-log plot we fit the data with a linear equation of the form: $log\left(R_i\right) = -\frac{2}{3}log\left(F_n\right) + \Gamma_i$, for $i = \alpha, \beta$ where Γ_i are a constants. The corresponding fits are presented in (b) in red and orange and show that the resistance scales with the contact area ups to a normal force value of around $F_n \approx 1\,nN$ for the α-phase (denoted by a dashed purple line). For the β-phase this behavior seems to extend ups to $F_n \approx 1.6\,nN$ (denoted by a dashed yellow line), the zero deflection point as can be seen in the FZ curve of figure 4.4.24 (d). The deviation of this behavior indicates that the resistance depends not only on the contact area but other factors such as film deformation or indentation. Is surprising that the deviation from a $R_c \propto F_n^{-2/3}$ for the α-phase occurs before the zero deflection point ($F_n \approx 1.6\,nN$). The reason for that could be related to the presence of the solitons in the α-phase whereas the β-phase presents a much more homogeneous film surface.

In this work our goal was not the investigation of the conductivity while deforming or indenting the SAMs of both phases, but to make a comparative study of the conductive behavior of both polymorphic phases. In order to do that, we focus our attention in the $I-V$ curves of the α and β-phases corresponding to F_n values close to the zero deflection point (yellow dashed lines in figures 4.4.25 and 4.4.24 d). In figure 4.4.26 the direct comparison of averaged $I-V$ characteristics over the zero deflection region of both polymorphic phases in linear (a) and semi logarithmic (b) scales are presented. The $I-V$ characteristics have been calculated averaging ~ 10 curves over the zero deflection region (marked by dashed lines in figure 4.4.24 (d)).

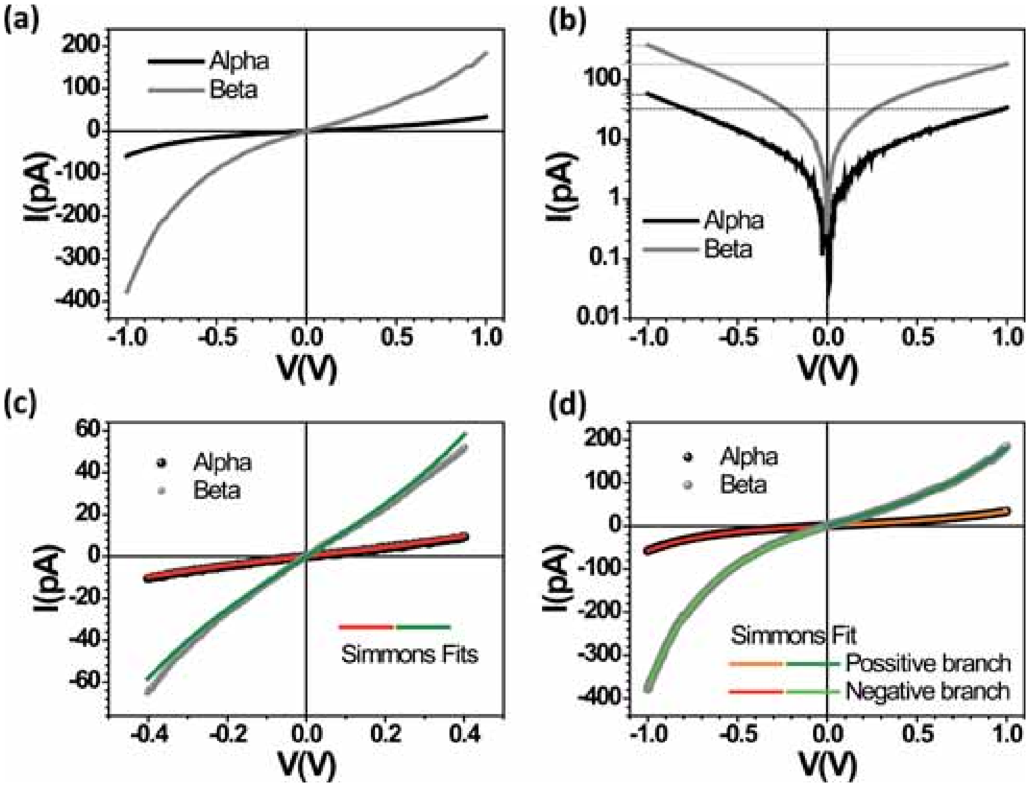

Figure 4.4.26: *Comparison of the* α *and* $\beta-$*phases* $I-V$ *characteristics corresponding to zero deflection point (green point in figure 4.4.24) are presented in linear (a) and semi logarithmic scales (b). The* $I-V$ *characteristics fits using the Simmons model for low voltage* ($\pm 0.4\,V$) *and complete range are shown in (c) and (d).*

We have compared these curves to what is expected for a simple tunnelling process using the simple Simmons model. Therefore, by fitting individual $I-V$ curves using equation 4.4.11, ϕ_B and λ values can be determined and the κ can be calculated from equation 4.4.13. This κ parameter is a structure-dependent factor that has emerged as a characteristic parameter of the junction and can be used to classify the ability of molecular structures to provide a medium that facilitates tunneling form one electrode to the other.

For estimating the tip-sample contact area (Λ) we use both JKR and DMT models (see section 3.2.4.1) and compare the results obtained by both of them. We use a nominal tip radius of $\approx 25nm$ (provided by the manufacturer), the experimental adhesion value of $1.5\,nN$ (calculated from the FZ curve of figure 4.4.24), for Pt Young modulus $E_{Pt} = 140GPa$ and Poisson ratio $\nu_{Pt} = 0.38$

[243], SAM Young modulus $E_{SAM} = 9GPa$ and $\nu_{SAM} = 0.33$ we found the contact area to be in a confident limit of $10 - 30\,nm^2$. For the SAM layer thicknesses, we make use of the value obtained by spectroscopic studies (ellipsometry and XPS)[153, 154] for the α-phase ($d_\alpha = 1.65\,nm$), and we derive d_β from the height difference measured by SFM ($\Delta d_{\alpha-\beta} \approx 1.2$Å, see section 4.4.1), i.e., $d_\beta = 1.53\,nm$ for the β-phase.

Because in the present case the $I-V$ curves are not symmetric the Simmon models fails for fits in the total $\pm 1\,V$. To solve this problem we used to different strategies: i) fit the curves in a lower voltage range and ii) to fit the positive and negative branches independently. In figure 4.4.26 (c) he $I-V$ characteristics fits using the Simmons model for low voltage ($\pm 0.4\,V$) are presented. The model reasonably reproduces the conductive characteristic of the α-phase, but fails in the case of β-phase. In the contrary, the Simmons model perfectly models the characteristic of the conductive response of both phases when is performed independently in each positive and negative branches (see figure 4.4.26 c). Two different red and green tones are used to differentiate the fits of each branch.

	Fit : Low voltage ($\pm 400mV$)	Fit: Negative branch	Fit : Positive branch
$\alpha - phase$	$\Phi_B = 1.55eV$ $\lambda = 0.77$ $\kappa = 0.982\text{Å}^{-1}$.	$\Phi_B = 1.54 \pm 0.04eV$ $\lambda = 0.77$ $\kappa = 0.979\text{Å}^{-1}$	$\Phi_B = 2.30eV$ $\lambda = 0.63$ $\kappa = 0.978\text{Å}^{-1}$
$\beta - phase$	$\Phi_B = 1.27eV$ $\lambda = 0.82$ $\kappa = 0.948\text{Å}^{-1}$.	$\Phi_B = 1.32eV$ $\lambda = 0.80$ $\kappa = 0.940\text{Å}^{-1}$	$\Phi_B = 2.15eV$ $\lambda = 0.63$ $\kappa = 0.947\text{Å}^{-1}$

Table 4.3: *The barrier heights Φ_B and λ constant values obtained from the Simmons model fits presented in figure 4.4.26 and the calculated tunneling decay constant κ are resumed.*

The results of the different fits are summarized in table4.3. We found that the barrier heights Φ_B and λ valued differ for the positive and negative branch fits in both polymorphic phases, but do not vary much in between polymorphic phases for the same fit approach. Interestingly, however we note that the κ parameters (calculated using equation 4.4.13) for both polymorphic phases calculated from the three different fits present nearly the same value, $\kappa \approx 0.98\text{Å}^{-1}$and $\kappa \approx 0.95\text{Å}^{-1}$. This κ values are in agreement with the result reported by Su et al. [170] , who by using spectroscopic STM measurements obtained a value of $\kappa_{BP4} = 0.97 \pm 0.7\text{Å}^{-1}$. In their experiments however, they do not find differences between the $I-V$ characteristics on top of both α and β-phases. The present result point that the barrier width (d) parameter, that is the molecular layer thickness would be the key parameter factor for the different measured conductance between the two polymorphic phases.

4.4.5 Understanding the apparent discrepancy between STM and SFM “topography” signals

It is important to note the difference between the SFM and STM measurements for characterizing non-homogeneous organic samples. In STM, current, not force, is used to control the z tip position and in consequence to build the so-called “topography” signal. Because the conducting properties of the molecules under study are generally unknown, the position of the probe with respect to the molecules might be uncertain. If the STM tip is not in contact with the monolayer, the junction transport properties are determined by the molecules and the vacuum (or air) gap between the molecules and the tip. CSFM does not have this difficulty because the tip- sample distance is controlled by the feedback in normal force, which allows accurate positioning the probe to be just in contact with the monolayer.

In previous section 4.4.1 we measured the height difference between the α and $\beta-$phases to be $d_{\alpha-\beta}$ = 1.2±0.2 $\AA$. This difference in height measured by SFM points to a larger difference in film thickness of the $h_{\alpha-\beta}$ = 0.8±0.2 $\AA$ obtained by cc-STM . Statistical analysis performed using different samples reveals that this difference is not due to experimental deviation but physical reasons must be resorted. In fact, it is known that the electron tunneling in STM reflects the density of states near the Fermi energy of the surface. Thus, differences in height (tip-sample distance) measured by cc-STM are influenced by the local conductive behavior and in consequence is usually denoted as “apparent height”. In other words, understanding the discrepancy between cc-STM and SFM topographic data requires decoupling electronic and topographic contributions and was one of the motivation for measuring CSFM. In the following we try to conciliate the topographic results obtained STM and SFM ($h_{\alpha-\beta}$ *vs* $d_{\alpha-\beta}$) by mean of the conductive measurement results presented in the previous section 4.4.4.

Previous works faced this problem in terms of the transconductance trough individual molecules within a two-layer (vacuum gap and film) tunnel junction model for cc-STM [244, 245]. Thus, we model our STM measurements using a two layer tunnel junction model for non resonant electron tunneling. The two layer model is schematically illustrated in figure 4.4.27. The assumption of

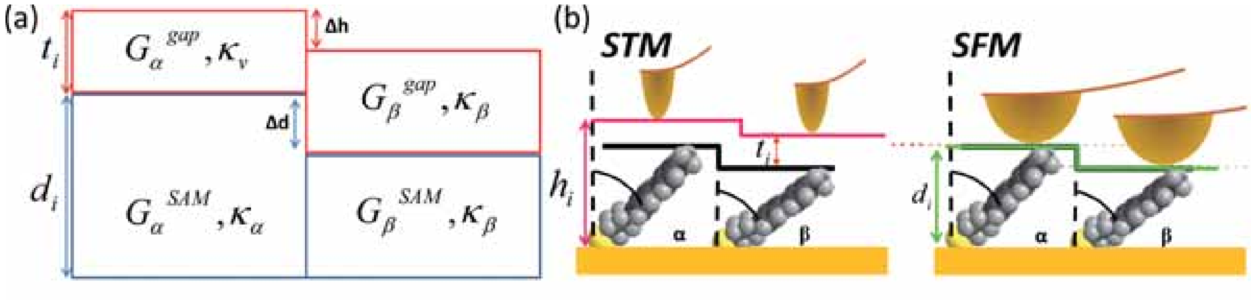

Figure 4.4.27: *Schematic representation of the two layer tunnel junction model. The tip-sample gap* (t_i) *and molecular layer* (d_i) *thicknesses are represented in red and blue in (a)* ($i = \alpha, \beta$).

a nonresonant mechanism is supported by the generally accepted values of the energy differences between the HOMO and the LUMO orbitals, which are around $5\,eV$ for the phenyl ring and $7\,eV$ for the aliphatic alkyl chain [170, 246]. We define the barrier width of the molecular layer (the one measured by SFM) by d; the barrier height in STM, i.e. the distance between tip and underlying gold substrate (the electrode), as h; and the gap distance between molecular layer and the STM tip as t. That is, we have that $h_i = d_i + t_i$ for $i = \alpha,\ \beta$. In consequence, the apparent height measured by STM can be expressed as:

$$\Delta h_{\alpha-\beta} = (d_\alpha + t_\alpha) - (d_\beta + t_\beta) = \Delta d_{\alpha-\beta} + \Delta t \tag{4.4.14}$$

where

$$\Delta d_{\alpha-\beta} = d_\alpha - d_\beta \quad and \quad \Delta t_{\alpha-\beta} = t_\alpha - t_\beta$$

The electron tunneling between the STM tip and the conductive substrate in the two layer model can be described by the composition of the molecular layer and tip-sample gap conductances as [7]:

$$G = G^{gap} G^{SAM}$$

and the conductance for each layer is described by:

$$G^i_j = C^i_j e^{-k^i_j z} \; for\; i = gap, SAM;\; j = \alpha, \beta$$

---

[7] The electron conductance is defined as the inverse of resistance, i.e., $G = R^{-1}$

where κ is the tunneling decay constant[8], z is the layer thickness and C_j^i is the contact conductance, i.e., C_i^g and C_i^s are the contact conductances of the tip-air and air-molecule respectively. In consequence the STM conductances for each polymorphic BP4 phase can be written as:

$$G_\alpha = G_\alpha^{gap} G_\alpha^{SAM} = C_\alpha^g e^{-\kappa^g t_\alpha} C_\alpha^s e^{-\kappa_\alpha d_\alpha} \tag{4.4.15}$$

$$G_\beta = G_\beta^{gap} G_\beta^{SAM} = C_\beta^g e^{-\kappa^g t_\beta} C_\beta^s e^{-\kappa_\beta d_\beta} \tag{4.4.16}$$

In a cc-STM measurement we have that the conductivity is maintained over all the scanned area, i.e. $G_\alpha = G_\beta$, in consequence:

$$G_\alpha^{gap} G_\alpha^{SAM} = G_\beta^{gap} G_\beta^{SAM} \tag{4.4.17}$$

By combining equations 4.4.15, 4.4.16 and 4.4.17 and making the reasonably assumption that the tip-air and air-layer contact conductances are the same for the two polymorphic phases ($C_\alpha^i = C_\beta^i \ for \ i = g, s$), we obtain that the molecular layer-tip gap distance difference ($\Delta t_{\alpha-\beta}$) can be rewritten as:

$$\Delta t_{\alpha-\beta} = -\frac{1}{\kappa^g} \left[\kappa_\alpha d_\alpha - \kappa_\beta d_\beta\right] \tag{4.4.18}$$

For the molecular layer thickness we make use α-phase layer thickness of $d_\alpha = 1.65nm$ measured by spectroscopic studies (ellipsometry and XPS)[153, 154] , and $d_\beta = 1.53\ nm$ for the β-phase (derived by the height difference measured by SFM, section 4.4.1$\Delta d_{\alpha-\beta} \approx 1.2$Å). For the vacuum decay factor we use the value of 2.2Å^{-1} from the literature [247]. If we use the $\kappa_i\,(i = \alpha, \beta)$ values determined by the CSFM measurements (in section 4.4.4), $\kappa_\alpha \approx 0.98\text{Å}^{-1}$ and $\kappa_\beta \approx 0.95\text{Å}^{-1}$, we obtain a value of $\Delta t \approx -0.7$Å. And if we approximate $\kappa_\alpha \approx \kappa_\beta \Rightarrow \kappa_{BP4} \approx 0.97\text{Å}^{-1}$ an averaged value of our two values that coincidences with the value reported by Su et al. for both polymorphic phases [170], then we have that $\Delta t_{\alpha-\beta} = -\frac{\kappa_{BP4}}{\kappa^g} \Delta d_{\alpha-\beta}$, and we obtain that $\Delta t \approx -0.5$Å. This results conciliate the two different "heights" $\Delta d_{\alpha-\beta} = 1.2 \pm 0.2\mathring{A}$ and $\Delta h_{\alpha-\beta} = 0.8 \pm 0.2\mathring{A}$ measured by SFM and STM ($\Delta h_{\alpha-\beta} = \Delta d_{\alpha-\beta} + \Delta t$).

---

[8] The tunneling decay coefficient is usually denoted by β, here however in order to avoid any confusion with the $BP4$ β-phase we denote it by κ.

This result concludes that the apparent height measured by STM strongly depends on the molecular conductance of each molecular phase. Using a two-barrier tunnel junction model, we are able to explain the differences between the measured topography in cc-STM and the true physical thickness of the organic layer.

4.5 Summary

Throughout this chapter we have characterized and investigated the surface properties of the BP4 SAM consisting of two polymorphic phases coexisting on $Au(111)$ surface. Thanks to the in situ reference that the coexistence of the two polymorphic phases offer, the investigation of the impact of the supramolecular order of the SAM into the morphological, tribological, electrostatic and conductive properties of the surface have been possible by scanning force microscopy and scanning tunneling microscopy. We have shown how the supramolecular order of the SAM is a decisive factor influencing such nanoscale properties.

We have gained knowledge on the morphological and structural differences of the phases and also on the soliton structures present in the α polymorphic phase. By mean of friction force microscopy (FFM) we found that the friction response varies for the two polymorphic phases. In addition, we show how molecular domains with different orientation can be distinguished by mean of friction anisotropy and asymmetry effects. Therefore making use of high sensitivity lateral force imaging we are able to reveal structural details of BP4 SAMs well beyond the topographical information provided by STM. We also reveal tribological differences over the α-phase solitons structures.

Furthermore, we have proven that the supramolecular order influences the electrostatic properties of Au(111) surface, that is, in the work function shift induced by molecular layer on the $Au(111)$ surface. The supramolecular order change modifies the work function shift of the gold in nearly a 14% from α to the β-phase. In addition, we study the relative contribution of the molecular density, molecular dipole and layer permittivity factors into the work function change measured between polymorphic phases and we have derived the difference on the dielectric constant and polarizability of the molecules in each phase.

We also characterized the conductive response of each polymorphic phase by mean of conducting SFM (CSFM). A clear difference between the conductive response of the molecular phases is found and is mainly attributed to the difference in thickness between molecular layers. In addition, based on electron current measurements, the combined use of STM and CSFM allows us interpreting the differences in apparent height as measured by one or the other technique in non-homogeneous organic layers and thus, decoupling the electronic and topographic contribution in the STM signal.

Chapter 5

Surface properties of chemically nanostructured $SrTiO_3$: self-organization and selective functionalization

5.1 Motivation

Hybrid materials based on oxide supported organic films are the subject of increasing interest because of the many practical applications they may find in nanotechnology. The control of growth and properties of these hybrid structures, on a length scale down to nanometric dimensions, is one of the major challenges in the field and surface science strategies based on the use of nanostructured substrate surfaces can be employed to initiate and control the growth in a bottom-up fashion.

For various reasons TiO_2 has been the archetypal material to be used either as substrate or as active element in uses as catalysis and electricity conversion. For instance, this oxide is used in photoactive and photochemical applications, as photovoltaics and photocatalysis [248], and the role of defects (vacancies, surface steps and so on) produced by reduction of crystal miss-cut has been exploited in the enhancement of TiO_2 surface reactivity [249]. On the other hand, the possible applicability of other titanium-based oxides, such as strontium titanate ($SrTiO_3$, STO), has been proposed in photo-catalysis [250] or to be used as optical anode materials for organic photoelectronic devices [251]. To resolve the STO optical transmittance being lower than that of the commonly used indium tin oxide (ITO), the use of thin films was proposed. It is known that high quality thin films need of extremely flat (atomically flat) substrates. However, though having substrates with extremely flat surfaces is already possible, the range of work functions needed for anode materials in typical organic light emitting diodes (OLEDs) seems unattainable with STO that becomes intensely colored after doping [252]. New approaches such as surface modification by organic molecular functionalization are promisingly envisaged. Organic self-assembled monolayers (SAMs) are of particular relevance in a wide variety of fields to improve or modify the characteristics of the materials surfaces. They are, for instance, employed in relatively conventional electromechanical devices as lubricating layers [7], or used to induce specific interface dipoles upon adsorption (as has been already seen in chapter 4), which tune the surface work function in optoelectronic systems [194, 201]. Thus both, the nanotribological properties of the organic films themselves and the surface contact potential modifications they induce on the substrates, are decisive and deserve in depth investigation.

The role of chemical surface termination of $STO(001)$, TiO_2 or SrO, has been observed down to the atomistic level [253–255] and because titanium dioxide (TiO_2) terminated surfaces are preferred in many applications, obtaining nanostructured surfaces having tailored TiO_2 termination is of enormous interest for further developments. Moreover, besides the appealing properties of the TiO_2 substrates and those of the materials growing on that surface, the capability of confining these properties at the nanoscale in a controlled way, although challenging, is of major technological interest in a variety of fields. Bachelet and co-workers [19] have recently obtained a reproducible procedure to obtain the simultaneous and separated presence of TiO_2 and SrO terminations on the $STO(001)$ surface. Furthermore, they have shown that this nanopatterned oxide surfaces can be employed as template for the selective growth of functional oxides, as $SrRuO_3$ [19], thanks to the different nucleation that the $SrRuO_3$ presents on TiO_2 and SrO surfaces.

In this chapter we explore the use of the nanopatterned STO (001) surface as template for the growth of organic SAMs. We find that carboxylic functionalized SAMs are selectively grown in the TiO_2 surface, what allows us to investigate SAMs adsorption influence into the mechanical and electrostatic properties of the oxide surface. We start addressing the main characteristics of the nanopatterned STO (001) surface and we devote the rest of the chapter to describe the selective adsorption of SAMs on the TiO_2 surface and discuss how this influences the local mechanical and electrostatic properties of the surface. The thermal treatment of the as-received substrates was done by Dr. Romain Bachelet and Dr. Florencio Sánchez from the group of Prof. Josep Fontcuberta (from the ICMAB). Prof. David B. Amabilino (from ICMAB) was involved in the selection of molecules chosen as candidates for their adsorption on the STO surface, and in the different deposition conditions that were tested.

5.2 Nanopatterned $SrTiO_3$ (001) surface

$SrTiO_3$(STO) is a cubic perovskite with a parameter $a_{STO} = 3.905$Å (see figure 5.2.1 a). Along the $\langle 001 \rangle$ directions alternating neutral TiO_2 and SrO layers spaced out half of one unit cell ($u.c.$) are staked as schematically shown in figure 5.2.1 (b). In consequence, the STO(001) single-crystal surfaces have two possible chemical terminations, TiO_2 or SrO. The inevitable misorientation in the cutting process of the single crystal through the rational crystallographic plane (001), gives rise to a step terrace morphology. Atoms reorganize into low energy surfaces planes creating a periodic pattern of terraces separated by one $u.c.$ in the surface. The width of the terraces is inversely related to the substrate miscut-angle, that is, the misorientation angle between the cutting and (001) plane. The smaller the miscut-angle the wider the terraces. For the present work commercially available STO single crystals from CrysTec [256] with miscut angles lower than $\sim 0.2°$ have been used, which result in hundreds of nanometers wide terraces. For dynamic mode SFM (dm-SFM) silicon tips mounted in rectangular cantilevers with force constant $k \approx 2.8\ N/m$ (Nanosensors) have been used. While for contact mode SFM (cm-SFM) measurements both silicon and Si_3N_4 tips mounted in rectangular cantilever ($k \approx 2.8\,N/m$, Nanosensors) and triangular ones ($k \approx 0.1 - 0.5\ N/m$, Veeco) have been used. All the measurements presented in this chapter have been performed under N_2 environment (with a relative humidity $RH < 5\%$) to diminish any possible humidity effect and keep the very same conditions from one measurement to another. cm-SFM measurements have been always performed at the lowest possible applied load close to the pull-off force, i.e. in the attractive regime, to maintain the very same load conditions for different samples, making possible the comparison of the friction force microscopy (FFM) results and preventing any sample damage or deformation in the case of STO surfaces functionalized by SAMs.

It is well known that the two TiO_2 and SrO termination coexist on as-received substrates. In

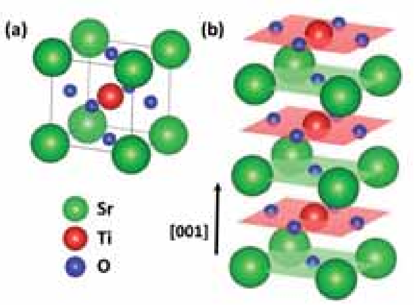

Figure 5.2.1: *Schematic crystal structure of the perovskite unit cell for $SrTiO_3$ is shown in (a). Along the ⟨001⟩ directions, alternating TiO_2 and SrO layers spaced out half of one unit cell are staked as highlighted in (b). Figures plotted using Vesta program [257].*

the dm-SFM topographic image of the as-received substrate in figure 5.2.2 (a), distinguishable steps and terraces having very irregular step-edges can be observed. In the corresponding height profile in 5.2.2 (b) the existence of one unit-cell ($u.c. \sim 3.9$Å) steps to which a fluctuating signal of amplitude larger than the level of noise is superimposed. This likely reflects the coexistence of random distribution of TiO_2 and SrO terminations that coexist in untreated substrates. R. Bachelet and co-workers have shown that starting from random distribution of both terminations in as-received surfaces and by appropriate thermal annealing at relatively high temperature ($1000 - 1200°C$) under oxidation conditions the nanopattern of the surface on separated and well ordered chemical terminations can be achieved [19]. Under annealing at relatively high temperatures and oxidizing conditions the Sr segregates [258–260], and the SrO self-organization can be achieved. In this case, the surface Sr diffusion results in the formation, along the substrate step-edges, of well-ordered array of half-unit-cell-deep trenches coexisting with atomically flat TiO_2 terraces in between. By tuning the annealing conditions (temperature and time), the size and distribution of SrO terminated areas can be controlled, from nanometer scale patches to highly ordered 1D-structures [19].

In the cm-SFM image shown in figure 5.2.2 (c) the effect of high-temperature annealing under air ($2h$, $1100°C$) on the surface STO (001) can be appreciated. Inspection of the topographic image reveals that high-temperature annealing leads to a great smoothing of the virgin surface with formation of smoother step-edges and flatter terraces ($rms \leq 1$Å). In addition, some darker (lower height) regions aligned along ascending step-edges appear. Indeed, the corresponding height profile (5.2.2 d) shows the existence of $1/2$ $u.c.$ deep topographic striped areas adjacent to step-

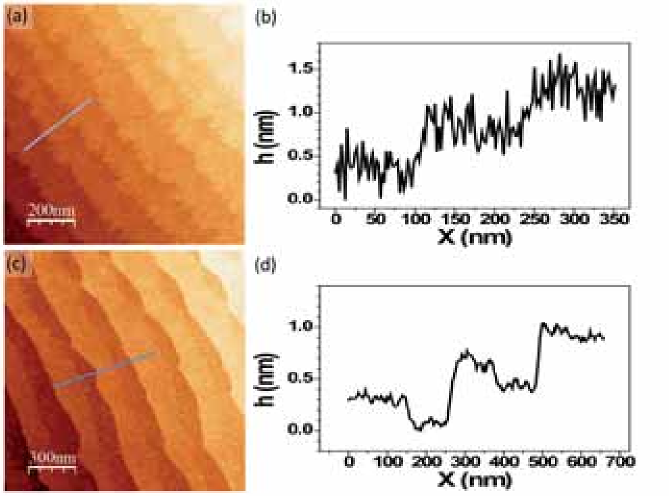

Figure 5.2.2: *dm-SFM topographic image of as-received (a) and cm-SFM image (1100 °C, 2h) of air-annealed (c) $SrTiO_3$(001) substrates are shown. In (b) and (d) the corresponding profiles from the locations marked in (a) and (b) are presented. Image (a) and corresponding profile (b) reproduced from [19].*

edges. The observed self-ordering of SrO (and consequently TiO_2) termination on $SrTiO_3$(001) surfaces implies chemical self-assembly and atomic diffusion. For this process to occur, a driving force must exist promoting SrO enrichment at step edges. Bachelet and co-workers suggest that the existing strain field at step-edges may play a role in the nucleation of the SrO termination in the step-edges, similarly to the basis of previous results indicating preferential nucleation of SrO nanocrystals on strained regions of STO surface [19, 258]. We devote the last part of this section to discuss the surface diffusion process that causes the chemical termination nanopatterning with trench and leaf shaped SrO location in the edge of the terraces, but we avoid any deep investigation of the reasons and processes that cause the other observed surface morphologies.

However, the high-temperature annealing of the STO (001) crystals does not always give rise to well self-ordered and nanopatterned surfaces. After studying the surface of several treated substrates we found that for some of the crystals, and even for different locations of the same substrate, very different surface topologies could be found. For instance, variety of terrace morphologies and step edge patterns were measured, with the presence of different shape and depth vacancy islands, different island geometries, cracks, etc. As an example of some of the different morphologies that were observed, some topographic images of different crystal or/and locations are presented in figure 5.4.1 in the end of this chapter (Appendix 5.4). We notice that some aspects in the atomic diffusion and self-assembly of those oxides surfaces under thermal treatments still remain unraveled and that they deserve further specific and directed studies. However, for the present work we focused in the most reproduced nanopatterned surfaces obtained by the high-temperature annealing, with well separated TiO_2 and SrO locations, where the SrO locations present a trench or leaf shapes at the edge of the terraces. Firstly because those are the most reproducible surface structures we obtained by the high-temperature treatment, and second, because those nanostructured surfaces offer an excellent template to investigate the functionalization of the STO(001) surface by SAMs.

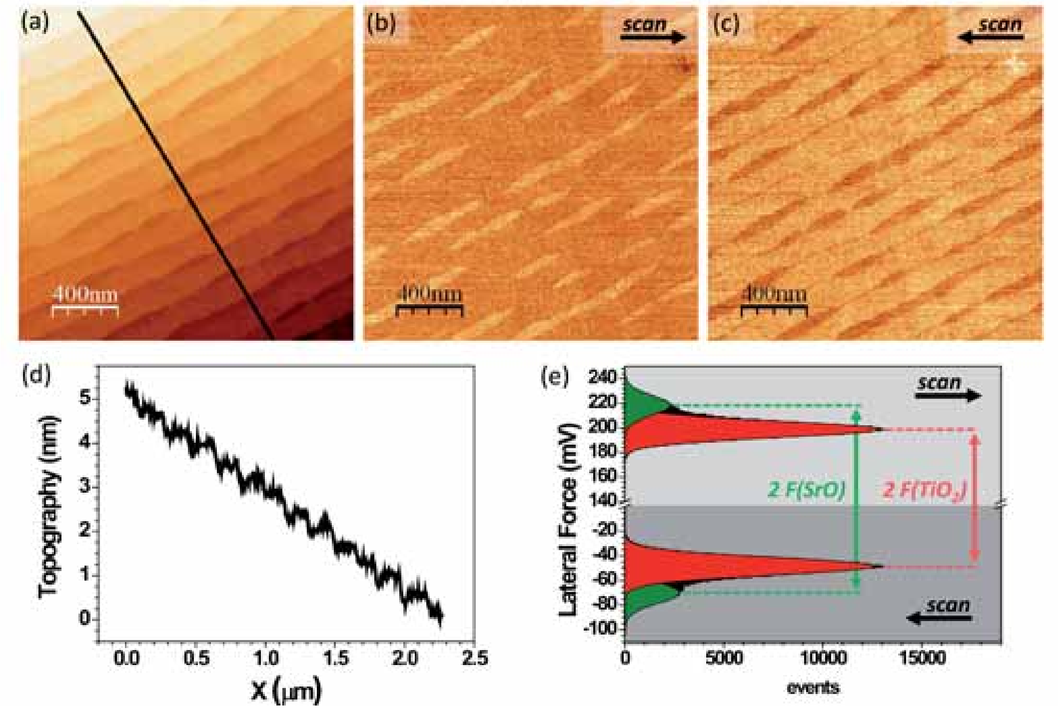

Figure 5.2.3: *Topographic (a) and lateral force forward (b) and backward (c) data simultaneously acquired on $STO(001)$ surface after $(1h, 1100°C)$ air-annealing treatment. (a) Topographic image and corresponding profile (d) . TiO_2 and SrO termination friction difference determination by lateral force forward (b) and backward (c) whole images histograms representation and corresponding peaks difference (e).*

In figure 5.2.3 a nanostructured STO (001) surface of a different crystal after a $(1h, 1100°C)$ thermal treatment is presented. In the topographic image of figure 5.2.3 (a), the lower height location that appear as trenches along step-edges are clearly visible. The lateral force (F_l) forward and backward images presented in figure 5.2.3 (b) and (c) evidence a clear friction contrast between the flat terraces and trenches, confirming their different chemical nature. In previous reported friction force microscopy (FFM) studies, the SrO termination was found to present a higher frictional response with respect to TiO_2 termination [19, 261, 262]. The higher frictional contrast of the SrO termination is attributed to the higher water affinity of this termination [262, 263].

Since the trenches present a higher frictional contrast, we assign the nature of the trenches regions as SrO terminated. It has to be mentioned Koster and co-workers [264, 265] have done the contrary assignation on the friction response of the two chemical terminations. In addition to be based in the results of Fompeyrine et al. and Iwahori et al. works [261, 262], our assignation of the high friction contrast to the SrO termination is supported by the combined SFM and XPS study of Bachelet and co-workers on STO(001) substrates presenting different ratios of the two chemical terminations[19, 266], and on the selective growth of $SrRuO_3$ on top of the TiO_2 surface which acts as a chemical probing method [19, 266].

To quantify the difference between friction responses of the two chemical terminations, instead of plotting the conventional friction loop of a certain line scan, we build a “statistical frictional loop” with the values of the whole lateral force forward and backward images, what allows us to take into account the friction differences over all the different TiO_2 and SrO terminations of the imaged area. In figure 5.2.3 (e) histograms of lateral force obtained out of the whole forward (light gray background) and backward (dark gray background) images are plotted, where the corresponding peaks referred to TiO_2 and SrO terminations appear colored in red and green respectively. The mean friction force is calculated by the half of the separation between forward and backward peaks ($F = {}^{|F_l^f - F_l^b|}/_2$, see section 3.2.5.1). By this methodology the friction is quantified to be about 17% higher at the trenches (SrO termination) than at the terraces (TiO_2 termination), that is $F(SrO)/F(TiO_2) = 1.17 \pm 0.06$. This percentage reaches higher values under higher humidity conditions, likely due to an enhanced water adsorption on the more hydrophilic SrO termination [261, 262, 267, 268].

A thorough analysis of the topographic difference between the two chemical termination and its correlation with the frictional response is done in figure 5.2.4. Instead of using conventional friction loop profile analysis, mean friction image is calculated and presented in (b). For calculating the friction image we use the procedure introduced in section 4.4.1, which consist in building the friction map by calculating the mean lateral force of the trace-retrace images. In agreement with the result presented in figure 5.2.3, the formation of nearly continuous trenches, along step-edges is well visible in the topographic image 5.2.4 a, with smooth step-edges and flat terraces separated by ${}^{1}/_{2}$ $u.c.$ deep low-lying regions. The topographic profile between trenches presented in figure 5.2.4 f (marked in black in (a)), nicely reproduce the $u.c.$ step height of ~ 3.9Å between two

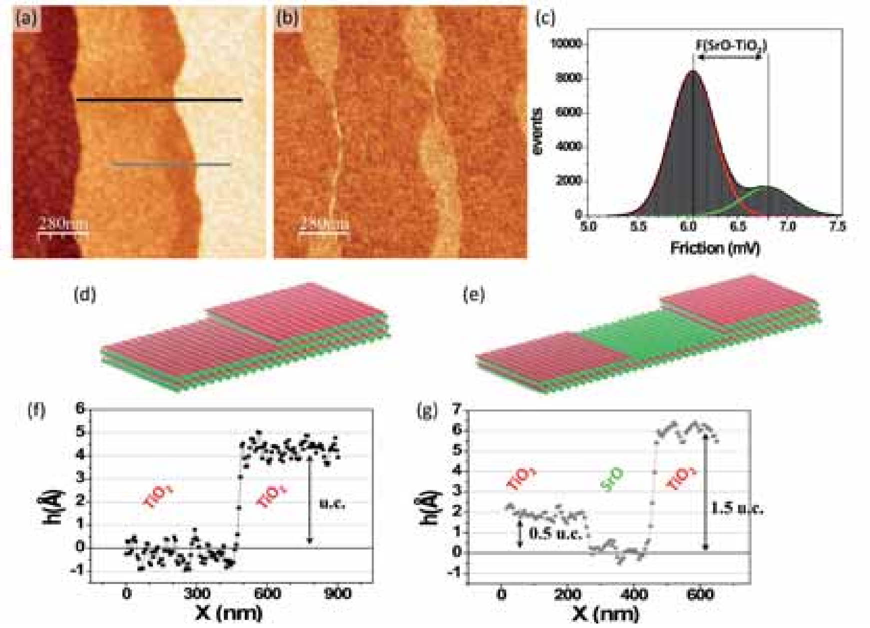

Figure 5.2.4: *Topographic and friction map of $SrTiO_3(001)$ surface after (1100 °C, 2h) air-annealing treatment. The corresponding profile (f) from the locations marked in the topographic image (a) shows the corresponding unit cell $\sim 3.9Å$ height difference between same TiO_2 termination consecutive terraces, while $1/2$ u.c. and $3/2$ u.c. height between SrO and adjacent TiO_2 terraces is clear in the profile presented in (g). The sketch of the deduced surface nanostructure has been placed correspondingly above the topographic profile (d,e). TiO_2 and SrO termination friction difference is determine by the peaks shift in the histogram representation (c) of the complete friction map (b). Figures (d) and (e) plotted using Vesta program [257].*

adjacent TiO_2 termination terraces and is directly correlated with the same frictional contrast found for both terraces (profile location marked by dashed black line in friction image (b)). The height difference between TiO_2 and SrO terminations is clearly determined from the line profile (g) that corresponds to the location marked in gray in (a). The SrO termination is $1/2\,u.c.$ and $3/2\,u.c.$ lower with respect to the two adjacent TiO_2 termination terraces and the topographic and frictional difference is established by comparison of the line profile location in (a) and (b) (solid and dashed gray line respectively). For the friction difference determination, statistical analysis of the complete friction image data is performed in the histogram plot of (c). The friction contrast is directly determined from the relative displacement of the corresponding peaks, and a 12% higher frictional response is found for SrO termination with respect to TiO_2 locations in this case $(F(SrO)/F(TiO_2) = 1.12 \pm 0.03)$, what is in agreement with the result obtained in figure 5.2.3 and in previously reported works [19].

In order to investigate the surface diffusion processes that cause chemical termination nanopatterning, a low miss-cut substrate (terrace width around 800 nm) was annealed at $\sim 1100°C$ for 30 min. Under these conditions, the chemical nanopatterning by surface diffusion is not complete and simultaneous topographic and lateral force monitoring permit a "dynamic" view of its formation process (figure 5.2.5).

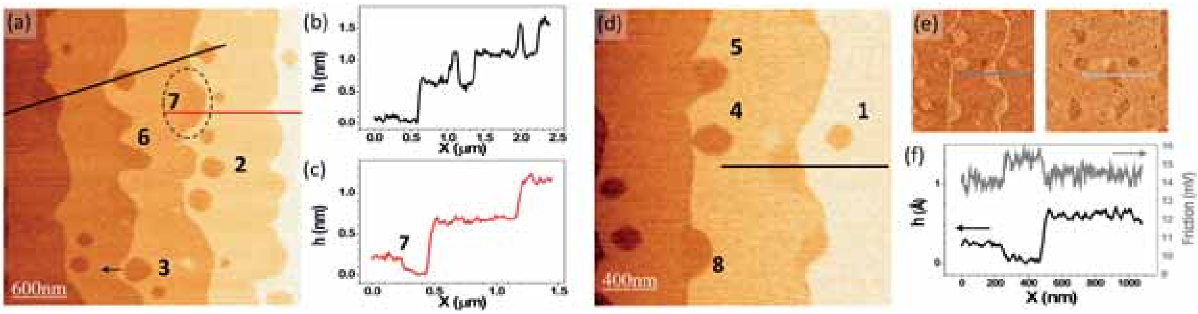

Figure 5.2.5: *Topographic and lateral force data for the incipient state of the bi-chemical termination nanostructuring of a STO substrate thermally treated at* $\sim 1100°C$ *for* 30 *min (a,d). The number labeling in (a) and (d) is used to describe the dynamics of the vacancy islands until formation of* SrO*-terminated patches at the edges of steps separating* TiO_2 *terraces (see text). Line profile panels taken in (a) cross different surface features (terraces, steps and vacancy islands), number* 7 *in the red profile serve as reference to locate one complete leaf shaped structure* $\sim 0.2\ nm$ *deep circled in (a), which is hardly seen in the topographic image due to a total vertical scale of* 3 *nm. A topographic profile as indicated in (d) is shown in black in (f) with the corresponding friction profile (in gray) calculated from the profiles in the lateral force forward and backward images ((e) left and right, respectively).*

Figure 5.2.5 (a) shows an incipient state of the self-assembly of the chemical terminations. The expected stepped surface, i.e. flat TiO_2 terraces separated by $\sim 0.4\,nm$ high steps (one $u.c.$ in height) do present other remarkable surface features such as meandering step-edges and some rounded holes in the flat terraces (figure 5.2.5 a and d). As-received STO substrates consist of terraces differing by 1 $u.c.$ in height with disordered steps and present coexistence of the two terminations (SrO and TiO_2), which differ by 0.5 $u.c$ (see figure 5.2.2). Therefore, the observed holes might originate from coalescence of much smaller ones pre-existing in the as-received substrates surface, which would not be visible because of the limited lateral resolution of SFM but inferred from a substantial surface roughness on the terraces of untreated samples [19]. As can be seen (figure 5.2.5), the holes have different diameters (from tens of nm to a few hundred nm), are located in the terraces at diverse distances from the descending step edges but, remarkably, are all 1.5 $u.c.$ ($\sim 0.6\,nm$) deep. Since SrO termination is a minority part of the (001) surface of untreated STO crystals [260], these 1.5 $u.c.$ deep holes should be vacancy islands with the appropriate depth to exhibit a SrO termination. This idea is further supported by the friction force measurements (forward and backward presented in figure 5.2.4 e) which are in agreement with previous assignment of the termination chemistry [19].

Holes of different sizes are the result of coalescence of smaller vacancy islands. Dynamics of the vacancy islands diffusion can be better appreciated by comparing the size and position of the holes. In figure 5.2.5 (a) and (d) some holes have been labeled (from 1 to 8) at progressively shorter distances from the step edges. Thus, several stages of the vacancy islands diffusion to these locations can be seen as frozen frames of a time resolved surface evolution. Once a specific vacancy island is close enough to the step edge, the resulting neck is subsequently narrowed (3, 4) until it is broken to minimize the island perimeter plus step border (5, 6). At this stage, the total ledge relaxation gives rise to leaf-shaped structures (7,8). More clearly developed in figure 5.2.6 (a), these structures have a $0.5\,u.c.$ and $1.5\,u.c.$ depth with respect to the lower and upper terrace levels. All line profiles in figure 5.2.5, are consistent with the dynamical picture outlined above in which initially $1.5\,u.c.$ deep holes formed at a given terrace, migrate to the descending step edges and are at the origin of SrO terminated regions ($0.5\,u.c.$ in depth) confined between terraces.

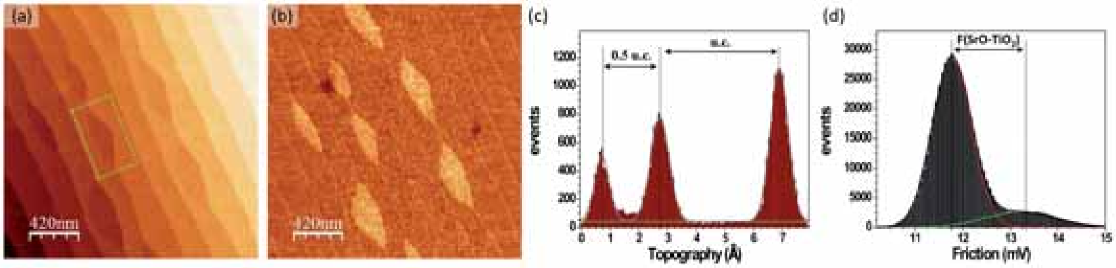

Figure 5.2.6: *Topographic and friction data of the nanostructured STO substrate, thermally treated at* $\sim 1100°C$ *for* $2h$*, presenting leaf-shaped* $0.5\,u.c.$*deep* SrO *regions. The* $0.5\,u.c.$ *height difference between* TiO_2 *and* SrO *termination is determined in the histogram plot presented in (c) of the location marked in (a). (d) shows the friction signal histogram plot of the whole image (b).*

Resulting from this diffusion of holes which expose the SrO termination, one expects that if the surface treatment is prolonged, these leaf structures will still evolve and eventually give rise to the formation of SrO trenches, $0.5\,u.c.$ deep with respect to the lower terrace level. In fact, after longer annealing ($\sim 2\,h$) at the same temperature ($1100°C$), step edges smoothen and the $0.5\,u.c.$ low-lying regions coalesce to form well-defined SrO-terminated regions running along the lower step edges in between TiO_2-terminated terraces (figure 5.2.6 a) [19]. Long-range elastic interactions can play an important role in the stabilization of these low-lying SrO regions at step edges [269]. The SrO nature of the low-lying regions in figure 5.2.6 (a) is confirmed by the higher friction contrast that they present (see figure 5.2.6 b). Besides, this low-lying SrO regions $0.5\,u.c.$ depth is confirmed in the height histogram plot of 5.2.6 (c) corresponding to the location marked in (a), where the $0.5\,u.c.$ height is determined in direct comparison to the one $u.c.$ height difference found between adjacent TiO_2 terraces. The SrO regions friction contrast is found to be a 13% higher than that of the TiO_2, in agreement with the presented previous results of figures 5.2.3 and 5.2.4.

The mechanism of vacancy islands coalescence detailed above and observed in real time for metallic surfaces [270, 271], has also been proposed to describe the dynamics of similar circular holes observed in low miss-cut STO substrates after chemical etching and annealing at $950°C$ for $\sim 1\,h$ aiming to get single TiO_2 termination [265]. However, in that case, the observed holes were only $1\,u.c.$ deep as expected from the single terminated TiO_2 surface used in those experiments, i.e. the holes exhibited the same TiO_2 termination as the surface terraces.

In the following sections we explore the deposition of organic molecules with carboxylic functionalization onto this nanopatterned oxide surface, and investigate how the self assembling of this organic molecule layer changes the mechanical and electrostatic properties of the oxide surfaces.

5.3 Selective adsorption of stearic acid into the nanopatterned $SrTiO_3(001)$ surface

Stearic acid ($n-C_{17}H_{35}COOH$) (denoted by Ac, its structure is shown in figures 5.3.1) was chosen because the carboxylate function can interact favorably with oxide surfaces [272, 273] as well as the fact that the alkyl chain can lead to ordering of the hydrophobic section (the alkyl chain) of the molecule through van der Waals interactions, a situation that arises in different types of self-assembled monolayers [8]. Furthermore, the dimensions of the molecule ($\sim 2.3\,nm$, calculated by the ChemDraw [179]) make it easy to locate on the surface and to determine its orientation. In addition, since this saturated fatty acid is commonly used as lubricant and is expected to present a conveniently oriented molecular dipole of measurable magnitude [274] this molecule appears suitable to explore changes on the STO surface properties under investigation here.

In order to deposit the stearic acid on a patterned STO surface as the ones shown in figure 5.2.4

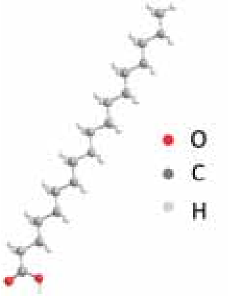

Figure 5.3.1: *Chemical structure of the stearic acid molecule* ($n - C_{17}H_{35}COOH$).

or 5.2.6, we first attempted incubation of the surface in a $2\,mM$ solution of the acid in absolute ethanol. Even for long periods of immersion time (up to $25\,h$), removal of the sample and rinsing with ethanol gave only signs of very little non-specific adsorption. In figure 5.3.2 (a) a cm-SFM topography image of laterally nanopatterned STO surface after a $24\,h$ immersion in $2\,mM$ stearic acid solution is presented. Even if some adsorption of molecules is deduced from the increase of the surface roughness and the apparent material drag by the scan of the tip, the corresponding profile shown in figure 5.3.2 (b) reproduces the one $u.c.$ height between TiO_2 terraces and $1/2\,u.c.$ between TiO_2 and SrO terminations. This observation indicates that the surface sites of the STO as it is prepared and subsequently handled in air are not sufficiently active to form covalent links with the acid over extended areas which enables the molecules to self-assembly.

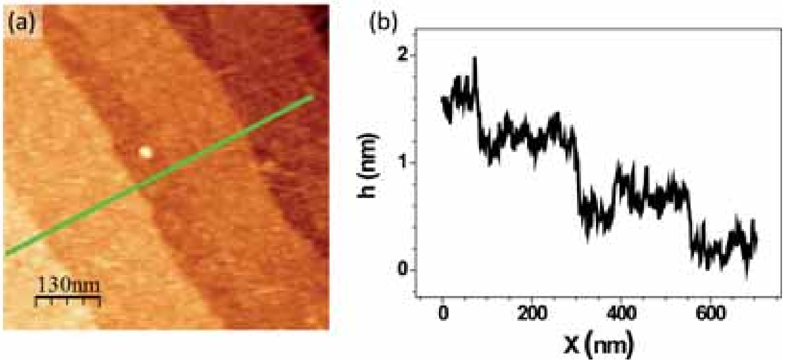

Figure 5.3.2: *cm-SFM mode topographic image of STO surfaces after its immersion in a* $2mM$ *solution of Ac in ethanol. Although it presents a higher roughness, the line profile presented in (b) reproduces the u.c. height difference between* TiO_2 *terraces and* $1/2\,u.c.$ *and* $3/2\,u.c.$ *between* TiO_2 *and* SrO *adjacent locations.*

In an alternative approach, the ethanolic solution of the acid was cast from a pipette onto the nanopatterned STO and the solvent was let to evaporate. The surface was then rinsed with absolute ethanol and dried under a N_2 stream. SFM images of STO surface prior and after the drop cast deposition are presented in figure 5.3.3 (a) and (b) respectively. The topographic image of (b) shows that the acid specifically adsorbs onto the TiO_2 termination, as is confirmed by the corresponding line profiles of (c) and (d). In topographic line profile (c), corresponding to the laterally nanopatterned virgin STO surface (figure 5.3.3 a), the $1/2$ $u.c.$ and $3/2$ $u.c.$ height difference between the SrO depression trench and adjacent TiO_2 terraces is visible. In contrast, in the line profile (d) corresponding to the STO Ac drop casted surface, the one $u.c.$ height difference between adjacent TiO_2 terraces is reproduced (right part of the profile) while a higher topography difference is found between SrO termination trenches and adjacent terraces, what proves that the Ac selectively absorbs on the TiO_2 surface. Growth of the first monolayer seemed to inhibit the growth of further organic layers on top and a nearly perfect SAM following the nanostructured chemical pattern of the underlying substrate is formed (see figure 5.3.4 a). This situation will be described in more detail later on. The casting procedure was tested at different deposition conditions, including sample post-annealing, without noticeable changes.

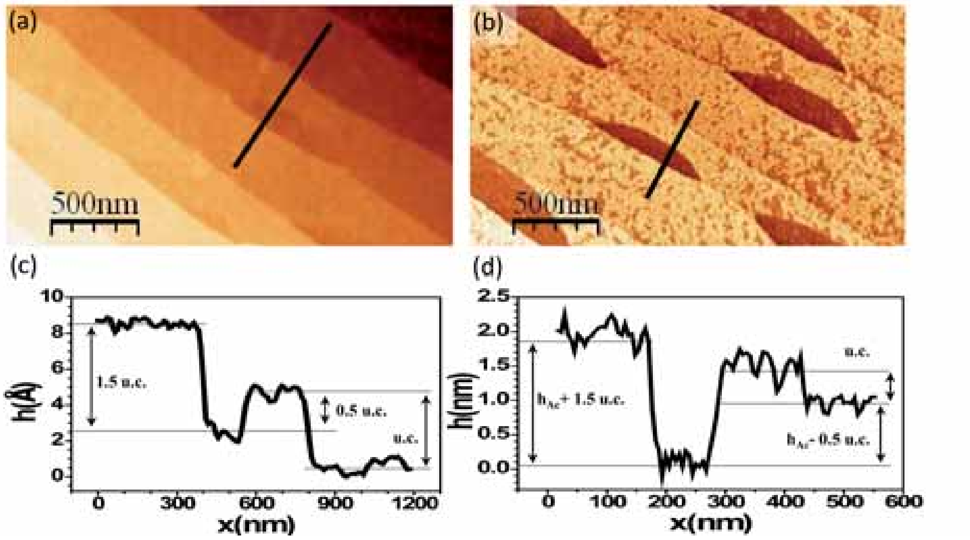

Figure 5.3.3: *cm-SFM topography images of STO surfaces prior (a) and after (b) the drop cast of stearic acid in ethanol. The corresponding line profile presented in (c) shows the* 0.5 *u.c. and* 1.5 *u.c. topography difference between adjacent* SrO *trenches and* TiO_2 *terraces, while in the relief profile (d) corresponding to the drop casted STO surface an extra height difference (denoted by* h_{Ac}*) is found between adjacent* SrO *and* TiO_2 *locations.*

In very few cases, local excess of stearic acid was found to give rise to some SrO occupation or even isolated multilayer islands formation (3D crystallites). In figure 5.3.4 (a and b) the partial coverage of the SrO termination trenches by Ac is evident. Due to the different hydrophilicity presented by the TiO_2 and SrO surfaces [261, 262, 267, 268], different attempts were done in order to rule out any thin water film influence on the inhibition of the Ac chemisorption on the more hydrophilic SrO termination. The experiments basically consist in annealing the STO sample prior to the drop cast deposition temperatures between 100 and 200°C in order to diminish the inevitable absorbed water film on the STO surface when exposed to air, in particular on the SrO terminations. In a first series of experiments, the STO crystals were annealed up to temperatures in the range of $\sim 200\,°C$ by placing the crystal on top of a hot plate stirrer for ~ 30 minutes. The crystal was allowed to cool down for a few minutes to room temperature before the drop cast of Ac was performed. With the goal of decreasing the sample-air exposure time at room temperature conditions, in a second kind of experiments, the drop cast of the Ac solution was deposited on top of STO crystal just after taking it out from hot plate held at $\sim 100-150\,°C$. Because the melting point of the stearic acid is 69.6 $°C$ [275], in this second attempt the molecules were supposed to crystallize with the substrate cooling. However, no correlation between Ac drop cast deposition conditions and Ac chemisorption on SrO surface was found and the selective absorption of Ac in TiO_2 surface was found in most of the experiments. In fact, previous results indicate that the SrO termination is not only more hydrophilic than the TiO_2 one, but that the hydroxylation of its surface occurs at much lower water partial pressures than the TiO_2 one [263] and even ambient conditions. This hydroxylation could not be removed by such a low temperature annealing of the samples, and thus the presence of the hydroxyl groups bonded to the Sr atoms could explain the inhibition of the of the adsorption of the Ac molecules in the SrO surface. The selective growth of the Ac molecules on the $STO(001)$ surface could also arise from specific adsorbate-surface interaction leading to a more favorable interaction with the TiO_2 termination than the other, where the carboxylic acid group forms hydrogen bonds with the TiO_2 rather than to the SrO areas.

In some cases, Ac multilayer island formation was observed. In figure 5.3.4 (c) a topography image of an isolated multilayer island is shown. These crystallite-like structures, is quite homogeneous in height and reproduces the substrate step morphology as can be seen in the topographic line profile in (f). The island presents a $5.3 \pm 0.2\,nm$ in height as can be derived from the line profile (e) performed along a substrate terrace (image 5.3.4 d), and exhibits a two levels top with extremely well defined inter-plane distance of $\sim 1.3 \pm 0.2\,nm$. As in single crystal structure, the Ac molecules are supposed to form head to head carboxylic tapes layers to build multilayers by van

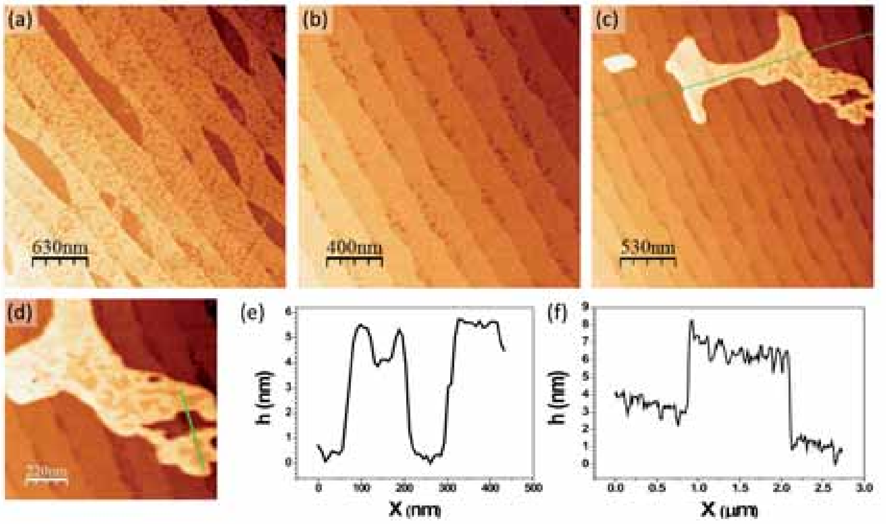

Figure 5.3.4: *Topographic cm-SFM data for three different stearic acid coverages (a, b and c) obtained on three different STO substrates. The line profile in (f) corresponding to the location marked in (c) shows the STO step terraces reproduction by the absorbed multilayer of stearic acid. A magnified region showing a multilayer of stearic acid (d) and a line profile (e) as indicated in (d). The total height (~* $5.3\,nm$*) is a multiple of the difference between the two superior levels* ($1.3\,nm$)*, which coincides with the monolayer thickness (see text). (a) scale* $8\,nm - 0\,nm$*, (b) scale* $5\,nm - 0\,nm$ *from bright to dark.*

der Waals interactions of the methyl end groups of the alkyl chains. Stearic acid single crystals however, have been shown to present different polymorphisms. Sato et al. [276] showed that the rapid crystallization when using polar solvents (as ethanol, as in our case) induces the Ac to crystallize in a monoclinic like structure (C type form). Using X-ray diffractometry, they report an β angle[1] of $\sim 58°$, while Malta et al. [277] and Sato et al. [278] reported a value around $\beta \approx 52°$. Stearic acid molecules (figure 5.3.1) are $\sim 2.3\,nm$ in length (calculated by the ChemDraw program [179]) and the monoclinic C-form single crystals c lattice parameter corresponding to a bilayer of Ac is of $\sim 5.09\,nm$ [278]. The measured heights in the Ac multilayer islands are consistent with layers of molecules standing up with a tilt angle of about $\sim 57 \pm 2°$ with respect to the surface normal, what is in agreement with the β angles reported for single crystals of Ac in the $C-form$. If this is the case, the three dimensional islands would consist of 4 molecular layers grown on the monolayer in direct contact with the TiO_2 terminated terraces of the substrate, which could then be considered as a wetting layer. We suggest that these 3D structures resulting from multilayer formation are observed rarely because are easily removed by the sample rinsing with ethanol due to the weak van der Waals interactions between methyl terminal group holding the island structure.

---

[1] β is the angle that **c** primitive vector forms with the ab plane in the monoclinic structure.

On the contrary, the selectively grown single layer shown in figure 5.3.3 (b), 5.3.5 and 5.3.6 was observed to form over the vast majority of the surface and was obtained repeatedly in different samples, as described in the following paragraphs.

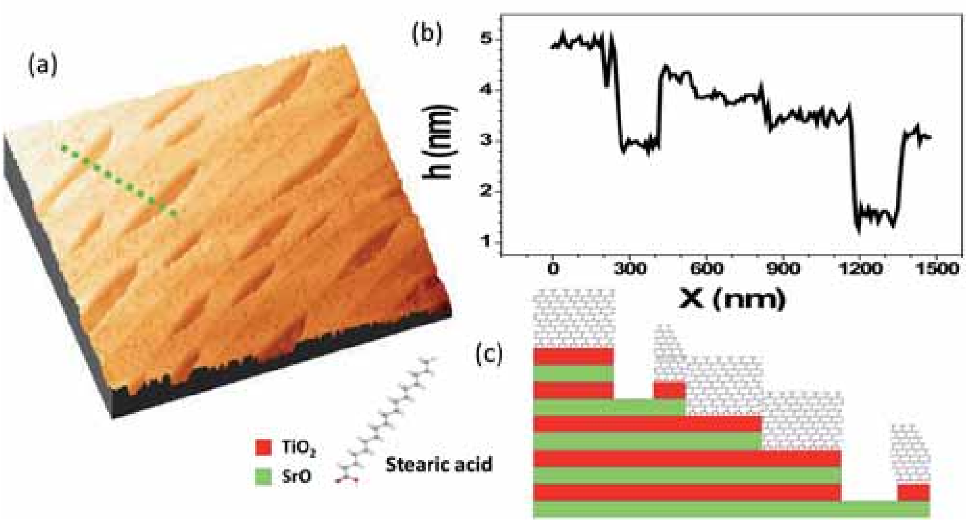

Figure 5.3.5: *(a) 3D representation of* cm-SFM *topographic image of STO surface after the selective absorption of stearic acid in* TiO_2 *surface. The corresponding line profile presented in (b) crosses consecutive regions consisting in* $(Ac/TiO_2) - (SrO) - (Ac/TiO_2) - (Ac/TiO_2) - (Ac/TiO_2) - (SrO) - (Ac/TiO_2)$ *surfaces, as is reproduced in the sketch presented in (c).*

With a solution concentration of $2\,mM$ and drop casting at room temperature and subsequent ethanol rinsing, rather homogeneous surfaces, in which a completely selective adsorption exists, were always observed. This can be seen in the 3D representation of the topographic image presented in figure 5.3.5 (a). The homogeneous coverage of TiO_2 surface reproduces the step morphology of the substrate with the low-lying depressions corresponding to bare SrO termination. In the line profile depicted in (b), five Ac covered TiO_2 surface steps and two bare SrO terminated region are crossed as is schematically represented in (c). The presence of the Ac covered one $u.c.$ height steps offers an in situ reference that allows the measurement of the organic layer thickness of $h_{ac} \sim$ 1.1–1.3 nm, which coincides with the inter-plane distance measured in the multilayered islands. An statistical analysis of the organic layer thickness is presented in the histogram plot of figure 5.3.6 (b) that corresponds to the height values of the location marked in the topographic image of figure 5.3.6 (a). The Ac monolayer thickness is determined by direct measurement of the height difference between two adjacent TiO_2 terraces covered by Ac, resulting in a $h_{ac} \approx 1.2 \pm 0.1\,nm$. This observation supports molecular self-assembly with stearic acid molecules tilted about $\sim 57°$

with respect to the surface normal. Such a large tilt angle has also been reported for similar alkane chain-based molecules like alkanethiols in $GaAs(100)$ [279] and $Au(111)$ [280] and ascribed to both optimization of the intermolecular van der Waals interaction between molecules (chain-chain distance $\sim 0.45\,nm$) [40, 281] and commensuration with the underlying substrate.

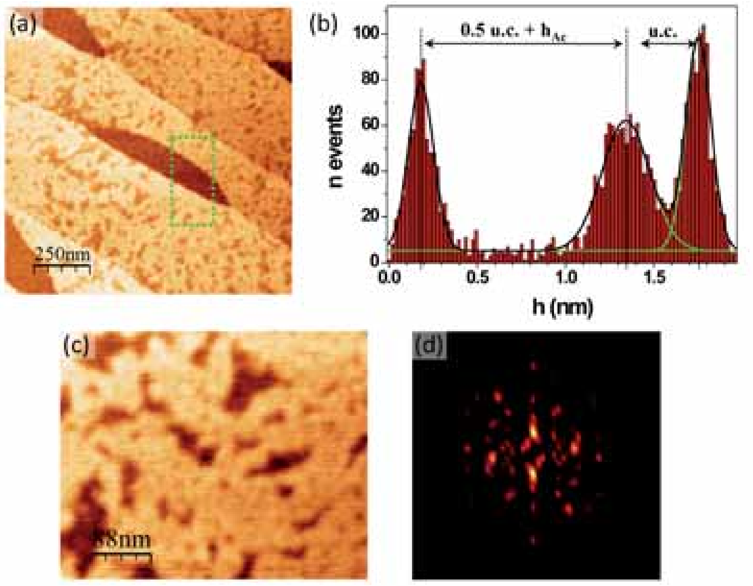

Figure 5.3.6: *(a) Topographic image of stearic acid deposited onto nanostructured STO substrate, (b) histogram representation of the topographic signal data of the location marked in (a). (c) magnified topographic image, (d) 2D-FFT (fast Fourier transform) of the image in (c).*

Carboxylate function molecules ($R-COO^-$) adsorption on TiO_2 surfaces has been extensively studied [273]. Carboxylic acid is known to adsorb dissociatively into TiO_2 and can present three different binding geometries to the Ti atoms [272, 273]. In the monodentate binding, one of the oxygens of the carboxyl group is bond to a Ti; in a dentate chelating binding, the two oxygens of the carboxyl are bonded to the same Ti atom and in a bidentate bridged bonding, each oxygen atom is bonded to a different Ti atom. Due to the large $Ti-Ti$ distances (~ 3.9Å) in the STO(001) surface compared to the oxigen distances (~ 2.2Å in carboxylic acid, data from ChemDraw program [179]), in the present case a monodentate or bidentate chelating bonding would be favored, that is a Ac molecule per each Ti atom. Noting however, that STO is a cubic perovskite with a lattice parameter of $0.3905\,nm$, matching between the molecular arrangement of tilted molecules and the TiO_2 squared surface, is not evident. The TiO_2 squared area (~ 16Å^2) is too small to hold an Ac molecule bonded to each Ti atom in close packed SAM structure. Such a close packed structure of the Ac would not be favored due to strong repulsive interactions between alkyl chains, essentially because the $Ti - Ti$ distance is smaller than the close packed chain-chain distance ($\sim$ 4.5Å) on SAMs. In fact, the closest packed structures in the case of octadecanethiol on $Au(111)$ is a $\sqrt{3} \times \sqrt{3}R30°$ with an area per molecule of $\sim$ 22Å^2. Supported by the fact that both the first Ac absorbed layer and inter-plane distance in the multilayer island coincides, most probably the molecular assembly is dominated in this case by the cohesion energy between molecules rather than the geometric constrains imposed by the surface. Effort was done trying to resolve the Ac supramolecular arrangement by molecular periodicity lateral force measurements (see section 3.2.5.1), without success. However, detailed inspection of the cm-SFM topographic image in 5.3.6 (c) reveals that the assembled molecules appear packed in small 2D clusters quite uniform in size ($\sim 25\,nm$ in diameter), which cover the TiO_2 terraces forming a nearly closed-packed layer (see the corresponding fast Fourier transform data in figure 5.3.6 d). The formation of the SAM by those small clusters of molecular domains could be originated by the forced fast assembly of the molecules on the employed drop cast deposition method, and could also explain the impossibility of resolving the molecular arrangement by lateral force molecular stick-slip measurements.

5.3.1 Influence of stearic acid into the mechanical properties of the TiO_2 surface

In order to know the change in the surface frictional response induced by the organic layer, simultaneously to topographic imaging the lateral force (forward and backward, F_l^i, $i = f, b$) images were also acquired in cm-SFM. In order to perform a reliable comparison, FFM measurements between Ac termination and SrO surface where always performed under low-humidity conditions ($RH \leq 5\%$) in order to keep the very same conditions as the ones used for the FFM measurements performed between TiO_2 and SrO terminations. The difference in frictional response between SrO and TiO_2 terminated regions previous to the organic layer deposition was found to be about $\sim 10 - 15\%$ (as has been presented in section 5.2), in accordance to the reported value of 15% for low humidity [19].

In figure 5.3.7 the simultaneous topographic (a) and lateral force forward (b) and backward (c) images of a nanostructured STO with Ac absorbed in the TiO_2 surface as that of the figure 5.3.3 (a) and 5.3.6 (a) are presented. The lateral force images reveal a clear frictional contrast between the uncovered SrO regions and the surrounding stearic covered TiO_2 terraces. From

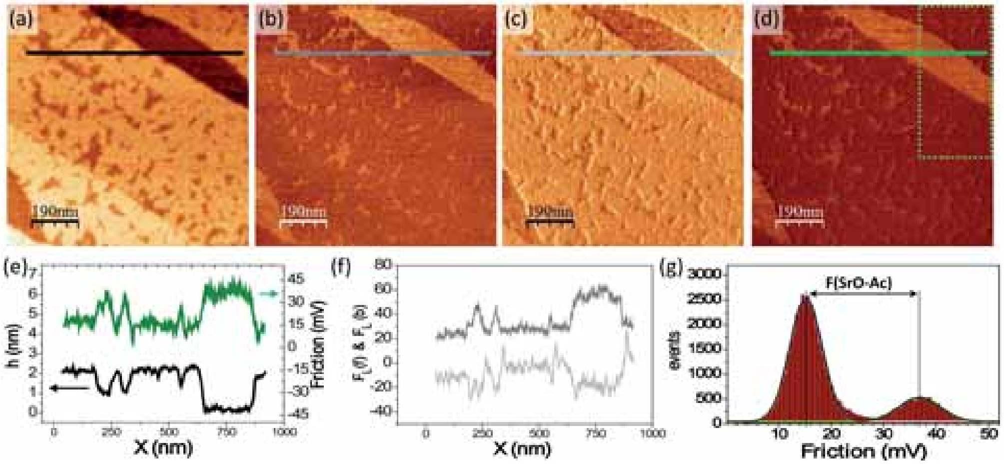

Figure 5.3.7: *Topographic and frictional data simultaneously acquired for Ac deposited onto a nanostructured STO substrate as that of figure 5.3.3 (a) and 5.3.6 (a). cm-SFM topographic (a), lateral force forward (b), lateral force backward (c) and friction (d) (calculated as* $\frac{1}{2}[F_l^f - F_l^b]$*) images. Topographic profile and the corresponding friction (e) calculated from the lateral forward and backward profiles in (f). The darker regions in the friction image correspond to the lower-friction stearic acid covered* TiO_2 *regions. The friction difference between* $Ac - SrO$ *termination is calculated from the histogram representation of the friction signal data of the location marked in (d).*

the half of the forward and backward lateral force images subtraction, the mean friction image is built and presented in (d). The lower frictional response of stearic acid surface compared to SrO surface is clear. Two different ways of calculating the friction are shown in the bottom panel of the figure 5.3.7. By the F_l^f and F_l^b line profiles presented in (f), the friction profile is calculated (e, right axis) and correlated with the corresponding profile of the simultaneous topographic image (e, left axis). Nearly same absolute lateral force contrast is found between F_l^f and F_l^b images, so any friction anisotropy or asymmetry effect that could arise from different azimuthal molecular domain orientation is discarded or at least are below our detection threshold. Additionally to the friction profile plot, an histogram representation of the friction corresponding to the location marked in (d) is presented in figure 5.3.7 (g). The frictional contrast is directly determined from the shift of the corresponding peaks. From statistical analysis of histogram representation of several location as the one addressed, the friction is quantified to be $\sim 60\%$ lower in the stearic acid with respect to the SrO termination ($F(SrO)/F(Ac) = 2.5 \pm 0.3$), i.e. the resistance to relative motion of the initial TiO_2 has been reduced about 50% after the organic coating ($F(TiO_2)/F(Ac) = 2.2 \pm 0.3$). We remark that this percentage could be even larger because of the highly hydrophobic character of the CH_3 terminated organic layer as compared to the hydrophilic character of the SrO regions.

5.3.2 Influence of stearic acid into the electrostatic properties of the TiO_2 surface

In addition to the evident improvement of the tribological properties, we will demonstrate in the following that the organic layer constitutes a convenient method to change the so called local work function (ϕ) of the TiO_2 surface in the STO. We will show that the local surface potential of the TiO_2 terraces is reduced upon adsorption of the stearic acid. In order to quantify this effect, we conducted Kelvin probe force microscopy (KPFM) (introduced in section 3.2.5.3) measurements on two types of surfaces in which SrO termination regions coexist either with bare or stearic acid covered TiO_2 terraces. Pt-Cr coated Si tips mounted on cantilevers with nominal $k \approx 3\ N/m$, resonance frequency around 75 kHz were employed for these measurements. The choice of cantilevers with appropriate stiffness allows us to pass from cm-SFM to dm-SFM measurements, under controlled experimental conditions without changing surface location, and verify surface contact potential characteristics of the very same surface region when desired and thus unambiguously correlate topography, chemical termination and electrostatic information. Frequency modulation KPFM (FM-KPFM, see section 3.2.5.3) was used for obtaining the presented results with typically an ac bias of $(500\, mV, 7\, kHz)$ applied to the tip, while STO crystal was electrically connected to a grounded metallic holder either by a mechanical clamp or silver paint. No significant variations where detected by using these two types of electrical contacts.

The choice of the set point for dm-SFM measurements performed with conductive tips was the most critical parameter in these KPFM measurements, because of enhanced instabilities found with respect to non conductive tips measurement conditions. Much shorter dynamic attractive regime range was typically found and changes to unstable conditions (with no controllable attractive-repulsive regime variations) were very sensitive to small set point variations [64, 79] (a more detailed explanation of this regimes in presented in section 3.2.4.2). This variation in the tip-sample interaction regime were probably caused by the enhancement of electrostatic interaction when biased conductive probes are employed. The procedure for the stable set point determination was the following. We approach the surface in dm-SFM mode with the ac bias on and the PLL feedback off, we start decreasing the amplitude set point by small steps until small phase shift is detected. At this point the PLL is turned on and we start scanning the surface and adjusting the feedback parameters with very small variation in the set point until a stable topography signal is obtained. At this moment the KPFM feedback was turned on. Amplitude and phase shift versus distance curves were usually acquired to establish the amplitude set point ranges where attractive-repulsive regimes coexist. Typically free oscillation amplitudes between 10 and 40 nm and small amplitude reduction ($\sim 10\%$) set point were employed for obtaining the results presented in this section.

Figure 5.3.8 shows a complete data series of cm-SFM and dm-SFM measurement on top and bottom panels respectively. Topography, friction and contact potential difference (CPD) data were obtained at the same STO substrate and the lateral force and excitation frequency signals provide reference for correlating each chemical termination with its CPD.

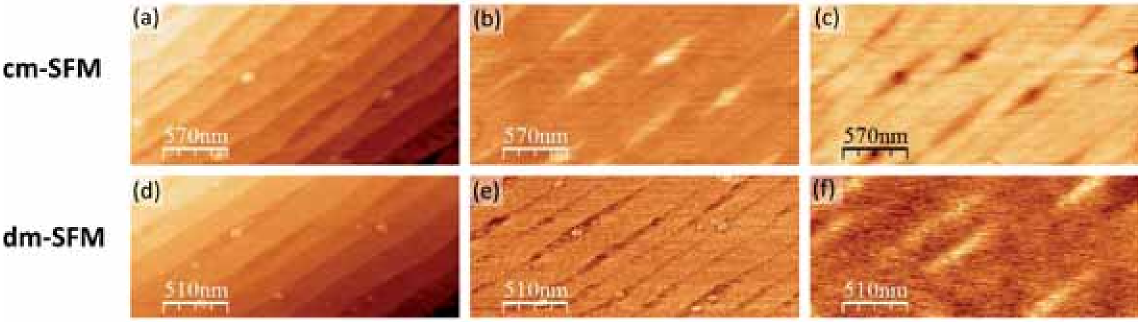

Figure 5.3.8: *cm-SFM and dm-SFM data of nanopatterned STO (001) surface are presented in top and bottom panels respectively (not exact same surface location). cm-SFM topography (a) and simultaneous lateral force forward (b) and backward (c) measurements allow the identification of the* TiO_2 *and* SrO *termination locations of the nanostructured* $SrTiO_3$ *substrate. dm-SFM topography (d), excitation frequency (e) and CPD (f) maps are presented in bottom line images. CPD map (f) color scale ranges 250mV from bright to dark.*

Although no so well resolved as with uncoated silicon tips, the low-lying SrO regions are differentiated in both cm-SFM (figure 5.3.8 a) and dm-SFM (d) topographic images. The measured friction contrast in the lateral force forward (b) and backward (c) signals confirm again the SrO nature of the $1/2$ $u.c.$ depressions. By changing from contact to dynamic mode CPD maps were acquired. The two chemical termination regions are well distinguished in the dm-SFM figure 5.2.3 (d) and phase shift (e) images. In the corresponding CPD map presented in figure 5.3.8 (f) a clear contrast between the two chemical terminations is detected, with the SrO locations presenting higher CPD with respect to TiO_2. A closer inspection of the two chemical terminations is performed in figure series 5.3.9, with dynamic and contact data in top and bottom panels, respectively. Lateral force (forward and backward in (d) and (e) respectively) allows us again to unambiguously identify each chemical termination and correlate its topography and CPD. In figure 5.3.9 (c) the direct correlation between topography and CPD signals is established by the corresponding topographic (in black) and CPD line profile (in red) performed in the location marked in (a) and (b). The KPFM results were cross-checked by direct measurement of the electrostatic force, $F_n(V_{tip}, z)$, with 3D mode experiments (see section 3.2.5.4) performed on top of each chemical termination (marked in (a) and (b)). From horizontal profiles (constant z profile) performed on F_n image, the characteristic of the quadratic dependence of the electrostatic force, i.e. F_n vs V_{tip} parabolic curve centered on CPD is obtained. The difference in CPD (ΔCPD) between two locations is directly determine from the relative shift of the parabola maximum obtained at each location (figure 5.3.9 f). As a result of KPFM and 3D mode measurements, a $\Delta CPD_{STO} \approx 45 \pm 10\,mV$ is measured thus implying $CPD_{SrO} > CPD_{TiO_2}$. The error was estimated as the convolution of the noise level that the instruments has and the statistical deviation of measuring KPFM and 3D modes on different locations and different samples up to total of 20 series.

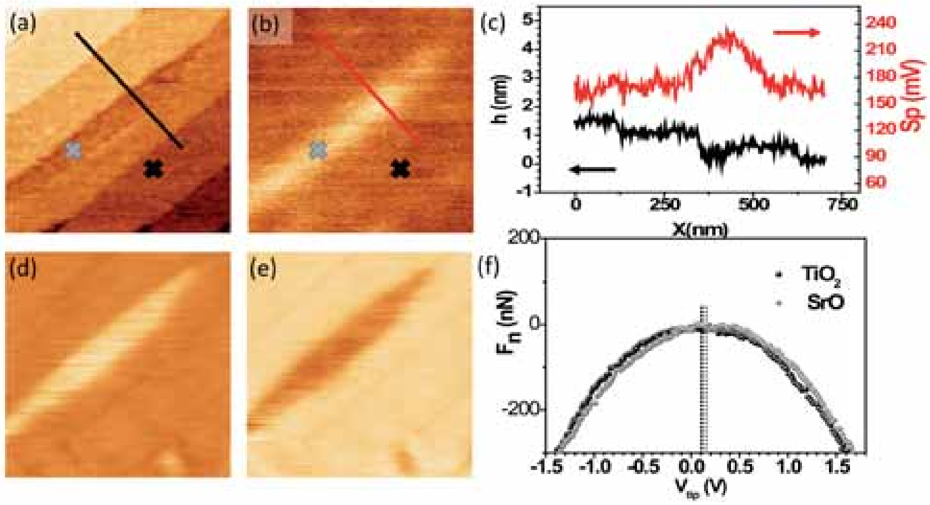

Figure 5.3.9: *dm-SFM topography (a), CPD (b) and contact mode lateral force forward (d) and lateral force backward (e) images of the very same location of nanostructured $SrTiO_3$ substrate. A line profile and the corresponding CPD signal are depicted in (c). Electrostatic force parabolas (f) obtained with the 3D approach on specific point locations (cross-marked points in the figure). Images size is of $1\mu m \times 1\mu m$.*

As introduced in section 3.2.5.3, during the last years the KPFM technique has been applied for the determination of CPD in variety of systems, such as metals, insulating thin films, molecules, etc...[282]. The meaning of the measured CPD quantity by KPFM is well established for the contact of two metal, where it is commonly associated to the local work function variation. However, for insulating samples as STO, no energetic alignment between tip and sample Fermi levels can be assumed, and thus the physical meaning of the magnitude measured by KPFM is in principle unknown. Even so, classical vibrating capacitor Kelvin method [283, 284] as well as KPFM measurements have been extensively applied in insulator samples [285–289]. The commonly accepted simple interpretation of the CPD measurements in insulators samples is that the CPD between tip and sample metallic holder is actually measured. Both, the classical vibrating capacitor method and KPFM are based in compensating electrostatic forces present between two metallic electrodes (two plates or the probe and sample), and for two electrically connected metallic materials separated by vacuum the potential drop generated by this electric field is actually the CPD. But when instead of vacuum there is a certain material in between the two electrodes, the physical properties of this material, as the permittivity, the presence of permanent dipoles or trapping charges etc... will induce a local variation of the electric field, i.e. the surface electric potential, and thus the measured CPD will be affected by them. In fact, this is one of the main applications of KPFM, the study of the local variation of surface potential due adsorbed species or surface modifications. This was the case in chapter 4, where the presence of small molecules induce a change on the local work function of the gold surface. In the present case, the presence of a $0.5\,mm$ thick insulating STO crystal will of course change the CPD measured between tip and holder, but because we are always measuring the relative ΔCPD between different locations, the measured ΔCPD_{TiO_2-SrO} will be only consequence of the presence of the two chemical terminations, and/or for the different species they have adsorbed on top (water, contamination or stearic acid layer). In this case, the difference in dielectric material thickness, consequence of the surface step morphology, can be considered negligible compared to the total crystal thickness.

TiO_2 and SrO are non-polar surfaces and the observation of a certain ΔCPD between each termination could be originated from the combined effect of distinct chemical termination and unavoidable electronic reconstructions induced by surface relaxation and rumpling, or by the different adsorbed species on surface. Due to the breaking of symmetry and to rumpling, surface dipoles are formed at SrO and TiO_2 terminations [290, 291], the resulting relaxed-surfaces having a different surface energy. We are also implicitly assuming pure TiO_2 and SrO terminated regions; however, a non fully complete separation of the chemical terminations after thermal treatments might remain. If a minor coexistence persists, the ΔCPD measured on each terrace would be an effective average further lowering ΔCPD. In fact, recent measurements performed in our group[2] in similar nanopatterned STO substrates by non contact SFM (NC-SFM) under ultra-high vacuum conditions, evidence the presence of Sr adatoms and small SrO islands on the TiO_2 terminated surface with similar structural features as the ones reported by Kubo et al. [292]. In addition, CPD contrast can also be affected by favored adsorption of a thin water film [293, 294] in the more hydrophilic SrO surface or by the presence of hydroxyl groups on the SrO termination [263]. Although measurements were done at low humidity conditions ($RH < 5\%$), the potential contribution to the ΔCPD of a thin water layer cannot be discarded, likely due to an enhanced water adsorption on the more hydrophilic SrO termination [261, 262, 267, 268].

On the other hand, we note that the measured CPD is surely an underestimation. The different chemical terminated regions are about $50 - 100\,nm$ wide, of the range of the tip size and close to our KPFM lateral resolution limit. In consequence a reduced ΔCPD would result from averaging. Moreover, neighboring regions of different chemical composition lie at different surface planes and are separated by step edges that would contribute with their own dipole to decrease the measured ΔCPD. Moreover, because of the finite size of the nanostructures, the surface potential difference decays rapidly perpendicularly to the surface plane [295]. Being difficult to definitely settle an ultimate interpretation of KPFM data in this insulating surfaces, our discussion relies on a comparative analysis of $TiO_2 - SrO$ and $AcTiO_2 - SrO$. Taking advantage of selectivity, i.e. the SrO location keep bare when Ac is adsorbed on the TiO_2 surface, we focus on the impact of the Ac adsorption on the electrostatic properties of the TiO_2 surface. As mentioned previously, although measurements were done at $RH < 5\%$, the potential contribution of a thin water layer cannot be discarded and its contribution to the CPD can vary from one sample to another. In order to take this factor into account, the surface potential of the bare STO substrate was always determined prior to and after stearic acid casting. As the stearic acid selectively adsorbs on the TiO_2 terminated regions, we can estimate the change in contact potential of these regions referred to that of non-covered SrO terminated patches, i.e., using ΔCPD_{STO} as a reference, regardless of the actual absolute value of CPD_{SrO}.

Topographic dm-SFM and simultaneous KPFM maps for a stearic acid covered STO substrate are presented in figure 5.3.10 (a) and (b), respectively. The topographic relief and its

---

[2] Measurements performed by Sonia Matencio.

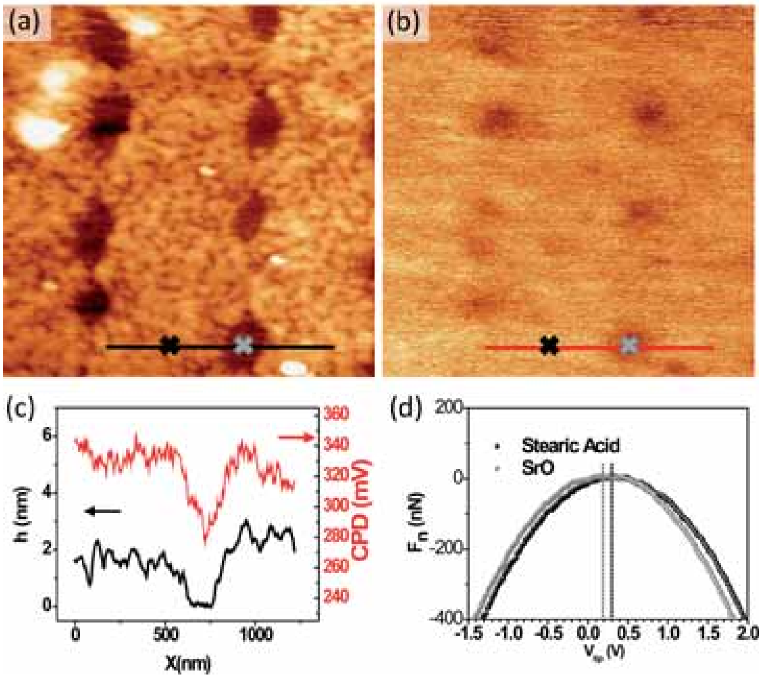

Figure 5.3.10: *Topographic (a) and CPD map (b) acquired by KPFM for stearic acid deposited onto a nanostructured STO substrate as that of figure 5.2.6. A line profile and the corresponding CPD signal are depicted in (c). Normal force versus applied tip voltage (d) measured on the two locations marked in the images (gray and black are used to indicate SrO and stearic acid regions, respectively). The lateral size of the images is* $1.5\mu m \times 1.5\mu m$.

corresponding surface potential profiles are also shown (figure 5.3.10 c). From the latter, where CPD_{AcTiO_2} is the surface potential on the stearic acid terminated TiO_2 terraces, we estimate a $\Delta CPD_{AcTiO_2-S_rO} = CPD_{AcTiO_2} - CPD_{S_rO} = 70 \pm 25 mV$. As the intrinsic accuracy of our set-up for these measurements is about 10 mV, the large error of the present measurement may be due to the fact that the lateral size of the SrO patches is similar to the lateral resolution of the KPFM measurements and an average between CPD_{S_rO} and CPD_{AcTiO_2}, resulting from convolution between terminations, would give an underestimation of $\Delta CPD_{AcTiO_2-S_rO}$. In order to overcome these problems, we estimated the CPD by the shift of the electrostatic parabolas (figure 5.3.10 d) obtained with the 3D approach measured on specific point locations (e.g. the marked with crosses in the figure). It is rewarding to notice that the obtained value of $\Delta CPD_{AcTiO_2-TiO_2} = 110 \pm 15\, mV$ compares fairly well to CPD of $\sim 160 - 180\, mV$ measured for stearic acid on NiO after heating and ether extraction [274] using a modified ionization method [296]. It is known [222] that the absolute value of the change in surface potential is dependent on the molecular packing (as was proven in chapter 4 section 4.4.3), parameter not easy to determine in the present case, and coverage [212, 213] of the organic film. In the frame of the present work, it is not the exact specific absolute value of $\Delta CPD_{AcTiO_2-S_rO}$ which is relevant for our purposes, but the fact that for the bare substrate we found $CPD_{S_rO} > CPD_{TiO_2}$, whereas after stearic acid adsorption $CPD_{S_rO} < CPD_{AcTiO_2}$. Independently of the exact value, the change allows us to clearly conclude that the specific stearic acid adsorption increases locally the contact surface potential of the TiO_2 surface. In terms of work function ($\sim 4.1 eV$ for Nb-doped (0.05 wt%) STO substrates) [297], the change in the local work function measured for stearic acid adsorption on TiO_2 is of about 2.7%. The combined ability to induce tribological changes with small variations in electrostatic properties is already appealing from a technological point of view, and in addition, the possibility of inducing controlled subtle variations in the local work function is also an important. However, here we notice that due to the synthetic capabilities of organic chemistry a more considerable work function changes can be achieved by choosing molecules with larger dipolar moments or even with an increase of the molecular coverage and packing [298].

5.4 Summary

Throughout this chapter we have characterized and investigated the use of nanopatternded $SrTiO_3$ (001) surfaces, which presents the coexistence of well differentiated TiO_2 and SrO chemical termination regions, as template for the adsorption of organic molecules. We have shown that a carboxylic acid function simple organic molecule can selectively form monolayers on the TiO_2 oxide termination. Thanks to selective adsorption of the organic molecules into the TiO_2 surface, and hence to the presence of the in situ reference that the bare SrO region offers, the investigation of the impact of the organic layer adsorption into the TiO_2 surface properties have been possible by scanning force microscopy techniques.

We have shown that selective adsorption can be used to create and modulate at the nanoscale both friction and work function of nanostructured surfaces with potential applications in several technologically and scientifically relevant emerging areas. The frictional response of the TiO_2 surface is lowered by a 50% with the organic layer adsorption, confirming that organic self-assembled monolayers (SAMs) are good candidates for their use as boundary lubricants for improving the tribological properties of the TiO_2 surface. Furthermore, we have proven that the use of SAMs to tune the local work function can be extended from metallic to insulating surfaces. By the adsorption of the stearic acid molecules, the $TiO_2(001)$ STO surface work function have lowered by around a 2.7%. However, a more considerable reduction (or increase) of the local work function would be possible varying the coverage [212, 213], the packing or/and the chemistry of adsorbed organic molecular layer [201, 210].

Bearing in mind that a simple casting approach has been used here, it seems likely that denser SAM and uniform packing will be achievable. We strongly believe that this technique and derivatives of it can be extended to other functional molecules, and furthermore that the spaces which are not adhered to can be used for the controlled growth of third molecular, metallic, or oxide species, a situation that would make STO a very interesting substrate for a sequential bottom-up route to patterned nanostructures.

In addition, we have added some insight about the the surface diffusion process that causes the chemical termination patterning of the $SrTiO_3(001)$ surface under high-annealing temperature $(1100 - 1200°C)$. We conclude that the formation of the low lying SrO chemical termination is consequence of the SrO region diffusion and coalescence in the TiO_2 step edges.

Appendix: Examples of some of the different $SrTiO_3(001)$ morphologies obtained after the high-temperature annealing in air

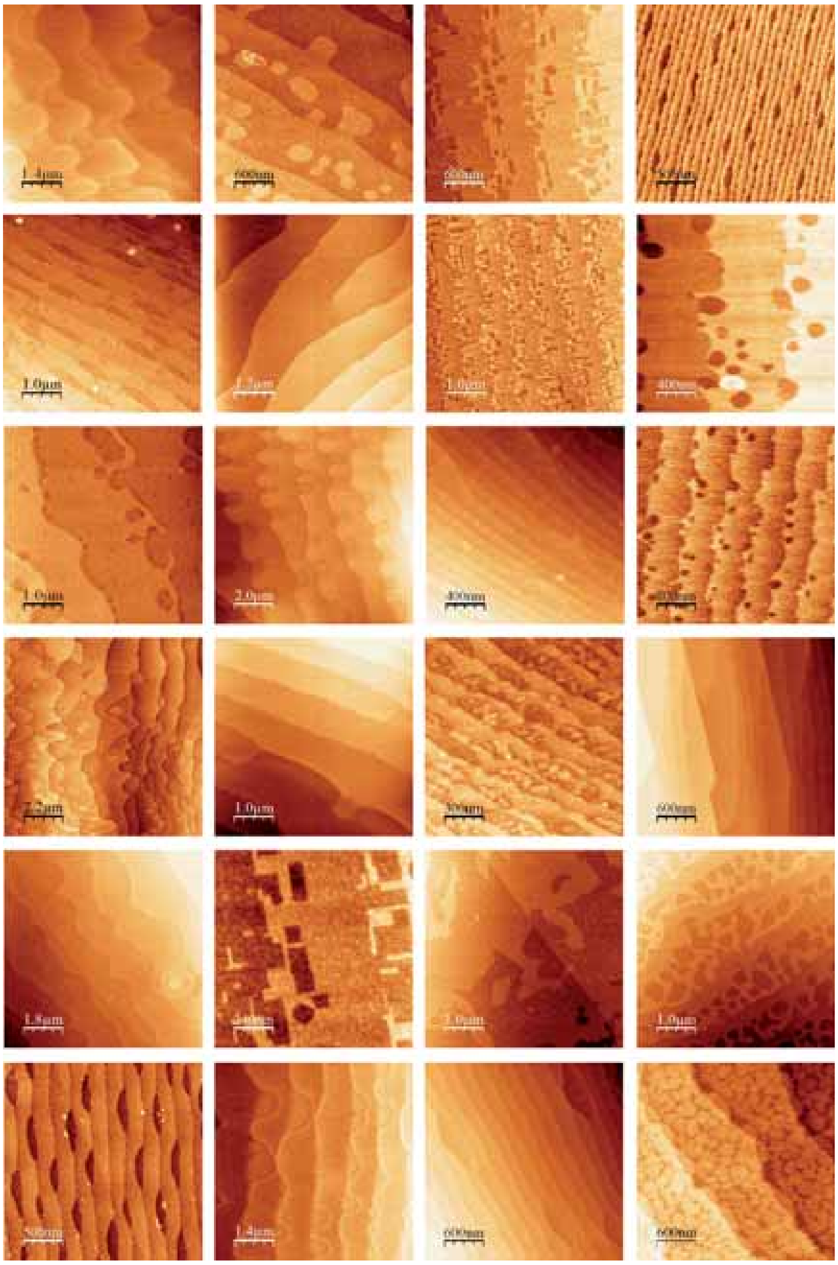

Figure 5.4.1: *SFM topographic images of some examples of the variety of morphologies obtained for different STO substrates under high temperature air-annealing treatment.*

Chapter 6

Tip induced of organic thin films modification

6.1 Motivation

Soft materials comprised of low molecular weight organic molecules are attracting increasing interest because their importance in the development of a number of emerging areas in nanoscience and technology, including molecular electronics, nanosystems for energy conversion, and devices in the widest sense. Although nanodevices are still in an early stage of development, future research on the field will have to face the requirement of devices integration and miniaturization as already occurred in silicon based technology.

In this chapter we present two different tip-induced effects we found while studying organic thin film materials which can be use to manipulate matter. We start addressing the mechanical induced growth of pentacene molecular layers in section 6.2. The observed phenomena could be used as a SFM nanolithography approach for the nanostructuration at future organic nanodevices. And in section 6.3 we provide a way for peeling a layered organic molecular material when a voltage is applied between the conducting system and the conducting probe of the SFM. The presented results indicate the importance of electric fields on the stability and performance of conducting organic systems at the nanoscale and provide a way to control matter manipulation and/or structuration.

6.2 Mechanical modification of organic thin films

6.2.1 Introduction

Among the variety of application of scanning probe microscopy (SPM), the scanning probe lithography (SPL) techniques constitute a powerful approach for structuring surfaces at the nanometer scale [23, 299–301]. SPL technique possess the versatility to locally modify a wide range of different materials such as metals, organic molecules, polymers and biological molecules. Moreover, the capability of SPM to characterize the surface morphologies of materials make them even a more powerful tool in nanotechnology, since they in-situ combine their capability of fabrication and characterization. Many SPL techniques have been developed in the last decades including force assisted indentation, nanomanipulation [302], dip-pen nanolithography (DPN) [303], scratching [304–306], nanografting [307], pressure induced restructuring [280, 308] or bias assisted electrostatic [309], local oxidation [310] or local resistive state [121, 311] among others.

In this section we present a different type of SPM manipulation in which we mechanically induce the growth of a 3D organic semiconducting film starting from a submonolayer film. The material in which we have performed our studies is the pentacene ($C_{22}H_{14}$) molecule deposited on SiO_2/Si. Pentacene is a polycyclic aromatic hydrocarbon consisting of five linearly-fused benzene rings (see figure 6.2.1), and probably is the most studied organic semiconducting molecule. Pentacene shows a preferential p-type behavior and relatively high field effect mobility. The capability of inducing and modifying the growth of molecular layers by SFM nanolithography could help on the nanostructuration of future organic nanodevices.

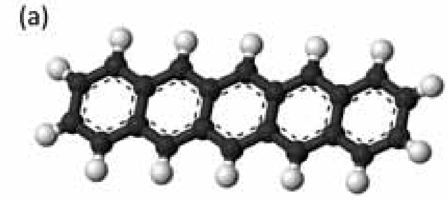

Figure 6.2.1: Molecular structure of the pentacene molecule.

6.2.2 Sample preparation and experimental procedure

The samples employed for the studies presented in this section consist of pentacene submonolayer islands grown on top of Si substrates covered by native SiO_2. The deposition of pentacene molecules was performed in UHV by the organic molecular beam deposition technique (OMBD) (described in section 3.4.4), typically at pressures in range of $10^{-7} - 10^{-8}$ $mbar$. The organic pentacene molecules were purified twice by gradient sublimation before use. The submonolayer material deposition was optimized by calibrating amount of material and rate growth on previous depositions performed on the same type of substrates. Silicon substrates were previously cleaned by successive sonication in acetone and ethanol (each ~ 5 minutes), transferred to the UHV chamber and annealed at a temperature of $\sim 300°C$) ($1h$). All the results presented in this section correspond to a sample consisting of 0.8 monolayer (ML) of pentacene on SiO_2/Si grown at a substrate temperature of around $\sim 25°C$ and a growth rate of $\sim 1/5$ ML per minute.

All the scanning force microscopy (SFM) measurements presented in this section were performed in contact mode (cm-SFM), at room temperature and for relative humidity (RH) ranges: ambient conditions (typically $RH \sim 60 - 80\%$) and low RH (under N_2 environment $RH < 5\%$). Tips mounted in low nominal force constant ($k \approx 0.5$ N/m) V-shaped cantilevers were employed to perform contact mode SFM (cm-SFM) measurements.

6.2.3 Pentacene thin films on SiO_2 : first evidence of tip induced 3D growth

Pentacene thin film structure on silicon oxide surface has been already studied by several authors [150, 312–314]. Fritz and co-workers [313] determined by grazing-angle incidence X-ray diffraction (GIXD) that the pentacene monolayer (ML) on SiO_2 forms a highly crystalline structure which differs from the bulk. The unit cell of the first pentacene layer on SiO_2 is formed by a near-rectangular in-plane with two molecules per unit cell ($a = 5.916$Å, $b = 7.588$Å,$\gamma = 89.95°$) with the molecules adopting a near-vertical orientation and arranged in a herringbone packing.

Figure 6.2.2 presents the cm-SFM topography and corresponding friction signal of pentacene islands on SiO_2. When measuring organic thin films by cm-SFM, to avoid any film compression or damage it is important to keep the measurement conditions in the attractive range and as close as possible to the pull-off force. To check the tip-sample conditions, the adhesion force is systematically determined from force versus distance curves (see sections 3.2.3.1 and 3.2.4.1). The pentacene layer covers a $\sim 75\%$ of the SiO_2 surface and from the topography image (figure 6.2.2 a) two different heights can be appreciated corresponding to the pentacene monolayer and bilayer (the different locations have been labeled in the image). The measured island height is of $\sim 1.7 nm$

and $\sim 3.3nm$ for the monolayer and bilayer respectively. In next section 6.2.4 we discuss in further detail the thickness of the pentacene molecular layers measured in our samples, but we avoid any deep investigation of the structure and surface morphologies of the layers.

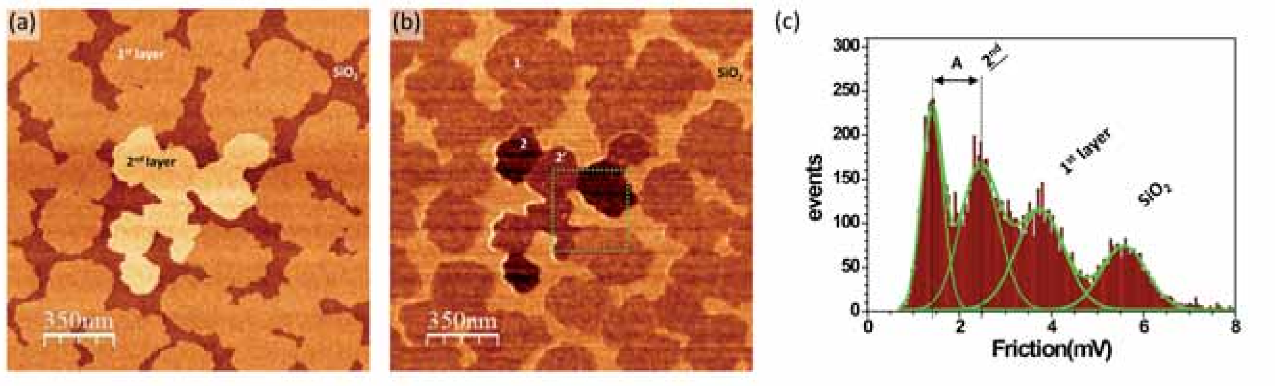

Figure 6.2.2: *cm-SFM topographic image (a) and the corresponding friction map (b) of pentacene mono and bilayer on SiO_2/Si. The friction difference between SiO_2, mono and bilayer of pentacene is determined by the peaks shift in the histogram representation (c) of the location marked in (b).*

The pentacene layers are also distinguished from the substrate by a darker contrast in the friction signal (b), due to the lower frictional force sensed by the tip on them as compared to the bare SiO_2. The friction image presented in figure 6.2.2 (b), built by calculating the mean lateral force of the trace-retrace images (procedure introduced in section 4.4.1), evidence a clear friction contrast not only between the bare SiO_2 surface and pentacene layers, but also between mono and bilayer locations of the organic layers. Interestingly, while the same friction value is observed for the pentacene monolayer regions, two different values are measured for the second layer (labeled as 2 and $2'$ in figure 6.2.2 b). As in the case presented in section 4.4.2, this observation can only be attributed to friction anisotropy (AN) [186, 191], i.e., a different resistance to sliding for different azimuthal orientations of the pentacene domains and the fast scanning direction of the SFM tip. In figure 6.2.2 (c) the determination of the friction force differences at zero load is statistically performed by histogram plots of the friction signal (F) of the location marked in (b). From the relative differences of the corresponding Gaussian peaks we found a ratio of $^{F^1}/_{F^{SiO_2}} \approx 0.7 \pm 0.2$ between the bare silicon oxide surface and the monolayer. The one labeled 2 has lower friction than the first monolayer by a factor of $^{F^2}/_{F^1} \approx 0.6 \pm 0.3$ whereas for the other one labeled $2'$ is $^{F^{2'}}/_{F^1} \approx 0.4 \pm 0.3$ times lower. With respect to the detection of AN between different molecular domains, it was not our aim to make a deep investigation of the structure of the pentacene layer, however we notice that in the present acquisition friction anisotropy is only sufficiently large for the second pentacene layer. Even though the monolayers also consists of domains of molecular domains with different crystallographic orientation grains[315], any difference seems to be below detection threshold in this image. The pentacene molecules on the monolayer present are near-vertical while the ones forming the second layer are a bit tilted, as will be prove in next section 6.2.4, in consequence a less pronounced influence of the relative orientation of the domains with respect to the tip scan direction is expected in the friction signal of the monolayer.

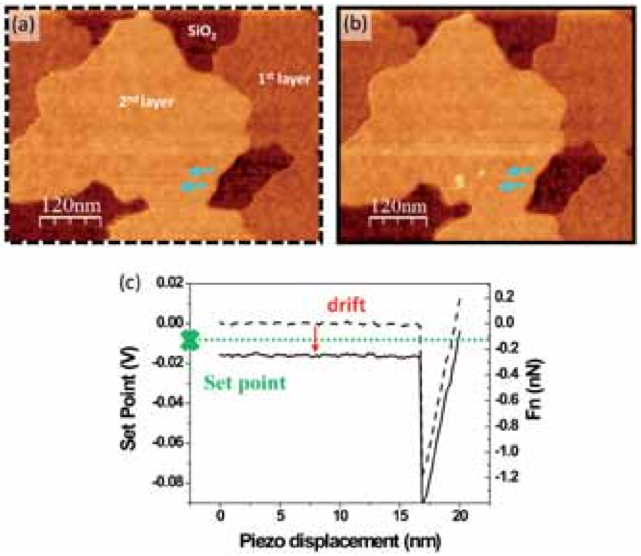

Figure 6.2.3: *First evidence of pentacene multilayer growth. cm-SFM topography images of the same surface location acquired with a time difference of* $\sim 15\,min$. *FZ curves corresponding to the measurement conditions of (a) and (b) are represented in (c) by dashed and solid lines respectively. The green dashed line in (c) represents the set point for both measurements.*

As commented above, commonly, during a cm-SFM measurement the tip sample conditions are periodically checked by mean of a FZ curve experiment in order to prevent any measurement condition variation. The inevitable drift on the tip-sample positioning or/and cantilever-laser alignment usually results in small variations on the position of the laser reflection on the photodiode. This is visualized as a change on the offset of the force versus distance curve and results in a variation of the tip-sample conditions. During a particular experiment performed on pentacene thin film on silicon oxide the sample scanning was left without attention for around 15 minutes and the growth of some pentacene material on a certain location was detected. Figure 6.2.3 shows in (a) the mentioned location where bare silicon oxide and pentacene monolayer and bilayer locations are present. In figure (b) the very same location with two small pentacene islands grown on top of the bilayer are detected. The islands locations have been pointed by blue arrows in both (a) and (b) images. In figure 6.2.3 (c) we present the FZ curves that correspond to the measurement conditions of each image (a and b, in dashed and solid lines respectively). The comparison of the FZ curves shows a small offset variation of around $0.4\,nN$ which, taking into account the fixed set point (in Volts, marked by green dashed line in c) results in a variation of the measurement conditions from attractive to repulsive regime.

This first evidence of material growth motivated us to further investigate the mechanism of organic material modification induced by the SFM tip and about the possibility manipulating in a controlled manner the material structure in desired locations. The next section 6.2.4 is devoted to present the different strategies and experiments carried out, focusing our attention in the ones which were successful.

6.2.4 Tip induced layer by layer multilayer growth

In order to investigate the mechanism of the observed pentacene island growth (figure 6.2.3) different test experiments were performed. The first experiment we carried out was to intentionally change the measurement conditions from the attractive to the repulsive regime as in the case of the experiment described in the previous section (figure 6.2.3). We focused on the center location of figure 6.2.2 (a) and deliberately increase the applied normal force (F_n) into the repulsive regime for a certain number of scanned lines in the top and bottom lines of the scanned area. The horizontal lines profiles of the center of the image (marked by dashed lines in figure 6.2.4 (1)) were always scanned in attractive regime conditions to avoid any film compression or damage. During this experiments we tested loading forces ranging from zero to a few nN in order to test the influence of the normal force on the material modification. The complete experiment consisted of 13 frames and total duration of about 10 minutes (complete movie available in the Supporting Information, movie 7-2-a). Figure 6.2.4 presents some selected frames of this experiment, where the number depicted in each image corresponds to the frame number of the complete movie. The scanned area was of $1 \times 1\,\mu m^2$ (with a 256×256 pixel grid) and the scanning speeds were of$\sim 17\,\mu m/s$ and $\sim 25\,nm/s$ for the fast and slow scan directions respectively.

The process of pentacene multilayer growth starts at the line profiles where the F_n is increased up to repulsive regime set points. Notice how in the bottom lines of frame (3) a rapid increase of the

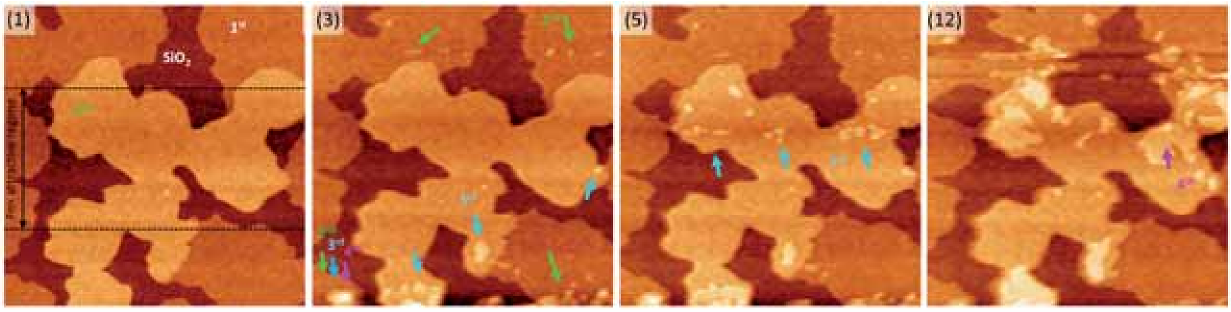

Figure 6.2.4: *Selected sequences of the topography movie (7-2-a) of the pentacene growth experiment. The number depicted in each image corresponds to the number of frame of the complete movie (12 frames in total).(total z scale of 9 nm)*

molecular layers is detected. The growth of second and third layer islands is evident in the bottom-right and bottom center of the image (marked by green and cyan arrows respectively) and even the growth of a second, third and fourth layer island is found in the bottom-left location. From this result seems that the pentacene molecules are dragged by the tip in its motion from some locations to others. Interestingly, the multilayer growth is not limited to those scanning lines where F_n was increased, but also to the central part of the image where the scanning conditions have been always kept in the attractive regime. The presence of a small third layer island is already detected in frame (3), and in (5) and (12) the appearance and growth of those island is much more evident. This finding suggests that the pentacene molecules are not only dragged short distances by the tip, but that are transported by it through longer distances than a few μm. In addition, the enlargement of the island from frame to frame suggests that the pentacene molecules tend to nucleate and self-assembly in location aggregating to already formed islands. We also notice how the growth of new pentacene layers is only found to occur on top of already pre-existing pentacene layers and there is no evidence of new pentacene monolayer formation on top of the bare SiO_2 neither at the borders of the pre-existing initial layers. This finding suggests that the growth induced by the tip follows an island-mode or Volmer-Weber growth mode, i.e., that the lateral and interlayer pentacene-pentacene interactions forming the multilayers are more important than the pentacene-pentacene and pentacene-substrate in the monolayer. This hypothesis could be supported by the fact that the pentacene molecules adopt a standing up nearly vertical configuration in the monolayer, while they adopt a more tilted configuration closer to the thick film crystalline structure in the second and subsequent layers. The different molecular layers thickness is analyzed in detail below.

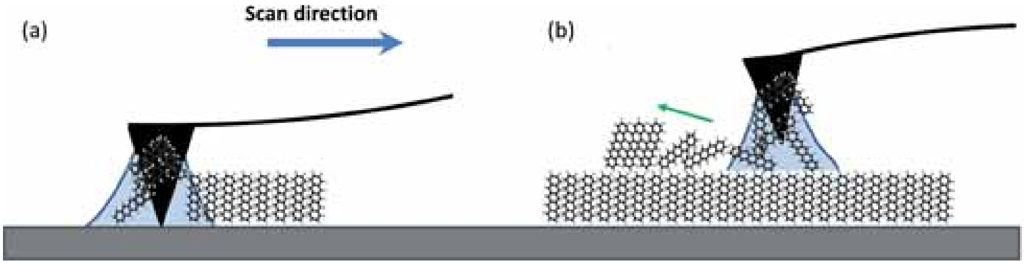

Figure 6.2.5: *Schematic illustration of the proposed mechanism for material drag (a) and deposition (b). The green arrow in (b) represents the self-assembling process of the pentacene molecules ones are deposited.*

Regarding to the mechanism by which the pentacene molecules are transferred from one location to the other, we propose a water meniscus mediated dip-pen mechanism [303]. Figure 6.2.5 presents an schematic representation of the mechanism proposed. When the sample is scanned in repulsive regime condition, the pentacene molecules are dragged and collected in the water meniscus formed in the tip-sample contact (situation a in figure 6.2.5). In attractive condition (situation b), thanks to capillary forces the tip holds in contact with the sample and the accumulated molecules are transferred to the surface where they self-assemble.

Even if there is an on going debate on the detailed mechanism for ink transport and diffusion, the deposition of the ink depends on different factors such as the properties of the tip (size, wettability etc) and substrate, tip–substrate spacing, time and the temperature [300]. We tested to vary the water meniscus size by changing the relative humidity from low humidity to ambient conditions (typically $RH \sim 60 - 80\%$), but no evidence of increase of the amount of transferred material was detected. We also tested to deliver pentacene molecules in a non continuous manner, that is, by inking the tip on a pentacene island, driving the tip out of contact, changing the location, driving the tip again to contact and trying to deposit the molecules in this new area. However, none of the tested experiments were successful.

With the experience gained after performing those multiple tests, we designed a more systematic experiment in order to study the transfer of molecules from one location to another without damaging the pre-existing molecular layers. The experimental procedure is presented in figure 6.2.6. We first choose an area of the as prepared sample, containing bare silicon as well as pentacene regions of one and double layer thickness, figure 6.2.6 (a). We define two parts on this area: i) The bottom part (delimited by the gray dashed line) that will be referred as the loading region, from which we will collect pentacene molecules (ink) with the tip by scanning in the repulsive regime, and ii) the upper part of the area (from the gray line to the top image) that will be always scanned in the attractive regime to transfer the molecules back to the surface while avoiding damage of the initial molecular layer. We will refer to this later as the delivering region.

During a complete experiment, the load is alternatively changed from $\sim 1\,nN$ (in the repulsive regime) to a given small and negative load value ($\sim -0.4nN$), e.g. dashed line in the corresponding FZ curve of 6.2.6 (c), depending on whether the loading or the delivering region is scanned, respectively.

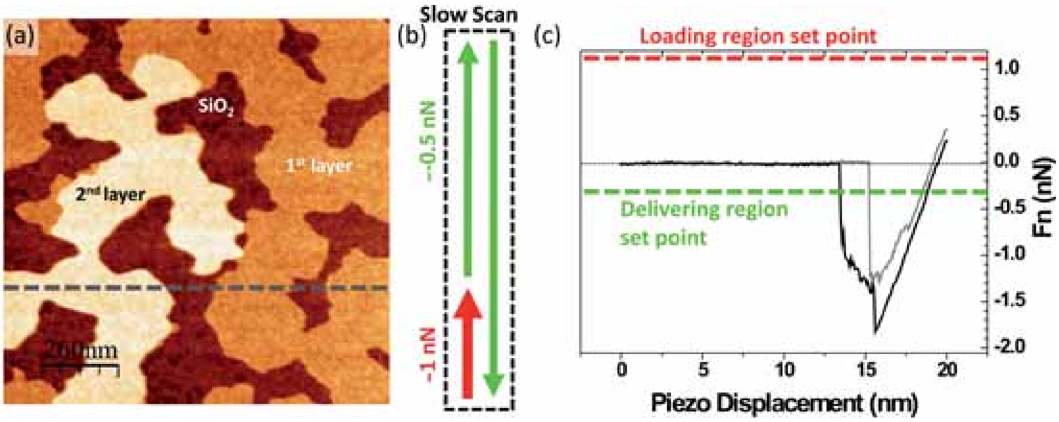

Figure 6.2.6: *The experimental procedure sketch of the experiment presented in figure 6.2.7 is shown. (a) cm-SFM topographic image of the chosen location with red and green vertical arrows in (b) pointing the slow scan direction loading (in red) and no-loading regimes. The loading and no-loading* F_n *conditions are marked in red and green with reference to the force versus distance curve presented in (c).*

An example of such experiment is presented in figure 6.2.7, where only the delivered region of selected frames out of 108 obtained during about 2 hours are shown. The scanned area was of $1.3 \times 1.3\,\mu m^2$(with a 512×512 pixel grid) and the scanning speeds of$\sim 37\,\mu m/s$ and $\sim 27\,nm/s$ for the fast and slow scan directions respectively. The complete experiment is available in the Supporting Information in movie format [1].

---

[1] Movie 7-2-b corresponds to the topographic signal of the complete experiment area including the loading and no-loading regions, whereas Movies 7-2-c and 7-2-d correspond to the topographic signal of the delivering region. The z scale color code of Movie 7-2-d can be found in description 6.3.5.

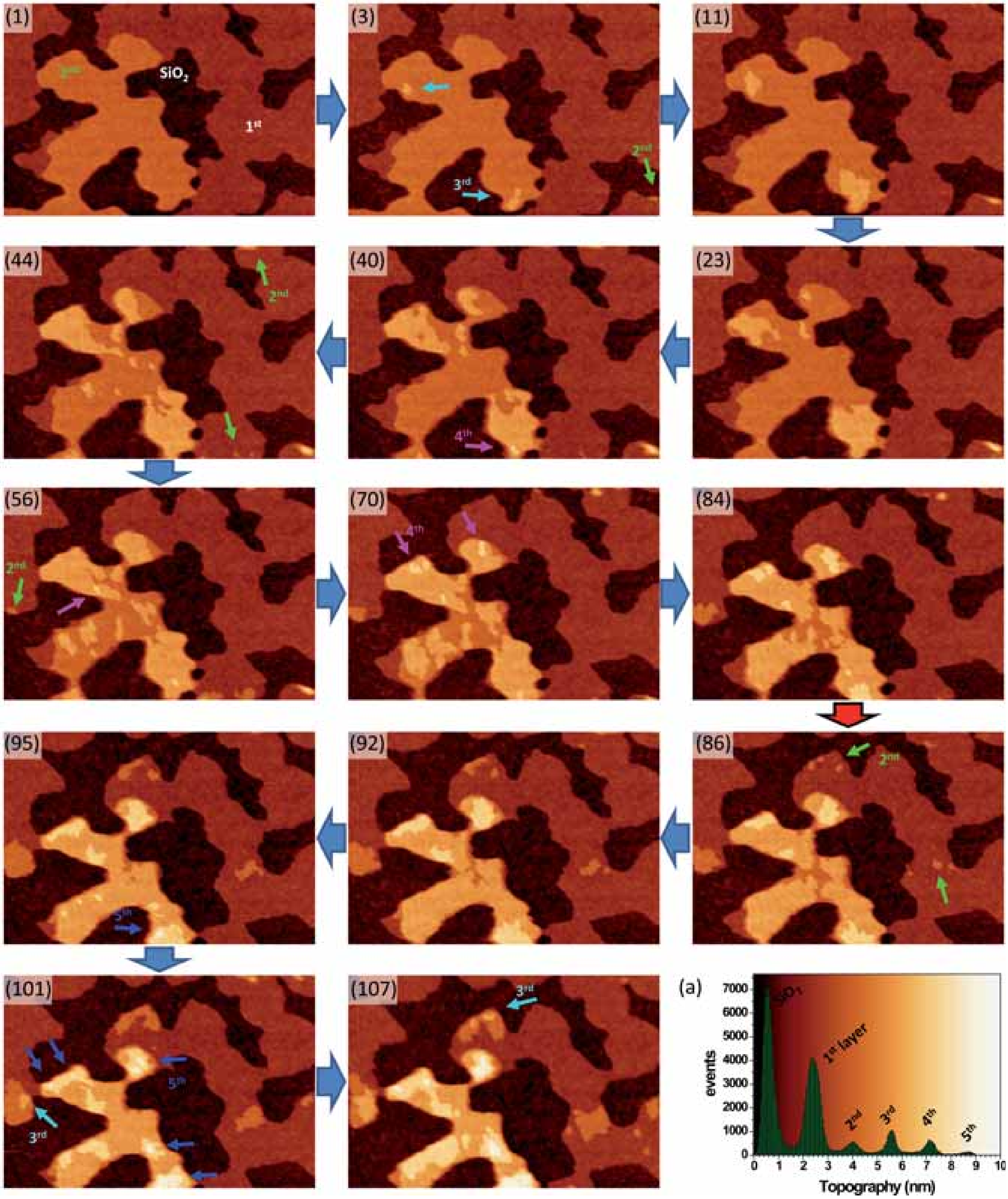

Figure 6.2.7: *Selected sequences of the topography movie (7-2-b) of the pentacene growth experiment described in 6.2.6. The number depicted in each image corresponds to the number of frame of the complete movie (108 frames in total). (a) histogram representation of the topographic signal data of 107 frame with the color code of all the images as back ground (total z scale of* 10 *nm).*

Figure 6.2.7 present some selected topographic pictures illustrating the process of the pentacene multilayer growth in the delivering region. The image number depicted corresponds to the number of frame of the complete movie. The initial surface, consisting of bare SiO_2, monolayer and bilayer regions is seen in frame (1). The first stage of the formation of a third layer is revealed by the detection of small islands in (3), in addition to the appearence of a second layer level at some places. In the subsequent frames $(11, 23, 40, 44)$ this third layer islands enlarge while no other island formation is detected. Only a small island in a fourth layer is detected in (40) but disappears in next frame. New small island regions of second layer and third layers are detected in (44). The growth of a fourth layer starts at (56) and the continuous growing can be followed in the subsequent frames. As was the case in the experiment of figure 6.2.4, we can conclude that the formation of a third layer is favored in comparison to a mono or bilayers islands nucleation. From frame (86) on the control of the applied F_n over all the scanned area was lost. Though F_n was mainly kept in the attractive regime it can not be discarded that some of the scans were done under repulsive regime conditions. Interestingly, from this frame on the growth of bilayer islands is found (marked by arrows in 86). An in addition, the fourth layer islands growth seems to increase faster and even a fifth layer is formed from frame (95) on. We think that the reason for this faster growth, and even the growth of a second layer, stem from the fact that larger number of molecules are collected by the tip under this conditions. Under this F_n not completely controlled scan conditions the tip does not only collect molecules from the loading region, but also molecules from the borders of the pre-existing initial layers in the delivering region. Notice how the pre-existing initial layers get narrowed in (107) in comparison to (84).

A thorough analysis of the topographic difference between the different pentacene layers is done in figure 6.2.8. The height difference between the silicon oxide and first, second and third pentacene layers is appreciated in the line profile presented in 6.2.8 (c) of the location marked in (a), and is determined by different topographic height histograms (corresponding to the complete image a). An example of the topography difference between third, fourth and fifth pentacene layers can be determined is presented from the histogram plot (figure 6.2.8 e) that corresponds to the area marked by a dashed square in (d). The histogram plot of the complete image (d) is presented in (f) where the six peaks corresponding to the silicon substrate and five different pentacene layers are distinguishable. By the detailed inspection of the height difference over several locations, first

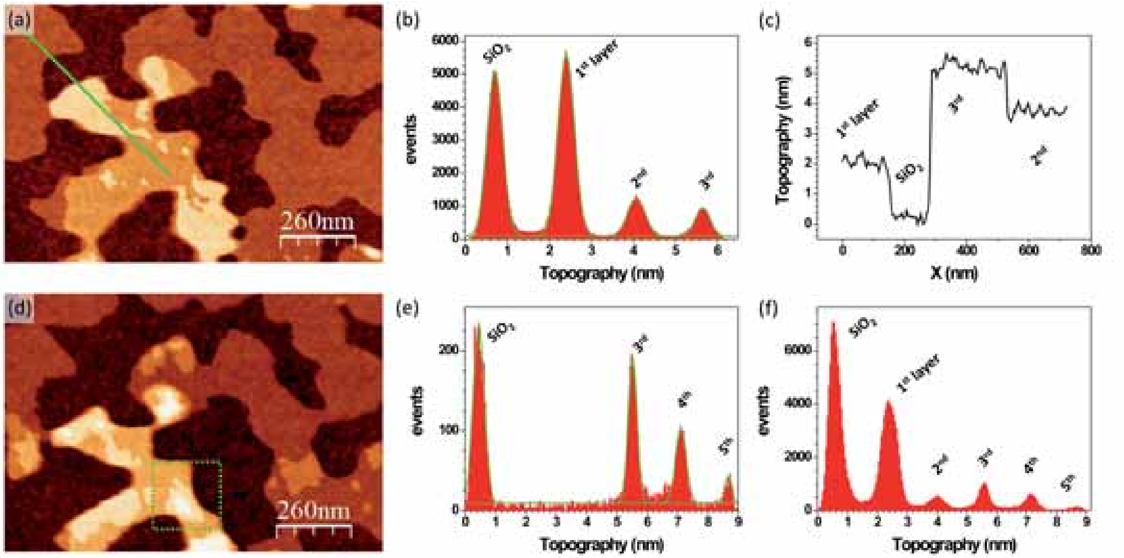

Figure 6.2.8: *(a) and (d) Topographic images corresponding to the 44th and 107th frames of the experiment presented in figure 6.2.7. (b) presents the histogram representation of the topographic signal of the complete image (a). The corresponding line profile presented in (c) shows the topography difference between adjacent pentacene layers. (f) and (e) show the histogram representations of the topographic signal data of the location of the complete image (d) and the location marked in (d) respectively.*

pentacene layer is found to have a thickness of $d_1 \approx 1.7 \pm 0.3\,nm$, the second has a thickness of $d_2 \approx 1.6 \pm 0.3\,nm$ thickness, and the third, fourth and fifth present $d_i \approx 1.5 \pm 0.3\,nm$ $(i = 3, 4, 5)$. The estimation of the error in the thickness of the layers is done by adding in quadrature the roughness of each region.

Pentacene thin film structure on silicon oxide surface has been already studied by several authors [150, 312–314]. The pentacene thin film on SiO_2 grow in a so-called *thin film structure* layered structure with a layer spacing of around $1.55nm$ [150] Fritz and co-workers [313] determined by grazing-angle incidence X-ray diffraction (GIXD) that the pentacene monolayer (ML) on SiO_2 forms a highly crystalline structure which differs from the bulk, and they measured by SFM a thickness of $d_1 \approx 1.60 \pm 0.06\,nm$ for the pentacene monolayer (ML). Ruiz and co-workers studied the structure of the molecular layers from submonolayer to multilayers [314] by GIXD and obtained a molecular layer thickness of $d_i \approx 1.543\,nm$ on multilayers. Our results slightly differ for thicknesses of the first and second layers. From our results $(d_1 > d_2 > d_i \; for \; i = 3-5)$ we that the pentacene molecules adopt a near-vertical orientation for the monolayer, they start to tilt a bit in the second layer and they adopt a "thick film" tilt configuration from the third layer on. This finding supports the hypothesis we pointed above regarding to favored nucleation of pentacene molecules in locations where they adopt a more tilted configuration closer to the thick film structure. That is, the grow of third, fourth, etc layers would be favored in the contrast to the second and first layers. This is exactly the case in the experiments presented above.

6.2.5 Summary

We have shown that the layer by layer growth of pentacene molecules can be induced by the SFM tip. This process allows the preparation of layers of homogeneous and well ordered molecular layers and could be used as a top-down strategy for the nanostructuration of organic molecular nanodevices. In addition, we would like to note that this procedure has been also extended to other organic semiconducting molecules as diindenoperylene (DIP), N,N'-dioctyl- 3,4,9,10- perylene tetracarboxylicdiimide ($PTCDI - C_8$) deposited also onto SiO_2/Si, supporting the feasibility of the wide applicability of the method.

6.3 Electropeeling of organic conducting material

6.3.1 Introduction

The interaction of organic materials with electrodes and their behavior under electric fields is a topic of vital significance, and one about very little is known in the nanoscale range. In this section, we provide evidence for the peeling of organic molecular material when a voltage is applied between the conducting system and the conducting probe of a scanning force microscope (SFM). The rate of removal of the material from the surface of the bulk conducting supramolecular material depends on the potential applied, but can clearly initiated at very low voltages as little as 200 mV for this particular material. The results indicate the importance of electric fields on the stability and performance of conducting organic systems at the nanoscale.

Very little is known about the effects of electric fields on organic conductors at the nanoscale, yet they are central to device performance because if any significant morphological or structural change comes about on applying potential a consequent modification of electrical transport properties will result [12, 316, 317]. It is known that essentially insulating self-assembled monolayers suffer electrical breakdown at potentials between 1.5 and 3.2 V, depending on the metal surface and type of molecule [318]. Also, multiwalled carbon nanotubes have been shown to be sequentially stripped of their concentric layers at potentials above 1.5 V in air (because of oxidation of the carbon material [319]) as well as in vacuum (because of thermolysis caused by the electrical current [320]). In conducting organic materials, there is precedent of the lithography of conducting polymers, using scanning force microscopy (SFM)-assisted electrostatic lithography whereby the electric field makes a (thermally induced) softened material flow [309, 321], as well as by local electrochemistry on a polymer [322, 323]. In all these cases, which involve different mechanisms of change in the various materials, relatively high potentials are implied. In contrast, we will show that very modest positive potentials are capable of peeling the surface of a nanostructured conducting organic material because of the electric field present between the material and a conducting SFM tip.

The material in which we have performed our studies is based on the 2-(thioacetooctadecylamide)-3-methylthio-6,7-ethyldithiotetrathiafulvalene π-electron rich molecule **1** (figure 6.3.1), containing an amide group to enable self-assembly through hydrogen bonds as well as a long alkyl chain which provides solubility and possibility of van der Waals interactions between the molecules themselves as well as with solvent. The molecule **1** was synthesized during the thesis work of Dr. Josep Puigmartí, from the group of Prof. D. Amabilino (from the ICMAB, who helped us to prepare the thin films).

1

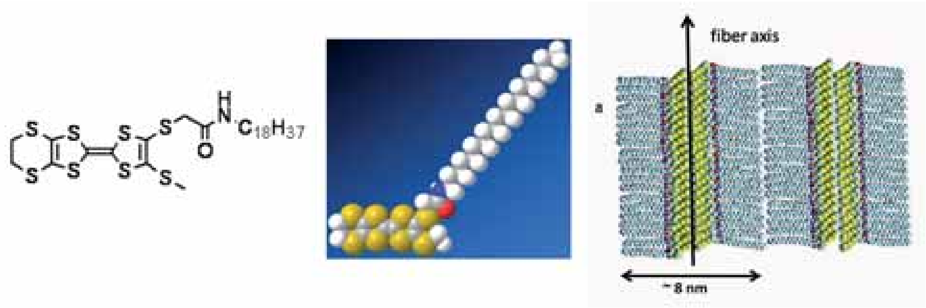

Figure 6.3.1: *The chemical structure of TTF derivative* **1***. This compound forms organogels in solvents such as hexane. The organization of the molecules in these gels is in a head-to-head arrangement with hydrogen bonds between the amide groups and* π*-stacking in between the TTF units, as shown in (right). Between these stacks, TTF derivatives can also enter into side-on sulphur-sulphur contacts.The diameter of the fibers is estimated from the individual molecular dimensions.*

The molecule forms a gel when warmed up in hexane followed by cooling of the resulting solution. Organogels are a very good route for the preparation of conducting nanoscopic fibers [324–326], because the fibers are formed spontaneously in a material which can be applied to a surface. The use of derivatives of the π-electron donor tetrathiafulvalene (TTF) in these systems has been shown to provide bulk semi-conductors [327], and in the case of **1** even nanofibers with apparently metallic conductivity [328]. The gels of this material are hypothesized to contain head-to-head TTF tapes which then interact in a side-on way (figure 6.3.1), as seen in physisorbed multilayers of the same molecule on graphite [329]. It is important to note that the long alkyl chains in **1** provide an insulating layer in between fibers oriented in the perpendicular side-on direction with respect to the interaction in figure 6.3.1 (b). While thin films of organic complexes of this type of donor have been used for data writing using a scanning tunneling microscope with voltage pulses of 4 V [330, 331], we have found that much lower potentials can have dramatic effects on conducting films of the TTF-derived material. The weak non-covalent interaction between layers leads to a removal of layers of material under application of an electric field.

6.3.2 Sample preparation

The xerogel material which is the subject of this study is quite rough if the gel formed by **1** is deposited as such on any surface and is then allowed to dry. This material is relatively difficult to image using SFM because of its irregular nature. Therefore, we sought a protocol which would produce thinner, flatter and more homogeneous samples. After this sample preparation, the surface morphology that resulted was a rather smooth thin film.

A drop of a solution of **1** in hexane (1 mg per ml) above the gel forming temperature was deposited onto freshly cleaved highly oriented pyrolytic graphite (HOPG) and was allowed to cool in air while the hexane evaporated, leaving a smooth thin film of **1** on the surface. The sample was then doped by exposing to iodine vapors for 2 minutes to generate the conducting material. To convert this doped material from the initially formed α phase into the more stable β phase, the sample was warmed at 80 $^\circ C$ for 30 minutes [328].

Earlier studies have shown the semiconductor-like behavior of this resulting β phase and that thermal treatment decreases sample macroscopic resistance in an order of magnitude (at room temperature since around 10^5 Ω to 10^4 Ω, figure 6.3.2 a) what provides conductivity around $3-5\times10^{-3}\Omega^{-1}cm^{-1}$ for ambient conditions. Moreover, the importance of the thermal treatment applied straight afterwardsof doping has been found relevant for this resistance decreasing. The doping time and iodine quantity in the initial α phase do not affect to the β phase conversion once thermal treatment is applied. Besides, some CSFM experiments have exhibited local metallic

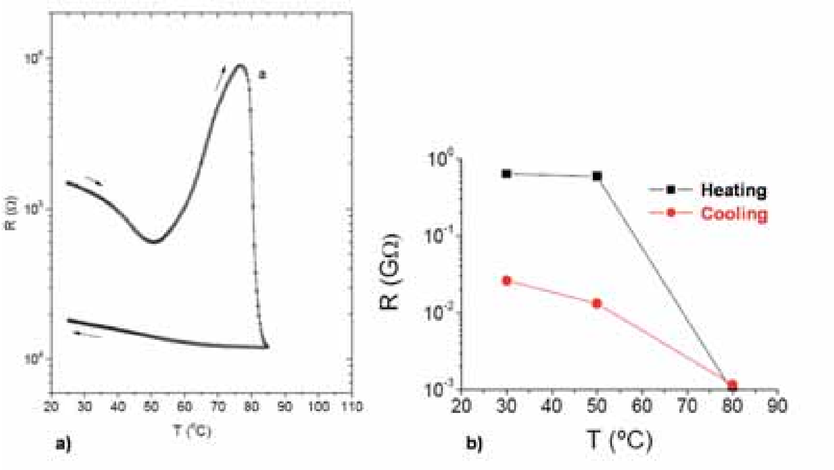

Figure 6.3.2: *Resistance-Temperature dependence of 1 xerogel doped with iodine. (a) four-probe dc resistance macroscopic measurement for a 2 minutes doped xerogel. (b) Local metallic behavior CSFM in measurements for a 10 minutes doped xerogel. (Graphics from Josep Puigmartí i Luis Thesis [332]).*

character, with resistances in the range of $10 - 100\, M\Omega$ once the thermal treatment is done (figure 6.3.2 b). Those previous CSFM results [328] are in agreement with the conductive measurements we carried out.

6.3.3 Experimental procedure

The CSFM measurements were performed under low humidity conditions ($RH < 5\%$, obtained in a N_2 atmosphere) using a commercial silicon Cr/Pt coated probes (Budgetsensors [36]) with cantilevers of nominal force constant of $k \simeq 3\, N/m$. To check tip–sample conditions, the adhesion force was systematically determined from force versus distance curves prior to and after each conductivity experiment. The same tip was used in all the CSFM experiments presented.

In order to minimize tip-sample contact and preserve the tip conductive coating, the first tip to sample approximation and choice of surface location was made in the dynamic mode (dm-SFM). Only once after, the conducting tip was placed in direct contact with the sample, under controlled load, i.e. by using a normal force feedback and the current was measured between tip and sample. The sample was always grounded and the voltage was applied to the tip. Although HOPG was used as a substrate, the direct electric contact to ground is established through a silver epoxy drop at the film border.

The conducting response of the sample surface was obtained by following different strategies:

i) Simultaneously acquiring topographic images z(x,y) and current maps I(x,y) over a given region at different voltages, what allows performing current versus voltage "movies" avoiding mechanical invasion (no film indentation) by using the contact operation mode at the lowest possible applied load needed, which is previously determined from force spectroscopy curves by method (iii).

ii) Simultaneously acquiring topographic images z(x,y) and current maps I(x,y) over a given region at constant time intervals, for a fixed voltage. This method serves to test the non invasive character of the tip scanning as well as determine the threshold voltage for the peeling process.

iii) Using the so called 3D modes, which are an alternative way of acquiring data (see section 3.2.5.4), in the $f_i(V,z)$ approach in order to quantify and separate the force and voltage induced effects (as film deformation or indentation) in the fibers films during the tip indentation.

6.3.4 Results and discussion

The topographic SFM images of the doped xerogel (figure 6.3.3) show that not only is the film quite homogeneous in thickness, but the fibers have a "muscular-like" appearance in contrast to the much more random morphology generated by applying a piece of the cold gel onto the substrate [328]. Thus, the present processing procedure produces areas of material in which relatively straight bundles of supramolecular fibers extend over several tens of microns in length.

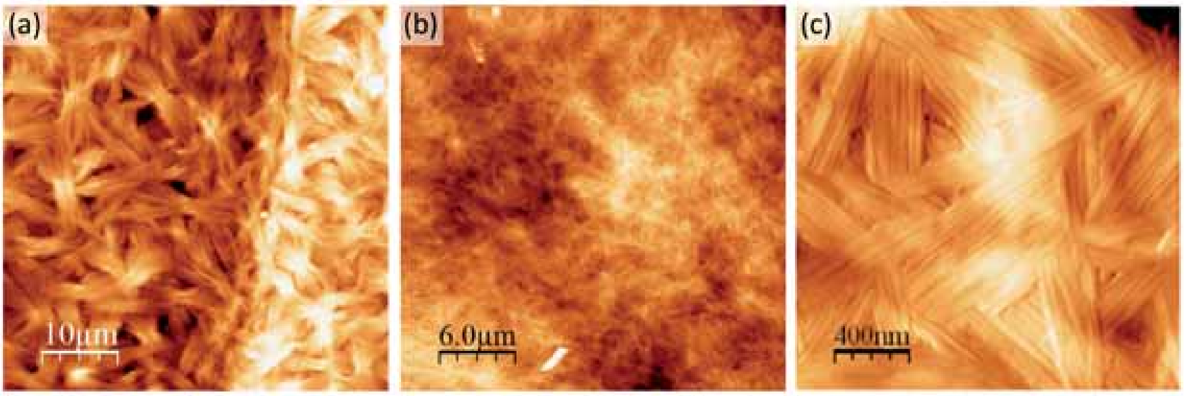

Figure 6.3.3: *Topographic SFM images taken at different magnifications showing the bundles of fibers formed in the xerogel thin film. Topography merge derivate image (right). The surface roughness measured as the root mean square is of about 15nm. Total z-scale: (a) 0-900nm; (b) 0-300nm; (c) 0-100nm.*

The fiber-like film homogeneously covers the graphite surface reproducing the substrate steps and has a low surface roughness in terms of root mean square ($rms \approx 15nm$) over areas as large as several hundreds of square micrometers. The measured fiber width is of about 8-9 nm, in agreement with the expected molecular organization (see figure 6.3.1). Because of the bundle appearance the individual fibers cannot be seen complete, but each fiber is, at least, several tens of micrometers long. Moreover, longitudinal interconnection between fibers is evident, as confirmed by the conducting experiments. The correlation between the topographic details and the simultaneously acquired current maps is perfectly established in the images shown in figure 6.3.4, where the error signal (ES) and the current sensing force microscopy (CSFM) images are shown for a negative tip voltages (Vtip= -1V) at which no film damage was observed. The electropeeling process has also been observed at negative tip voltages. However, the threshold or breakdown onset value appears to be lower for positive than for negative tip voltages. This is an additional support to rule out the sweeping effect of the SFM tip. The ES signal values supplied by the SFM feedback when imaging at constant applied load mimic the topographic derivative, thus providing an excellent way to correlate the electric field effect with changes observed in the surface relief. The experiments indicate that the measured electrical current flows between the tip-fiber point contact and the grounded Ag contact (at the film border), all along the fibers, i.e., mainly parallel and not perpendicularly to the organic film surface. To give evidence of that hypothesis, a couple of current paths have been marked by arrows in the figure. In fact, even if the bundles cross each other, current is measured along the complete length of each fiber, meaning the current flows mainly along its axis rather than between fibers.

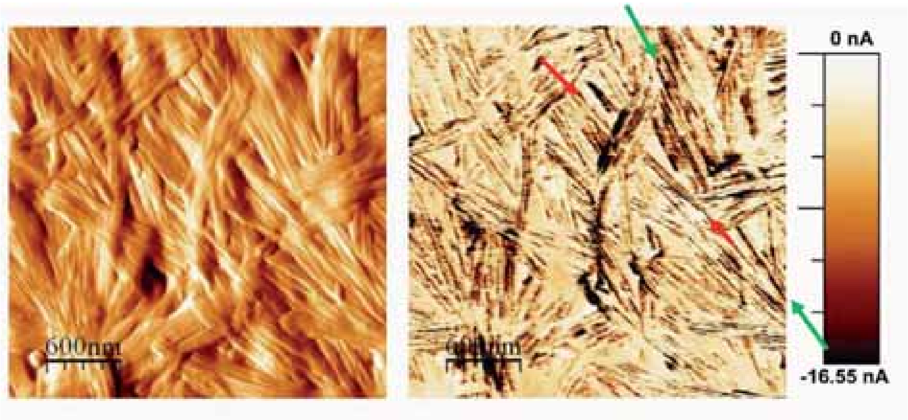

Figure 6.3.4: *Simultaneous error signal (ES, left) and current sensing force microscopy image (C-SFM, right) taken at a tip voltage of* $V_{tip} = -1V$. *The colour code scale corresponds only to the CSFM image and gives the measured intensity. The arrows indicate two of the current paths (dark lines) showing that the current flows along the fibers axis..*

Figure 6.3.5 shows an example of the morphological disruption during the electropeeling process for positive tip voltages. The process starts at the very end of the fibers, which are peeled out along their axis as shown in some of them by the arrows in the figure. As will be put forward, this is not a mechanically-induced [333] but a voltage-induced disruption. Because electropeeling starts mostly at the fiber extremes and point defects, in order to facilitate the observation, some fibers at the topmost surface of the film were intentionally cut by performing a series of load induced indentations by means of the 3D modes strategy. After this treatment, the applied load was decreased to a value below the indentation onset (close to the pull off force) and simultaneous topographic, error signal and current movies were obtained by computer-aided monitoring of the same area at constant voltage intervals.

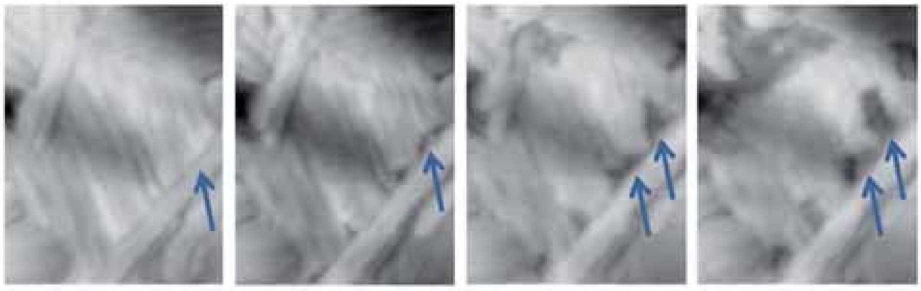

Figure 6.3.5: *SFM topographic images (750 nm x 920 nm) of the xerogel surface film obtained at different tip voltages* (V_{tip} = 0, 2, 3 *and* $4V$)*. The arrows show that the electropeeling process starts at the very end of the fibers, which are longitudinally peeled out.*

To make clearer the correspondence between morphological changes and local electric field effects, the merged ES and CSFM images are presented in figure 6.3.6 (left column) besides their corresponding topographic images (right column). Each couple of images in the figure corresponds to selected sequences of the respective movie. The top left frame taken at 0V, which only contains the ES data (I= 0) and its corresponding topographic image, where some of the intentional marks are indicated, serve as the time reference (t= 0).

In this particular case, the complete topographic and current movies (available in the Supporting Information Movies 7-3-a and 7-3-b, respectively) consisted of 20 frames and a total duration of about 2 hours obtained at constant voltage intervals, from frame to frame, of $\Delta V_{tip} = 200mV$, ranging from 0 to 4 V. Some selected pictures illustrate the process. Labels at the left top of the images indicate the corresponding tip voltage (figure 6.3.6). The top and bottom left images are

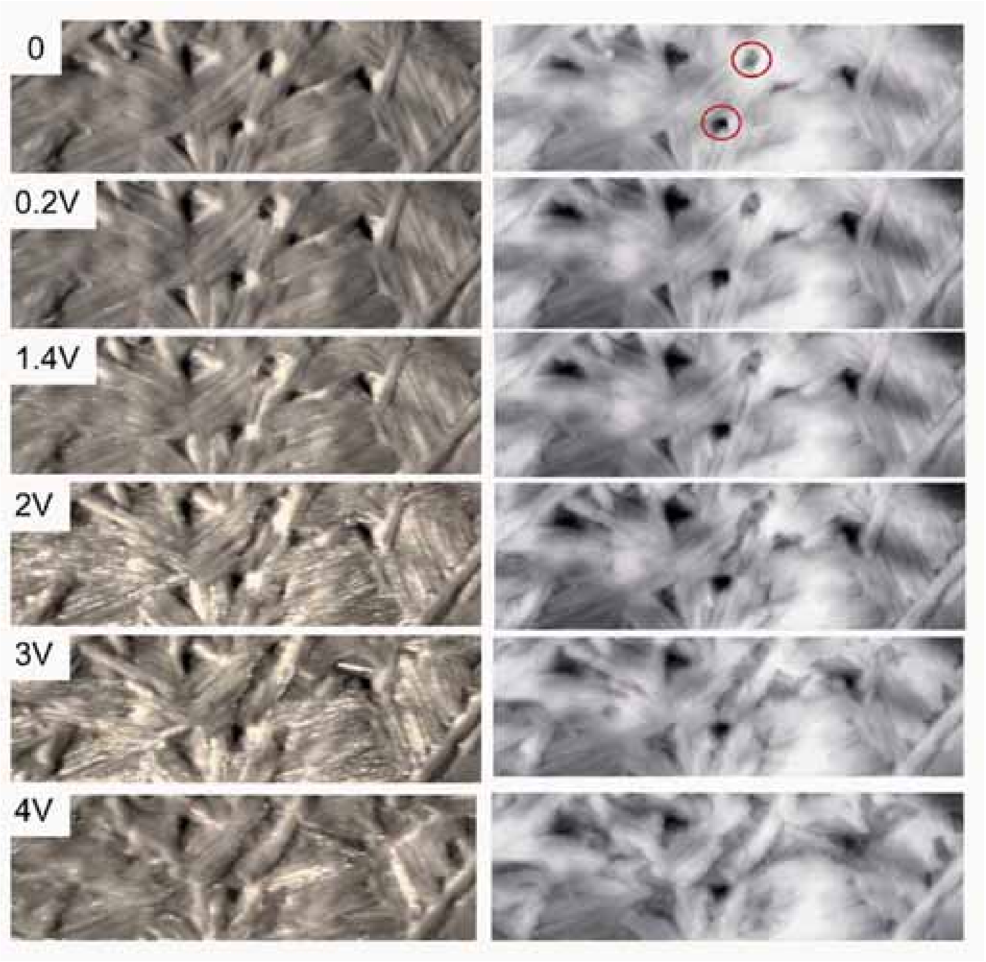

Figure 6.3.6: *Selected sequences of the current map (merged ES and CSFM) movie and the corresponding topographic sequences of the doped film of* ***1****. The tip voltage range is 0 to 4 V from top to bottom. Intentional indentations (circled) enhance the process.*

the initial and final states, respectively. The voltage is increased as going from top to bottom. At 0.2 V some current intensity was already detected at the defects borders, and as will be described below this can be considered, in this case, the onset of electropeeling at positive voltages. Voltage excursions beyond 0.6 V resulted in clearly observable morphological changes. The images taken at 1.4 V serve to see that the electropeeling process starts at specific locations (defects and fibers open extremes) where the maximum current is detected. At intermediate voltages (2 V), straight bright lines appear along the fibers, indicating the current flux path. As the bias is progressively increased, the current lines become shorter and shorter until they eventually disappear. Comparison of the current image with the corresponding topographic one reveals that we are dealing with a phenomenon involving longitudinal fiber disruption accompanying the rapid passage of an

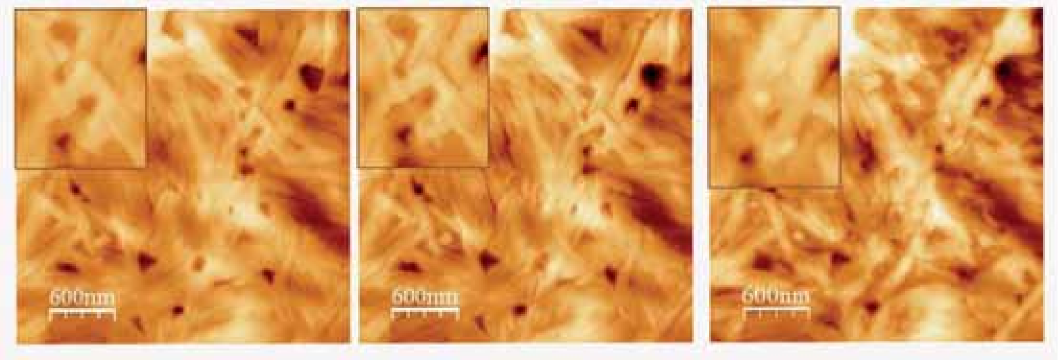

Figure 6.3.7: *Topographic SFM images showing the damage produced on the doped xerogel surface during the electropeeling process. Images taken at* $V_{tip} = 0$, 1.4 *and* 4V. *The damage is clearer around some indentation marks intentionally made on the surface. The magnifications (insets) illustrate the one fiber layer peeling.*

electric front. Interestingly, as will be demonstrated below, the fibers are removed in a layer by layer fashion following what results in a surface peeling.

Evidence for the layer by layer peeling is summarized in figure 6.3.7 and figure 6.3.8. The three large area images in figure 6.3.7 correspond to the topographic relief at three moments of the movie. The film disruption is obvious; a relatively homogeneous initial fiber-like film starts peeling out around pre-existing defects. The fibers are eliminated leading to a surface which appears dramatically different to the original one. However, though the morphological aspect has completely changed, the true surface roughness in terms of rms has not changed significantly, and remains at approximately 10 nm over more than ten square micrometers. Careful inspection of magnified regions (insets) reveals that the reason for this observation is that fibers deeper in the film are not removed till the ones on top are completely removed. The extremely flat region in the last situation (right) permits measurement of the thickness of the removed layer, which turns out to be $\sim 8\,nm$, in excellent agreement with the expected lateral dimensions of one fiber. Figure 6.3.8 further illustrates this effect. Images at the top-left (figure 6.3.8 a and b) show how the opening of a hole (one layer deep) uncovers the underlying film. In Figure 6.3.8 (e) comparison between the line profiles taken along the same locations of the corresponding topographic images in (c) and (d) reinforces the one-layer-deep peeling of the fiber-like film (the peeling of the one fiber layer from c to d is well observed in Movie 7-3-c, available in the Supporting Information). A further convincing test is presented in figure 6.3.8 (f). In this topographic image up to three layers are exposed because peeling out of the second layer of the xerogel film already started at the voltage employed (4V). A line profile (figure 6.3.8 g) from the deepest layer and crossing all three levels to the topmost one, demonstrates the layer by layer removal mechanism.

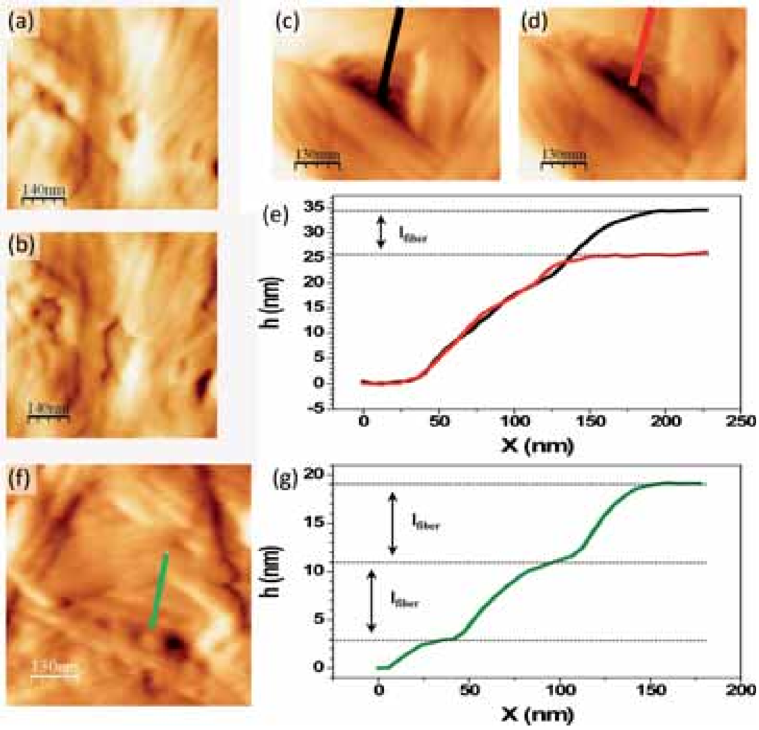

Figure 6.3.8: *Topographic cm-SFM images of three regions (a-b, c-d and f) of the doped gel film surface. After peeling the outermost fibers of (c), the second layer is exposed in (d). Line profiles (e) between two situations, before (black) and after (red) electropeeling reveal that, in this location, only one fiber deep layer has been removed. Topographic image (f) shows how the second layer of the xerogel film is peeled when tip voltage is increased ($V_{tip} = 4V$). As a consequence, three layers are exposed. The line profile (g) (with height origin at the deeper layer) serves to demonstrate the layer by layer mechanism of the electropeeleing.*

Conversely, when the voltage is kept to low values, peeling of the film only occurs after relatively long periods of time. This is illustrated in figure 6.3.9, which by means of selected sequences shows the film surface while continuously scanning at a constant and very low positive tip voltage ($\approx 200mV$). Electropeeling is also observed but much longer times are needed (the complete simultaneously acquired topographic and current movies are available in the Supporting Information, Movies 7-3-d and 7-3-e, respectively). In this case the movies consisted of 103 frames and the time elapsed from the first (top left) to the last (bottom left) situations was as long as 11h. These two frames are considered as corresponding to the initial and final states, respectively. As seen in the figure, at this low bias, our sensitivity was not enough to detect intensity along the fibers, where the tip is in contact with the alkyl chains of 1, located at the fibers shell. However, though lower than 0.5 nA, current was measured at the end of the fibers, the only locations where the tip directly contacts the π-stacking in between the TTF units, reachable at the open side of the conducting core of the fibers. As time passes while imaging at the same tip voltage, the fibers retract from their end and along their axis, which remains being the conducting path (between tip and ground), without the need of higher voltages. Because 200 mV was the lowest voltage at which electropeeling was observed, it is considered as the threshold voltage for the process. It is important to note that images at $V_{tip} = 0$ taken under the load employed during this movie, were obtained without apparent damage, within the same time scale, on defect free areas of the same sample. This demonstrates the non invasive effect of the scanning tip in all experiments presented here and strengthens the reported peeling as material removal in a voltage induced controlled fashion.

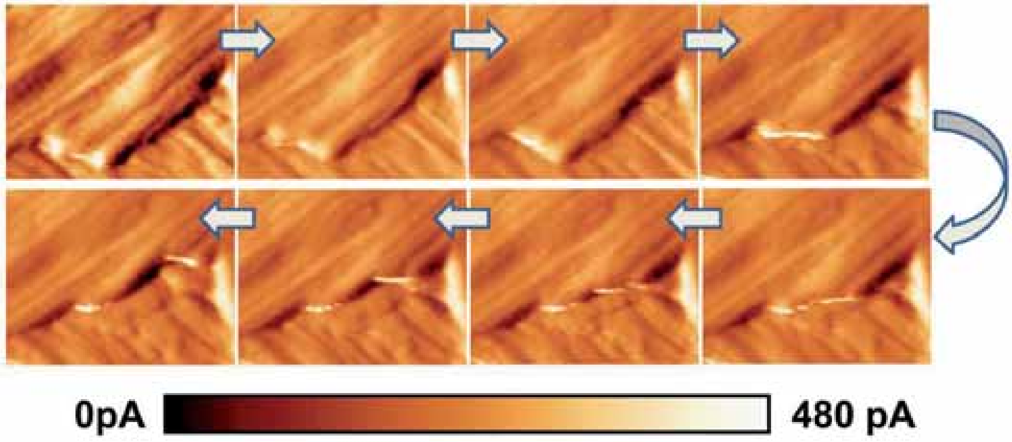

Figure 6.3.9: *Current maps (merged ES and C-SFM) at different time intervals extracted from larger frames of a real time movie taken at a constant* ($V_{tip} = 200V$)*. The lateral size of each image is* $415\,nm \times 320\,nm$*. Time evolution is indicated by the solid arrows. The time interval between frames is of about 80 min, with a total duration of the movie of about 11h.*

It is known that the conduction pathways in organic material depend on the internal molecular structure of the individual entities (building blocks) forming the organic conductor as well as the way they are packed, in the case presented here into fibers. The fact that electric intensity is observed only on the remaining part of the fibers during the peeling process (Figure 6.3.6), indicates that the current flows predominantly along the fiber axis (parallel to the surface) and not so much between piled up fibers (perpendicular to the surface, although this process must occur to some degree in order for the material to be a bulk conductor). This hypothesis is consistent with a conduction pathway through the π-orbitals overlapping between adjacent TTF molecules forming the fiber (see figure 6.3.1), similar to the situation in the crystalline state in this kind of molecule in a mixed valence stack [334]. The overall conduction pathway along and between fibers is not evident but, as commented above, clearly implies interconnection along the fibers rather than parallel inter-fiber connection. Adjacent (parallel) fibers are in contact through the non-conducting alkyl chain shell surrounding the TTF conducting core of the fibers and consequently, transversal inter-fiber conduction is disfavored. This hypothesis is also supported by the fact that higher voltages are needed to induce current through freshly peeled and defect free fibers, which are left exposed to the clean N_2 atmosphere (2% RH) after removal of the topmost layer. In figure 6.3.10 the CSFM controlled electropeeling reported here is schematically explained.

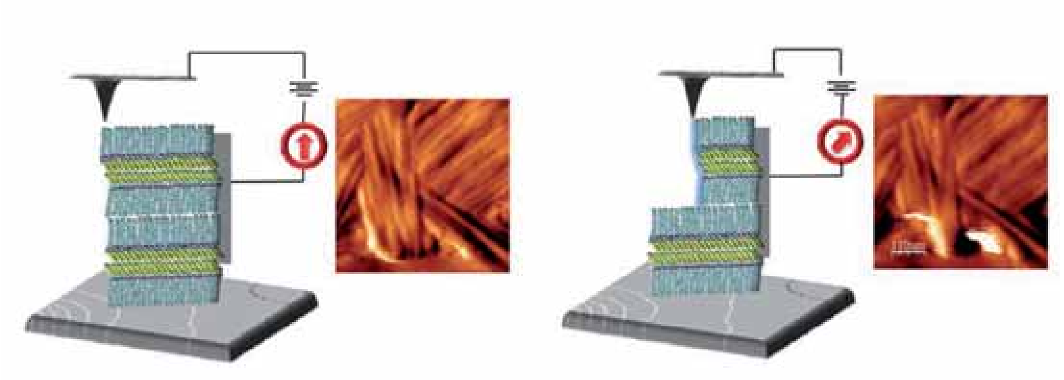

Figure 6.3.10: *Schematic illustration of the proposed mechanism for material removal. The electrical contact between tip and molecular film is established via a silver epoxy drop at the film border (gray mark)..*

From correlation between the applied voltage and the detected current in the carried experiments, we can conclude that the conducting resistance along the TTF stacks is in the $10-100M\Omega$ range, what is in excellent agreement with the previous studies mentioned in section 6.3.2. To overcome the hurdle of electrical breakdown for their integration in devices, it is important to investigate the maximum power held by the organic component. As expected, this power depends on the local structure of the conducting film surface and, in particular, on the number and type of defects present over the region under analysis. Though this variance makes it impossible to obtain a precise evaluation, the power held for a fiber before breakdown is found to be in the range of a few hundreds of nW for our experimental conditions.

Regarding the mechanism by which the layers are removed, we should remark that any sweeping effect of the tip can be ruled out as the source of removal of material because care was taken to always keep the load at the pull of value, well below the onset of non-mechanical deformation. Moreover, the current flows along the fibers, following the direction of their disruption, whatever their orientation over the surface is, while no correlation with the scanning direction exists. We also discard resistive heating as possible mechanism describing our observations. If this were to be the case, the fibers would break randomly in the middle of the fiber because of differences in temperature. Temperature gradients are expected to arise along the fibers because of, for instance, the different heat dissipation between locations where the fibers appear somehow separated (lower dissipation) and other locations where evident fiber pile up (massive regions) or bundling exists. It is the intensity of the electric field (higher at the fiber borders) which induces an increase of the current (the fibers appear brighter) typical of the onset of a breakdown phenomena as that observed here. Taking into account that a thin contamination layer covers the tip and/or sample surfaces transferred to the controlled humidity box through air, the electric field at the fiber extreme is estimated to be of about $2 \times 10^8\ V/m$ during the breakdown onset. We note that, as commented, higher fields are needed to provoke peeling of fibers only exposed to the electric field under controlled environment (N_2 flux, $RH < 5\%$). This reminds us of the influence of the atmosphere in other nanometric systems electrical breakdown [335].

6.3.5 Summary

To conclude, we have shown that the preparation method used to obtain thin films with fiber morphology from organogels can be greatly improved by depositing from the solution state. This process allows the preparation of layers of homogeneous thickness opening the way to well defined fibers.

A layer by layer peeling phenomenon has been uncovered by using a conducting scanning probe microscope tip. The removal of molecular material starts at voltage excursions beyond some hundreds of mV and results in an increase in current and irreversible morphological changes (mechanical disruption) without applying any mechanical compression. The process starts at the fibers ends or close to the bundles borders. It never starts in the middle of the fiber. Once the process begins (breakdown), it triggers the peeling of the fiber similarly to a staircase burning reaction.

The reported observations, are described in terms of a mechanism based in a “peeling the fibers out" by the effect of the applied electric field (electropeeling), which is found to remove the molecules, pulling them out from the fibers extremes, and sequentially destroying the conducting wires. The presented results are relevant to understand the limits of energy transport through organic fibers, which is of enormous importance in molecular components for electronic circuits and organic based sensors.

Summary

This concluding chapter summarizes the results of the present thesis. The thesis was dedicated to the study of the morphological, mechanical, electrostatic and conductive properties of different self-assembled and nanostructured systems, including organic thin films and inorganic surfaces. We accessed such properties by mean of scanning probe microscopy, both scanning force microscopy and scanning tunneling microscopy techniques under controlled ambient conditions. We mainly focused on the use of SFM in contact, dynamic, friction force microscopy (FFM), conductive scanning force microscopy (CSFM) and Kelvin probe force microscopy (KPFM) operating modes for such a purpose. Tough the suitability of the scanning force microscopy to address studies at the nanometre scale has been demonstrated since its invention in the 80th, this work constitutes one more example of the versatility offered by this technique to investigate different aspects of material surfaces.

Below follow the main results obtained from our studies.

We have investigated the influence of the supramolecular order of a self-assembled monolayer (SAM) into the $Au(111)$ surface properties. For that purpose, we have characterized the $\omega-(4'-methylbiphenyl-4-yl)butane-1-thiol$ $(BP4)$ SAM consisting of two polymorphic phases coexisting on $Au(111)$ surface. Thanks to the coexistence of the two polymorphic phases in surface, the investigation of the impact of the supramolecular order of the SAM into the surface properties have been possible by SPM techniques with in situ references. We have shown how the supramolecular order of the SAM is a decisive factor influencing such nanoscale properties. We have gained knowledge on the morphological and structural differences of the phases as well as in the details of the solitons structures present in the α polymorphic phase. By mean of friction force microscopy (FFM) we found that the friction response varies for the two polymorphic phases. In addition, we show how molecular domains with different orientation can be distinguished by mean of friction anisotropy and asymmetry effects. Therefore making use of high sensitivity lateral force imaging we are able to reveal structural details of BP4 SAMs well beyond the topographical information provided by STM. We also reveal tribological differences over the α-phase solitons structures.

Furthermore, we have proven that the supramolecular order in influences the electrostatic properties of Au(111) surface, i.e., in the work function shift induced on the $Au(111)$ surface. We found that the supramolecular order change modifies the work function shift of the gold in nearly a 14% from α to the β-phase. In addition, we study the relative contribution of the molecular density, molecular dipole and permittivity factors between polymorphic phases into the work function shift induced by the SAM in $Au(111)$. For the present case we found that the difference on molecular density and effective permittivity ratios contribute nearly the same but in an opposite sign to the work function shift induced by each molecular phase, whereas the difference on molecular tilt angle and in consequence of the normal component of the dipolar moment contributes around 30% less than the two others. We have also derived the difference on the dielectric constant and polarizability of the molecules in each polymorphic phase and found that the polarizability of the molecule in each supramolecular phase plays an important role in the variation of the local dielectric constant of the layer.

We also characterized the conductive response of each polymorphic phase by mean of conducting SFM (CSFM). A clear difference between the conductive response of the molecular phases is found and is mainly attributed to the difference in thickness between molecular layers. In addition, based on electron current measurements, the combined use of STM and CSFM allows us interpreting the differences in apparent height as measured by one or the other technique in non-homogeneous organic layers and thus, decoupling the electronic and topographic contribution in the STM signal.

We have characterized and investigated the use of nanopatternded $SrTiO_3$ (001) oxide surfaces, which presents the coexistence of well differentiated TiO_2 and SrO chemical termination regions, as template for the adsorption of organic molecules. We have shown that a carboxylic acid function organic molecules can selectively form monolayers on the TiO_2 oxide termination and have investigated the impact of the organic layer adsorption into the TiO_2 surface properties. The frictional response of the TiO_2 surface is lowered by a 50% with the organic layer adsorption, confirming that organic self-assembled monolayers (SAMs) are good candidates for their use as boundary lubricants for improving the tribological properties of the TiO_2 surface. Furthermore, we have proven that the use of SAMs to tune the local work function can be extended from metallic to insulating surfaces. By the adsorption of the stearic acid molecules, the $TiO_2(001)$ STO surface work function have lowered by around a 2.7%. In consequence, we have shown that selective adsorption can be used to create and modulate at the nanoscale both friction and work function of nanostructured oxide surfaces with potential applications in several technologically and scientifically relevant emerging areas.

In addition, we have added some insight about the surface diffusion process that causes the chemical termination patterning of the $SrTiO_3(001)$ surface under high-annealing temperature $(1100 - 1200°C)$. We conclude that the formation of the low lying SrO chemical termination is consequence of the SrO region diffusion and coalescence in the TiO_2 step edges.

We have presented two different tip-induced effects we found while studying organic thin film materials which can be use to manipulate matter:

i) We have shown that the layer by layer growth of pentacene molecules can be induced by the SFM tip. The pentacene molecules are dragged and collected in the water meniscus formed in the tip-sample contact when the sample is scanned in repulsive regime, and the accumulated molecules are transferred to the surface where they self-assemble when attractive measurement conditions are employed. This process allows the preparation of layers of homogeneous and well ordered molecular layers and could be used as a top-down strategy for the nanostructuration of organic molecular nanodevices.

ii) A layer by layer electropeeling phenomenon has been also uncovered on a tetrathiafulvalene (TTF) derivative organogel forming fiber like structure by using a conducting scanning probe microscope tip. The removal of TTF derivative molecular material starts at voltage excursions beyond some hundreds of mV without applying any mechanical compression. The process starts at the fibers ends or close to the bundles borders. It never starts in the middle of the fiber. Once the process begins (breakdown), it triggers the peeling of the fiber similarly to a staircase burning reaction. The presented results are relevant to understand the limits of energy transport through organic fibers, which is of enormous importance in molecular components for electronic circuits and organic based sensors.

Symbols and Abbreviations

2D	Two-dimensional
3D	Three-dimensional
μCP	Microcontact printing
Ac	Stearic acid
AF	Adhesion force
AM-KPFM	Amplitud modulation kelvin probe microscopy
AM-SFM	Amplitud modulation scanning force microscopy
AN	Friction anisotropy
AS	Friction asymmetry
BP4	w-(4'-methylbiphenyl-4-yl)butane-1-thiol
cc-STM	Constant current scanning tunneling microscopy
cm-SFM	Contact mode scanning force microscopy
CPD	Contact potential difference
CSFM	Conductive scanning force microscopy
CSIC	Spanish National Research Council
DFT	Density functional theory
dm-SFM	Dynamic mode scanning force microscopy
DMT	Derjaguin, Muller and Toporov model
EFM	Electrostatic force microscopy
ES	Error signal
FFM	Friction force microscopy
Fl	Lateral Force
FM-KPFM	Frequency modulation kelvin probe microscopy
FM-SFM	Frequency modulation scanning force microscopy

Fn	Normal force
FWHM	Full width at half maximum
GIXD	Grazing-angle incidence X-ray difraction
HOMO	Highest occupied molecular orbital
HOPG	Highly oriented pyrolytic graphite
ICMAB	Institut of Material Science of Barcelona
IRRAS	Infrared reflection absorption spectroscopy
ITO	Indium tin oxide
JKR	Johnson, Kendall and Roberts model
KPFM	Kelvin probe force microscopy
LB	Langmuir-Blodgett
LUMO	Lowest unoccupied molecular orbital
MEM	Microelectromechanical system
ML	Monolayer
NEM	Nanoelectromechanical system
NEXAFS	Near-edge X-ray absorption fine structure spectroscopy
OLED	Organic light emitting diode
OMBD	Organic molecular beam deposition
PDMS	Polymethylsiloxane
PLL	Phase locked loop
RH	Relative humidity
rms	Root mean square
SAM	Self-assembled monolayer
SEM	Scanning electron microscopy
SFM	Scanning force microscopy
SI	International system of units
Sp	Surface potential
SPL	Scanning probe lithography
SPM	Scanning probe microscopy
STM	Scanning tunneling microscopy

STO	Strontium titanate, $SrTiO_3$
TTF	Tetrathiafulvalene
u.c.	Unit cell
UHV	Ultra-high vacuum
XPS	X-ray photoelectron spectroscopy

Supplementary information

List of movies

The following movies are attached to the thesis manuscript in pdf format in the provided CD.

Chapter 4

- Movies 4-4-4-a. Topography-Forward. $2\,\mu m\ \times 2\,\mu m$. Consist of 33 frames. Total time $\sim 3\,h\ 25\,min$. $\Delta V_{tip} = 10\,mV$ from frame to frame, ranging from $0\ to\ 330\,mV$. Reproduction speed $5\ frames/s$.

- Movies 4-4-4-b. Topography-Backward. $2\,\mu m\ \times 2\,\mu m$. Consist of 33 frames. Total time $\sim 3\,h\ 25\,min$. $\Delta V_{tip} = 10\,mV$ from frame to frame, ranging from $0\ to\ 330\,mV$. Reproduction speed $5\ frames/s$.

- Movies 4-4-4-c. Lateral force-Forward. $2\,\mu m\ \times 2\,\mu m$. Consist of 33 frames. Total time $\sim 3\,h\ 25\,min$. $\Delta V_{tip} = 10\,mV$ from frame to frame, ranging from $0\ to\ 330\,mV$. Reproduction speed $5\ frames/s$.

- Movies 4-4-4-d. Lateral force-Backward. $2\,\mu m\ \times 2\,\mu m$. Consist of 33 frames. Total time $\sim 3\,h\ 25\,min$. $\Delta V_{tip} = 10\,mV$ from frame to frame, ranging from $0\ to\ 330\,mV$. Reproduction speed $5\ frames/s$.

- Movies 4-4-4-e. Current-Forward. $2\mu m \times 2\mu m$. Consist of 33 frames. Total time $\sim 3h\ 25min$. $\Delta V_{tip} = 10\ mV$ from frame to frame, ranging from $0\ to\ 330\ mV$. Reproduction speed $5\ frames/s$.

- Movies 4-4-4-f. Current-Backward. $2\ \mu m\ \times 2\ \mu m$. Consist of 33 frames. Total time $\sim 3\ h\ 25\ min$. $\Delta V_{tip} = 10\ mV$ from frame to frame, ranging from $0\ to\ 330\ mV$. Reproduction speed $5\ frames/s$.

Chapter 6

- Movies 7-2-a. Topography. $1\ \mu m\ \times 1\ \mu m$. Consist of 12 frames. Total time $\sim 10\ min$. Reproduction speed $4\ frames/s$.

- Movies 7-2-b. Topography. $1.3\,\mu m \times 1.3\,\mu m$. Consist of 108 frames. Total time $\sim 2h$. Reproduction speed 4 $frames/s$.
- Movies 7-2-c. Topography. $1.3\,\mu m \times 0.89\,\mu m$. Consist of 108 frames. Total time $\sim 2h$. Reproduction speed 4 $frames/s$.
- Movies 7-2-d. Topography. $1.3\,\mu m \times 0.89\,\mu m$. Consist of 108 frames. Total time $\sim 2h$. Reproduction speed 4 $frames/s$.

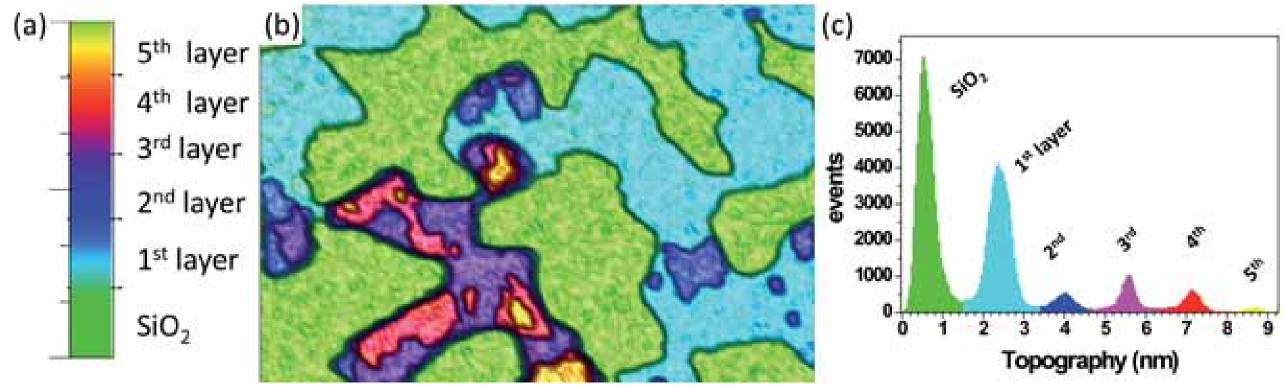

Image (b) shows the last frame of Movie 7-2-d. The histogram plot of the topography signal of (b) is presented in (c). The color code of the topography signal of the movie (a) is chosen in function of this histogram plot (c).

- Movies 7-3-a. Topography. $3\,\mu m \times 1.9\,\mu m$. Consist of 21 frames. Total time $\sim 2h$. $\Delta V_{tip} = 200\,mV$ from frame to frame, ranging from 0 *to* $4\,V$. Reproduction speed 5 $frames/s$.
- Movies 7-3-b. Current. $3\,\mu m \times 1.9\,\mu m$. Consist of 21 frames. Total time $\sim 2h$. $\Delta V_{tip} = 200\,mV$ from frame to frame, ranging from 0 *to* $4\,V$. Reproduction speed 5 $frames/s$.
- Movies 7-3-c. Topography. $674\,nm \times 516\,nm$. Consist of 12 frames. $\Delta V_{tip} = 200\,mV$ from frame to frame, ranging from 0 *to* $2.2\,V$. Reproduction speed 4 $frames/s$.
- Movies 7-3-d. Topography. $415\,nm \times 320\,nm$. Consist of 103 frames. Total time $\sim 11h$. Constant $V_{tip} = 200\,V$. Reproduction speed 10 $frames/s$.
- Movies 7-3-e. Current. $415\,nm \times 320\,nm$. Consist of 103 frames. Total time $\sim 11h$. Constant $V_{tip} = 200\,V$. Reproduction speed 10 $frames/s$.

Bibliography

[1] H.-E. Schaefer, *Nanoscience: The Science of the Small in Physics, Engineering, Chemistry, Biology and Medicine* (Springer, 2010).

[2] G. M. Whitesides and B. Grzybowski, Science **295**, 2418 (2002).

[3] J. V. Barth, G. Costantini, and K. Kern, Nature **437**, 671 (2005).

[4] J. D. Halley and D. A. Winkler, Complexity **14**, 10 (2008).

[5] F. Schreiber, Journal of Physics: Condensed Matter **16**, R881 (2004).

[6] F. Schreiber, Progress in Surface Science **65**, 151 (2000).

[7] R. W. Carpick and M. Salmeron, Chemical Reviews **97**, 1163 (1997).

[8] A. Ulman, Chemical Reviews **96**, 1533 (1996).

[9] J. C. Love, L. A. Estroff, J. K. Kriebel, R. G. Nuzzo, and G. M. Whitesides, Chemical Reviews **105**, 1103 (2005).

[10] C. Wöll, *Physical and chemical aspects of Organic Electronics* (Wiley-VCH, 2009).

[11] H. Klauk, *Organic Electronics-Materials, Manufacturing and Applications*, edited by D. H. Klauk (WILEY-VCH, 2006).

[12] C. Dimitrakopoulos and P. Malenfant, Advanced Materials **14**, 99 (2002).

[13] G. Horowitz, Journal of Materials Research **19**, 1946 (2004).

[14] J. Shinar, ed., *Organic light-emitting devices: a survey* (Springer, 2004).

[15] H. Hoppe and N. S. Sariciftci, Journal of Materials Research **19**, 1924 (2004).

[16] E. Laukhina, R. Pfattner, L. R. Ferreras, S. Galli, M. Mas-Torrent, N. Masciocchi, V. Laukhin, C. Rovira, and J. Veciana, Advanced Materials **22**, 977 (2009).

[17] I. Ratera and J. Veciana, Chemical Society Reviews **41**, 303 (2012).

[18] B. D. Gates, Q. Xu, M. Stewart, D. Ryan, C. G. Willson, and G. M. Whitesides, Chemical Reviews **105**, 1171 (2005).

[19] R. Bachelet, F. Sánchez, J. Santiso, C. Munuera, C. Ocal, and J. Fontcuberta, Chemistry of Materials **21**, 2494 (2009).

[20] G. Binnig and H. Rohrer, Helvetica Physica Acta **55**, 726 (1982).

[21] G. Binnig, H. Rohrer, C. Gerber, and E. Weibel, Physical Review Letters **49**, 57 (1982).

[22] G. Binnig, C. F. Quate, and C. Gerber, Physical Review Letters **56**, 930 (1986).

[23] J. Loos, Advanced Materials **17**, 1821 (2005).

[24] C. Munuera, *Structural, mechanical and transport characterization of organosulphur nanoscaled molecular films*, Ph.D. thesis, Universitat Autónoma de Madrid- Instituto de Ciencia de Materiales de Madrid-CSIC (2007).

[25] C. Wöll, S. Chiang, R. J. Wilson, and P. H. Lippel, Physical Review B **39**, 7988 (1989).

[26] D. D. Chambliss, R. J. Wilson, and S. Chiang, Journal of Vacuum Science and Technology B **9**, 933 (1991).

[27] $Nanotec^{TM}Electronica$, $Nanotec^{TM}Electronica$.

[28] W. F. Kolbe, D. F. Ogletree, and M. B. Salmeron, Ultramicroscopy **42-44, Part 2**, 1113 (1992).

[29] I. Horcas, R. Fernandez, J. M. Gomez-Rodriguez, J. Colchero, J. Gomez-Herrero, and A. M. Baro, Review of Scientific Instruments **78**, 013705 (2007).

[30] $Agilent - Technologies$, $Agilent - Technologies$.

[31] $Nanosensors^{TM}$, $Nanosensors^{TM}$.

[32] $MikroMasch$, $MikroMasch$.

[33] J. E. Sader, J. W. M. Chon, and P. Mulvaney, Review of Scientific Instruments **70**, 3967 (1999).

[34] $Bruker$, $Bruker$.

[35] Olympus, .

[36] BudgetSensor, .

[37] S. Alexander, L. Hellemans, O. Marti, J. Schneir, V. Elings, P. K. Hansma, M. Longmire, and J. Gurley, Journal of Applied Physics **65**, 164 (1989).

[38] G. Meyer and N. M. Amer, Applied Physics Letters **56**, 2100 (1990).

[39] B. Bhushan, *Handbook of Nano-technology*, edited by Springer (Springer, 2004).

[40] J. N. Israelachvili, *Intermolecular and Surface Forces*, edited by A. Press (1992).

[41] H.-J. Butt, B. Cappella, and M. Kappl, Surface Science Reports **59**, 1 (2005).

[42] E. Meyer, H. J. Hug, and R. Bennewitz, *Scanning Probe Microscopy. The lab on a tip*, edited by Springe-Verlag (Springe-Verlag, 2004).

[43] J. Colchero, A. Storch, M. Luna, J. Gómez Herrero, and A. M. Baró, Langmuir **14**, 2230 (1998).

[44] X. Xiao and L. Qian, Langmuir **16**, 8153 (2000).

[45] O. H. Pakarinen, A. S. Foster, M. Paajanen, T. Kalinainen, J. Katainen, I. Makkonen, J. Lahtinen, and R. M. Nieminen, Modelling and Simulation in Materials Science and Engineering **13**, 1175 (2005).

[46] M. Köber, E. Sahagún, P. García-Mochales, F. Briones, M. Luna, and J. J. Sáenz, Small **6**, 2725 (2010).

[47] B. L. Weeks, M. W. Vaughn, and J. J. DeYoreo, Langmuir **21**, 8096 (2005).

[48] A. Gil, J. Colchero, J. Gomez-Herrero, and A. M. Baro, Nanotechnology , 332 (2003).

[49] H. O. Jacobs, P. Leuchtmann, O. J. Homan, and A. Stemmer, Journal of Applied Physics **84**, 1168 (1998).

[50] A. L. Weisenhorn, P. K. Hansma, T. R. Albrecht, and C. F. Quate, Applied Physics Letters **54**, 2651 (1989).

[51] B. Cappella and G. Dietler, Surface Science Reports **34**, 1 (1999).

[52] B. Luan and M. O. Robbins, Nature **435**, 929 (2005).

[53] Y. Mo, K. T. Turner, and I. Szlufarska, Nature **457**, 1116 (2009).

[54] K. Johnson, *Contact Mechanics* (Cambridge: Cambridge University Press)., 1985).

[55] K. L. Johnson, K. Kendall, and A. D. Roberts, Proceedings of the Royal Society of London. Series A, Mathematical and Physical Sciences **324**, 301 (1971).

[56] B. V. Derjaguin, V. M. Muller, and Y. P. Toporov, Journal of Colloid and Interface Science **53**, 314 (1975).

[57] A. Lio, D. H. Charych, and M. Salmeron, The Journal of Physical Chemistry B **101**, 3800 (1997), doi: 10.1021/jp963918e.

[58] M. Salmeron, Tribology Letters **10**, 69 (2001).

[59] G. J. Leggett, N. J. Brewer, and K. S. L. Chong, Physical Chemistry Chemical Physics **7**, 1107 (2005).

[60] V. M. Muller, V. S. Yushchenko, and B. V. Derjaguin, Journal of Colloid and Interface Science **77**, 91 (1980).

[61] D. Maugis, Journal of Colloid and Interface Science **150**, 243 (1992).

[62] K. L. Johnson and J. A. Greenwood, Journal of Colloid and Interface Science **192**, 326 (1997).

[63] R. W. Carpick, D. F. Ogletree, and M. Salmeron, Journal of Colloid and Interface Science **211**, 395 (1999).

[64] R. García and R. Pérez, Surface Science Reports **47**, 197 (2002).

[65] F. J. Giessibl, Reviews of Modern Physics **75**, 949 (2003).

[66] T. R. Albrecht, P. Grutter, D. Horne, and D. Rugar, Journal of Applied Physics **69**, 668 (1991).

[67] W. A. Ducker, R. F. Cook, and D. R. Clarke, Journal of Applied Physics **67**, 4045 (1990).

[68] M. Luna, J. Colchero, J. Gómez-Herrero, and A. M. Baró, Applied Surface Science **157**, 285 (2000).

[69] H. Hölscher and B. Anczykowski, Surface Science **579**, 21 (2005).

[70] H. Hölscher and U. D. Schwarz, International Journal of Non-Linear Mechanics **42**, 608 (2007).

[71] S. J. T. Van Noort, K. O. Van der Werf, B. G. De Grooth, N. F. Van Hulst, and J. Greve, Ultramicroscopy **69**, 117 (1997).

[72] A. Knoll, R. Magerle, and G. Krausch, Macromolecules **34**, 4159 (2001).

[73] E. Palacios-Lidón, C. Munuera, C. Ocal, and J. Colchero, Ultramicroscopy **110**, 789 (2010).

[74] M. Fritz, M. Radmacher, J. P. Cleveland, M. W. Allersma, R. J. Stewart, R. Gieselmann, P. Janmey, C. F. Schmidt, and P. K. Hansma, Langmuir **11**, 3529 (1995).

[75] A. Verdaguer, S. Santos, G. Sauthier, J. J. Segura, M. Chiesa, and J. Fraxedas, Physical Chemistry Chemical Physics (2012).

[76] S. Sadewasser and M. C. Lux-Steiner, Physical Review Letters **91**, 266101 (2003).

[77] S. Sadewasser, P. Carl, T. Glatzel, and M. C. Lux-Steiner, Nanotechnology **15**, S14 (2004).

[78] A. Kühle, A. H. Sorensen, J. B. Zandbergen, and J. Bohr, Applied Physics A: Materials Science & Processing **66**, S329 (1998).

[79] R. García and A. San Paulo, Physical Review B **60**, 4961 (1999).

[80] J. P. Cleveland, B. Anczykowski, A. E. Schmid, and V. B. Elings, Applied Physics Letters **72**, 2613 (1998).

[81] S. N. Magonov, V. Elings, and M. H. Whangbo, Surface Science **375**, L385 (1997).

[82] T. Fukuma, T. Ichii, K. Kobayashi, H. Yamada, and K. Matsushige, Applied Physics Letters **86**, 034103 (2005).

[83] E. Palacios-Lidón, B. Perez-Garcia, and J. Colchero, Nanotechnology **20**, 085707 (2009).

[84] T. Fukuma and S. P. Jarvis, Review of Scientific Instruments **77**, 043701 (2006).

[85] U. Dürig, O. Zuger, and A. Stalder, Journal of Applied Physics **72**, 1778 (1992).

[86] U. Durig, H. R. Steinauer, and N. Blanc, Journal of Applied Physics **82**, 3641 (1997).

[87] R. García and A. San Paulo, Ultramicroscopy **82**, 79 (2000).

[88] X. Chen, M. C. Davies, C. J. Roberts, S. J. B. Tendler, P. M. Williams, and N. A. Burnham, Surface Science **460**, 292 (2000).

[89] l. S. Paulo and R. García, Physical Review B **66**, 041406 (2002).

[90] B. Anczykowski, D. Krüger, and H. Fuchs, Physical Review B **53**, 15485 (1996).

[91] B. Anczykowski, D. Krüger, K. L. Babcock, and H. Fuchs, Ultramicroscopy **66**, 251 (1996).

[92] R. García and A. San Paulo, Physical Review B **61**, R13381 (2000).

[93] D. Ziegler and A. Stemmer, Nanotechnology **22**, 075501 (2011).

[94] R. Bennewitz, *Fundamentals of Friction and Wear*, edited by Springer, Vol. 1 (Springer, 2007) pp. 1–14.

[95] D. F. Ogletree, R. W. Carpick, and M. Salmeron, Review of Scientific Instruments **67**, 3298 (1996).

[96] C. A. Clifford and M. P. Seah, Nanotechnology **16**, 1666 (2005).

[97] R. J. Cannara, M. Eglin, and R. W. Carpick, Review of Scientific Instruments **77**, 053701 (2006).

[98] H. Bluhm, U. D. Schwarz, and R. Wiesendanger, Physical Review B **57**, 161 (1998).

[99] S. Morita, S. Fujisawa, and Y. Sugawara, Surface Science Reports **23**, 1 (1996).

[100] A. Vanossi, N. Manini, M. Urbakh, S. Zapperi, and E. Tosatti, Reviews of Modern Physics **85**, 529 (2013).

[101] H. Hölscher, U. D. Schwarz, O. Zwörner, and R. Wiesendanger, Physical Review B **57**, 2477 (1998).

[102] S. Hembacher, F. J. Giessibl, J. Mannhart, and C. F. Quate, Proceedings of the National Academy of Sciences **100**, 12539 (2003).

[103] B. Blushan, H. Fuchs, and T. M, "Applied scanning probe methods viii," (2008) Chap. Probing Electrical Transport Properties at the Nanoscale by Current-Sensing Atomic Force Microscopy, pp. 421–450.

[104] M. Nonnenmacher, M. P. O'Boyle, and H. K. Wickramasinghe, Applied Physics Letters **58**, 2921 (1991).

[105] W. A. Zisman, Review of Scientific Instruments **3**, 367 (1932).

[106] L. Kelvin, Philosophical Magazine **46**, 82 (1898).

[107] K. Wandelt, Applied Surface Science **111**, 1 (1997).

[108] D. Cahen and A. Kahn, Advanced Materials **15**, 271 (2003).

[109] N. W. Ashcroft and N. D. Mermin, *Solid State Physics*, edited by D. G. Crane (Harcourt College Publishers, 1976).

[110] T. Glatzel, M. Lux-Steiner, E. Strassburg, A. Boag, and Y. Rosenwaks, in *Scanning Probe Microscopy*, edited by S. Kalinin and A. Gruverman (Springer New York, 2007) pp. 113–131.

[111] D. W. Abraham, C. Williams, J. Slinkman, and H. K. Wickramasinghe, Journal of Vacuum Science & Technology B **9**, 703 (1991).

[112] J. Kopanski, in *Scanning Probe Microscopy*, edited by S. Kalinin and A. Gruverman (Springer New York, 2007) pp. 88–112.

[113] S. Kitamura and M. Iwatsuki, Applied Physics Letters **72**, 3154 (1998).

[114] J. Colchero, A. Gil, and A. M. Baró, Physical Review B **64**, 245403 (2001).

[115] T. Glatzel, S. Sadewasser, and M. C. Lux-Steiner, Applied Surface Science **210**, 84 (2003).

[116] E. Palacios-Lidón and J. Colchero, Nanotechnology **17**, 5491 (2006).

[117] H. O. Jacobs, H. F. Knapp, S. Müller, and A. Stemmer, Ultramicroscopy **69**, 39 (1997).

[118] H. O. Jacobs, H. F. Knapp, and A. Stemmer, Review of Scientific Instruments **70**, 1756 (1999).

[119] C. Gómez-Navarro, A. Gil, M. Álvarez, P. J. D. Pablo, F. Moreno-Herrero, I. Horcas, R. Fernández-Sánchez, J. Colchero, J. Gómez-Herrero, and A. M. Baró, Nanotechnology **13**, 314 (2002).

[120] C. Munuera, E. Barrena, and C. Ocal, Nanotechnology **18**, 125505 (2007).

[121] C. Moreno, *New features in solution $La_{0.6}Sr_{0.4}MnO_3$ thin films: spontaneous outcropping and nanoscale reversible resistive switching*, Ph.D. thesis, Universitat Autònoma de Barcelona- Institut de Ciència de Materials de Barcelona-CSIC (2010).

[122] N. Crivillers, C. Munuera, M. Mas-Torrent, C. Simão, S. T. Bromley, C. Ocal, C. Rovira, and J. Veciana, Advanced Materials **21**, 1177 (2009).

[123] N. Crivillers, M. Paradinas, M. Mas-Torrent, S. T. Bromley, C. Rovira, C. Ocal, and J. Veciana, Chemical Communications **47**, 4664 (2011).

[124] E. Palacios-Lidón, J. Abellan, J. Colchero, C. Munuera, and C. Ocal, Applied Physics Letters **87**, 154106 (2005).

[125] M. Jaafar, *Procesos de imanación en la nanoescala mediante microscopía de fuerzas magnéticas*, Ph.D. thesis, Universitat Autónoma de Madrid- Instituto de Ciencia de Materiales de Madrid-CSIC (2009).

[126] M. Jaafar, O. Iglesias-Freire, L. Serrano-Ramon, M. Ricardo Ibarra, J. Maria de Teresa, and A. Asenjo, Beilstein Journal of Nanotechnology **2**, 552 (2011).

[127] M. Jaafar, J. Gómez-Herrero, A. Gil, P. Ares, M. Vázquez, and A. Asenjo, Ultramicroscopy **109**, 693 (2009).

[128] P. K. Hansma and J. Tersoff, Journal of Applied Physics **61**, R1 (1987).

[129] J. Bardeen, Physical Review Letters **6**, 57 (1961).

[130] J. Tersoff and D. R. Hamann, Physical Review Letters **50**, 1998 (1983).

[131] J. Tersoff and D. R. Hamann, Physical Review B **31**, 805 (1985).

[132] C. J. Chen, *Introduction to Scanning Tunneling Microscopy* (Oxford University Press, Oxford, 1993).

[133] D. A. Bonnell, *Scanning tunneling microscopy and spectroscopy. Theory, techniques and applications.* (VCH Publishers, New York, 1993).

[134] R. Wiesendanger, *Scanning Probe Microscopy and Spectroscopy: methods and applications* (Cambridge University Press, 1994).

[135] *Arrandee*^{TM}, *Arrandee*^{TM} .

[136] *Georg Albert PVD Beschichtungen*, *Georg Albert PVD Beschichtungen* .

[137] M. H. Dishner, M. M. Ivey, S. Gorer, J. C. Hemminger, and F. J. Feher, Journal of Vacuum Science & Technology A: Vacuum, Surfaces, and Films **16**, 3295 (1998).

[138] *Romil – SpS*, *Romil – SpS* .

[139] *HellmaAnalytics*, *HellmaAnalytics* .

[140] A. Kumar and G. M. Whitesides, Applied Physics Letters **63**, 2002 (1993).

[141] A. Kumar, H. A. Biebuyck, and G. M. Whitesides, Langmuir **10**, 1498 (1994).

[142] Y. Xia and G. M. Whitesides, Angewandte Chemie International Edition **37**, 550 (1998).

[143] Y. N. Xia and G. M. Whitesides, Annual Review of Materials Science **28**, 153 (1998).

[144] A. Perl, D. N. Reinhoudt, and J. Huskens, Advanced Materials **21**, 2257 (2009).

[145] J. C. McDonald and G. M. Whitesides, Accounts of Chemical Research **35**, 491 (2002).

[146] E. Delamarche, H. Schmid, A. Bietsch, N. B. Larsen, H. Rothuizen, B. Michel, and H. Biebuyck, The Journal of Physical Chemistry B **102**, 3324 (1998).

[147] R. K. Smith, P. A. Lewis, and P. S. Weiss, Progress in Surface Science **75**, 1 (2004).

[148] *Eurotherm*, *Eurotherm* .

[149] S. R. Forrest, Chemical Reviews **97**, 1793 (1997).

[150] D. G. de Oteyza, *Fluorinated copper-phthalocyanines in organic thin-films, heterostructures and 2D supramolecular assemblies*, Ph.D. thesis, Universidad Autónoma de Madrid- Max Planck Institut für Metallforschung (2006).

[151] T. N. Krauss, *Directed Self-Assembly of Organic Semiconductors in Different Dimensionalities*, Ph.D. thesis, Max Planck Institut für Metallforschung (2009).

[152] P. Cyganik and M. Buck, Journal of the American Chemical Society **126**, 5960 (2004).

[153] P. Cyganik, M. Buck, T. Strunskus, A. Shaporenko, J. D. E. T. Wilton-Ely, M. Zharnikov, and C. Wöll, Journal of the American Chemical Society **128**, 13868 (2006).

[154] H.-T. Rong, S. Frey, Y.-J. Yang, M. Zharnikov, M. Buck, M. Wühn, C. Wöll, and G. Helmchen, Langmuir **17**, 1582 (2001).

[155] W. Azzam, P. Cyganik, G. Witte, M. Buck, and C. Wöll, Langmuir **19**, 8262 (2003).

[156] J. F. Kang, A. Ulman, S. Liao, R. Jordan, G. Yang, and G.-y. Liu, Langmuir **17**, 95 (2001).

[157] W. Azzam, C. Fuxen, A. Birkner, H.-T. Rong, M. Buck, and C. Wöll, Langmuir **19**, 4958 (2003).

[158] T. Y. B. Leung, P. Schwartz, G. Scoles, F. Schreiber, and A. Ulman, Surface Science **458**, 34 (2000).

[159] G. Yang, Y. Qian, C. Engtrakul, L. R. Sita, and G.-y. Liu, The Journal of Physical Chemistry B **104**, 9059 (2000).

[160] G. Yang and G.-y. Liu, The Journal of Physical Chemistry B **107**, 8746 (2003).

[161] D. Käfer, G. Witte, P. Cyganik, A. Terfort, and C. Wöll, Journal of the American Chemical Society **128**, 1723 (2006).

[162] K. Heister, H. T. Rong, M. Buck, M. Zharnikov, M. Grunze, and L. S. O. Johansson, The Journal of Physical Chemistry B **105**, 6888 (2001).

[163] P. Cyganik, M. Buck, W. Azzam, and C. Wöll, The Journal of Physical Chemistry B **108**, 4989 (2004).

[164] Y.-T. Long, H.-T. Rong, M. Buck, and M. Grunze, Journal of Electroanalytical Chemistry **524-525**, 62 (2002).

[165] I. Thom and M. Buck, Surface Science **581**, 33 (2005).

[166] T. Felgenhauer, H. T. Rong, and M. Buck, Journal of Electroanalytical Chemistry **550-551**, 309 (2003).

[167] S. Frey, H. T. Rong, K. Heister, Y. J. Yang, M. Buck, and M. Zharnikov, Langmuir **18**, 3142 (2002).

[168] P. Cyganik, M. Buck, T. Strunskus, A. Shaporenko, G. Witte, M. Zharnikov, and C. Wöll, The Journal of Physical Chemistry C **111**, 16909 (2007).

[169] G. E. Poirier, Langmuir **15**, 1167 (1999).

[170] G. J. Su, R. Aguilar-Sanchez, Z. Li, I. Pobelov, M. Homberger, U. Simon, and T. Wandlowski, ChemPhysChem **8**, 1037 (2007).

[171] F. Vervaecke, S. Wyczawska, P. Cyganik, Z. Postawa, M. Buck, R. E. Silverans, P. Lievens, and E. Vandeweert, The Journal of Physical Chemistry C **112**, 2248 (2008).

[172] M. Zharnikov, S. Frey, H. Rong, Y.-J. Yang, K. Heister, M. Buck, and M. Grunze, Physical Chemistry Chemical Physics , 3359 (2000).

[173] A. Ulman, Accounts of Chemical Research **34**, 855 (2001).

[174] D. P. Woodruff, Physical Chemistry Chemical Physics **10**, 7211 (2008).

[175] K. Edinger, A. Goelzhaeuser, K. Demota, C. Wöll, and M. Grunze, Langmuir **9**, 4 (1993).

[176] P. Cyganik, M. Buck, J. D. E. T. Wilton-Ely, and C. Wöll, The Journal of Physical Chemistry B **109**, 10902 (2005).

[177] J. R. Taylor, *An Introduction to Error Analysis: The Study of Uncertainties in Physical Measurements*, university Science Books, U.S.; 2nd Revised ed. (1997).

[178] F. J. McCarthy, M. Buck, and G. Hähner, The Journal of Physical Chemistry C **112**, 19465 (2008).

[179] *ChemDraw*, *ChemDraw* .

[180] C. Munuera, E. Barrena, and C. Ocal, The Journal of Physical Chemistry A **111**, 12721 (2007).

[181] N. N. Gosvami, P. Egberts, and R. Bennewitz, The Journal of Physical Chemistry A **115**, 6942 (2011).

[182] L. Lu and Y. Cai, Langmuir **27**, 5953 (2011).

[183] J. Y. Park, D. F. Ogletree, M. Salmeron, R. A. Ribeiro, P. C. Canfield, C. J. Jenks, and P. A. Thiel, Science **309**, 1354 (2005).

[184] M. Kwak and H. Shindo, Physical Chemistry Chemical Physics **6**, 129 (2004).

[185] M. Campione and E. Fumagalli, Physical Review Letters **105**, 166103 (2010).

[186] M. Liley, D. Gourdon, D. Stamou, U. Meseth, T. M. Fischer, C. Lautz, H. Stahlberg, H. Vogel, N. A. Burnham, and C. Duschl, Science **280**, 273 (1998).

[187] K. Hisada and C. M. Knobler, Colloids and Surfaces A: Physicochemical and Engineering Aspects **198-200**, 21 (2002).

[188] R. W. Carpick, D. Y. Sasaki, and A. R. Burns, Tribology Letters **7**, 79 (1999).

[189] J. J. Segura, A. Verdaguer, L. Garzon, E. Barrena, C. Ocal, and J. Fraxedas, The Journal of Chemical Physics **134**, 124705 (2011).

[190] H. Bluhm, U. D. Schwarz, K. P. Meyer, and R. Wiesendanger, Applied Physics A: Materials Science & Processing **61**, 525 (1995).

[191] D. Gourdon, N. A. Burnham, A. Kulik, E. Dupas, F. Oulevey, G. Gremaud, D. Stamou, M. Liley, Z. Dienes, H. Vogel, and C. Duschl, Tribology Letters **3**, 317 (1997).

[192] K. Busuttil, M. Geoghegan, C. A. Hunter, and G. J. Leggett, Journal of the American Chemical Society **133**, 8625 (2011).

[193] G.-P. Charbonneau and Y. Delugeard, Acta Crystallographica Section B **32**, 1420 (1976).

[194] X. Cheng, Y.-Y. Noh, J. Wang, M. Tello, J. Frisch, R.-P. Blum, A. Vollmer, J. P. Rabe, N. Koch, and H. Sirringhaus, Advanced Functional Materials **19**, 2407 (2009).

[195] D. M. Taylor and G. F. Bayes, Physical Review E **49**, 1439 (1994).

[196] I. H. Campbell, S. Rubin, T. A. Zawodzinski, J. D. Kress, R. L. Martin, D. L. Smith, N. N. Barashkov, and J. P. Ferraris, Physical Review B **54**, R14321 (1996).

[197] I. H. Campbell, J. D. Kress, R. L. Martin, D. L. Smith, N. N. Barashkov, and J. P. Ferraris, Applied Physics Letters **71**, 3528 (1997).

[198] V. De Renzi, R. Rousseau, D. Marchetto, R. Biagi, S. Scandolo, and U. del Pennino, Physical Review Letters **95**, 046804 (2005).

[199] G. Heimel, L. Romaner, J.-L. Bredas, and E. Zojer, Physical Review Letters **96**, 196806 (2006).

[200] P. C. Rusu and G. Brocks, Physical Review B **74**, 073414 (2006).

[201] B. de Boer, A. Hadipour, M. M. Mandoc, T. van Woudenbergh, and P. W. M. Blom, Advanced Materials **17**, 621 (2005).

[202] D. M. Taylor, Advances in Colloid and Interface Science **87**, 183 (2000).

[203] S. Howell, D. Kuila, B. Kasibhatla, C. P. Kubiak, D. Janes, and R. Reifenberger, Langmuir **18**, 5120 (2002).

[204] M. L. Sushko and A. L. Shluger, The Journal of Physical Chemistry B **111**, 4019 (2007).

[205] J. Lü, E. Delamarche, L. Eng, R. Bennewitz, E. Meyer, and H. J. Güntherodt, Langmuir **15**, 8184 (1999).

[206] H. Sugimura, K. Hayashi, N. Saito, N. Nakagiri, and O. Takai, Applied Surface Science **188**, 403 (2002).

[207] P. C. Rusu and G. Brocks, The Journal of Physical Chemistry B **110**, 22628 (2006).

[208] G. Heimel, L. Romaner, E. Zojer, and J.-L. Brédas, Nano Letters **7**, 932 (2007).

[209] V. Palermo, A. Liscio, M. Palma, M. Surin, R. Lazzaroni, and P. Samori, Chemical Communications , 3326 (2007).

[210] D. A. Egger, F. Rissner, G. M. Rangger, O. T. Hofmann, L. Wittwer, G. Heimel, and E. Zojer, Physical Chemistry Chemical Physics **12**, 4291 (2010).

[211] H. Fukagawa, H. Yamane, S. Kera, K. K. Okudaira, and N. Ueno, Physical Review B **73**, 041302 (2006).

[212] L. Romaner, G. Heimel, and E. Zojer, Physical Review B **77**, 045113 (2008).

[213] H. Li, Y. Duan, P. Paramonov, V. Coropceanu, and J.-L. Brédas, Journal of Electron Spectroscopy and Related Phenomena **174**, 70 (2009).

[214] J. Ivanco, B. Winter, F. P. Netzer, and M. G. Ramsey, Advanced Materials **15**, 1812 (2003).

[215] H. Fukagawa, H. Yamane, T. Kataoka, S. Kera, M. Nakamura, K. Kudo, and N. Ueno, Physical Review B **73**, 245310 (2006).

[216] N. Koch, I. Salzmann, R. L. Johnson, J. Pflaum, R. Friedlein, and J. P. Rabe, Organic Electronics **7**, 537 (2006).

[217] M. P. Nikiforov, U. Zerweck, P. Milde, C. Loppacher, T.-H. Park, H. T. Uyeda, M. J. Therien, L. Eng, and D. Bonnell, Nano Letters **8**, 110 (2007).

[218] S. Duhm, G. Heimel, I. Salzmann, H. Glowatzki, R. L. Johnson, A. Vollmer, J. P. Rabe, and N. Koch, Nature Materials **7**, 326 (2008).

[219] S. Duhm, Q. Xin, N. Koch, N. Ueno, and S. Kera, Organic Electronics **12**, 903 (2011).

[220] E. Ito, T. Arai, M. Hara, and J. Noh, Bulletin of the Korean Chemical Society **30**, 1309 (2009).

[221] D. M. Alloway, M. Hofmann, D. L. Smith, N. E. Gruhn, A. L. Graham, R. Colorado, V. H. Wysocki, T. R. Lee, P. A. Lee, and N. R. Armstrong, The Journal of Physical Chemistry B **107**, 11690 (2003).

[222] L. Romaner, G. Heimel, C. Ambrosch-Draxl, and E. Zojer, Advanced Functional Materials **18**, 3999 (2008).

[223] A. Natan, N. Kuritz, and L. Kronik, Advanced Functional Materials **20**, 2077 (2010).

[224] J. Nara, S. Higai, Y. Morikawa, and T. Ohno, The Journal of Chemical Physics **120**, 6705 (2004).

[225] J. A. Rodriguez, J. Dvorak, T. Jirsak, G. Liu, J. Hrbek, Y. Aray, and C. González, Journal of the American Chemical Society **125**, 276 (2002).

[226] D. Otálvaro, T. Veening, and G. Brocks, The Journal of Physical Chemistry C **116**, 7826 (2012).

[227] A. Cossaro, R. Mazzarello, R. Rousseau, L. Casalis, A. Verdini, A. Kohlmeyer, L. Floreano, S. Scandolo, A. Morgante, M. L. Klein, and G. Scoles, Science **321**, 943 (2008).

[228] G. Heimel, L. Romaner, J.-L. Brédas, and E. Zojer, Langmuir **24**, 474 (2008).

[229] O. L. A. Monti and M. P. Steele, Physical Chemistry Chemical Physics **12**, 12390 (2010).

[230] M. Iwamoto, Y. Mizutani, and A. Sugimura, Physical Review B **54**, 8186 (1996).

[231] D. Cornil, Y. Olivier, V. Geskin, and J. Cornil, Advanced Functional Materials **17**, 1143 (2007).

[232] J. R. Macdonald and J. C. A. Barlow, The Journal of Chemical Physics **39**, 412 (1963).

[233] B. L. Maschhoff and J. P. Cowin, The Journal of Chemical Physics **101**, 8138 (1994).

[234] J. Topping, Proceedings of the Royal Society of London. Series A, Containing Papers of a Mathematical and Physical Character **114**, pp. 67 (1927).

[235] *MATLAB*, *MATLAB* .

[236] B. Rosi, M. P. Fontana, I. Dozov, and N. Kirov, Physical Review A **36**, 2879 (1987).

[237] J. Tobik and A. D. Corso, The Journal of Chemical Physics **120**, 9934 (2004).

[238] J. G. Simmons, Journal of Applied Physics **34**, 1793 (1963).

[239] R. E. Holmlin, R. Haag, M. L. Chabinyc, R. F. Ismagilov, A. E. Cohen, A. Terfort, M. A. Rampi, and G. M. Whitesides, Journal of the American Chemical Society **123**, 5075 (2001).

[240] W. Wang, T. Lee, and M. A. Reed, Physica E: Low-dimensional Systems and Nanostructures **19**, 117 (2003).

[241] V. B. Engelkes, J. M. Beebe, and C. D. Frisbie, Journal of the American Chemical Society **126**, 14287 (2004).

[242] R. M. Metzger, Journal of Materials Chemistry **18**, 4364 (2008).

[243] Y. Qi, X. Liu, B. L. M. Hendriksen, V. Navarro, J. Y. Park, I. Ratera, J. M. Klopp, C. Edder, F. J. Himpsel, E. E. H. Fréchet, J.M.J. anad Haller, and M. Salmeron, Langmuir **26**, 16522 (2010).

[244] L. A. Bumm, J. J. Arnold, T. D. Dunbar, D. L. Allara, and P. S. Weiss, The Journal of Physical Chemistry B **103**, 8122 (1999).

[245] K. Moth-Poulsen, L. Patrone, N. Stuhr-Hansen, J. B. Christensen, J.-P. Bourgoin, and T. Børnholm, Nano Letters **5**, 783 (2005).

[246] R. L. McCreery, Chemistry of Materials **16**, 4477 (2004).

[247] F. v. Wrochem, F. Scholz, A. Schreiber, H.-G. Nothofer, W. E. Ford, P. Morf, T. Jung, A. Yasuda, and J. M. Wessels, Langmuir **24**, 6910 (2008).

[248] A. L. Linsebigler, G. Lu, and J. T. Yates, Chemical Reviews **95**, 735 (1995).

[249] U. Diebold, Surface Science Reports **48**, 53 (2003).

[250] J. Yin, J. Ye, and Z. Zou, Applied Physics Letters **85**, 689 (2004).

[251] N. Sato, Y. Harada, T. Terashima, R. Kanda, and M. Takano, Applied Surface Science **244**, 588 (2005).

[252] R. Meyer, R. Waser, J. Helmbold, and G. Borchardt, Journal of Electroceramics **9**, 101 (2002).

[253] D. S. Deak, Materials Science and Technology **23**, 127 (2007).

[254] R. Herger, P. R. Willmott, O. Bunk, C. M. Schleputz, B. D. Patterson, B. Delley, V. L. Shneerson, P. F. Lyman, and D. K. Saldin, Physical Review B **76**, 195435 (2007).

[255] Q. Jiang and J. Zegenhagen, Surface Science **367**, L42 (1996).

[256] *CrysTec GmbH*, *CrysTec GmbH* .

[257] K. Momma and F. Izumi, Journal of Applied Crystallography **44**, 1272 (2011).

[258] K. Szot and W. Speier, Physical Review B **60**, 5909 (1999).

[259] J. Huijbregtse, J. Rector, and B. Dam, Physica C: Superconductivity **351**, 183 (2001).

[260] T. Ohnishi, K. Shibuya, M. Lippmaa, D. Kobayashi, H. Kumigashira, M. Oshima, and H. Koinuma, Applied Physics Letters **85**, 272 (2004).

[261] J. Fompeyrine, R. Berger, H. P. Lang, J. Perret, E. Machler, C. Gerber, and J.-P. Locquet, Applied Physics Letters **72**, 1697 (1998).

[262] K. Iwahori, S. Watanabe, M. Kawai, K. Kobayashi, H. Yamada, and K. Matsushige, Journal of Applied Physics **93**, 3223 (2003).

[263] H. Guhl, W. Miller, and K. Reuter, Physical Review B **81**, 155455.

[264] G. Koster, B. L. Kropman, G. J. H. M. Rijnders, D. H. A. Blank, and H. Rogalla, Applied Physics Letters **73**, 2920 (1998).

[265] G. Koster, G. Rijnders, D. H. A. Blank, and H. Rogalla, Physica C: Superconductivity **339**, 215 (2000).

[266] R. Bachelet, F. Sanchez, F. J. Palomares, C. Ocal, and J. Fontcuberta, Applied Physics Letters **95**, 141915 (2009).

[267] K. Iwahori, S. Watanabe, M. Kawai, K. Mizuno, K. Sasaki, and M. Yoshimoto, Journal of Applied Physics **88**, 7099 (2000).

[268] H. S. Kato, S. Shiraki, M. Nantoh, and M. Kawai, Surface Science **544**, L722 (2003).

[269] V. A. Shchukin and D. Bimberg, Reviews of Modern Physics **71**, 1125 (1999).

[270] M. Eβer, K. Morgenstern, G. Rosenfeld, and G. Comsa, Surface Science **402-404**, 341 (1998).

[271] J. de la Figuera, J. E. Prieto, C. Ocal, and R. Miranda, Solid State Communications **89**, 815 (1994).

[272] J. N. Wilson and H. Idriss, Langmuir **21**, 8263 (2005).

[273] A. G. Thomas and K. L. Syres, Chemical Society Reviews **41**, 4207 (2012).

[274] C. O. Timmons and W. A. Zisman, The Journal of Physical Chemistry **69**, 984 (1965).

[275] F. Francis and S. H. Piper, Journal of the American Chemical Society **61**, 577 (1939).

[276] K. Sato and M. Okada, Journal of Crystal Growth **42**, 259 (1977).

[277] V. Malta, G. Celotti, R. Zannetti, and A. F. Martelli, Journal of the Chemical Society B: Physical Organic , 548 (1971).

[278] K. Sato, M. Kobayashi, and H. Morishita, Journal of Crystal Growth **87**, 236 (1988).

[279] C. W. Sheen, J. X. Shi, J. Maartensson, A. N. Parikh, and D. L. Allara, Journal of the American Chemical Society **114**, 1514 (1992).

[280] E. Barrena, C. Ocal, and M. Salmeron, The Journal of Chemical Physics **114**, 4210 (2001).

[281] A. Kitaigorodskii, *Organic Chemical Crystallographic*, edited by C. Bureau (Consultant Bureau, New York, 1961).

[282] C. Barth, A. S. Foster, C. R. Henry, and A. L. Shluger, Advanced Materials **23**, 477 (2011).

[283] L. B. Harris and J. Fiasson, Journal of Physics C: Solid State Physics **18**, 4845 (1985).

[284] G.-N. Luo, K. Yamaguchi, T. Terai, and M. Yamawaki, Journal of Alloys and Compounds **349**, 211 (2003).

[285] C. Barth and C. R. Henry, Applied Physics Letters **89**, 252119 (2006).

[286] C. Barth and C. R. Henry, Physical Review Letters **98**, 136804 (2007).

[287] C. Barth and C. R. Henry, Physical Review Letters **100**, 096101 (2008).

[288] L. Nony, A. S. Foster, F. Bocquet, and C. Loppacher, Physical Review Letters **103**, 036802 (2009).

[289] J. Zabaleta, *Growth and advanced characterization of solution-derived nanoscale* $La_{0.6}Sr_{0.4}MnO_3$ *heteroepitaxial systems*, Ph.D. thesis, Universitat Autònoma de Barcelona-Institut de Ciència de Materials de Barcelona-CSIC (2011).

[290] H. J. Zhang, G. Chen, and Z. H. Li, Applied Surface Science **253**, 8345 (2007).

[291] R. I. Eglitis and D. Vanderbilt, Physical Review B **77**, 195408 (2008).

[292] T. Kubo and H. Nozoye, Physical Review Letters **86**, 1801 (2001).

[293] A. Verdaguer, G. M. Sacha, H. Bluhm, and M. Salmeron, Chemical Reviews **106**, 1478 (2006).

[294] A. Verdaguer, M. Cardellach, and J. Fraxedas, The Journal of Chemical Physics **129**, 174705 (2008).

[295] S. V. Kalinin and D. A. Bonnell, Physical Review B **63**, 125411 (2001).

[296] K. W. Bewig, Review of Scientific Instruments **35**, 1160 (1964).

[297] M. Minohara, I. Ohkubo, H. Kumigashira, and M. Oshima, Applied Physics Letters **90**, 132123 (2007).

[298] G. Heimel, F. Rissner, and E. Zojer, Advanced Materials **22**, 2494 (2010).

[299] A. A. Tseng, A. Notargiacomo, and T. P. Chen, Journal of Vacuum Science & Technology B **23**, 877 (2005).

[300] X. N. Xie, H. J. Chung, C. H. Sow, and A. T. S. Wee, Materials Science and Engineering: R: Reports **54**, 1 (2006).

[301] L. G. Rosa and J. Liang, Journal of Physics: Condensed Matter **21**, 483001 (2009).

[302] F. J. Rubio-Sierra, W. M. Heckl, and R. W. Stark, Advanced Engineering Materials **7**, 193 (2005).

[303] R. D. Piner, J. Zhu, F. Xu, S. Hong, and C. A. Mirkin, Science **283**, 661 (1999).

[304] O. Shekhah, N. Roques, V. Mugnaini, C. Munuera, C. Ocal, J. Veciana, and C. Wöll, Langmuir **24**, 6640 (2008).

[305] O. Shekhah, H. Wang, M. Paradinas, C. Ocal, B. Schupbach, A. Terfort, D. Zacher, R. A. Fischer, and C. Wöll, Nature Materials **8**, 481 (2009).

[306] V. Mugnaini, M. Paradinas, O. Shekhah, N. Roques, C. Ocal, C. Wöll, and J. Veciana, Journal of Materials Chemistry C **1** (2013).

[307] S. Xu and G.-y. Liu, Langmuir **13**, 127 (1997).

[308] E. Barrena, E. Palacios-Lidón, C. Munuera, X. Torrelles, S. Ferrer, U. Jonas, M. Salmeron, and C. Ocal, Journal of the American Chemical Society **126**, 385 (2004).

[309] S. F. Lyuksyutov, R. A. Vaia, P. B. Paramonov, S. Juhl, L. Waterhouse, R. M. Ralich, G. Sigalov, and E. Sancaktar, Nature Materials **2**, 468 (2003).

[310] H. C. Day and D. R. Allee, Applied Physics Letters **62**, 2691 (1993).

[311] C. Moreno, C. Munuera, S. Valencia, F. Kronast, X. Obradors, and C. Ocal, Nano Letters **10**, 3828 (2010).

[312] R. Ruiz, D. Choudhary, B. Nickel, T. Toccoli, K.-C. Chang, A. C. Mayer, P. Clancy, J. M. Blakely, R. L. Headrick, S. Iannotta, and G. G. Malliaras, Chemistry of Materials **16**, 4497 (2004).

[313] S. E. Fritz, S. M. Martin, C. D. Frisbie, M. D. Ward, and M. F. Toney, Journal of the American Chemical Society **126**, 4084 (2004).

[314] R. Ruiz, A. C. Mayer, G. G. Malliaras, B. Nickel, G. Scoles, A. Kazimirov, H. Kim, R. L. Headrick, and Z. Islam, Applied Physics Letters **85**, 4926 (2004).

[315] V. Kalihari, E. B. Tadmor, G. Haugstad, and C. D. Frisbie, Advanced Materials **20**, 4033 (2008).

[316] A. Salleo, Materials Today **10**, 38 (2007).

[317] A. M. Nardes, R. A. J. Janssen, and M. Kemerink, Advanced Functional Materials **18**, 865 (2008).

[318] R. Haag, M. A. Rampi, R. E. Holmlin, and G. M. Whitesides, Journal of the American Chemical Society **121**, 7895 (1999).

[319] P. G. Collins, M. Hersam, M. Arnold, R. Martel, and P. Avouris, Physical Review Letters **86**, 3128 (2001).

[320] J. Y. Huang, S. Chen, S. H. Jo, Z. Wang, D. X. Han, G. Chen, M. S. Dresselhaus, and Z. F. Ren, Physical Review Letters **94**, 236802 (2005).

[321] G. Jiang, A. Baba, and R. Advincula, Langmuir **23**, 817 (2007).

[322] S. Jegadesan, P. Taranekar, S. Sindhu, R. C. Advincula, and S. Valiyaveettil, Langmuir **22**, 3807 (2006).

[323] S. Y. Jang, M. Marquez, and G. A. Sotzing, Synthetic Metals **152**, 345 (2005).

[324] F. S. Schoonbeek, J. H. van Esch, B. Wegewijs, D. B. A. Rep, M. P. de Haas, T. M. Klapwijk, R. M. Kellogg, and B. L. Feringa, Angewandte Chemie International Edition **38**, 1393 (1999).

[325] T. Kitahara, M. Shirakawa, S.-i. Kawano, U. Beginn, N. Fujita, and S. Shinkai, Journal of the American Chemical Society **127**, 14980 (2005).

[326] C. Wang, D. Zhang, and D. Zhu, Journal of the American Chemical Society **127**, 16372 (2005).

[327] T. Kitamura, S. Nakaso, N. Mizoshita, Y. Tochigi, T. Shimomura, M. Moriyama, K. Ito, and T. Kato, Journal of the American Chemical Society **127**, 14769 (2005).

[328] J. Puigmartí-Luis, V. Laukhin, A. Pérez del Pino, J. Vidal-Gancedo, C. Rovira, E. Laukhina, and D. B. Amabilino, Angewandte Chemie International Edition **46**, 238 (2007).

[329] S. Lei, J. Puigmartí-Luis, A. Minoia, M. Van der Auweraer, C. Rovira, R. Lazzaroni, D. B. Amabilino, and S. De Feyter, Chemical Communications , 703 (2008).

[330] Y. Chen, J. Li, and Z. Xue, Applied Physics A: Materials Science & Processing **77**, 379 (2003).

[331] J. Li, Z. Xue, W. Liu, S. Hou, X. Li, and X. Zhao, Physics Letters A **266**, 441 (2000).

[332] J. Puigmartí i Luis, *Organitzacions de Tetratiafulvalens en Monocapes i Fils*, Ph.D. thesis, Universitat Autònoma de Barcelona- Institut de Ciència de Materials de Barcelona-CSIC (2007).

[333] J. Caro, P. Gorostiza, F. Sanz, and J. Fraxedas, Synthetic Metals **121**, 1417 (2001).

[334] J. F. Farges, *Organic Conductors: Fundamentals and Applications*, edited by M. Dekker (Marcel Dekker, 1994).

[335] P. G. Collins, M. S. Arnold, and P. Avouris, Science **292**, 706 (2001).

Publications

Publications related to the thesis contents

- "Layer-By-Layer Electropeeling of Organic Conducting Material Imaged In Real Time" Carmen Munuera, Josep Puigmartí-Luis, Markos Paradinas, Luis Garzón, David B. Amabilino and Carmen Ocal (*Small*, **2009**, 5, 214 - 220) (DOI: 10.1002/smll.200800878)

- "Tuning the local frictional and electrostatic responses of nanostructured $SrTiO_3$-surfaces by self-assembled molecular monolayers" Markos Paradinas, Luis Garzón, Florencio Sánchez, Romain Bachelet, David B. Amabilino, Josep Fontcuberta and Carmen Ocal (*Physical Chemistry Chemical Physics*, **2010**, 12, 4452 - 4458) (DOI: 10.1039/B924227A)

- "Heterogeneous nanotribological response of polymorphic self-assembled monolayers arising from domain and phase dependent friction" Markos Paradinas, Carmen Munuera, Christophe Silien, Manfred Buck and Carmen Ocal (*Physical Chemistry Chemical Physic*s, **2013**, 15 (4), 1302 - 1309) (DOI:10.1039/C2CP43769D)

Other publications

- "Controlling interpenetration in metal-organic frameworks by liquid phase epitaxy" Osama Shekhah, Hui Wang, Markos Paradinas, Carmen Ocal, Björn Schüpbach, Andreas Terfort, Denise Zacher, Roland A. Fischer and Christof Wöll (*Nature Materials*, **2009**, 8, 481 - 484) (DOI: 10.1038/nmat2445)

- "Tuning the Supramolecular Chirality of One- and Two-Dimensional Aggregates with the Number of Stereogenic Centers in the Component Porphyrins" Patrizia Iavicoli, Hong Xu, Lise N. Feldborg, Mathiu Linares, Markos Paradinas, Sven Stafström, Carmen Ocal, Belen Nieto-Ortega, Juan Casado, Juan T. López Navarrete, Roberto Lazzaroni, Steven De Feyter and David B. Amabilino (*Journal of the American Chemical Society,* **2010**, 132 (27), 9350 - 9362) (DOI: 10.1021/ja101533j)

- "Negative Differential Resistance (NDR) in similar molecules with distinct redox behaviour" Núria Crivillers, Markos Paradinas, Marta Mas-Torrent, Stefan T. Bromley, Concepció

Rovira, Carmen Ocal and Jaume Veciana (*Chemical Communications*, **2011**, 47, 4664 - 4666) (DOI: 10.1039/ C1CC10677E)

- “Effect of Processing Parameters on Performance of Spray-deposited Organic Thin-Film Transistors” Jack W. Owen, Natalia A. Azarova, Marsha A. Loth, Markos Paradinas, Mariona Coll, Carmen Ocal, John E. Anthony and Oana D. Jurchescu (*Journal of Nanotechnology*, **2011**, vol. 2011, Article ID 914510, 6 pages) (DOI: 10.1155/2011/914510)

- “PTM Radicals for Molecular-Based Electronic Devices” Núria Crivillers, Marta Mas-Torrent, Cláudia Simão, Markos Paradinas, Carmen Munuera, Carmen Ocal, Stefan T. Bromley, Concepció Rovira and Jaume Veciana (*Architecture & Design of Molecule Logic Gates and Atom Circuits. Serie: Advances in Atom and Single Molecule Machines.* Springer. **2013**. Editors: Nicolas Lorente and Christian Joachim) (ISBN 978-3-642-33136-7)

- “Surface grafting of a dense and rigid coordination polymer based on tri-para-carboxy- polychlorotriphenylmethyl radical and copper acetate” Veronica Mugnaini, Markos Paradinas, Osama Shekhah, Nans Roques, Carmen Ocal, Christof Wöll and Jaume Veciana (*Journal of Materials Chemistry C*, **2012**) (DOI: 10.1039/C2TC00037G)

- “Influence of the relative molecular orientation on interfacial charge transfer excitons at donor/acceptor nanoscale heterojunctions” Mahdieh Aghamohammadi, Anton Fernández, Malte Schmidt, Ana Pérez-Rodríguez, Alejandro Rodolfo Goñi, Jordi Fraxedas, Guillaume Sauthier, Markos Paradinas, Carmen Ocal and Esther Barrena. *Journal of Physical Chemistry C.* **2014**, 118, 14833 - 14839) (DOI: 10.1021/jp5041579)

- “Room temperature reversible giant piezoresistance in Sr_2IrO_4 thin films at the nanoscale” Neus Domingo, Laura López-Mir, Markos Paradinas, Vaclav Holy, Jakub Zelezny, Di Yi, Siriyara Suresha, Kian Liu, Ramamoorthy Ramesh, Xavi Martí, Carmen Ocal and Gustau Catalan. *Submitted.*

Acknowledgements

In those few lines I would like to express my dear thanks to all the people that have helped me in one way or another in this period of my PhD thesis. In these years I have had the opportunity to learn much, not only about science but also about this... called *life* and even more importantly, about *myself*. In consequence, not only the work presented in this thesis, but also all the experiences, feelings and emotions lived in this period would not have been possible without the support, care, friendship and work of many many people. Many thanks to all of you...

En primer lugar me gustaría agradecer a Carmen Ocal por haberme dado la oportunidad de trabajar y aprender tanto formando parte de su grupo de investigación. Por su contagiosa dedicación y entusiasmo que tiene por la ciencia, y sobre todo, por su confianza, cercanía y infinita infinita paciencia[2] . Carmen...tantos años dan para mucho y por supuesto que ha habido momentos mejores y peores, cosas buenas y no tan buenas, pero supongo que de todo se aprende y estoy agradecido por todo ello. Solo me gustaría decirte que me lo he pasado muy bien, que creo que he aprendido muchas cosas y que he disfrutado mucho durante todos estos años. Aunque...para que negarlo, donde más he disfrutado y donde *más en casa* me siento es en el labo! Que sepas que sonrío cuando pienso en ello.

Tanto en mí llegada al ICMAB como en estos últimos años, he tenido la suerte de contar con el apoyo de dos compañeras de grupo entusiastas en el trabajo y alegres un día sí y otro también. Creo que cada una en su tiempo y a su manera ha jugado un papel fundamental para mí durante estos años y para el trabajo que se presenta aquí. Gracias Carmen Munuera por todo tu apoyo. Los comienzos nunca son fáciles, pero creo que yo tuve la suerte de tener a mi lado a la mejor profesora de SFM que se pueda tener en el labo. Gracias por la paciencia durante esos primeros meses, por toda esa confianza que se puede transmitir también a través del skype en los siguientes

---

[2] La repetición de la palabra *infinita* no ha sido un error de escritura.

años, por las cervezas en Stuttgart, por esas charlas de *último empujón* en Bilbao y Barcelona y... por todo lo demás! Gracias Esther Barrena por tu apoyo, tus ánimos y tu constante alegría en el trabajo. Gracias por todas las discusiones sobre microscopías y moleculillas. Por haberme recibido con los brazos abiertos en Stuttgart, por animarme a abrirlos a mí en algunos otros casos y a dar puntapies en otros.

Un agradecimiento especial se merece también la rama masculina del grupo. Un tándem de *hermanos mayores* que también, cada uno a su manera, me ha ayudado mucho. Gracias a César Moreno por haberme transmitido toda su confianza desde el primer día, por animarme a ser valiente (aunque tenga la sensación de no haberlo sido nunca), por estar siempre disponible para tratar sobre estos temas *subterráneos* que nos acompañan en este mundo académico y sobre todo, por su amistad. Muchas gracias también a mi yin yan particular Lucho (Luis Garzón), compañero inseparable durante unos cuantos años. Qué bien me lo pasé y cuando me reí a tu lado Luchin, cuantos buenos momentos en el labo... gracias por tu constante serenidad, tus consejos sobre la vida, por intentar transmitirme que en la vida hay que mirar siempre para adelante (estoy en proceso de aprendizaje todavía) y que aunque parezca que no, con esa pausa y poca a poco se va haciendo camino... gracias también... por haberme enseñado un nuevo Castellano!

Muchas gracias también a las nuevas generaciones del grupo. Gracias a Ana Pérez, Sonia Matencio, Mahdieh Aghamohammadi, Anton Fernández, Laura López Mir y Ivan Nikitski. Porque creo que he aprendido también mucho trabajando con vosotros, por todo vuestro cariño y todos esos ánimos.

Un agradecimiento especial también a Veronica Mugnaini. Grazie mille por todo lo que me has enseñado de *cosillas* del laboratorio, preparación de soluciones, las bombas etc... Por todo lo que hemos trabajado juntos, incluso hasta aquellas horas intempestivas en Bessy...

Quiero agradecer a mis compañeros y amigos del ICMAB por haberme hecho sentirme tan a gusto en esta *casa* durante todos estos años. Gracias especialmente a aquellos con los que he convivido más en el despacho, labo, pasillos, comedor...entre ellos en especial a Ángela, Wojtek, María, Cristina, Marta R., Alessandro, Jone, Marta V., Jaume, Mariona, Evelyn, Cesar, Elisa, Nico, Oriol, Josep, Romen, Carlos, Laura, Marixa, Ana, Nerea, Anna, Xavi, etc...

I would also like to thank the people of the Organic group for their help and friendship during my stay in the Max-Planck Institute für Metallforschung of Stuttgart. Specially, I would like thank

Esther Barrena, Carmen Munuera, Tobias Krauss , Felix Maye and Minh Nguyen for making my stay in Stuttgart worthy and entertaining.

I would like to thank Prof. Manfred Buck for giving me the opportunity of working at his group in the School of Chemistry of the University of St Andrews. Many thanks to Zhe She and Dr. Isabella Cebulla for teaching and helping me in the use and practice of the STM, and for their unforgettable golf lessons.

I would like to specially acknowledge the people from other groups that contributed to the results presented in this thesis (in order of chapters...): Prof. Manfred Buck, Dr. Christophe Silien, Prof. Josep Fontcuberta, Dr. Florencio Sánchez, Dr. Romain Bachelet, Prof. David B. Amabilino and Dr. Josep Puigmartí-Luis.

In parallel to the PhD project, during those years I also had the chance to work with many different people from different groups on variety of systems. The list is long and therefore I'll skip the possibility of forgetting someone, but I just want you to know that I feel grateful for having the opportunity of working and discussing the scientific results with all of you.

Me gustaria agradecer también a toda la gente de Nanotec Electrónica, por estar siempre dispuestos a ayudar y intentar resolver cualquier duda sobre los microscopios y por socorrerme en momentos puntuales incluso para poder tratar con el WSxM las imagenes de STM obtenidas con otro instrumento. Gracias especialmente a Adriana, Pablo y Nacho.

Gracias también al Prof. Jordi Pascual por haber sido mi tutor de tesis, por las agradables conversaciones que hemos tenido en momentos puntuales, por sus buenos consejos (que no siempre he cumplido) y por haberme facilitado los trámites administrativos.

Gracias a los miembros del tribunal, Carmen Morant, Imma Ratera, Dimas Garcia de Oteyza, Albert Verdaguer y César Moreno por su disposición para conformarlo.

Many thanks to my friend Etor Emanuel Lucio for helping me with the cover drawing.

For financial support I would like to thank to EU project under contract No. NMP4-CT-2006-032109 (STREP "SURMOF"), that under its contract I could join Carmen's group for my Master Degree period. I would also like to thank the Spanish Ministery project CONSOLIDER CSD2007-00041 Nanoselect project. Special thanks to the Spanish Ministery of Science and Innovation (Ministerio de Ciencia e Innovación-MICINN) for the FPI fellowship (reference number BES-2008-003588 under the project MAT2007-62732) under its finacial support I have carried out my research

activity that yields to this PhD thesis.

No por la consecución de esta tesis, sino simplemente porque es una buena oportunidad para dejar por escritas unas cuantas verdades, quiero dedicar estas próximas lineas a toda esa gente que forma mi entorno *de ahí afuera*, fuera de la ciencia.

Gracias a todos mis amigos. Especialmente: Nire betiko-betirako Donostiko lagunei, Artz, Mansoa, Iñaki eta Anna, Eneko, Iker, Ander, Aitor,... Bilboko Physics Crew-ri! A toda esa kuadrilla de Madrid, muy especialmente a Anartz, Etor, Miguel, Fernando,...A los amigos con los que he compartido estos últimos años en Barcelona. A Ledicia, Marina y Nacho, por haberme recibido con los brazos abiertos en Barcelona. Un gran abrazo se merece la familia Bargentina: Mery, Nazarena, Carolina, Nacho, Pablo, Matias, Carmen, Filipo y Zoe, que bueno ha sido el encontrarnos! Gracies tambe al meus amics del Horta esportiva, molt especialment a los compains de grup de corredors. Gracias también a Fran y Carles, por toda vuestra confianza y por todo lo que se aprende a vuestro lado.

Un agradecimiento muy especial a María. Gracias por haber estado a mi lado en esta última temporada de *empujón final*, por haberme abrazado, escuchado, aceptado y ayudado durante todo este tiempo.

Milesker berezi bat Oihane-ri... milesker elkarrekin egon garen urte guzti horietan lagundu nauzun guztiagatik, zure besoetan ain maitatua sentituarazteagatik... Oraindik guztiz ulertu ezin ditudan arrazoiengatik bizitzak bide ezberdinak hartzera eraman gaituen arren erarenbatean beti beti beti nire barrenean izango zarelako, niretzat beti *hor* zaudelako, muxu bat.

Por último, el agradecimiento más especial es para toda mi familia. A una parte eta besteari, alde bati y a la otra. Por ser como sois, por vuestro cariño y apoyo incondicional. Milesker beti nire aldamenean egoteagatik, zuen laguntza eta maitasun guztia eskeintzeagatik.

Bereziki.... eskerrikasko nire Ama eta Aitari, gertatzen dena gertatzen dela beti beti hor zaudetelako eta zuen seme izateaz arro sentitzen naizelako. Muxu handiena zuentzako.

Eta mila esker eta besarkada handiena nire anai *gazte-handi* Iosu-ri. Milesker inork baino hobeto gure izana ulertzeagatik eta gehienetan fisikoki urrun egon arren zure gertutasuna beti sentiarazteagatik. Aupa hi!!!

Mmm..... eheheh.....

Y gracias, ¡¿por qué no?!, al bosque de Collserola. Gracias por tan buenos momentos en bici, en moto, a pie o corriendo; con los calores del verano, *frio* del invierno o tormentas de primavera; por los jabalís, zorros, perdices y conejos; por todos esos tonos verdes mediterráneos a los que no estaba habituado. Has sido una válvula de escape difícilmente reemplazable!!!

Horta, Setembre 2014